

Copyright
by
Mark Christopher Jesick
2012

The Dissertation Committee for Mark Christopher Jesick
certifies that this is the approved version of the following dissertation:

**Optimal Lunar Orbit Insertion from a Free Return
Trajectory**

Committee:

Cesar Ocampo, Supervisor

Wallace Fowler

David Hull

Belinda Marchand

Ryan Russell

**Optimal Lunar Orbit Insertion from a Free Return
Trajectory**

by

Mark Christopher Jesick, B.S., M.S.

DISSERTATION

Presented to the Faculty of the Graduate School of
The University of Texas at Austin
in Partial Fulfillment
of the Requirements
for the Degree of

DOCTOR OF PHILOSOPHY

THE UNIVERSITY OF TEXAS AT AUSTIN

May 2012

Acknowledgments

First and foremost, I thank my advisor, Cesar Ocampo, for providing invaluable direction and guidance in my research and my career. His courses inspired me to pursue my degree in spacecraft trajectory design and optimization. I also thank the other members of my dissertation committee for reviewing my work and offering feedback.

This research was funded primarily by the National Aeronautics and Space Administration's Graduate Student Researchers Program through Johnson Space Center. I thank Jerry Condon for serving as technical advisor on this grant and for several discussions about my research. Through discussions, questions, and comments, many others have helped me along the way to this degree, including Ryan Whitley and Juan Senent at Johnson Space Center. I also thank Jacob Williams for originally starting me on this research topic.

Byron Tapley of the University of Texas at Austin deserves my thanks for funding me as a graduate research assistant for two years at the Center for Space Research. My friends at UT have also contributed to this work through discussions and feedback.

I thank my parents for their support and for fostering in me a love of education and a drive to achieve my goals. Finally, I thank my fiancée for her love and inspiration.

Optimal Lunar Orbit Insertion from a Free Return Trajectory

Mark Christopher Jesick, Ph.D.
The University of Texas at Austin, 2012

Supervisor: Cesar Ocampo

With the discovery of water ice at the moon's south pole, future human lunar exploration will likely occur at polar sites and, therefore, require high inclination orbits. Also of importance for human missions is the capability to abort if unfavorable circumstances arise. This dissertation addresses both of these concerns by creating an automated, systematic architecture for constructing minimum propellant lunar orbit insertion sequences while ensuring crew safety by maintaining a ballistic Earth return trajectory. To ensure a maneuver-free abort option, the spacecraft is required to depart Earth on a free return trajectory, which is a ballistic Earth-moon-Earth segment that requires no propulsive maneuvers after translunar injection. Because of the need for global lunar access, the required spacecraft plane change at the moon may be large enough that a multi-maneuver sequence offers cost savings. The combination of this orbit insertion sequence with the free return orbit increases the likelihood of a safe Earth return for crew while not compromising the ability to achieve any lunar orbit.

A procedure for free return trajectory generation in a simplified Earth-moon system is presented first. With two-body and circular restricted three-body models, the algorithm constructs an initial guess of the translunar injection state and time of flight. Once the initial trajectory is found, a square system of nonlinear equations is solved numerically to target Earth entry interface conditions leading to feasible free return trajectories. No trial and error is required to generate the initial estimate. The automated algorithm is used to generate families of free return orbits for analysis.

A targeting and optimization procedure is developed to transfer a spacecraft from a free return trajectory to a closed lunar orbit through a multi-maneuver sequence in the circular restricted three-body model. The initial estimate procedure is automated, and analytical gradients are implemented to facilitate optimization. Cases are examined with minimum time, variable symmetric, and general free returns. The algorithm is then upgraded to include a more realistic solar system model with ephemeris-level dynamics. An impulsive engine model is used before conversion to a finite thrust model. Optimal control theory is applied and the results are compared with the linearly steered thrust model. Trends in the flight time and propellant for various orbit insertion sequences are analyzed.

Table of Contents

Acknowledgments	iv
Abstract	v
List of Tables	xi
List of Figures	xii
Chapter 1. Introduction	1
1.1 Background	4
1.2 Document Organization	7
Chapter 2. Spacecraft Dynamics in the Earth-Moon System	9
2.1 Circular Restricted Three-Body Model	9
2.1.1 Scaling	11
2.1.2 Variational Equations	12
2.2 Four-Body Model	14
2.2.1 Variational Equations	16
2.3 Other Perturbations	18
2.3.1 Earth Oblateness	18
2.3.2 Solar Radiation Pressure	20
2.3.3 Variational Equations	20
2.4 Reference Frames	21
Chapter 3. Free-Return Trajectories in the Earth-Moon System	24
3.1 Background	24
3.2 Theorem of Image Trajectories	27
3.3 Lunar Flyby Geometry	31
3.4 Initial Estimate	32

3.5	Numerical Targeting	35
3.5.1	Continuation Method	36
3.6	Symmetric Free Returns	37
3.7	General Free Returns	48
Chapter 4. Optimal Spacecraft Trajectories		56
4.1	Introduction	56
4.2	Parameter Optimization	57
4.2.1	Optimization Algorithms	59
4.2.2	Analytical Gradients	61
4.2.2.1	Gradient Validation	67
4.2.3	Scaling	68
4.3	Optimal Control Theory	70
4.3.1	Optimal Thrust Pointing	74
4.3.1.1	Switching Function Evolution	77
4.3.2	Adjoint Control Transformation	81
4.3.3	Optimal Control Variational Equations	84
Chapter 5. Lunar Orbit Insertion from a Free Return in the Three-Body Model		87
5.1	Initial Estimate	88
5.2	Lunar Orbit Insertion from a Fixed Free Return	102
5.2.1	Optimization Algorithm	102
5.2.2	Numerical Optimization Setup	105
5.2.3	Analytical Gradients	105
5.2.4	Numerical Results	110
5.2.5	Retargeting Time Variation	115
5.3	Lunar Orbit Insertion from a Variable Symmetric Free Return	117
5.3.1	Optimization Algorithm	117
5.3.2	Analytical Gradients	120
5.3.3	Numerical Results	125
5.4	Lunar Orbit Insertion from a General Free Return	133
5.4.1	Optimization Algorithm	135

5.4.2	Analytical Gradients	137
5.4.3	Numerical Results	138
Chapter 6.	Lunar Orbit Insertion from a Free Return in the Four-Body Model	144
6.1	Lunar Orbit Insertion with an Impulsive Engine Model	144
6.1.1	Numerical Algorithm	145
6.1.2	Initial Estimate	147
6.1.3	Free Return Targeting Strategy	149
6.1.4	Analytical Gradients	149
6.1.5	Numerical Results	152
6.1.6	Algorithm Extensions	162
6.1.6.1	Epoch Variation	163
6.1.6.2	Force Model Extension	164
6.1.6.3	Multi-Objective Optimization	165
6.2	Lunar Orbit Insertion with a Finite Thrust Engine Model	167
6.2.1	Impulse Conversion	170
6.2.2	System Dynamics	171
6.2.3	Analytical Gradients	173
6.2.4	Numerical Results	177
6.2.5	One-Burn Lunar Orbit Insertion	181
6.3	Lunar Orbit Insertion with an Optimal Control Finite Thrust Engine Model	183
6.3.1	System Dynamics	183
6.3.2	One-Burn Formulation	185
6.3.2.1	Analytical Gradients	187
6.3.2.2	Numerical Results	189
6.3.3	Three-Burn Formulation	192
6.3.3.1	Numerical Results	195
Chapter 7.	Conclusions	197
7.1	Summary	197
7.2	Final Conclusions	200

Appendices	202
Appendix A. Gravitational Potential	203
A.1 Spherical Harmonics	203
A.2 Oblateness Acceleration	209
Appendix B. Lunar Flyby Velocity	211
Appendix C. Optimal Control Necessary Conditions	214
Appendix D. R and C Matrix Notation	218
Appendix E. Ideal Rocket Equation	220
E.1 Changing Mass Systems	220
E.2 Rocket Equation	222
Bibliography	225
Vita	235

List of Tables

2.1	Four-body model parameters	15
3.1	Free return classification	40
5.1	Free parameters for fixed free return example case	113
5.2	Constraints for fixed free return example case	113
5.3	Maximum flyby azimuth for type 1 free returns	121
5.4	Maximum flyby latitude for type 2 free returns	121
5.5	Optimal parameters for variable symmetric example	130
5.6	Constraints for variable symmetric example	131
5.7	Free parameters for general free return example case	142
5.8	Constraints for general free return example case	143
6.1	Spacecraft accelerations at EEI	166

List of Figures

1.1	Apollo 13 service module	2
1.2	Free return and lunar orbit insertion	3
2.1	Barycentered CRTBP rotating reference frame	11
2.2	Lunar geometry variations	15
2.3	Lunar acceleration difference	17
2.4	Rotating reference frame	23
3.1	Free return trajectory	26
3.2	Image trajectories	30
3.3	Lunar flyby parameterization	31
3.4	Two-body initial estimate	34
3.5	Free parameters and constrained quantities	36
3.6	Symmetric free return targeting algorithm	38
3.7	Type 1 free return	39
3.8	Type 2 free return	39
3.9	Planar circumlunar free returns	41
3.10	Planar cislunar free returns	42
3.11	Circumlunar free return families	44
3.12	Cislunar free return families	45
3.13	Type 1 free return surfaces	46
3.14	Type 2 free return surfaces	47
3.15	Asymmetric free return	50
3.16	General free return flight time	53
3.17	General free return TLI impulse	54
3.18	General free return EEI velocity	55
4.1	Transfer segments with three state discontinuities	64

4.2	General transfer segments with n ballistic arcs	67
4.3	Orbit transfer problem	78
5.1	Earth to moon transfer	89
5.2	LLO orientation	96
5.3	Initial estimate	99
5.4	Initial estimate cost	100
5.5	Feasible LOI sequence cost	101
5.6	Transfer segments	106
5.7	Initial and feasible LOI sequence	111
5.8	Optimal hybrid Earth to moon transfer	112
5.9	Minimum LOI cost contours with fixed free return formulation	115
5.10	Effect of variable retargeting time	116
5.11	Maximum out-of-plane free return angle	120
5.12	Type 1 free return and LOI	127
5.13	Type 2 free return and LOI	129
5.14	Effect of maximum free return flight time on LOI sequence	132
5.15	Type 1 free return LOI ΔV contours	134
5.16	Type 2 free return LOI ΔV contours	134
5.17	General free return and LOI	141
5.18	LOI cost contours with general free return formulation	142
6.1	Initial estimate position error at patch point	148
6.2	Minimum hybrid mission LOI cost	152
6.3	Hybrid trajectory for the maximum ΔV requirement	156
6.4	Hybrid trajectory for the minimum ΔV requirement	156
6.5	Additional views for the maximum cost hybrid trajectory	157
6.6	Additional views for the minimum cost hybrid trajectory	158
6.7	LOI cost and relative declination	159
6.8	LOI cost and flight time	159
6.9	Free return types	160
6.10	LOI cost as a function of free return flight time	161
6.11	Retargeting maneuver magnitude variation	161

6.12	Epoch variation and LOI cost	164
6.13	Effect of Earth oblateness and solar radiation pressure	165
6.14	Multi-objective optimization example	168
6.15	Impulse to finite burn conversion	172
6.16	Finite burn node nomenclature	175
6.17	Maximum propellant finite burn hybrid trajectory	179
6.18	Hybrid mission propellant mass contours	180
6.19	Minimum propellant mass comparison with rocket equation	180
6.20	Two-burn lunar orbit insertion	182
6.21	One-burn lunar orbit insertion	182
6.22	One-burn optimal control lunar orbit insertion	190
6.23	Switching function evolution for one-burn formulation	191
6.24	Three-burn optimal control lunar orbit insertion	196
A.1	General gravitating body	204
B.1	Basis transformation	212
E.1	Changing mass system	220
E.2	Rocket and control volume	223

Chapter 1

Introduction

No matter what technology is developed, space travel is inherently more dangerous for humans than travel on the surface of the Earth and within its atmosphere. Due to the challenges of surviving in space—including the hazards of weightlessness, solar radiation, cosmic radiation, micrometeoroids, and temperature extremes—humans must be adequately shielded from the environment and be equipped with supplies for the duration of the mission. If adverse circumstances arise that threaten the spacecraft or the crew, it is necessary to return to Earth to increase the probability of survival. Examples of adverse circumstances include incomplete engine firing, loss of propulsive power, and shortage of crew consumables. Due to these challenges, it is prudent to anticipate problems and design missions with abort options that provide a safe return to Earth. On the Apollo 13 flight to the moon, for example, an oxygen tank exploded on the service module (Fig. 1.1). Had it not been for abort planning, the mission may have resulted in loss of life. Mission abort planning, therefore, is a necessary component of human spaceflight; it can also assuage the fears of those who question whether the risks of human space exploration are worth the rewards.

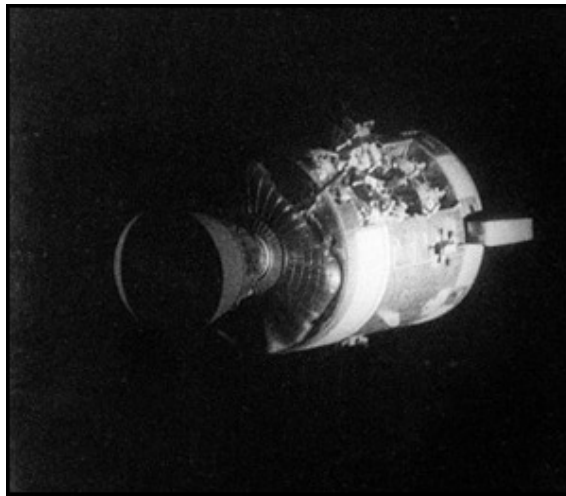


Figure 1.1: Apollo 13 service module after the explosion of an oxygen tank.¹

Contingency planning is necessary for all phases of flight, including launch, ascent, orbit, descent, and landing, for both Earth-orbiting missions and missions beyond Earth orbit. This dissertation deals specifically with orbital abort planning for human lunar missions. For these missions in the Earth-moon system, both direct returns and lunar flybys can be used to return astronauts to Earth ahead of the nominal return time. One abort option utilizes the free return trajectory, a ballistic Earth-moon-Earth segment that requires no propulsive maneuvers after Earth departure. Apollo 12–14 used a hybrid free return profile where the spacecraft remained on a free return trajectory from translunar injection (TLI) until later retargeting for lunar orbit insertion (LOI). Figure 1.2 shows an overview of the hybrid mission where four maneuvers are used to transfer the spacecraft from the free

¹Image available at http://www.jsc.nasa.gov/jscfeatures/photos/Apollo13_35th/as13-59-8500.jpg [accessed 25 April 2012].

return to the closed lunar parking orbit. The time spent on the free return—where a maneuver-free Earth return is guaranteed—affords a period to evaluate spacecraft systems before deciding to retarget for lunar orbit. Apollo missions targeted near-equatorial lunar landing sites and, thus, did not require as much plane change as may be necessary to reach high inclination orbits. The discovery of water ice at the moon’s south pole [1–3], most recently confirmed by the Lunar Crater Observation and Sensing Satellite mission [4,5], will likely focus future human lunar exploration at polar sites and require high inclination lunar orbits [6]. Though many abort strategies exist, the use of a free return trajectory is attractive because no propulsive maneuvers are required to return to Earth. Thus, if all forces acting on the spacecraft could be modeled perfectly, no maneuvers would be required for the spacecraft to reach the targeted Earth entry interface conditions by flying on the free return. But it is impossible to perfectly model all spacecraft perturbations; therefore, mid-course trajectory correction maneuvers are required to achieve a specified final state. These maneuvers, when performed beginning on a free return, will be smaller in magnitude than those required for Earth return from a non-free return path [7].

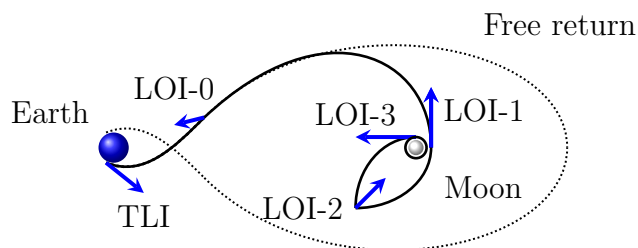


Figure 1.2: Free return and lunar orbit insertion.

1.1 Background

Much post-TLI abort planning and trajectory design for lunar missions was done during the Apollo program since this was the only time to date where humans have traveled beyond low Earth orbit. In 1962, Braud [8] examined impulsive aborts from a planar, circumlunar free return trajectory in the circular restricted three-body problem (CRTBP) with a maximum propulsive capability of 2500 m/s. Trends in time from abort to reentry, reentry velocity, and maximum distance from Earth after abort were documented. Abort points were considered on both the outbound and inbound legs of the free return. Braud found that aborts from the inbound leg are inadvisable because of small reductions in return time and unacceptably high reentry velocities. Kelly and Adornato [9] used an impulsive engine model with two-body and four-body force models to study single-maneuver aborts from the outbound leg of a circumlunar free return. Merrick and Callas [10] performed similar work for aborts on both the outbound and inbound legs of a reference circumlunar trajectory. In 1966, Foggatt [11] explored two-impulse time-critical abort trajectories with a patched conic method. Laszlo [12] examined two- and three-impulse transearth aborts from an elliptic lunar orbit following a partially failed LOI capture maneuver. Babb [13, 14] studied the use of single- and multiple-impulse aborts to a transearth trajectory in the event of LOI failure from a non-free return trajectory. The analysis assumed a total loss of the service propulsion system (SPS) main engine, requiring the use of the lunar module's (LM) descent propulsion system (DPS) that would nominally be used for descent to the lunar surface. Because of the DPS's limited performance capability relative to the SPS, Babb proposed

to jettison the entire service module (SM) to increase the effective ΔV produced by the DPS, allowing the LM to perform the transearth injection (TEI) maneuver. In 1968, Weber [15] analyzed contingency scenarios during and immediately following the TLI maneuver, and Weber and Fuller [16] researched minimum time and minimum fuel aborts. At the end of Apollo’s lunar missions, Hyle, Foggatt, and Weber [17] summarized strategies for managing emergencies in every mission phase, from launch through Earth return. This is not an exhaustive list of all abort planning done during this period;² for example, see Refs. [18–22]. More recently, Senent [7, 23] considered the targeting of direct and lunar flyby return trajectories during partially failed TLI, post-TLI, and partially failed LOI abort scenarios using pseudostate theory [24].

Most of the aforementioned works focus on abort scenarios from a pre-computed nominal trajectory—typically a circumlunar free return—without discussing the method of how the free return is constructed. Early work was done by Egorov [25] who documented two-dimensional circumlunar trajectories in the CRTBP. Work in the United States on lunar free returns supported the Apollo requirement of a safe Earth return option for astronauts. Penzo [26] researched circumlunar free returns with patched conic techniques. Schwaniger [27] targeted free returns in the CRTBP, and Gibson [28] combined patched conic and multi-body models to generate circumlunar free returns. More recently, Miele, Wang,

²In 1963, AT&T established Bellcomm, Inc. to support NASA with engineering analysis for human spaceflight programs. The extensive research Bellcomm performed, including work on lunar free returns and abort planning, was archived by the National Air and Space Museum. A listing of the collection contents is available at http://www.nasm.si.edu/research/arch/findaids/bellcomm/bci_sec_1.html [accessed 15 March 2012].

and Mancuso [29] studied optimal lunar free return trajectories with the restricted three-body model. Trends in the injection velocity and flight time of circumlunar free returns have been extensively reported, but less discussion has been devoted to free return generation. Gibson and Penzo outline schemes to construct posigrade, circumlunar trajectories with a finite sphere of influence patched conic model. The algorithm discussed in this dissertation is applicable to all symmetric and asymmetric single-flyby free return types. The simplicity of this method relies on a Keplerian initial estimate and a numerical algorithm that utilizes a continuation method to adjust the altitude and orientation of the trajectory at lunar flyby.

Much LOI work was also done during the Apollo program. For example, Corey [30] discussed the merits of one- and two-burn insertion strategies, and Jenkins and Munford [31] used a two-body model to estimate propulsive requirements to enter a retrograde lunar orbit. More recently, LOI strategies have been documented for a series of robotic lunar missions, such as the Lunar Reconnaissance Orbiter [32] and the Gravity Recovery and Interior Laboratory (GRAIL) mission [33]. The GRAIL spacecraft used a modified ballistic lunar capture strategy for LOI [34–36]. Though this method reduces the propulsive requirements for LOI, it is probably undesirable for human missions due to an increased flight time which increases the amount of crew consumables and complicates problems such as propellant boil-off [37, 38], if cryogenic fuels are used. With application to human lunar missions, Garn, Qu, and Chrone, et al. [39] and Condon [40] explored the design and optimization of three-burn LOI sequences for high latitude sites without a free return requirement. A goal of the present research is to study the cost of using the hybrid

free return trajectory for a range of target low lunar orbits, including high inclination orbits. This dissertation will outline an automated, systematic architecture for constructing minimum fuel LOI sequences while maintaining the ballistic Earth return option and allowing the free return geometry to vary during the optimization process.

1.2 Document Organization

This dissertation contains six chapters. The second describes the dynamics of spacecraft in the Earth-moon system for each force model used. Chapter 3 presents an algorithm for the generation of lunar free returns and examines the characteristics of a broad range of these trajectories, including circumlunar, cis-lunar, and asymmetric free returns. A proof of the symmetry properties of the CRTBP is given because the properties are useful in the generation of symmetric free returns. The work on symmetric free returns was previously published by the author in Ref. [41]. In Chapter 4, an overview of numerical optimization is given along with the optimality conditions. The differential of a general n -segment trajectory with $n + 1$ state discontinuities is derived for later use in developing analytical gradients. Numerical issues such as scaling and choice of optimizer are discussed. Finally, the necessary conditions for the optimal control problem are presented along with an adjoint control transformation to estimate the costates based on linearly steered finite thrust maneuvers. Chapter 5 presents the optimization of lunar orbit insertion from a free return trajectory in the CRTBP. The first case, published by the author in Ref. [42], utilizes the minimum time free return that remains fixed

throughout the optimization process. The second case, published by the author in Ref. [43], requires the free return to remain symmetric but allows it to move out of the Earth-moon plane and vary during optimization. The final case allows the free return to vary asymmetrically. All cases in this chapter utilize an impulsive engine model. Chapter 6 transitions optimal solutions from the CRTBP to the ephemeris model and adds a finite thrust spacecraft engine. These results were presented by the author in Ref. [44]. Example cases are also shown with a variable mission epoch and the addition of accelerations due to an aspherical Earth and solar radiation pressure. Finally, an optimal control propulsion model is applied to enable further propellant savings.

Chapter 2

Spacecraft Dynamics in the Earth-Moon System

This chapter presents the dynamics of spacecraft in the Earth-moon system and develops the linearized variational equations associated with the dynamics. The two primary dynamical models used in this investigation are the circular restricted three-body problem (CRTBP) and the four-body problem. The CRTBP is used to provide an adequate initial estimate of free returns and lunar orbit insertion (LOI) sequences in the more realistic solar system model, and the four-body model captures the primary forces affecting the spacecraft—the gravitational forces of the Earth, moon, and sun. The forces due to the Earth’s oblateness and solar radiation pressure are also considered. The chapter concludes with a discussion of the reference frames used for numerical integration and visualization throughout this investigation.

2.1 Circular Restricted Three-Body Model

The motion of a spacecraft in the Earth-moon system is first approximated with the CRTBP. The spacecraft of negligible mass travels under the gravitational attraction of the Earth and moon, which move about their barycenter in circular orbits at constant angular velocity. The origin of a rotating frame of reference is placed at the Earth-moon barycenter with the $\hat{x}\hat{y}$ plane representing the plane of

Earth and moon revolution about their center of mass. The $\hat{\mathbf{x}}$ axis is coincident with the Earth-moon line, positive in the direction from the Earth to the moon; the $\hat{\mathbf{y}}$ axis is positive in the direction of the moon's velocity; and the $\hat{\mathbf{z}}$ axis completes the right-handed coordinate system and is coincident with the system's angular momentum. The acceleration of a spacecraft in this system is

$$\ddot{\mathbf{r}} = -\frac{\mu_E}{r_{EP}^3}\mathbf{r}_{EP} - \frac{\mu_M}{r_{MP}^3}\mathbf{r}_{MP} - 2\boldsymbol{\omega} \times \dot{\mathbf{r}} - \boldsymbol{\omega} \times (\boldsymbol{\omega} \times \mathbf{r}) \quad (2.1)$$

where μ_E and μ_M are the gravitational parameters of the Earth and moon, \mathbf{r}_{EP} and \mathbf{r}_{MP} are the Earth-spacecraft and moon-spacecraft vectors, $\boldsymbol{\omega}$ is the angular velocity of the rotating frame, $\dot{\mathbf{r}}$ is the spacecraft velocity, and \mathbf{r} is the spacecraft position relative to the Earth-moon barycenter. The system's angular velocity is

$$\boldsymbol{\omega} = \sqrt{\frac{\mu_E + \mu_M}{r_{EM}^3}} \hat{\mathbf{z}} \quad (2.2)$$

The physical constants used in this model are $r_{EM} = 384400$ km, $\mu_E = 3.986 \times 10^5$ km³/s², $\mu_M = 4.9 \times 10^3$ km³/s², $R_E = 6378$ km, and $R_M = 1738$ km, where R_E and R_M are the radii of the Earth and moon.¹ An extensive description of the CRTBP is presented by Szebehely [45].

Because the eccentricity of the moon's orbit about the Earth is approximately 0.05, and because of the sun's influence, the circular model is inadequate in accurately describing the Earth-moon system dynamics. This dissertation will show, however, that the converged trajectories constructed in the CRTBP are adequate as an initial estimate in the ephemeris model even with the addition of solar

¹Data available at <http://nssdc.gsfc.nasa.gov/planetary/factsheet/moonfact.html> [accessed 15 March 2012]

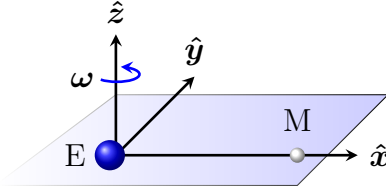


Figure 2.1: Barycentered CRTBP rotating reference frame.

gravity, Earth-oblateness effects, and solar radiation pressure. One advantage of the CRTBP when transitioning to a more realistic model is the ability to scale the Earth-moon distance to match the true value at any chosen epoch.

2.1.1 Scaling

The mass ratio μ_M/μ_E uniquely defines the system dynamics of the CRTBP. If the Earth-moon distance changes while the mass ratio remains the same, an equivalent trajectory in a system with $r_{EM}(t_1)$ is a dilation of the equivalent trajectory in the other system with $r_{EM}(t_2) \neq r_{EM}(t_1)$. This is useful because a hybrid free return and LOI trajectory in the base system with $r_{EM} = 384400$ km can be scaled to the actual Earth-moon distance at a given epoch.

In the CRTBP, the distance unit is the distance between the two primaries, denoted r_{EM} in the Earth-moon system. Because the moon's orbit is not circular, r_{EM} is a function of time in the ephemeris model. Thus, the required scaling in distance units from the Earth-moon system at time t_1 to the system at time t_2 is

$$\frac{DU_2}{DU_1} = \frac{r_{EM}(t_2)}{r_{EM}(t_1)} \quad (2.3)$$

where DU_i represents the distance unit of the circular restricted system at t_i . The

time unit in the CRTBP is based on the system's angular velocity. One time unit is defined as $TU = 1/\omega$. Thus, the time unit ratio between Earth-moon systems with different values of r_{EM} is given by

$$\frac{TU_2}{TU_1} = \frac{\frac{1}{\omega_2}}{\frac{1}{\omega_1}} \quad (2.4)$$

$$= \frac{\sqrt{\frac{r_{EM}^3(t_2)}{\mu_E + \mu_M}}}{\sqrt{\frac{r_{EM}^3(t_1)}{\mu_E + \mu_M}}} \quad (2.5)$$

$$= \left(\frac{r_{EM}(t_2)}{r_{EM}(t_1)} \right)^{\frac{3}{2}} \quad (2.6)$$

Last, the velocity ratio that relates the dilated systems is given by

$$\frac{VU_2}{VU_1} = \frac{\frac{DU_2}{TU_2}}{\frac{DU_1}{TU_1}} \quad (2.7)$$

$$= \frac{r_{EM}(t_2)}{r_{EM}(t_1)} \left(\frac{r_{EM}(t_1)}{r_{EM}(t_2)} \right)^{\frac{3}{2}} \quad (2.8)$$

$$= \sqrt{\frac{r_{EM}(t_1)}{r_{EM}(t_2)}} \quad (2.9)$$

2.1.2 Variational Equations

If a state vector is defined as

$$\mathbf{x} \equiv \begin{bmatrix} \mathbf{r} \\ \mathbf{v} \end{bmatrix} \quad (2.10)$$

where the spacecraft position is $\mathbf{r} \equiv [x \ y \ z]^\top$ and the spacecraft velocity is $\mathbf{v} \equiv [v_x \ v_y \ v_z]^\top$, then linearization about a nominal trajectory gives the variational equations as

$$\delta \dot{\mathbf{x}} = \mathbf{F}(t) \delta \mathbf{x} \quad (2.11)$$

where $\mathbf{F}(t)$ is the state propagation matrix. The solution of Eq. (2.11) is

$$\delta\mathbf{x}(t) = \mathbf{\Phi}(t, t_0)\delta\mathbf{x}(t_0) \quad (2.12)$$

where the state transition matrix $\mathbf{\Phi}(t, t_0)$ satisfies

$$\mathbf{\Phi}(t, t_0) = \frac{\partial\mathbf{x}(t)}{\partial\mathbf{x}(t_0)} \quad (2.13)$$

The time derivative of the state transition matrix is

$$\dot{\mathbf{\Phi}}(t, t_0) = \mathbf{F}(t)\mathbf{\Phi}(t, t_0) \quad (2.14)$$

with initial condition $\mathbf{\Phi}(t_0, t_0) = \mathbf{I}$. The state propagation matrix is

$$\mathbf{F}(t) = \frac{\partial\dot{\mathbf{x}}}{\partial\mathbf{x}} = \begin{bmatrix} \mathbf{0} & \mathbf{I} \\ \mathbf{G} & \mathbf{H} \end{bmatrix}_{6 \times 6} \quad (2.15)$$

where the gravity gradient matrix \mathbf{G} is

$$\mathbf{G} = \frac{\mu_E}{r_{ES}^3} \left(\frac{3\mathbf{r}_{ES}\mathbf{r}_{ES}^\top}{r_{ES}^2} - \mathbf{I} \right) + \frac{\mu_M}{r_{MS}^3} \left(\frac{3\mathbf{r}_{MS}\mathbf{r}_{MS}^\top}{r_{MS}^2} - \mathbf{I} \right) - \boldsymbol{\omega} \times (\boldsymbol{\omega} \times \mathbf{I}) \quad (2.16)$$

and the velocity gradient matrix \mathbf{H} is

$$\mathbf{H} = -2\boldsymbol{\omega} \times \mathbf{I} \quad (2.17)$$

With Eq. (2.14), the state transition matrix can be computed numerically along each continuous trajectory segment. A more thorough treatment of the state transition matrix is given in Ref. [46].

2.2 Four-Body Model

The four-body model includes the gravity of the spherical Earth, moon, and sun. The equations of motion are derived with Newton’s universal law of gravitation and Newton’s second law with the solar system barycenter assumed to be an inertial point. The spacecraft acceleration in a non-rotating reference frame with origin at the moon is

$$\ddot{\mathbf{r}} = -\frac{\mu_M}{r^3}\mathbf{r} - \mu_E \left[\frac{\mathbf{r} - \mathbf{r}_{ME}}{|\mathbf{r} - \mathbf{r}_{ME}|^3} + \frac{\mathbf{r}_{ME}}{r_{ME}^3} \right] - \mu_S \left[\frac{\mathbf{r} - \mathbf{r}_{MS}}{|\mathbf{r} - \mathbf{r}_{MS}|^3} + \frac{\mathbf{r}_{MS}}{r_{MS}^3} \right] \quad (2.18)$$

where \mathbf{r} is the position relative to the moon, μ_S is the gravitational parameter of the sun, and \mathbf{r}_{ME} , \mathbf{r}_{MS} are the time-varying moon-Earth and moon-sun vectors. All LOI segments are integrated in the non-rotating J2000 moon-centered frame, and the free return segments are integrated in the non-rotating J2000 Earth-centered frame. Numerical integration is performed with the DLSODE variable stepsize integrator [47]. The fundamental plane is the Earth’s equator at the J2000 epoch with $\hat{\mathbf{z}}$ axis normal to the equator and positive in the direction of the north pole. The principal direction along the positive $\hat{\mathbf{x}}$ axis points to the vernal equinox at the J2000 epoch. The $\hat{\mathbf{y}}$ axis completes the right-handed system. Accurate celestial data are accessed with the planetary and lunar ephemeris DE 421 [48]. In this system, ephemeris time is used as the independent variable in the equations of motion. Ephemeris time measures the number of seconds from the J2000 epoch, which corresponds to a Gregorian date of 12:00 PM Jan. 1, 2000. Table 2.1 lists the physical constants used in this model.

In the ephemeris model, the moon’s orbit is no longer constant as was assumed in the CRTBP. Figures 2.2(a)-2.2(b) show the variation of the moon’s dis-

Table 2.1: Four-body model parameters [48]

Parameter	Value	Units
Earth gravitational parameter	398600.436233	km^3/s^2
Moon gravitational parameter	4902.800076	km^3/s^2
Sun gravitational parameter	132712440040.944000	km^3/s^2
Earth mean radius	6371.01	km
Moon mean radius	1737.4	km
Sun mean radius	696000.0	km

tance from the Earth and the moon’s orbital inclination relative to the Earth’s equatorial plane. During the calendar year 2024, the minimum Earth-moon distance is approximately 356910 km, and the maximum distance is approximately 406510 km. Between 2020 and 2040, the maximum lunar inclination is approximately 28.7 deg, and the minimum inclination is approximately 18.1 deg. The cyclic variation of the lunar inclination has a period of approximately 18.6 years and is called the Metonic cycle.

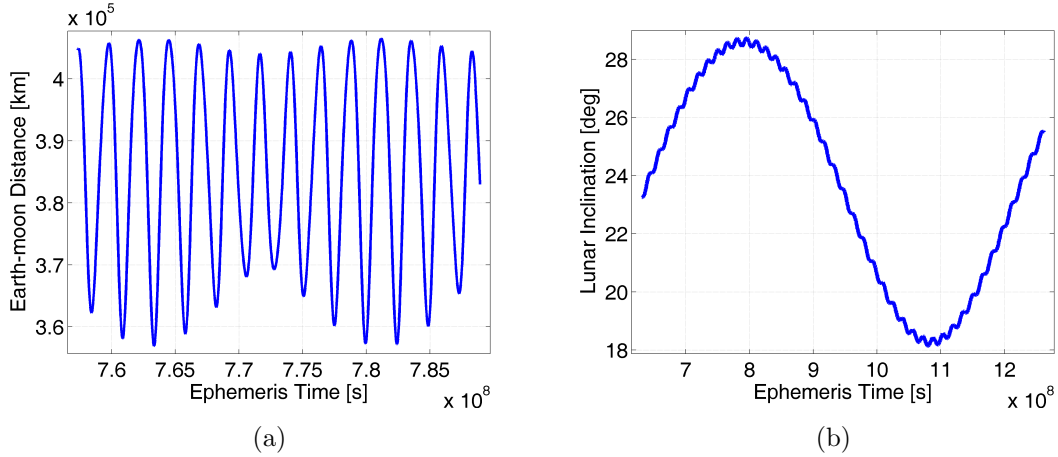


Figure 2.2: Lunar geometry variations: a) Earth-moon distance from Jan. 1, 2024 to Jan. 1, 2025, and b) lunar orbital inclination from Jan. 1, 2020 to Jan. 1, 2040.

In the derivation of the four-body equations of motion, it was assumed that the moon’s inertial acceleration is due entirely to the gravitational forces of the Earth and sun. While these are the dominant drivers of the moon’s motion, other factors such as planetary gravitational forces and tidal forces affect lunar motion. An alternative means of determining lunar acceleration is to compute a finite difference gradient of the moon’s velocity, tabulated in the ephemeris. Figure 2.3 shows the difference between the assumed lunar acceleration along each axis and the finite differenced values based on the tabulated velocity. The data span a 20 year period, covering 2020–2040, and the average acceleration error along the $\hat{\boldsymbol{x}}$ axis is -2.94×10^{-11} km/s²; the average acceleration error along the $\hat{\boldsymbol{y}}$ axis is -2.72×10^{-11} km/s²; and the average acceleration error along the $\hat{\boldsymbol{z}}$ axis is -1.07×10^{-11} km/s². The maximum acceleration errors along the $\hat{\boldsymbol{x}}$, $\hat{\boldsymbol{y}}$ and $\hat{\boldsymbol{z}}$ axes are 2.96×10^{-10} km/s², 2.94×10^{-10} km/s² and 1.17×10^{-10} km/s². Because the Earth and sun’s gravitational acceleration on the moon is at least 1000 times larger in each component than these differences, the discrepancy is determined to be negligible. This may be an issue, however, if high precision orbit determination is necessary, but this is not the case in this dissertation since the aim here is only to analyze trends in free returns and the hybrid LOI mission.

2.2.1 Variational Equations

The state propagation matrix in the four-body model is

$$\boldsymbol{F} = \frac{\partial \dot{\boldsymbol{x}}}{\partial \boldsymbol{x}} = \begin{bmatrix} \mathbf{0} & \boldsymbol{I} \\ \boldsymbol{G} & \mathbf{0} \end{bmatrix} \quad (2.19)$$

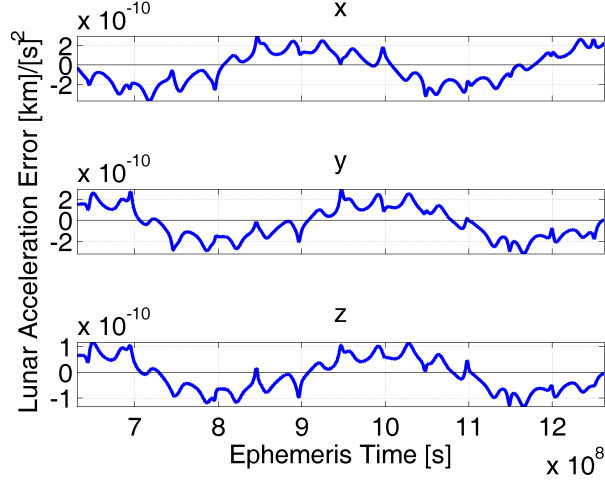


Figure 2.3: Lunar acceleration difference between four-body acceleration and finite-differenced ephemeris velocities during the years 2020–2040.

where $\partial \ddot{\mathbf{r}} / \partial \dot{\mathbf{r}} = \mathbf{0}$ since the spacecraft acceleration is not explicitly dependent on its velocity. The gravity gradient matrix in the moon-centered frame is

$$\begin{aligned}
 \mathbf{G} &= \frac{3\mu_M}{r^5} \mathbf{r} \mathbf{r}^\top - \frac{\mu_M}{r^3} \mathbf{I} \\
 &+ \frac{3\mu_E}{|\mathbf{r} - \mathbf{r}_{ME}|^5} (\mathbf{r} - \mathbf{r}_{ME})(\mathbf{r} - \mathbf{r}_{ME})^\top - \frac{\mu_E}{|\mathbf{r} - \mathbf{r}_{ME}|^3} \mathbf{I} \\
 &+ \frac{3\mu_S}{|\mathbf{r} - \mathbf{r}_{MS}|^5} (\mathbf{r} - \mathbf{r}_{MS})(\mathbf{r} - \mathbf{r}_{MS})^\top - \frac{\mu_S}{|\mathbf{r} - \mathbf{r}_{MS}|^3} \mathbf{I} \quad (2.20)
 \end{aligned}$$

The spacecraft’s acceleration and associated gravity gradient matrix are similar in the Earth-centered frame where the spacecraft experiences direct gravitational acceleration from the Earth and both direct and indirect gravitational accelerations from the moon and sun.

2.3 Other Perturbations

The dominant forces acting on a spacecraft in cislunar space are the gravitational forces of the Earth, moon, and sun. Other forces acting on the spacecraft include perturbations from other planetary bodies, solar radiation pressure, disturbing forces due to aspherical bodies, and possibly atmospheric drag, lift, and magnetic effects. Because the present mission focuses on flight in the Earth-moon system and does not require high precision orbit determination, disturbing forces from other planetary bodies are ignored. Additionally, atmospheric drag is ignored since the spacecraft spends little time near Earth. In fact, the targeted final conditions at Earth entry interface (EEI) are chosen to be the point at which atmospheric entry begins, and atmospheric flight is not modeled here. But for a more realistic simulation, the effects of Earth's oblateness and solar radiation pressure are considered.

2.3.1 Earth Oblateness

In the four-body model, all planets were assumed to be spherical and, thus, gravitating as point masses. The asphericity of celestial bodies, however, can have a significant effect on spacecraft trajectories, with the effects becoming more pronounced with decreasing orbital radius. As derived in Appendix A, the general expression for the gravitational potential of the Earth is

$$\begin{aligned}
 U = & \frac{\mu_E}{r} - \frac{\mu_E}{r} \sum_{\ell=1}^{\infty} \left(\frac{R_E}{r} \right)^{\ell} P_{\ell}(\sin \phi) J_{\ell} \\
 & + \frac{\mu_E}{r} \sum_{\ell=1}^{\infty} \sum_{m=1}^{\ell} \left(\frac{R_E}{r} \right)^{\ell} P_{\ell,m}(\sin \phi) [C_{\ell,m} \cos m\lambda + S_{\ell,m} \sin m\lambda] \quad (2.21)
 \end{aligned}$$

where r is the distance from the Earth's center of mass to the spacecraft, P_ℓ is the ℓ th Legendre polynomial, J_ℓ , $C_{\ell,m}$, and $S_{\ell,m}$ are gravity coefficients of degree ℓ and order m , ϕ is the spacecraft's geocentric latitude, and λ is the spacecraft's longitude. The Earth can be characterized as an oblate spheroid, indicating it is wider at its equator than at its poles. Though higher order asphericities exist, the oblateness produces the most pronounced effects. In the spherical harmonic expansion of the gravitational potential, the second zonal harmonic, denoted J_2 , represents the oblateness of the central body. An Earth satellite's orbit will experience variation in its longitude of the ascending node and argument of perigee due to oblateness [49].

The acceleration of the spacecraft due only to Earth's oblateness is determined by taking the gradient of the oblateness potential function U_2 with respect to the spacecraft position \mathbf{r} as

$$\ddot{\mathbf{r}}_{J_2} = \left(\frac{\partial U_2}{\partial \mathbf{r}} \right)^\top \quad (2.22)$$

where the oblateness potential is

$$U_2 = -\frac{3\mu_E J_2}{2r} \left(\frac{R_E}{r} \right)^2 \left[\left(\frac{\mathbf{r}^\top \hat{\mathbf{z}}}{r} \right)^2 - \frac{1}{3} \right] \quad (2.23)$$

As shown in Appendix A, the spacecraft acceleration due only to J_2 effects is

$$\ddot{\mathbf{r}}_{J_2} = -\frac{3}{2} J_2 \mu_E \frac{R_E^2}{r^5} \left(\mathbf{J} - \frac{5(\mathbf{r}^\top \hat{\mathbf{z}})^2}{r^2} \mathbf{I} \right) \mathbf{r} \quad (2.24)$$

where $\mathbf{J} \equiv \text{diag}(1, 1, 3)$. As given in Ref. [49], the value of the second zonal harmonic is $J_2 = 0.001082636$.

2.3.2 Solar Radiation Pressure

Photons of light that impact a spacecraft can impart momentum if absorbed or reflected; thus, when a spacecraft is exposed to sunlight, it experiences a disturbing force due to solar radiation. The acceleration due to this force is

$$\ddot{\mathbf{r}}_{SRP} = \frac{p_{SR}c_R A}{m} \hat{\mathbf{r}}_{SP} \quad (2.25)$$

where $p_{SR} = 4.51 \times 10^{-6}$ N/m² is the approximate solar pressure near the Earth, c_R is the coefficient of reflectivity, A is the spacecraft area exposed to the sun, m is the spacecraft mass, and $\hat{\mathbf{r}}_{SP}$ is the sun-spacecraft unit vector [50]. The coefficient of reflectivity is zero for a transparent body, one for a black body, and two for a body that reflects all incoming radiation. This value is difficult to determine since it requires knowledge of the material properties of the spacecraft and which surfaces and materials are exposed to the sun at a given time.

2.3.3 Variational Equations

With the addition of Earth's oblateness and solar radiation pressure, the spacecraft acceleration in the moon-centered frame becomes

$$\begin{aligned} \ddot{\mathbf{r}} = & -\frac{\mu_M}{r^3} \mathbf{r} - \mu_E \left[\frac{\mathbf{r} - \mathbf{r}_{ME}}{|\mathbf{r} - \mathbf{r}_{ME}|^3} + \frac{\mathbf{r}_{ME}}{r_{ME}^3} \right] - \mu_S \left[\frac{\mathbf{r} - \mathbf{r}_{MS}}{|\mathbf{r} - \mathbf{r}_{MS}|^3} + \frac{\mathbf{r}_{MS}}{r_{MS}^3} \right] \\ & + -\frac{3}{2} J_2 \mu_E R_E^2 \left(\mathbf{J} - \frac{5 [(\mathbf{r} - \mathbf{r}_{ME})^\top \hat{\mathbf{z}}]^2}{|\mathbf{r} - \mathbf{r}_{ME}|^2} \mathbf{I} \right) \frac{\mathbf{r} - \mathbf{r}_{ME}}{|\mathbf{r} - \mathbf{r}_{ME}|} + \frac{p_{SR}c_R A}{m} \frac{\mathbf{r} - \mathbf{r}_{MS}}{|\mathbf{r} - \mathbf{r}_{MS}|} \end{aligned} \quad (2.26)$$

Note that since the Earth's oblateness effects on the moon have been ignored, this formulation cannot be used for high precision orbit propagation. The state propa-

gation matrix with this model is

$$\mathbf{F} = \frac{\partial \dot{\mathbf{x}}}{\partial \mathbf{x}} = \begin{bmatrix} \mathbf{0} & \mathbf{I} \\ \mathbf{G} & \mathbf{0} \end{bmatrix} \quad (2.27)$$

The gravity gradient matrix is

$$\mathbf{G} = \mathbf{G}_4 + \mathbf{G}_{J_2} + \mathbf{G}_{SRP} \quad (2.28)$$

where \mathbf{G}_4 is the gravity gradient matrix associated with the four-body problem, \mathbf{G}_{J_2} is the portion associated with Earth oblateness effects, and \mathbf{G}_{SRP} is the portion associated with solar radiation pressure. Explicitly, the components are

$$\begin{aligned} \mathbf{G}_{J_2} = & -\frac{3}{2} J_2 \mu_E R_E^2 \left[\mathbf{J} \left(\frac{\mathbf{I}}{r_{EP}^5} - \frac{5 \mathbf{r}_{EP} \mathbf{r}_{EP}^\top}{r_{EP}^7} \right) - \frac{5 (\mathbf{r}_{EP}^\top \hat{\mathbf{z}})^2}{r_{EP}^2} \left(\frac{\mathbf{I}}{r_{EP}^5} - \frac{5 \mathbf{r}_{EP} \mathbf{r}_{EP}^\top}{r_{EP}^7} \right) \right. \\ & \left. - \frac{\mathbf{r}_{EP}}{r_{EP}^7} \left(10 (\mathbf{r}_{EP}^\top \hat{\mathbf{z}}) \hat{\mathbf{z}}^\top - \frac{10 (\mathbf{r}_{EP}^\top \hat{\mathbf{z}})^2 \mathbf{r}_{EP}^\top}{r_{EP}^2} \right) \right] \end{aligned} \quad (2.29)$$

and

$$\mathbf{G}_{SRP} = \frac{p_{SRCRA}}{m} \left[\frac{\mathbf{I}}{|\mathbf{r} - \mathbf{r}_{MS}|} - \frac{(\mathbf{r} - \mathbf{r}_{MS})(\mathbf{r} - \mathbf{r}_{MS})^\top}{|\mathbf{r} - \mathbf{r}_{MS}|^3} \right] \quad (2.30)$$

The gravity gradient matrix is similar in the Earth-centered frame.

2.4 Reference Frames

In the CRTBP, all numerical integration is performed in the barycentered rotating frame. This frame is used for visualization along with Earth- and moon-centered non-rotating frames. In the ephemeris model, integration and visualization are performed in J2000 Earth- and moon-centered frames. Additionally, it is useful to create a reference frame analogous to the rotating frame of the CRTBP. The

principal direction is the Earth-moon line with corresponding unit vector given by

$$\hat{\mathbf{r}}(t) \equiv \frac{\mathbf{r}_{EM}(t)}{|\mathbf{r}_{EM}(t)|} \quad (2.31)$$

where $\mathbf{r}_{EM}(t)$ is the time-dependent Earth-moon vector. The fundamental plane is the moon's instantaneous orbital plane about the Earth, and the unit vector normal to this plane is

$$\hat{\mathbf{n}}(t) \equiv \frac{\mathbf{r}_{EM}(t) \times \mathbf{v}_{EM}(t)}{|\mathbf{r}_{EM}(t) \times \mathbf{v}_{EM}(t)|} \quad (2.32)$$

where $\mathbf{v}_{EM}(t)$ is the moon's velocity relative to the Earth. The right-handed coordinate system is completed with

$$\hat{\mathbf{t}}(t) \equiv \hat{\mathbf{n}}(t) \times \hat{\mathbf{r}}(t) \quad (2.33)$$

where $\hat{\mathbf{t}}(t)$ is not parallel to $\mathbf{v}_{EM}(t)$ in general. If $\hat{\mathbf{r}}$, $\hat{\mathbf{t}}$, and $\hat{\mathbf{n}}$ are expressed in the J2000 frame, the transformation matrix from the rotating frame to the non-rotating frame is

$$\mathbf{R}(t) = [\hat{\mathbf{r}} \ \hat{\mathbf{t}} \ \hat{\mathbf{n}}]_{3 \times 3} \quad (2.34)$$

where it is understood that $\hat{\mathbf{r}}$, $\hat{\mathbf{t}}$, and $\hat{\mathbf{n}}$ are functions of time. Since \mathbf{R} is an orthogonal matrix [51], the transformation matrix from the non-rotating frame to the rotating frame is \mathbf{R}^\top . This reference frame is shown in Fig. 2.4.

The Earth-moon distance is variable, so in an Earth-centered rotating frame, the moon will oscillate on the $\hat{\mathbf{r}}$ axis. To fix the moon in this frame, each vector will be scaled by the Earth-moon distance, $\mathbf{r}_{EM}(t)$. The reference frame is now termed a rotating-pulsating frame because the distance unit pulsates with time. A position

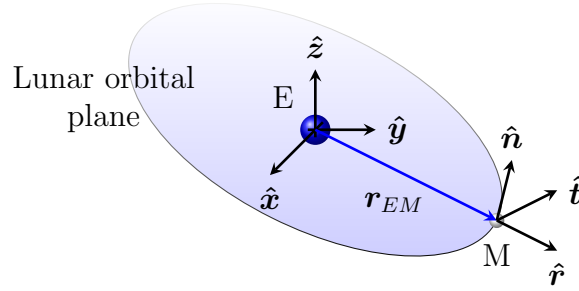


Figure 2.4: Rotating reference frame.

vector in the rotating-pulsating frame is given by

$$\mathbf{r}^{rtn} = \frac{1}{r_{EM}(t)} \mathbf{R}^\top \mathbf{r}^{xyz} \quad (2.35)$$

where \mathbf{r}^{xyz} is the position vector in the J2000 frame. Thus, the moon's position in this frame is $[1 \ 0 \ 0]^\top$.

Chapter 3

Free-Return Trajectories in the Earth-Moon System

In this chapter, single-flyby free return trajectories are generated and analyzed in the circular restricted three-body problem (CRTBP). The free returns are targeted with an automated technique that requires no user input. Trends in round trip flight time, translunar injection (TLI) velocity impulse, and Earth entry interface (EEI) velocity are presented. All symmetric single-flyby free returns are examined within a lunar flyby altitude of 20000 km.

3.1 Background

The benefit of the free return orbit was realized during the Apollo program as the first three Apollo missions to the moon flew free returns from TLI to lunar orbit insertion (LOI) [52–54]. The next three missions performed a cislunar maneuver to depart the free return path approximately one day after TLI to target conditions more favorable for LOI; this translunar trajectory was called a hybrid non-free return profile [55–57]. Before LOI, the non-free return path was constrained to be within the capability of the lunar module’s (LM) descent propulsion system (DPS) to perform a transearth injection (TEI) maneuver sufficient for reentry. The final

three missions did not use a free return trajectory; rather, their translunar coast was required to remain within the TEI capability of the LM’s DPS or the command and service module’s reaction control system [58–60].

Lunar free return trajectories similar to those utilized during Apollo missions could prove useful for future human lunar missions, though different free returns must be studied to accommodate the polar orbits necessary for exploration of high latitude sites. Free returns also present utility for robotic missions. For example, these trajectories provide the capability to alter geocentric orbits through lunar gravity assist [61–64] as demonstrated when a lunar free return was used in 1998 to reposition an errant communication spacecraft into a geosynchronous orbit [65]. A free return for a robotic lunar mission could also provide the option of returning the spacecraft for service in Earth orbit if a hardware problem occurred on the translunar portion of the mission. Periodic free returns may prove useful for repeatedly transporting cargo between the Earth and moon, or for continuous measurement and observation of the Earth-moon system.

Lunar free returns include circumlunar and cislunar trajectories, departures from posigrade and retrograde Earth orbits, and trajectories in and out of the Earth-moon plane. Circumlunar free returns have lunar flyby on the far side of the moon relative to Earth, and cislunar free returns have lunar flyby on the near side of the moon relative to Earth. Posigrade free returns have $\mathbf{h}(t_{TLI}) \cdot \hat{\mathbf{z}} \geq 0$, and retrograde free returns have $\mathbf{h}(t_{TLI}) \cdot \hat{\mathbf{z}} < 0$, where $\mathbf{h}(t_{TLI})$ is the spacecraft’s angular momentum at Earth departure, and the $\hat{\mathbf{z}}$ axis points in the direction of the moon’s angular velocity about the Earth. Plotted in a frame of reference with its origin

at the Earth-moon barycenter and rotating with the Earth-moon line, Fig. 3.1(a) shows an example of a free return trajectory that departs Earth in a posigrade orientation, circumnavigates the moon with a lunar flyby altitude of 100 km, arrives at Earth at an altitude of 121 km, and has a round trip flight time of 5.6 days. Figure 3.1(b) shows the same trajectory plotted in a non-rotating frame with its origin at the Earth where the moon is plotted at the time of the free return's lunar flyby.

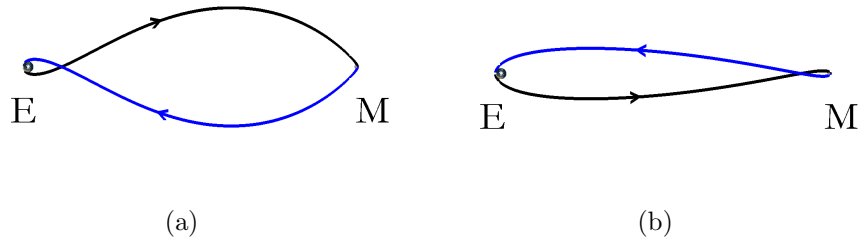


Figure 3.1: Free return trajectory: a) barycentered rotating frame, and b) Earth-centered non-rotating frame.

On any single-flyby free return, the time of flight from Earth departure to Earth arrival is on the order of days while the time spent in the vicinity of the moon is on the order of hours; thus, the initial velocity magnitude and orientation must be selected such that the spacecraft encounters the moon at the proper time and direction to ensure a post-flyby state that leads to the specified EEI conditions. In the numerical generation of free returns, the initial estimate of the orbit geometry is critical to attaining a converged solution because of the sensitivity of the final state to the TLI maneuver, and flight time. If initial conditions can be generated that produce a trajectory with geometry similar to the desired free return, an iterative

numerical procedure can likely converge on a feasible free return. ‘Similar geometry’ is defined here as meeting both the Earth departure directional requirement (prograde or retrograde) and the lunar encounter requirement (circumlunar or cislunar). An analytical method of constructing feasible initial conditions for each free return lying in the Earth-moon plane is discussed in this chapter along with a numerical procedure that can produce any free return trajectory in or out of the Earth-moon plane. The automated algorithm requires no user input other than the desired features of the free return: altitude and orientation at lunar flyby, and altitude and flight path angle at Earth return. The algorithm is later modified to remove the symmetry constraint.

3.2 Theorem of Image Trajectories

The CRTBP exhibits symmetry useful in the generation of free return trajectories. As shown in Ref. [66], additional valid trajectories in the rotating frame may be obtained from a nominal trajectory through reflections across a plane or rotations about an axis. A trajectory’s geometric image with respect to a reference plane is obtained by reflecting it across that plane; this is equivalent to reversing the sign of the position coordinate perpendicular to that plane. A trajectory’s geometric image with respect to a reference axis is obtained by rotating the trajectory 180 deg about the reference axis, and this is equivalent to reversing the sign of the two position coordinates perpendicular to that axis. To determine which image trajectories are consistent with the equations of motion of the CRTBP, three position

transformations and one time transformation are made as follows:

$$\begin{aligned}x_* &\equiv Ax & y_* &\equiv By \\z_* &\equiv Cz & t_* &\equiv Dt\end{aligned}\tag{3.1}$$

where valid values of the real scalars A , B , C , and D are to be determined. The time transformation is included because the direction of motion in time of each geometric image relative to the nominal trajectory is unknown. After making the transformations, the resulting equations of motion are compared to the nominal equations of motion to determine if the image trajectory is valid and establish all permissible sets of transformations.

Rearranging Eq. (2.1), the equations of motion of the CRTBP become

$$\ddot{\mathbf{r}} + 2\boldsymbol{\omega} \times \dot{\mathbf{r}} + \boldsymbol{\omega} \times (\boldsymbol{\omega} \times \mathbf{r}) + \frac{\mu_1}{r_1^3}\mathbf{r}_1 + \frac{\mu_2}{r_2^3}\mathbf{r}_2 = \mathbf{0}\tag{3.2}$$

where \mathbf{r} is the barycentric spacecraft position, $\boldsymbol{\omega}$ is the system's angular velocity, μ_1 and μ_2 are the gravitational parameters of the first and secondary primary bodies, and \mathbf{r}_1 and \mathbf{r}_2 are vectors from the first and second primary bodies to the spacecraft. Expanding in three orthogonal coordinates,

$$\ddot{x} - 2\omega\dot{y} - \omega^2x + \frac{\mu_1}{r_1^3}(x - x_1) + \frac{\mu_2}{r_2^3}(x - x_2) = 0\tag{3.3}$$

$$\ddot{y} + 2\omega\dot{x} - \omega^2y + \frac{\mu_1}{r_1^3}y + \frac{\mu_2}{r_2^3}y = 0\tag{3.4}$$

$$\ddot{z} + \frac{\mu_1}{r_1^3}z + \frac{\mu_2}{r_2^3}z = 0\tag{3.5}$$

After applying the transformations of Eqs. (3.1), the equations of motion become

$$\ddot{\mathbf{r}}_* + 2\boldsymbol{\omega} \times \dot{\mathbf{r}}_* + \boldsymbol{\omega} \times (\boldsymbol{\omega} \times \mathbf{r}_*) + \frac{\mu_1}{r_{1*}^3}\mathbf{r}_{1*} + \frac{\mu_2}{r_{2*}^3}\mathbf{r}_{2*} = \mathbf{0}\tag{3.6}$$

where $\mathbf{r}_* \equiv [x_* \ y_* \ z_*]^\top$ is the transformed position, $\dot{\mathbf{r}}_* \equiv d\mathbf{r}_*/dt_*$ is the transformed velocity, and $\ddot{\mathbf{r}}_* \equiv d^2\mathbf{r}_*/dt_*^2$ is the transformed acceleration. Expanding Eq. (3.6) gives

$$\frac{A}{D^2}\ddot{x} - \frac{B}{D}2\omega\dot{y} - A\omega^2x + \frac{\mu_1}{r_{1*}^3}(Ax - x_1) + \frac{\mu_2}{r_{2*}^3}(Ax - x_2) = 0 \quad (3.7)$$

$$\frac{B}{D^2}\ddot{y} + \frac{A}{D}2\omega\dot{x} - B\omega^2y + \frac{\mu_1}{r_{1*}^3}By + \frac{\mu_2}{r_{2*}^3}By = 0 \quad (3.8)$$

$$\frac{C}{D^2}\ddot{z} + \frac{\mu_1}{r_{1*}^3}Cz + \frac{\mu_2}{r_{2*}^3}Cz = 0 \quad (3.9)$$

The magnitude of a transformed position vector relative to the i th body is

$$r_{i*} = \sqrt{(Ax - x_i)^2 + (By)^2 + (Cz)^2} \quad (3.10)$$

so setting $A = 1$, $B = \pm 1$, $C = \pm 1$ satisfies $r_{i*} = r_i$. Examining the $\hat{\mathbf{x}}$ component, the last three nonzero terms of Eq. (3.7) are now equal to the last three nonzero terms of Eq. (3.3). For agreement between the second terms of Eq. (3.3) and Eq. (3.7), set $B = D$. The first terms are already equivalent since $A = 1$ and $D^2 = 1$. Examining the $\hat{\mathbf{y}}$ components of the equations of motion, Eq. (3.4) and Eq. (3.8), these two equations are already equivalent by the analysis done for the $\hat{\mathbf{x}}$ component equation. If $A = 1$ and $B = 1 = D$, the equations are identical. If $A = 1$ and $B = -1 = D$, the sign of each term of Eq. (3.8) is reversed, and the equations are again equivalent. Examining the $\hat{\mathbf{z}}$ components of the equations of motion, Eq. (3.5) and Eq. (3.9), equivalence is achieved since $C = \pm 1$ and $D^2 = 1$.

Thus, the sets of scalar constants satisfying the equations of motion are

$$\begin{aligned} A = 1 & & B = D \\ C = \pm 1 & & D = \pm 1 \end{aligned} \quad (3.11)$$

This result, known as the theorem of image trajectories and illustrated in Fig. 3.2, gives four solution sets which represent four valid trajectories in the CRTBP. The nominal trajectory is given by $A = B = C = D = 1$. The first image trajectory, denoted as image 1 in Fig. 3.2, is given by $A = B = 1$, $C = -1$, and $D = 1$, which is the reflection of the nominal trajectory across the $\hat{x}\hat{y}$ plane, flown in the same direction as the nominal path. The second image trajectory, image 2, is given by $A = 1$, $B = -1$, $C = 1$, and $D = -1$, which is the reflection of the nominal trajectory across the $\hat{x}\hat{z}$ plane, flown in the opposite direction. The third image trajectory, image 3, is given by $A = 1$ and $B = C = D = -1$, which represents the rotation of the nominal trajectory about the \hat{x} axis, flown in the opposite direction. This result is useful in the design of free returns since a trajectory from the Earth to the moon with an orthogonal crossing of the \hat{x} axis or the $\hat{x}\hat{z}$ plane guarantees a symmetric ballistic return from the moon to the Earth.

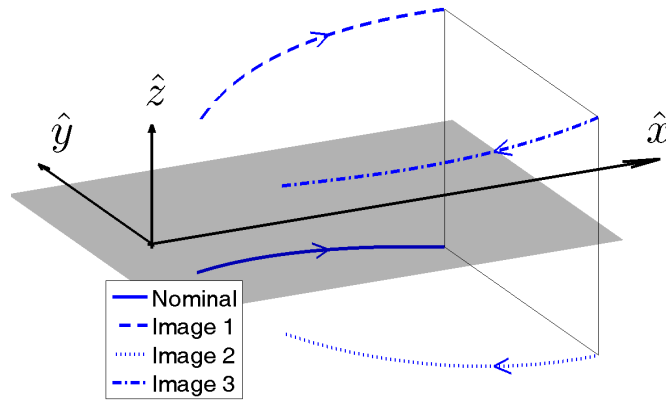


Figure 3.2: Image trajectories.

3.3 Lunar Flyby Geometry

Free returns are constructed by shooting one or two segments from a point near the moon, called the lunar flyby point, to the Earth. If a symmetric free return is constructed, the lunar flyby velocity is perpendicular to either the Earth-moon line or the vertical ($\hat{x}\hat{z}$) plane. The flyby state of a symmetric free return is parameterized by its lunar altitude h , latitude ϕ relative to the Earth-moon plane, and velocity azimuth θ , measured east from north, where east and north are defined as

$$\hat{e} \equiv \frac{\hat{z} \times \mathbf{r}_{MP}}{|\hat{z} \times \mathbf{r}_{MP}|} \quad \hat{n} \equiv \frac{\mathbf{r}_{MP} \times \hat{e}}{|\mathbf{r}_{MP} \times \hat{e}|} \quad (3.12)$$

and \mathbf{r}_{MP} is the flyby position relative to the moon. If an asymmetric free return is targeted, the flyby state is parameterized by its altitude, latitude, azimuth, and flight path angle γ . Figure 3.3 illustrates these quantities where \mathbf{v} is the flyby velocity and \mathbf{h} is the angular momentum about the moon.

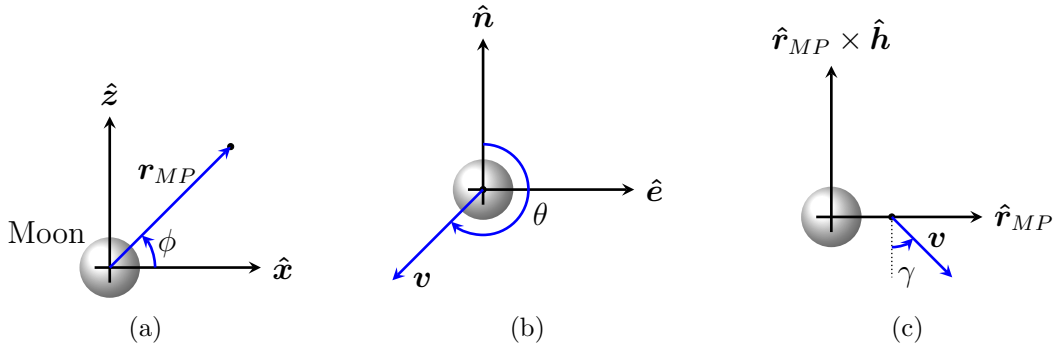


Figure 3.3: Lunar flyby parameterization: a) altitude and latitude, b) azimuth, and c) flight path angle.

The flyby position relative to the Earth-moon barycenter is

$$\begin{aligned} \mathbf{r} &= [x_M + (R_M + h) \cos \phi] \hat{\mathbf{x}} \\ &+ (R_M + h) \sin \phi \hat{\mathbf{z}} \end{aligned} \quad (3.13)$$

where x_M is the distance from the Earth-moon barycenter to the moon's center, and R_M is the mean lunar radius. As shown in Appendix B, the velocity expressed in the $\hat{\mathbf{x}}\hat{\mathbf{y}}\hat{\mathbf{z}}$ basis is

$$\begin{aligned} \mathbf{v} &= v (\cos \phi \sin \gamma - \sin \phi \cos \theta \cos \gamma) \hat{\mathbf{x}} \\ &+ v (\sin \theta \cos \gamma) \hat{\mathbf{y}} \\ &+ v (\sin \phi \sin \gamma + \cos \phi \cos \theta \cos \gamma) \hat{\mathbf{z}} \end{aligned} \quad (3.14)$$

where the velocity azimuth and flight path angle are measured in the rotating frame.

3.4 Initial Estimate

Utilizing a two-body Earth-spacecraft model where the terminal attraction of the moon on the spacecraft is ignored, a simple targeting algorithm is developed to construct an approximation for the free return outbound trajectory. First, define a reference frame centered at the Earth with the $\hat{\mathbf{i}}$ axis along the Earth-moon line at the time of apogee on the Earth departure leg, the $\hat{\mathbf{j}}$ axis along the direction of the moon's velocity at that point, and the $\hat{\mathbf{k}}$ axis completing the right handed system. Construct a Hohmann transfer with angular momentum about the Earth in the $+\hat{\mathbf{k}}$ direction and with a line of apsides coincident with the $\hat{\mathbf{i}}$ axis. Also require perigee to occur at an altitude h_{TLI} above the Earth's surface and apogee to occur at an

altitude R_M above the moon's surface on the far side of the moon, to guarantee a circumlunar passage. Figure 3.4(a) shows the moon at the time of apogee, and the outbound trajectory, which is posigrade about the Earth at departure and has a circumlunar passage. The position and velocity at perigee are

$$\mathbf{r}_{TLI} = -(R_E + h_{TLI}) \hat{\mathbf{i}} \quad (3.15)$$

$$\mathbf{v}_{TLI} = -\sqrt{2\mu_E \left(\frac{1}{r_{TLI}} - \frac{1}{r_{TLI} + r_{EM} + 2R_M} \right)} \hat{\mathbf{j}} \quad (3.16)$$

The flight time from perigee to apogee is

$$t_f = \pi \sqrt{\frac{a^3}{\mu_E}} \quad (3.17)$$

where $a = \frac{1}{2}(r_{TLI} + r_{EM} + 2R_M)$ is the semi-major axis of the transfer ellipse. The initial state is then transferred to the CRTBP and numerically propagated to t_f in the barycentered rotating frame.

This initial estimate targets a posigrade circumlunar free return, but other geometries are possible. The translunar portions of retrograde and cislunar free returns are similarly approximated with the two-body model and are shown in Figs. 3.4(b)–3.4(d). The only differences are the direction of flight and apogee location of the transfer ellipse. An alternate approach in constructing the translunar trajectory is a finite sphere of influence patched conic model where an Earth departure ellipse is joined with a moon-focused hyperbola. This method was also implemented, but the two-body model proved superior to the patched conic method in ensuring the proper orientation of lunar passage.

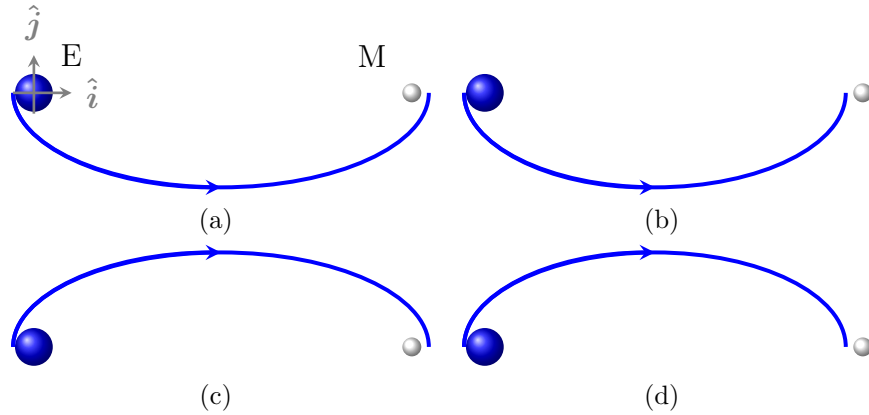


Figure 3.4: Two-body initial estimate: a) posigrade circumlunar, b) posigrade cislunar, c) retrograde circumlunar, and d) retrograde cislunar.

With the initial state and time of flight estimated, the trajectory is propagated in the CRTBP where the gravity of the Earth and moon are active at all times. Stopping conditions of $|\mathbf{r} \cdot \hat{\mathbf{y}}| < 50$ km and $\dot{\mathbf{r}} \cdot \hat{\mathbf{y}} < 0$ km/s are imposed on the integration to determine the time of flight such that the trajectory terminates near the Earth-moon line. While holding the TLI position and direction fixed, the TLI velocity magnitude and flight time that produce an orthogonal crossing of the Earth-moon line at lunar flyby are determined numerically with the root-finding algorithm NS11,¹ which solves a square system of nonlinear equations via Broyden's method [67]. With a perpendicular crossing of the $\hat{\mathbf{x}}$ axis, a symmetric free return is guaranteed by the theorem of image trajectories.

¹Information available at <http://www.hsl.rl.ac.uk/archive/specs/ns11.pdf> [accessed 15 March 2012]

3.5 Numerical Targeting

Once the base free return has been constructed, all subsequent symmetric free returns are generated with a method where a single trajectory is propagated from lunar flyby to the Earth in the CRTBP. The lunar flyby position and velocity are oriented to be consistent with the desired free return type. Note, however, that free returns do not exist for all sets of flyby conditions; it will be seen that the maximum feasible latitude and azimuth at lunar flyby are a function of the flyby altitude. Once the flyby state is initialized, the root-finding algorithm varies the flyby velocity magnitude and flight time to produce the desired altitude and flight path angle at Earth. Once converged, this guarantees a free return since the state at flyby necessitates a symmetric trajectory. This method, outlined in Ref. [27], is advantageous because only the moon to Earth leg must be integrated on each iteration. Also, the sensitivity is reduced by shooting the trajectory from the moon into the larger gravity well of the Earth instead of propagating an entire Earth-moon-Earth trajectory. Care must be exercised at Earth to ensure the trajectory returns in the proper orientation.

The current problem is a system of two nonlinear equations with two unknowns, and the free parameters are

$$\mathbf{x}_p \equiv \begin{bmatrix} v \\ t_{EEI} \end{bmatrix} \quad (3.18)$$

where v is the velocity magnitude at lunar flyby and t_{EEI} is the moon to Earth flight time. The constraints to be satisfied are

$$\mathbf{c} \equiv \begin{bmatrix} h_{EEI} - h_{T_2} \\ \gamma_{EEI} - \gamma_{T_2} \end{bmatrix} = \mathbf{0} \quad (3.19)$$

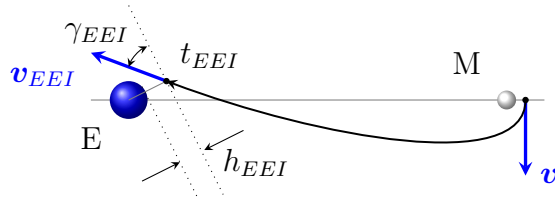


Figure 3.5: Free parameters and constrained quantities for targeting all types of symmetric free returns, including non-planar trajectories.

where h_{EEI} and h_{T_2} are the actual and targeted altitude at EEI, and γ_{EEI} and γ_{T_2} are the actual and targeted flight path angle at EEI. The free parameters and constrained quantities are shown in Fig. 3.5. The problem is solved with NS11 which has proved through repeated trials to be stable given an initial orbit geometrically similar to the desired result. Stability is improved by scaling the free parameters and constraints to achieve scaled values on the order of one. Numerical integration is performed in the barycentered rotating reference frame of the CRTBP, and convergence is determined when

$$\left(\sum_{i=1}^2 c_i^2 \right)^{1/2} < 10^{-8} \quad (3.20)$$

3.5.1 Continuation Method

After producing a converged planar free return, the lunar flyby altitude is advanced in increments of Δh until the desired flyby altitude is reached. Each previously converged solution is used as the initial estimate for the next case with a modified flyby altitude. Once the planar trajectory has been reached with the desired value of h , the out-of-plane velocity angle at lunar flyby is advanced incre-

mentally until the targeted value is reached. If symmetric free returns are targeted, only the flyby velocity azimuth or the flyby latitude is incremented, and the flight path angle is always zero. If asymmetric free returns are targeted, the latitude and azimuth at lunar passage may be simultaneously nonzero, and the flight path angle may be nonzero.

The maximum values of Δh , $\Delta\phi$, and $\Delta\theta$ are important parameters in ensuring convergence. Increasing the stepsize will decrease the number of required intermediate trajectories in the continuation procedure, but if any stepsize is too large, the previously converged solution may not reconverge at the updated lunar flyby state. A value of $\Delta h = 25$ km is used for retrograde, cislunar free returns, and $\Delta h = 100$ km is used for all other free returns. All angular values are incremented in stepsizes of one degree. These stepsizes ensure convergence from the previous trajectory for all free returns studied in this dissertation. The symmetric free return targeting algorithm is outlined in Fig. 3.6.

3.6 Symmetric Free Returns

As indicated by the theorem of image trajectories, two classes of symmetric, single-flyby circumlunar free returns exist, characterized by the orientation at lunar passage. Type 1 free returns, illustrated in Fig. 3.7, exhibit rotational symmetry about the Earth-moon line; the moon to Earth path is given by a rotation of 180 deg of the Earth to moon path about the Earth-moon line. Type 2 free returns, illustrated in Fig. 3.8, have symmetry across the plane containing the Earth-moon line and the system's angular velocity vector, called the vertical plane; the moon to Earth

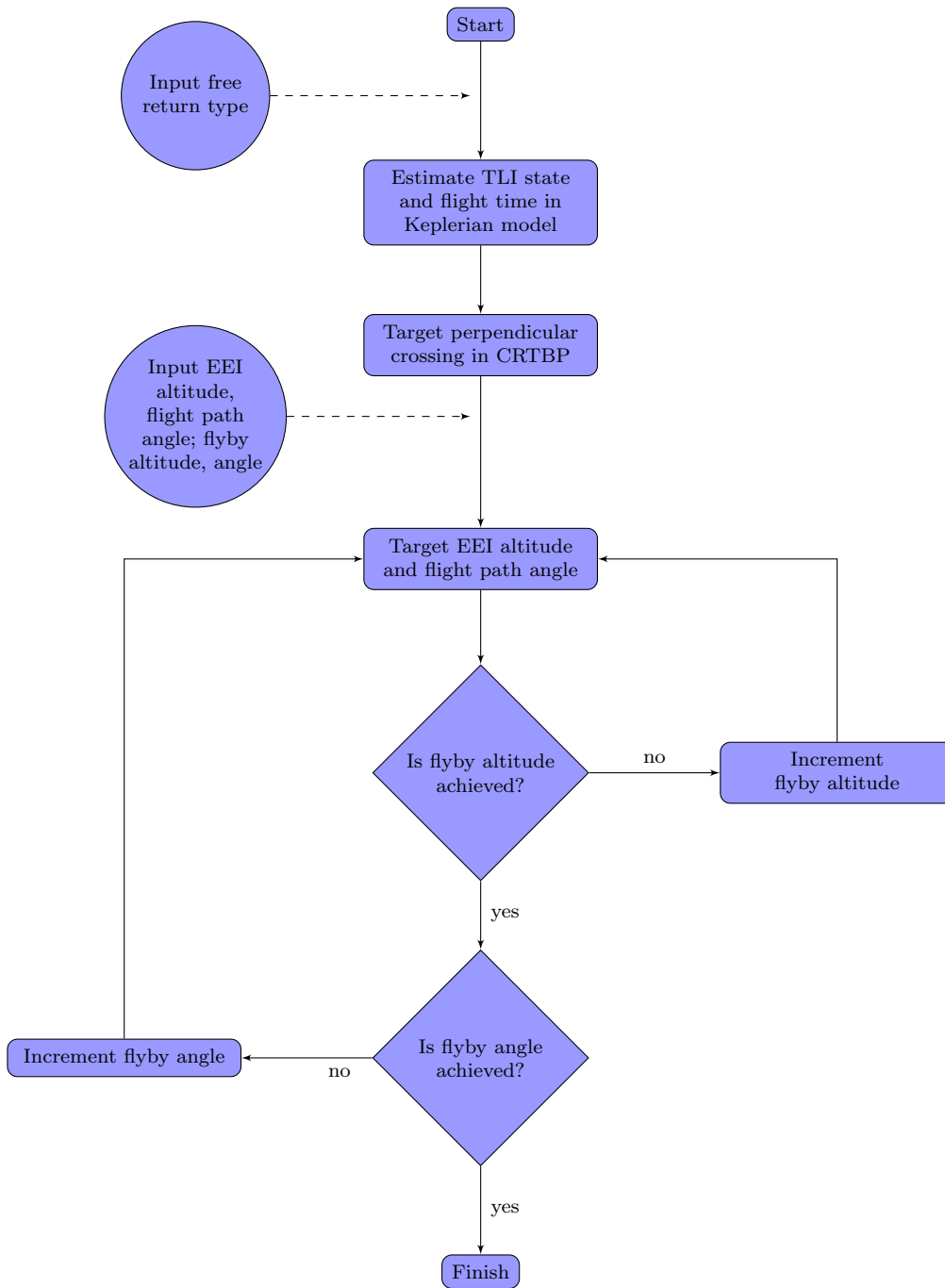


Figure 3.6: Symmetric free return targeting algorithm.

path is given by a reflection of the Earth to moon path across this plane. Thus, type 1 free returns must orthogonally intersect the Earth-moon line, and type 2 free returns must have a perpendicular crossing of the vertical plane. Type 0 free returns remain in the Earth-moon plane and represent the intersection of type 1 and type 2 free returns. Thus, type 0 free returns are symmetric about the Earth-moon line and across the vertical plane. The symmetric free return with minimum TLI impulse and flight time for a given lunar flyby altitude is the type 0 free return.

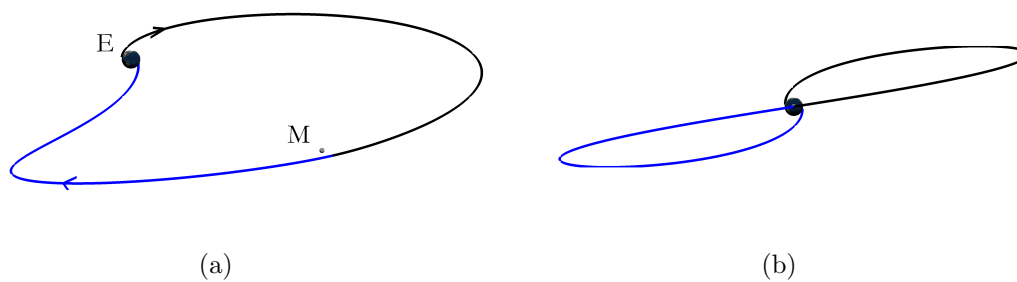


Figure 3.7: Type 1 free return in barycentered rotating frame: a) oblique view, and b) view normal to moon-Earth line illustrating symmetry.

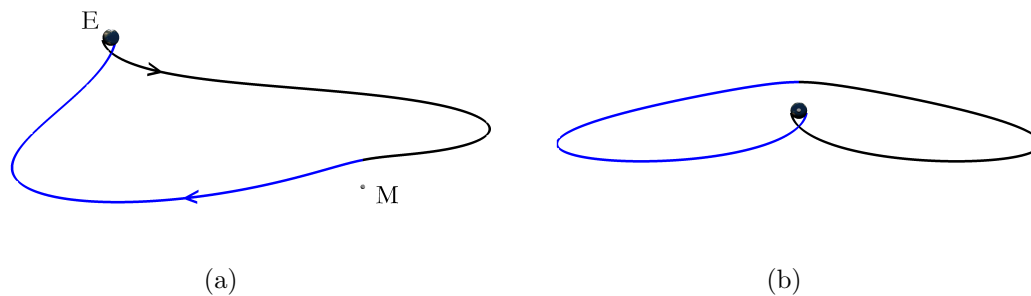


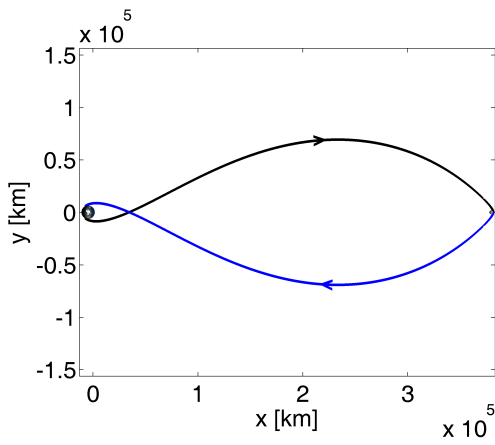
Figure 3.8: Type 2 free return in barycentered rotating frame: a) oblique view, and b) view along moon-Earth line illustrating symmetry.

Figures 3.9–3.10 show the four types of type 0 free returns. Each trajectory has a lunar flyby altitude of 100 km, and the EEI conditions require an altitude of 121 km and a flight path angle of -6 deg, similar to the Apollo entry conditions [68]. Summarized in Table 3.1, the free return classification is based on symmetry, lunar passage orientation, and Earth departure orientation. In the rotating frame, the

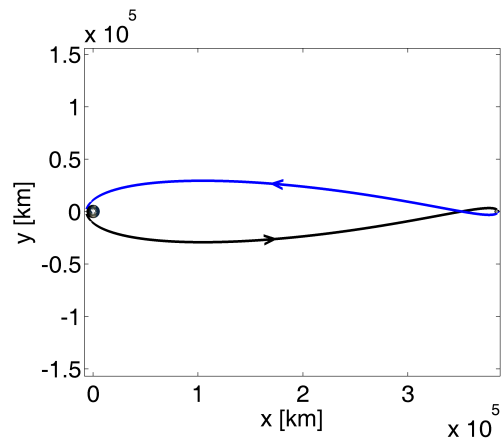
Table 3.1: Free return classification

Characteristic	Value	Definition
Symmetry	0	Symmetric across \hat{x} axis, remains in $\hat{x}\hat{y}$ plane
	1	Symmetric under 180 deg rotation about \hat{x} axis
	2	Symmetric under reflection across $\hat{x}\hat{z}$ plane
Lunar passage	A	Circumlunar
	B	Cislunar
Earth departure	i	Posigrade
	ii	Retrograde

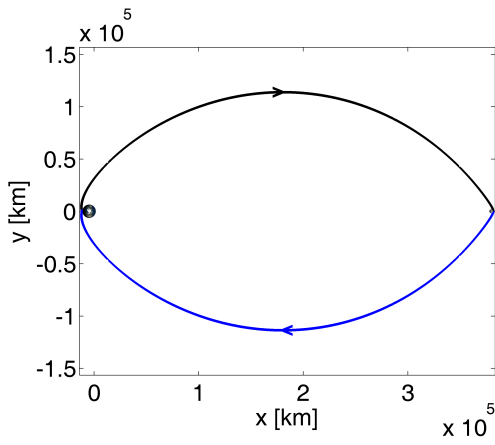
trajectories are symmetric with respect to the Earth-moon line whereas in the non-rotating frame the symmetry remains about the Earth-moon line at the time of the lunar flyby. Before and after the close approach to the moon, the trajectory is approximately an Earth-focused ellipse; in the vicinity of the moon, the trajectory is approximately a moon-focused hyperbola. As seen in Figs. 3.9(b), 3.9(d), 3.10(b), and 3.10(d), circumlunar free returns encounter the moon before reaching apogee on the Earth departure ellipse, but cislunar free returns pass through apogee before the lunar encounter and, thus, have a greater time of flight. Additionally, at this flyby altitude, circumlunar free returns remain within 150000 km of the Earth-moon line whereas cislunar free returns diverge from the Earth-moon line by more than 500000 km. This indicates that in a multibody force model, the solar perturbation will be more significant for these cislunar free returns.



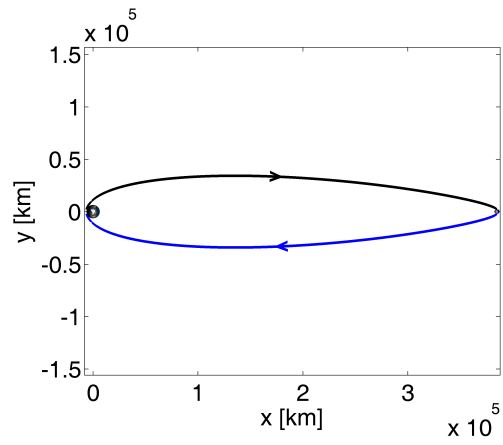
(a)



(b)

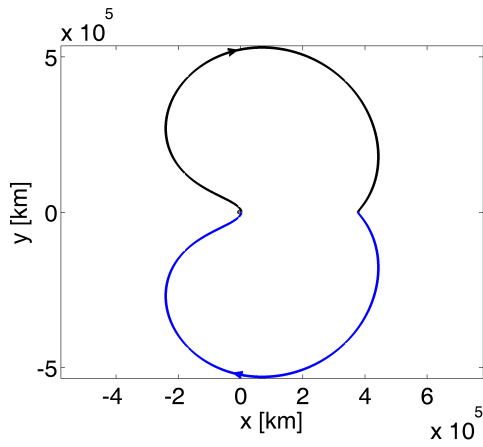


(c)

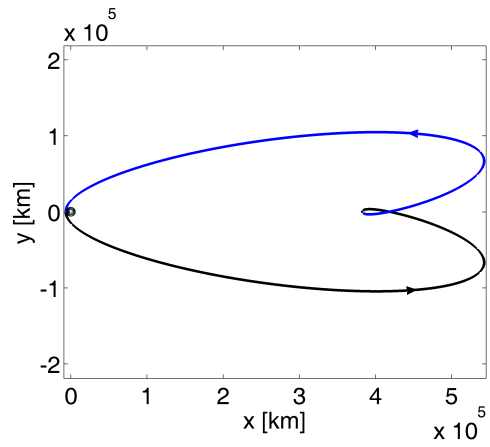


(d)

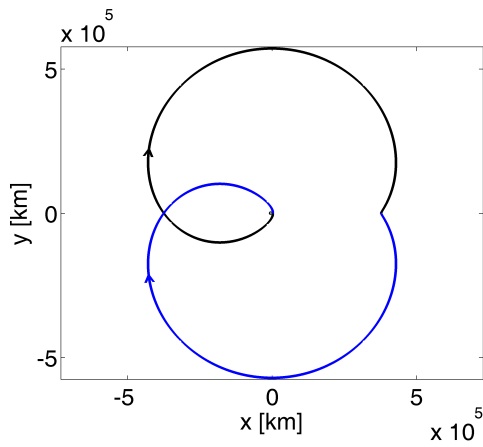
Figure 3.9: Planar circumlunar free returns: a)–b) type 0A_i in rotating and non-rotating frames, and c)–d) type 0A_{ii} in rotating and non-rotating frames.



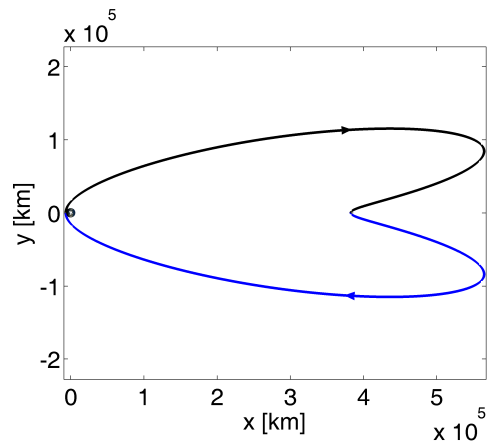
(a)



(b)



(c)

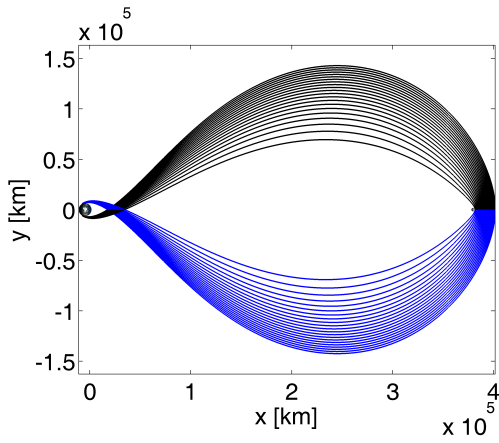


(d)

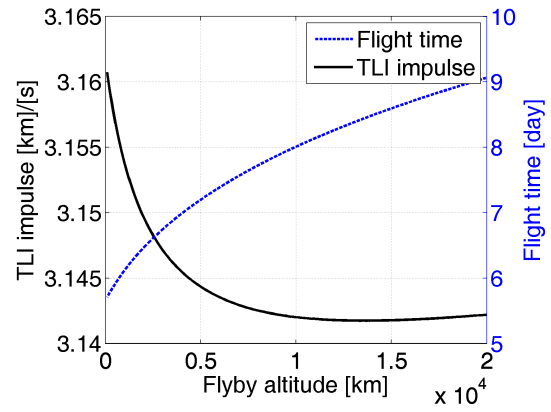
Figure 3.10: Planar cislunar free returns: a)–b) type 0Bi in rotating and non-rotating frames, and c)–d) type 0Bii in rotating and non-rotating frames.

Figures 3.11–3.12 show the four types of type 0 free return families with flyby altitude spanning 100 km to 20000 km, along with the TLI velocity impulse magnitude and round trip flight time plotted as a function of lunar flyby altitude. The velocity impulse shown is the impulse required to transfer from a circular Earth orbit at the same altitude. For type 0Ai trajectories, the required impulse decreases with increasing flyby altitude, reaches a minimum near 13000 km, and increases beyond that point. In general, for circumlunar flight, retrograde trajectories have a higher flight time and TLI velocity impulse than posigrade trajectories at the same flyby altitude. Circumlunar flight times increase with increasing altitude at the moon, and cislunar flight times decrease with increasing altitude at the moon. The minimum time type 0Ai free return occurs at $h = 100$ km, which is the minimum flyby altitude allowed in this dissertation. The minimum impulse trajectory offers a TLI savings of approximately 25 m/s while incurring a 65 hr increase in flight time relative to the minimum time trajectory. Because of the required increase in the amount of life support for increased flight time, and the delayed Earth return, the minimum impulse trajectory would not be as advantageous for human missions.

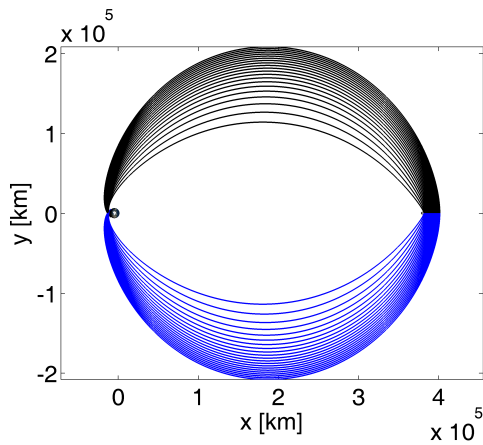
Figures 3.13–3.14 show the four types of symmetric non-planar free returns over the range of all possible lunar flyby orientations at a flyby altitude of 20000 km. For each type, there exists a posigrade and retrograde solution at a given flyby angle. In most cases, the posigrade free return has both a lower TLI velocity impulse and round trip flight time. Type 1 free returns enable a flyby azimuth less than 12 deg out of the Earth-moon plane whereas type 2 free returns allow any flyby latitude at this altitude. The latitude range of type 2 free returns, however, is more restrictive



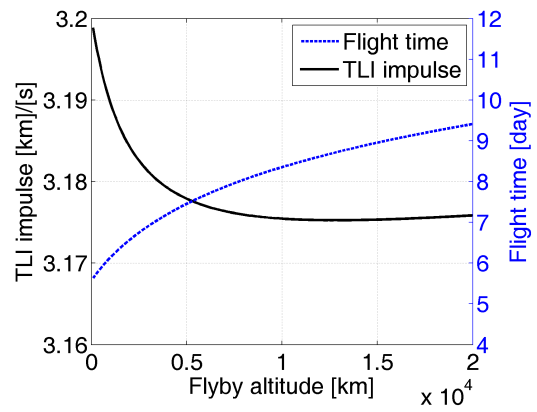
(a)



(b)



(c)



(d)

Figure 3.11: Circumlunar free return families: a) type 0Ai family (rotating frame), b) type 0Ai TLI impulse and flight time variation, c) type 0Aii family (rotating frame), and d) type 0Aii TLI impulse and flight time variation.

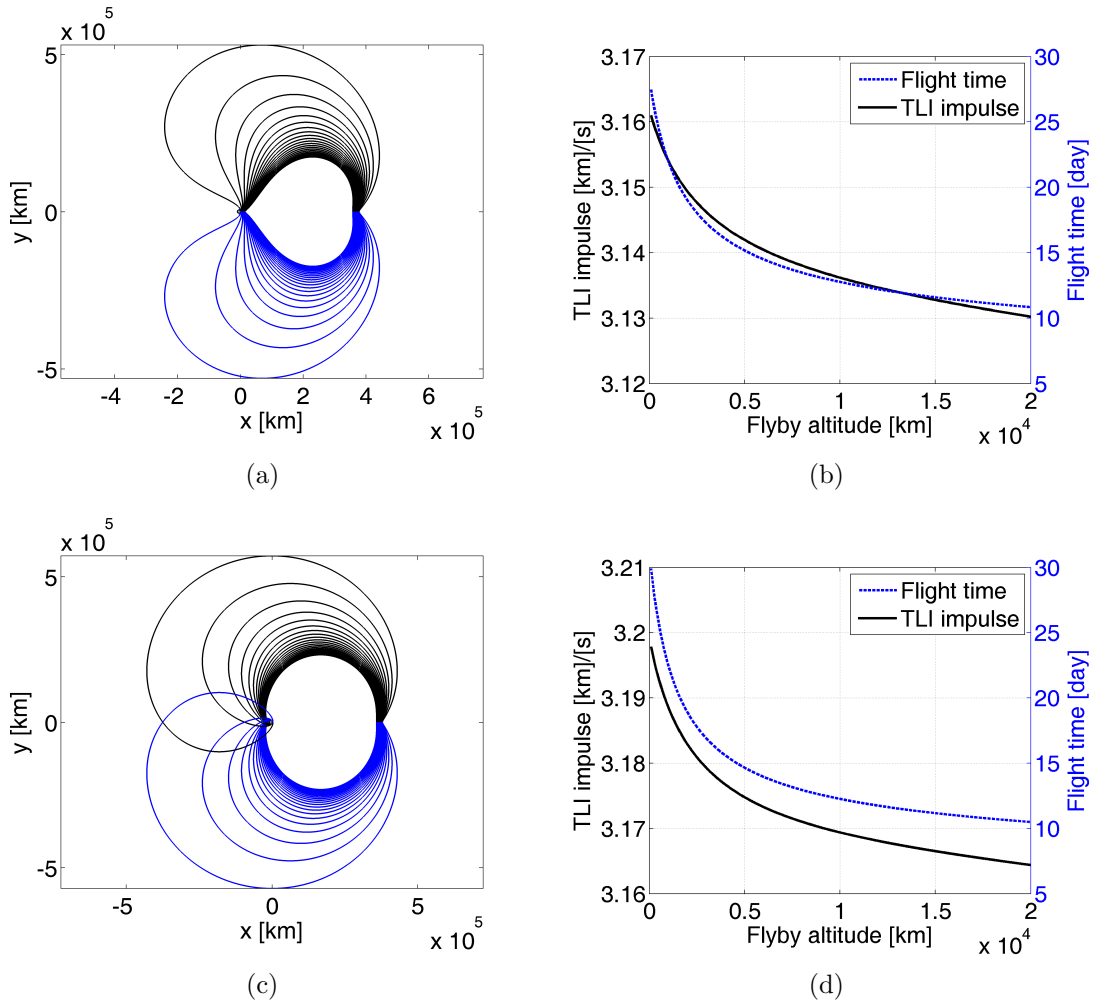


Figure 3.12: Cislunar free return families: a) type 0Bi family (rotating frame), b) type 0Bi TLI impulse and flight time variation, c) type 0Bii family (rotating frame), and d) type 0Bii TLI impulse and flight time variation.

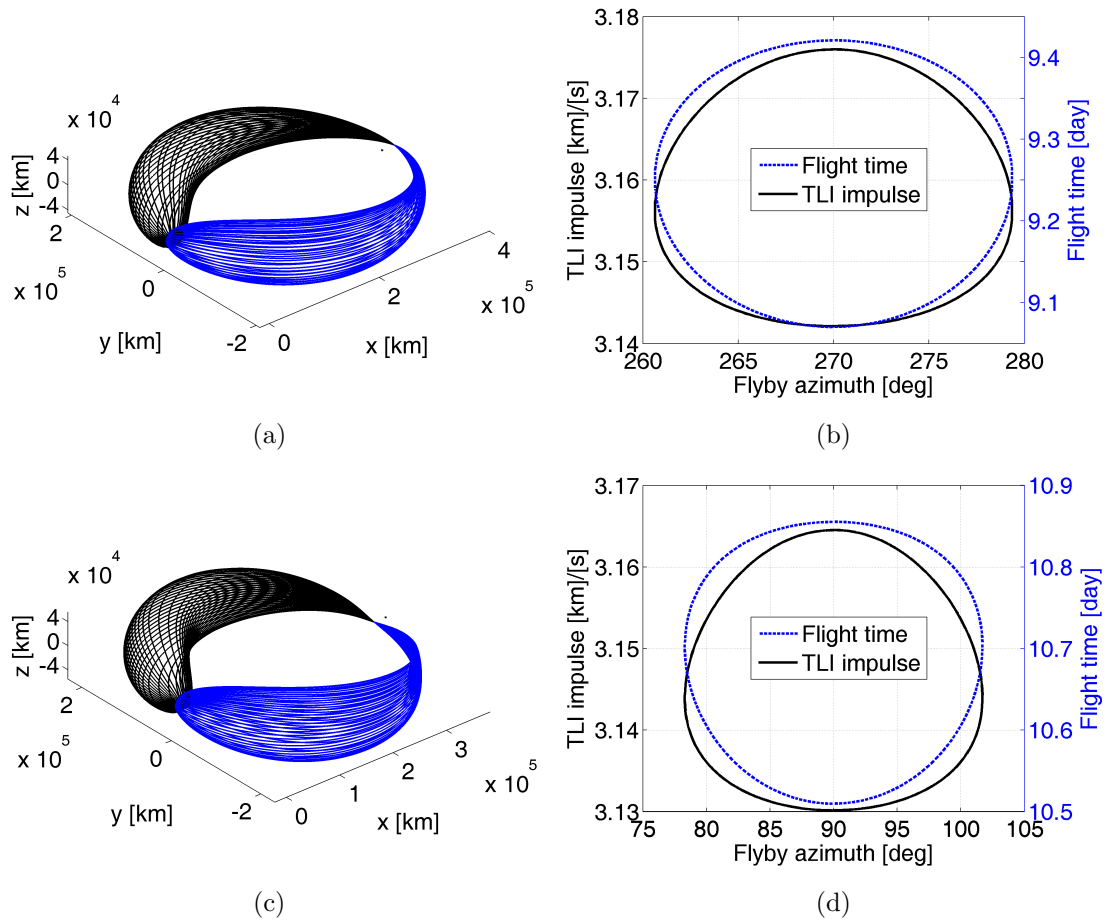


Figure 3.13: Type 1 free return surfaces: a) type 1A surface (rotating frame), b) type 1A TLI impulse and flight time variation, c) type 1B surface (rotating frame), and d) type 1B TLI impulse and flight time variation.

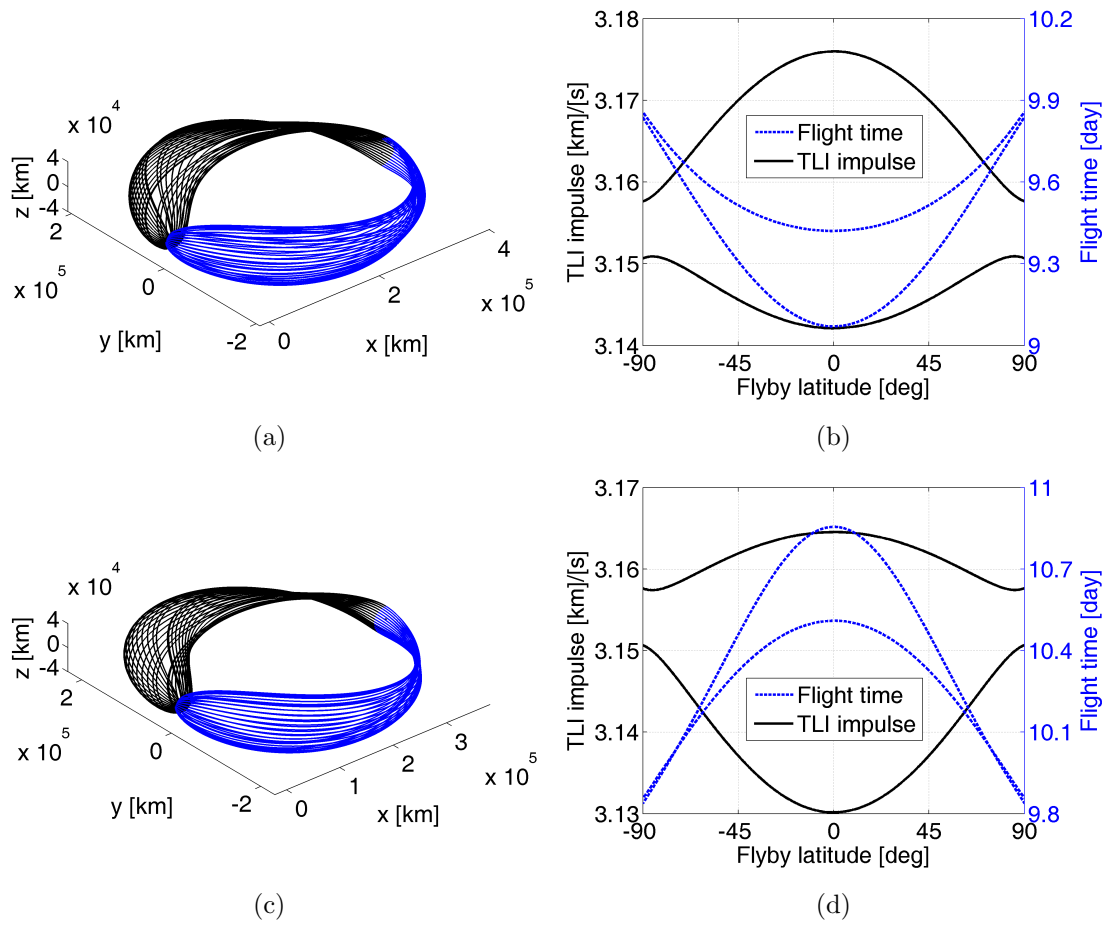


Figure 3.14: Type 2 free return surfaces: a) type 2A surface (rotating frame), b) type 2A TLI impulse and flight time variation, c) type 2B surface (rotating frame), and d) type 2B TLI impulse and flight time variation.

as the flyby altitude decreases. In general, the TLI velocity impulse increases as the free return moves out of the Earth-moon plane for posigrade trajectories; the trend is opposite for retrograde trajectories. The increase in TLI impulse between type 2Ai free returns of latitude 0 deg and 90 deg, for example, is approximately 10 m/s.

Free returns with a flyby latitude near 90 deg may be useful for future human missions interested in exploration of the lunar poles. However, in the planning of a realistic mission, limits on Earth launch azimuth must be considered. During the Apollo 8 mission, for example, the launch azimuth at Kennedy Space Center, measured east from north, was constrained to lie between 72 deg and 108 deg [69]. A similar range would be expected for future launches from this site. Other missions, launched from Vandenberg Air Force Base or the Baikonur Cosmodrome, for example, will offer different launch azimuth ranges. This is of concern in the current case because free returns that pass over the lunar poles require a TLI azimuth at Earth that is nearly due north or due south relative to the Earth-moon plane.

3.7 General Free Returns

An asymmetric ballistic segment that departs Earth, encounters the moon, and returns to Earth is called an asymmetric, or general, free return. If the latitude and azimuth at lunar flyby are simultaneously nonzero, the free return will be asymmetric since there will not be an orthogonal crossing of the Earth-moon line, and there will not be a perpendicular crossing of the vertical plane. The free return will always be asymmetric if the lunar flyby flight path angle is nonzero. Asymmetric posigrade circumlunar free returns are targeted in this section. Other asymmetric

free return types are not considered because they are not used in the remainder of this investigation. The asymmetry allows targeting of unequal Earth departure and return conditions; it also enables a broader range of geometry at lunar passage.

Because general free returns do not include a perpendicular crossing of the Earth-moon line or the vertical plane, the theorem of image trajectories does not apply. Therefore, a method with two trajectory segments is used where one segment is propagated from flyby to EEI, and the other segment is propagated from the flyby backwards in time to TLI. The state at lunar passage is continuous by the definition of a free return. At TLI, a flight path angle of $\gamma_{T_1} = 0$ deg and an altitude of $h_{T_1} = 350$ km are targeted; at EEI, a flight path angle of $\gamma_{T_2} = -6$ deg and an altitude of $h_{T_2} = 121$ km are targeted. Thus, the constraints are

$$\mathbf{c} \equiv \begin{bmatrix} h_{TLI} - h_{T_1} \\ \gamma_{TLI} - \gamma_{T_1} \\ h_{EEI} - h_{T_2} \\ \gamma_{EEI} - \gamma_{T_2} \end{bmatrix} = \mathbf{0} \quad (3.21)$$

To satisfy all four constraints, four free parameters are specified. The lunar flyby velocity magnitude and moon to Earth flight time on the EEI segment will be free, as in the targeting of symmetric free returns. Since the TLI segment is now integrated separately, its flight time is chosen as a free parameter. Finally, the flight path angle at lunar flyby is chosen to be free, creating a system with four constraints and four unknowns. The parameter vector is

$$\mathbf{x}_p \equiv \begin{bmatrix} v \\ t_{EEI} \\ t_{TLI} \\ \gamma \end{bmatrix} \quad (3.22)$$

The problem is solved numerically with NS11, and the initial estimate is a type 0Ai free return, constructed with the symmetric targeting algorithm. From the initial trajectory, a continuation method is used to advance to a feasible free return with the specified values of altitude, latitude, and azimuth at lunar flyby. The altitude is advanced first; next, the latitude is advanced; finally, the flyby azimuth is advanced to the desired value.

Figure 3.15 shows an example of a general free return. The altitude at lunar flyby is 15000 km, the latitude is 50 deg, and the azimuth is 280 deg. The round trip flight time is 9.45 days and the flight path angle at lunar flyby is -6.78 deg. The asymmetry is apparent in Fig. 3.15(b) which shows that this free return is similar to a type 2 free return with an elongated Earth to moon segment and a shortened moon to Earth segment.

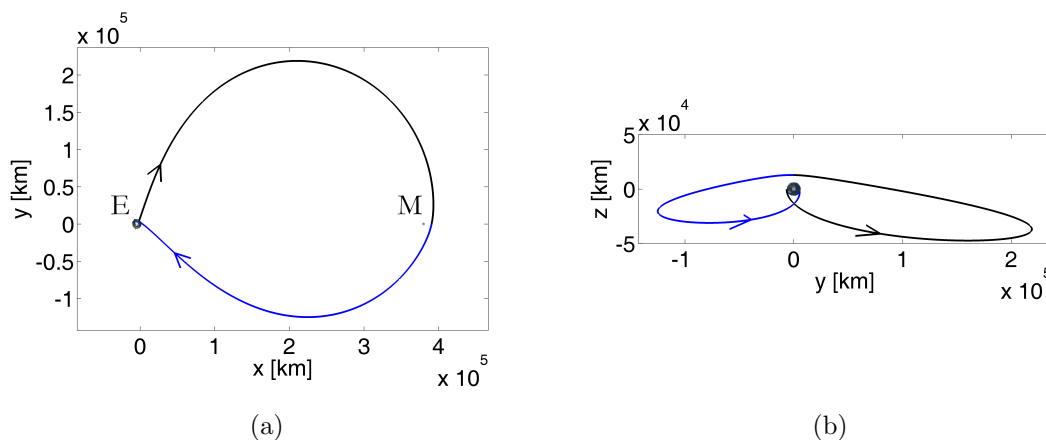


Figure 3.15: General free return (rotating frame): a) view normal to $\hat{x}\hat{y}$ plane, and b) view along moon-Earth line illustrating asymmetry.

Figs. 3.16–3.18 show trends in round trip flight time, TLI impulse magnitude, and EEI velocity magnitude. The vacant regions on the plots indicate that no feasible single-flyby free return is possible at this combination of altitude, latitude, and azimuth. At a flyby altitude of 100 km, the maximum possible latitude is ± 13 deg with the range of feasible flyby azimuths decreasing as the magnitude of the latitude increases. The region of feasibility in the latitude-azimuth plane is similar at a flyby altitude of 1000 km. As the flyby altitude increases, however, the feasible region grows, increasing to allow any latitude at $h = 20000$ km. At this altitude, the range of possible azimuths increases with increasing flyby latitude. Round trip flight time increases with increasing altitude at the moon, in general, with some cases requiring a flight time of approximately 30 days near the boundary of the feasibility region at $h = 15000$ km and $h = 20000$ km.

Figure 3.17 shows the variation in the TLI impulse magnitude. In this algorithm, the location and orientation of TLI are free to float, subject to the targeted conditions of altitude and flight path angle. The variation in the TLI impulse is therefore a result of the post-TLI velocity magnitude since the pre-TLI orbit is always a circular orbit in the instantaneous plane of the free return at that point. Knowledge of the TLI velocity magnitude is essential for mission design because the capability of an Earth-departure booster may limit the choice of a given free return. Figure 3.18 shows the EEI velocity as a function of the lunar flyby latitude and azimuth. The EEI velocity is also an important quantity in mission planning since the reentry thermal protection system of the vehicle may not be able to withstand certain reentry velocities. It would therefore be ideal to find a free return with a low TLI

requirement and a low EEI reentry velocity. By examining Figs. 3.17–3.18, it is seen that at flyby altitudes of 100 km and 1000 km, the regions with the minimum TLI requirements also incur the greatest reentry speeds. In the design of Apollo lunar reentry trajectories, the maximum allowed reentry velocity was 11.0743 km/s [11]; the maximum reentry velocity during a mission was 11.0685 km/s on Apollo 10; and the minimum was 11.0003 km/s on Apollo 17 [52]. All free returns shown here fall under the Apollo maximum except for some cases near the boundary of the feasibility region at a flyby altitude greater than or equal to 15000 km. The maximum allowed reentry velocity will depend upon the capability of the heat shield.

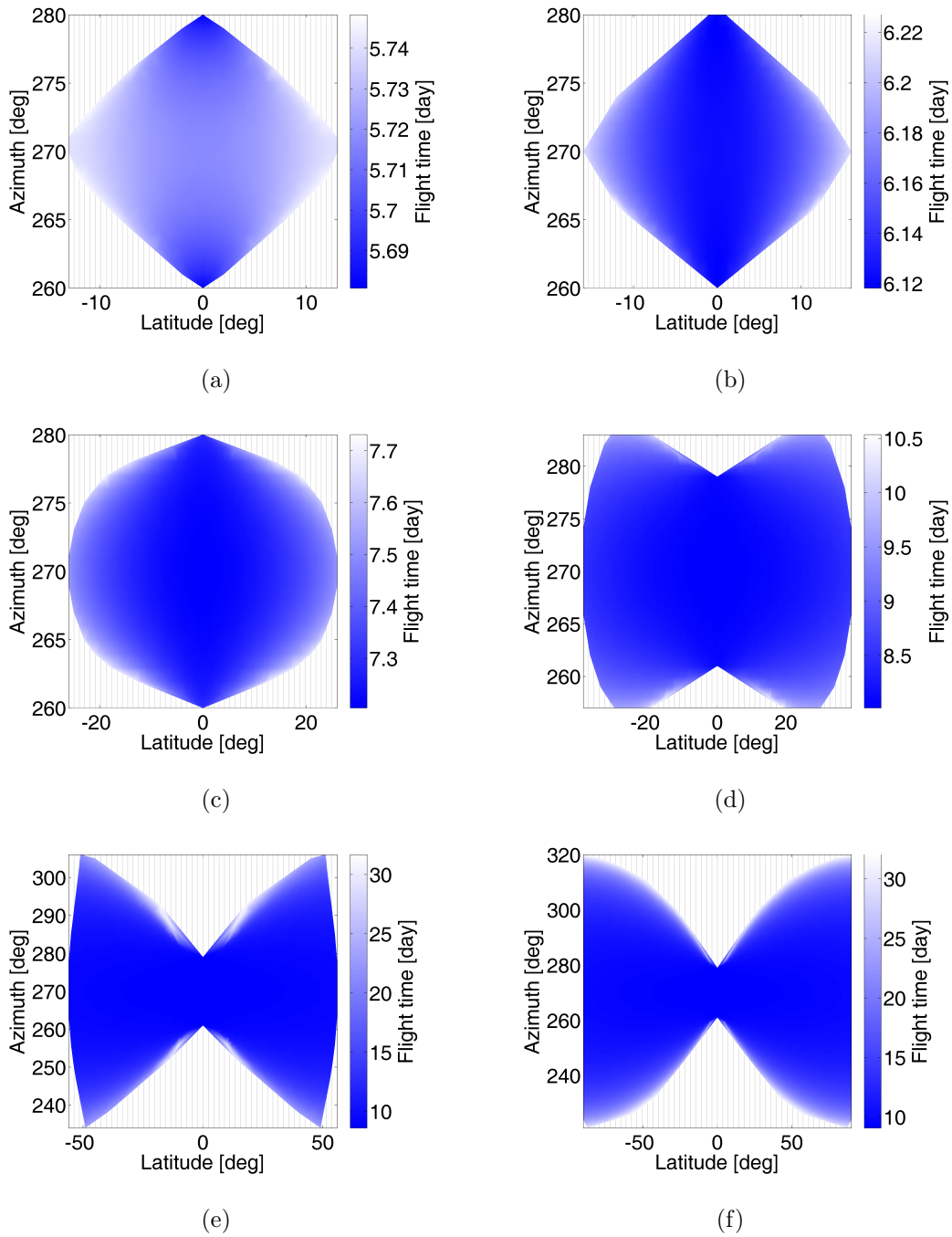


Figure 3.16: General free return flight time and feasibility region: a) $h = 100$ km, b) $h = 1000$ km, c) $h = 5000$ km, d) $h = 10000$ km, e) $h = 15000$ km, and f) $h = 20000$ km.

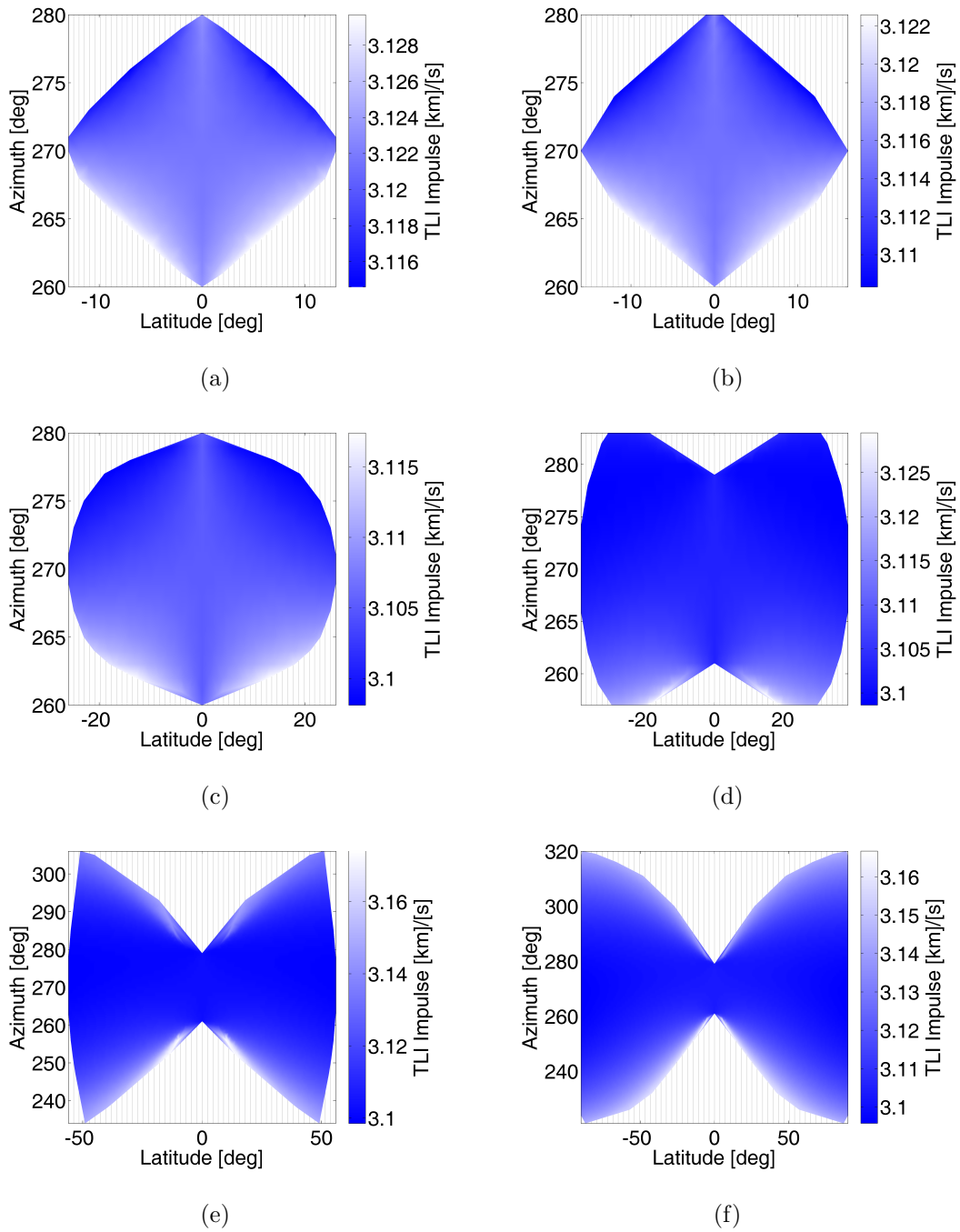


Figure 3.17: General free return TLI impulse and feasibility region: a) $h = 100$ km, b) $h = 1000$ km, c) $h = 5000$ km, d) $h = 10000$ km, e) $h = 15000$ km, and f) $h = 20000$ km.

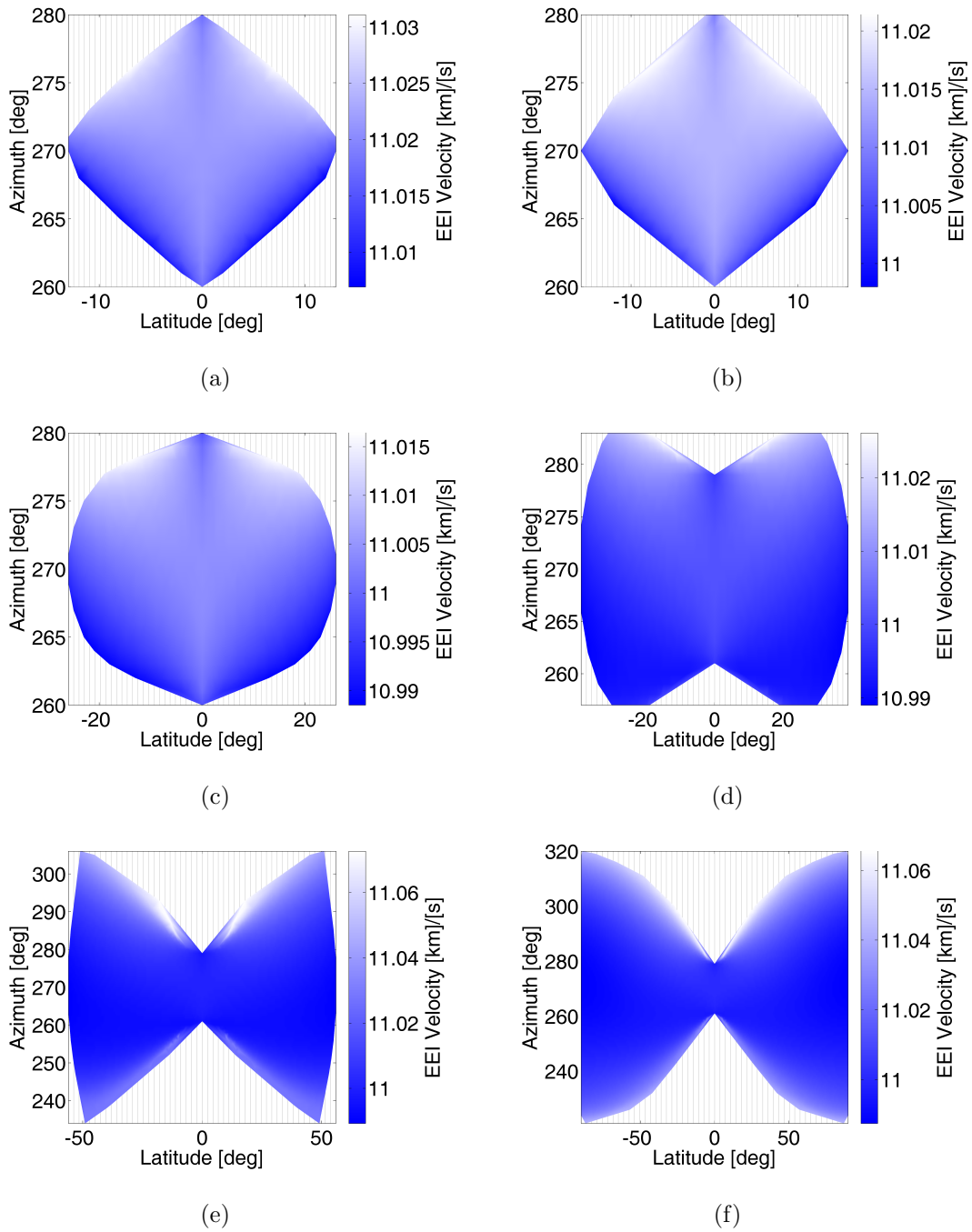


Figure 3.18: General free return EEI velocity and feasibility region: a) $h = 100$ km, b) $h = 1000$ km, c) $h = 5000$ km, d) $h = 10000$ km, e) $h = 15000$ km, and f) $h = 20000$ km.

Chapter 4

Optimal Spacecraft Trajectories

This chapter presents an overview of optimization techniques necessary for the solution of the free return and lunar orbit insertion problem. The chapter includes numerical optimization techniques and the supporting theory with an emphasis on the methods used in this investigation for nonlinear orbital trajectories. A discussion on analytical gradients features the derivation of a closed-form expression for computing gradients along an n -impulse trajectory in a completely general force field. Also included are numerical issues such as scaling and comparing analytical gradients to finite difference gradients. Finally, an overview of optimal control theory is presented with the derivation of the accompanying variational equations and an adjoint control transformation for estimating the costates of the optimal control problem.

4.1 Introduction

Optimization is a mathematical technique for finding the best solution among a set of alternative options. The criterion by which solutions are judged is user-defined and is called the performance index, objective function, or cost function. Typically, it may be desired to find the minimum value of some function subject

to constraints that define what solutions are acceptable. An optimization problem may include a nonlinear cost function and nonlinear constraints, as is often the case in multibody trajectory optimization.

The numerical solution of optimization problems may be divided into direct and indirect methods. Direct methods extremize a scalar performance index subject to constraints. Indirect methods optimize a performance index by solving a boundary value problem with differential constraints arising from the calculus of variations. Optimization with direct methods relies on parameter optimization and indirect optimization methods rely on optimal control theory. Hybrid solution methods combine aspects of the direct and indirect approaches.

4.2 Parameter Optimization

The general parameter optimization problem is to minimize a performance index subject to equality constraints and inequality constraints. The performance index $f(\mathbf{x})$ is a function of the $n \times 1$ parameter vector \mathbf{x} . The m equality constraints require

$$\mathbf{c}(\mathbf{x}) = \mathbf{0} \tag{4.1}$$

and the p inequality constraints require

$$\mathbf{d}(\mathbf{x}) \geq \mathbf{0} \tag{4.2}$$

The inequality constraints are converted to equality constraints with slack variables by requiring

$$\mathbf{d}(\mathbf{x}) - \mathbf{s}^2 = \mathbf{0} \tag{4.3}$$

where $\mathbf{s} \in \mathbb{R}^p$ is a vector of slack variables and

$$\mathbf{s}^2 \equiv \text{diag}(\mathbf{s}) \mathbf{s} = \begin{bmatrix} s_1 & & & \\ & s_2 & & \\ & & \ddots & \\ & & & s_p \end{bmatrix} \begin{bmatrix} s_1 \\ s_2 \\ \vdots \\ s_p \end{bmatrix} = \begin{bmatrix} s_1^2 \\ s_2^2 \\ \vdots \\ s_p^2 \end{bmatrix} \quad (4.4)$$

Thus, if the constraint is off-boundary or “inactive,” $d_i > 0$ and $s_i \neq 0$. If the constraint is on-boundary or “active,” $d_i = 0$ and $s_i = 0$.

The constraints are adjoined to the performance index to form the Lagrangian as

$$L(\mathbf{x}, \boldsymbol{\mu}, \boldsymbol{\nu}, \mathbf{s}) = f(\mathbf{x}) + \boldsymbol{\mu}^\top \mathbf{c}(\mathbf{x}) + \boldsymbol{\nu}^\top (\mathbf{d}(\mathbf{x}) - \mathbf{s}^2) \quad (4.5)$$

where $\boldsymbol{\mu}$ and $\boldsymbol{\nu}$ are Lagrange multipliers. The necessary conditions require the first derivative to vanish at an optimal point. Therefore, the following conditions must be satisfied:

$$\mathbf{0}^\top = \frac{\partial L}{\partial \mathbf{x}} = \frac{\partial f}{\partial \mathbf{x}} + \boldsymbol{\mu}^\top \frac{\partial \mathbf{c}}{\partial \mathbf{x}} + \boldsymbol{\nu}^\top \frac{\partial \mathbf{d}}{\partial \mathbf{x}} \quad (4.6)$$

$$\mathbf{0}^\top = \frac{\partial L}{\partial \boldsymbol{\mu}} = \mathbf{c}^\top(\mathbf{x}) \quad (4.7)$$

$$\mathbf{0}^\top = \frac{\partial L}{\partial \boldsymbol{\nu}} = (\mathbf{d}(\mathbf{x}) - \mathbf{s}^2)^\top \quad (4.8)$$

$$\mathbf{0}^\top = \frac{\partial L}{\partial \mathbf{s}} = -2\boldsymbol{\nu}^\top \mathbf{S} \quad (4.9)$$

where $\mathbf{S} \equiv \text{diag}(\mathbf{s})$. These are known as the Kuhn-Tucker optimality conditions [70]. If the i th inequality constraint is inactive, $s_i \neq 0$ by Eq. (4.8), so Eq. (4.9) requires $\nu_i = 0$. If the i th inequality constraint is active, $s_i = 0$ by Eq. (4.8).

4.2.1 Optimization Algorithms

Numerical optimization algorithms can be classified based on whether or not the derivatives of the performance index and constraint functions are required. Zeroth order methods rely solely on evaluation of the performance index throughout the solution space to determine the set of parameters that optimizes the performance index. Examples of zeroth order methods include the grid search, the simplex method [71], and genetic algorithms [72–75]. Alternatively, higher order methods require at least the first derivatives of the performance index and the constraints. Examples of these include the gradient method, Newton-Raphson algorithms, and variable metric methods [76]. Direct comparison of the performance index and exploration of the solution space with a zeroth order method may produce a globally optimal solution whereas a higher order method may locate only a locally optimal solution in the vicinity of the initial point. Due to the size of the solution space in multibody trajectory optimization problems, however, the use of gradient-based methods instead of a zeroth order method is attractive because a global search of the solution space may be time-prohibitive.

An optimizer that uses a gradient-based method can search for a parameter vector \mathbf{x} that satisfies the constraints and minimizes the cost by adjoining the active constraints to the objective function and satisfying the Kuhn-Tucker optimality conditions. At an optimal point, $\mathbf{c}(\mathbf{x}) = 0$, $\mathbf{d}(\mathbf{x}) \geq 0$, and $f(\mathbf{x})$ is a local minimum such that any perturbation in \mathbf{x} in the neighborhood of the minimum that still satisfies the constraints will increase the value of f . It is not possible to say without a comprehensive exploration of the solution space, however, whether or not the

solutions are globally optimal. An optimal solution using a gradient-based method is understood to be a locally optimal solution.

An algorithm that on each iteration minimizes a quadratic approximation of the performance index subject to linearized constraints is known as a sequential quadratic programming (SQP) algorithm. The Lagrangian is

$$L(\mathbf{x}, \boldsymbol{\mu}) = f(\mathbf{x}) + \boldsymbol{\mu}^\top \mathbf{c}(\mathbf{x}) \quad (4.10)$$

where active inequality constraints have been added to \mathbf{c} . An active inequality constraint means that $d_i(\mathbf{x}) = 0$, so the inequality constraint is functioning as an equality constraint. The quadratic approximation of the updated Lagrangian is

$$L(\mathbf{x} + \Delta\mathbf{x}, \boldsymbol{\mu}) \approx L(\mathbf{x}, \boldsymbol{\mu}) + \frac{\partial L}{\partial \mathbf{x}} \Delta\mathbf{x} + \frac{1}{2} \Delta\mathbf{x}^\top \frac{\partial}{\partial \mathbf{x}} \left(\frac{\partial L}{\partial \mathbf{x}} \right)^\top \Delta\mathbf{x} \quad (4.11)$$

where the first derivative, or Jacobian, and second derivative, or Hessian, of the Lagrangian are evaluated at \mathbf{x} and $\boldsymbol{\mu}$. The change in the value of the Lagrangian is

$$\Delta L = L(\mathbf{x} + \Delta\mathbf{x}, \boldsymbol{\mu}) - L(\mathbf{x}, \boldsymbol{\mu}) \quad (4.12)$$

$$\Delta L = \frac{\partial L}{\partial \mathbf{x}} \Delta\mathbf{x} + \frac{1}{2} \Delta\mathbf{x}^\top \frac{\partial}{\partial \mathbf{x}} \left(\frac{\partial L}{\partial \mathbf{x}} \right)^\top \Delta\mathbf{x} \quad (4.13)$$

The updated linearized constraints are given by

$$\mathbf{c}(\mathbf{x} + \Delta\mathbf{x}) = \mathbf{c}(\mathbf{x}) + \frac{\partial \mathbf{c}}{\partial \mathbf{x}} \Delta\mathbf{x} \quad (4.14)$$

Since the updated constraints should be satisfied, set $\mathbf{c}(\mathbf{x} + \Delta\mathbf{x}) = \mathbf{0}$. Equation (4.14) becomes

$$\frac{\partial \mathbf{c}}{\partial \mathbf{x}} \Delta\mathbf{x} = -\mathbf{c}(\mathbf{x}) \quad (4.15)$$

Now the quadratic performance index ΔL of Eq. (4.13) is minimized subject to the linearized constraints of Eq. (4.15). The Hessian of the Lagrangian is not always known, and it may be computationally expensive to calculate, so it is often estimated [77–82].

The SQP algorithm VF13 is used for optimization in this dissertation.¹ Also considered was SNOPT, an SQP algorithm developed for problems with sparse Jacobians [83]. Both algorithms were implemented to solve the problems in this investigation, but VF13 proved to be more consistent in locating the optimal solution. The intrinsic ability of VF13 that allows the user to quickly and explicitly bound individual inter-iteration parameter stepsizes is essential for convergence due to the nonlinearities associated with the orbit insertion sequence.

4.2.2 Analytical Gradients

Problems involving trajectories in multibody gravitational fields may contain nonlinear functions that do not have simple analytical derivatives, so these gradients are typically estimated numerically with finite differencing, automatic differentiation [84, 85], or complex-step differentiation [86, 87]. However, the gradients can be derived analytically with linear perturbation theory in which the partial derivative of the state at one time with respect to the state at another time is given by the state transition matrix (STM). Derivatives computed in this manner are referred to as “variational derivatives” or “analytical derivatives.” In most cases the STM

¹Information available at <http://www.hsl.rl.ac.uk/archive/specs/vf13.pdf> [accessed 15 March 2012]

must be numerically integrated, so the derivatives are not truly analytical. Some simple cases do exist where an analytic expression exists for the STM, but this is not the case for multibody gravitational fields.

The use of linear perturbation theory to compute gradients eliminates the need for finite differencing to compute derivatives and offers advantages over differencing techniques. First, to obtain accurate derivatives by finite differencing, stepsizes must be chosen for each parameter that avoid truncation error and round-off error. These stepsizes are different for each parameter, may be different for each function, and may change during the optimization process. The process of computing optimal stepsizes is not trivial; one method of determining suitable stepsizes is given in Ref. [88]. Second, the computation of derivatives via finite differencing may be more time intensive than STM-based derivatives since differencing requires the independent perturbation of each parameter and integration through the final time. While STM-based derivatives require the propagation of the full STM once per iteration, central differencing, for example, requires full state propagation twice per parameter on each iteration. So, even though integrating the STM necessitates the numerical propagation of $n + n^2$ quantities for an n -element state vector, a time savings over finite differencing can be achieved depending on the number of parameters. Third, within the linear region of the nominal trajectory, the only error in the analytical gradients results from errors in numerical integration. The most significant disadvantage of STM-based derivatives is the amount of work required to derive and implement the gradients. The formulation used here is based on a generalized variational procedure described in Ref. [89]. Examples of success-

ful implementation of analytical gradients are seen in studies on multi-impulse and finite-burn lunar transearth injection [90, 91], and Earth-Saturn trajectories with intermediate planetary gravity assist [92, 93].

The differential of a function $\mathbf{f}(x_1, x_2, \dots, x_n)$ of n independent variables satisfies

$$d\mathbf{f} = \frac{\partial \mathbf{f}}{\partial x_1} dx_1 + \frac{\partial \mathbf{f}}{\partial x_2} dx_2 + \dots + \frac{\partial \mathbf{f}}{\partial x_n} dx_n \quad (4.16)$$

The partial derivative of \mathbf{f} with respect to any x_i is determined by finding the coefficient of dx_i in the differential of \mathbf{f} . Thus, if the total differential of a function can be derived in terms of independent differentials, the gradients with respect to the free parameters may be determined. For some cases, the differential may be computed directly; for complex spacecraft trajectories, linear perturbation theory is required to compute the total differential of the spacecraft state at a given time.

Consider the simplified transfer segments shown in Fig. 4.1 with two ballistic arcs and three state discontinuities. This can represent, for example, a ballistic spacecraft trajectory with velocity impulse maneuvers at the initial, intermediate, and final times. But the discontinuities may represent an impulsive change in any state element, and the state vector \mathbf{x} can be defined by the user to accommodate other mission design scenarios. Regardless of how the state and discontinuities are defined, the total differential of the final state is derived so that the partial derivatives necessary for optimization may be obtained. The state at the final time is

$$\mathbf{x}_2^+ = \mathbf{x}_2^- + \Delta \mathbf{x}_2 \quad (4.17)$$

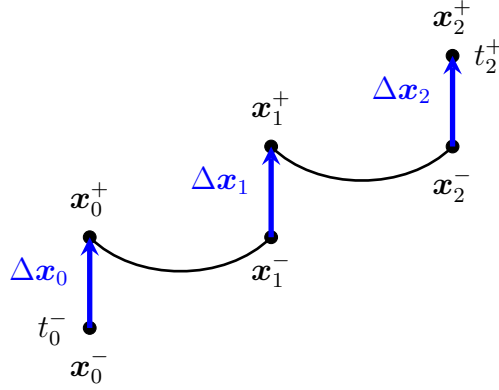


Figure 4.1: Transfer segments with three state discontinuities.

Taking the differential,

$$d\mathbf{x}_2^+ = d\mathbf{x}_2^- + d(\Delta\mathbf{x}_2) \quad (4.18)$$

Substituting for the total differential at t_2^- gives

$$d\mathbf{x}_2^+ = \delta\mathbf{x}_2^- + \dot{\mathbf{x}}_2^- dt_2 + d(\Delta\mathbf{x}_2) \quad (4.19)$$

Utilizing Eq. (2.12), the total differential becomes

$$d\mathbf{x}_2^+ = \Phi(t_2, t_1)\delta\mathbf{x}_1^+ + \dot{\mathbf{x}}_2^- dt_2 + d(\Delta\mathbf{x}_2) \quad (4.20)$$

where it is understood that

$$\Phi(t_i, t_{i-1}) \equiv \Phi(t_i^-, t_{i-1}^+) \quad (4.21)$$

Continuing,

$$d\mathbf{x}_2^+ = \Phi(t_2, t_1) [d\mathbf{x}_1^+ - \dot{\mathbf{x}}_1^+ dt_1] + \dot{\mathbf{x}}_2^- dt_2 + d(\Delta\mathbf{x}_2) \quad (4.22)$$

$$d\mathbf{x}_2^+ = \Phi(t_2, t_1) \left\{ \Phi(t_1, t_0) [d\mathbf{x}_0^+ - \dot{\mathbf{x}}_0^+ dt_0] + d(\Delta\mathbf{x}_1) - \Delta\dot{\mathbf{x}}_1 dt_1 \right\} + \dot{\mathbf{x}}_2^- dt_2 + d(\Delta\mathbf{x}_2) \quad (4.23)$$

$$d\mathbf{x}_2^+ = \Phi(t_2, t_1) \left\{ \Phi(t_1, t_0) [d\mathbf{x}_0^- + d(\Delta\mathbf{x}_0) - \dot{\mathbf{x}}_0^+ dt_0] + d(\Delta\mathbf{x}_1) - \Delta\dot{\mathbf{x}}_1 dt_1 \right\} + \dot{\mathbf{x}}_2^- dt_2 + d(\Delta\mathbf{x}_2) \quad (4.24)$$

where

$$\Delta\dot{\mathbf{x}}_i \equiv \dot{\mathbf{x}}_i^+ - \dot{\mathbf{x}}_i^- \quad (4.25)$$

Rearranging Eq. (4.24) gives

$$\begin{aligned} d\mathbf{x}_2^+ = & \Phi(t_2, t_1) \Phi(t_1, t_0) [d\mathbf{x}_0^- + d(\Delta\mathbf{x}_0) - \dot{\mathbf{x}}_0^+ dt_0] + \\ & \Phi(t_2, t_1) [d(\Delta\mathbf{x}_1) - \Delta\dot{\mathbf{x}}_1 dt_1] + \\ & \dot{\mathbf{x}}_2^- dt_2 + d(\Delta\mathbf{x}_2) \end{aligned} \quad (4.26)$$

Equation (4.26) is used to determine the gradient of the final state with respect to any state discontinuity or discontinuity time. For example, the gradient of the final state with respect to the time of the intermediate discontinuity is

$$\frac{\partial \mathbf{x}_2^+}{\partial t_1} = -\Phi(t_2, t_1) \Delta\dot{\mathbf{x}}_1 \quad (4.27)$$

by finding the coefficient of dt_1 in Eq. (4.26). The same procedure is used for the remaining gradients. Next, consider the final state differential for a case with three

ballistic arcs and four state discontinuities given by

$$\begin{aligned}
d\mathbf{x}_3^+ &= \Phi(t_3, t_2)\Phi(t_2, t_1)\Phi(t_1, t_0) \left[d\mathbf{x}_0^- + d(\Delta\mathbf{x}_0) - \dot{\mathbf{x}}_0^+ dt_0 \right] + \\
&\quad \Phi(t_3, t_2)\Phi(t_2, t_1) \left[d(\Delta\mathbf{x}_1) - \Delta\dot{\mathbf{x}}_1 dt_1 \right] + \\
&\quad \Phi(t_3, t_2) \left[d(\Delta\mathbf{x}_2) - \Delta\dot{\mathbf{x}}_2 dt_2 \right] + \\
&\quad \dot{\mathbf{x}}_3^- dt_3 + d(\Delta\mathbf{x}_3)
\end{aligned} \tag{4.28}$$

where the derivation is similar to that of the two arc case. Examining Eq. (4.26) and Eq. (4.28), it is seen that differentials associated with the t_0 node are multiplied by each STM through the final node. Terms associated with internal nodes are multiplied by each subsequent STM. Terms associated with the final node are not multiplied by any STM. Extending this pattern through n ballistic arcs as shown in Fig. 4.2, the general form of the final state differential with an impulsive state discontinuity occurring at each node is

$$\begin{aligned}
d\mathbf{x}_n^+ &= \left[\prod_{i=1}^n \Phi(t_{i-1}, t_i) \right]^{-1} \left(d\mathbf{x}_0^- + d(\Delta\mathbf{x}_0) - \dot{\mathbf{x}}_0^+ dt_0 \right) + \\
&\quad \sum_{i=1}^{n-1} \left\{ \left[\prod_{j=i}^{n-1} \Phi(t_j, t_{j+1}) \right]^{-1} \left(d(\Delta\mathbf{x}_i) - \Delta\dot{\mathbf{x}}_i dt_i \right) \right\} + \dot{\mathbf{x}}_n^- dt_n + d(\Delta\mathbf{x}_n)
\end{aligned} \tag{4.29}$$

for $n > 1$. This result allows the gradients of the spacecraft state at a given time with respect to the free parameters to be obtained. The inverted coefficients in Eq. (4.29) are used for notational brevity; but because it is known that

$$\Phi^{-1}(t_j, t_i) = \Phi(t_i, t_j) \tag{4.30}$$

no matrix inversion is necessary to compute the coefficients in Eq. (4.29).

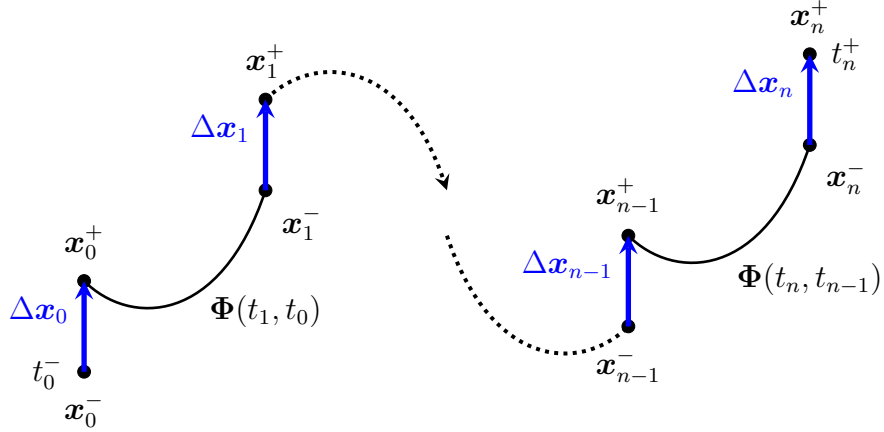


Figure 4.2: General transfer segments with n ballistic arcs and $n + 1$ state discontinuities.

4.2.2.1 Gradient Validation

To validate the analytically derived gradients, they are compared to finite difference gradients computed with a method that minimizes the roundoff error and truncation error. This algorithm² is essential when using parameters that cannot always be intuitively estimated, such as the costates of the optimal control problem. Once the analytical and finite difference gradients have been generated, a difference metric is used to compare an analytic gradient α to a finite difference gradient β . The chosen difference metric is

$$d \equiv 100 \operatorname{sign}(\alpha\beta) \frac{|\alpha - \beta|}{1 + |\beta|} \quad (4.31)$$

which is similar to that suggested in Ref. [94]. This metric behaves as a relative percent difference at large values of the gradient and as an absolute difference at

²Restrepo, R. L., “Gradient Tuning Algorithm,” Unpublished, Department of Aerospace Engineering and Engineering Mechanics, University of Texas at Austin, Oct. 2011.

small values of the gradient. An error is clearly indicated if $d < 0$ since this indicates the gradients are of opposite sign, and experience has shown that there is usually an error in the analytical gradient derivation or in the implementation if $d > 2$. However, there is no unequivocal standard by which to know a gradient is incorrect. The value of d can also be influenced by an inaccurate finite difference gradient or by errors in numerical integration that affect both the analytical and numerical gradient.

4.2.3 Scaling

Scaling the cost function, constraints, and free parameters is essential for convergence of trajectory optimization problems. Various authors stress the importance of scaling and suggest appropriate methods [94–96]. For most problems presented here, it is sufficient to use a simple scaling scheme given by

$$\tilde{f} = \frac{1}{s_f} f \tag{4.32}$$

$$\tilde{\mathbf{x}} = \mathbf{S}_x^{-1} \mathbf{x} \tag{4.33}$$

$$\tilde{\mathbf{c}} = \mathbf{S}_c^{-1} \mathbf{c} \tag{4.34}$$

$$\tilde{\mathbf{d}} = \mathbf{S}_d^{-1} \mathbf{d} \tag{4.35}$$

where \tilde{f} , $\tilde{\mathbf{x}}$, $\tilde{\mathbf{c}}$, $\tilde{\mathbf{d}}$ are the scaled objective function, parameters, equality constraints, and inequality constraints; s_f is cost scale, and \mathbf{S}_x , \mathbf{S}_c , \mathbf{S}_d are diagonal matrices consisting of the parameter scales, equality constraint scales, and inequality constraint scales, respectively. In an effort to achieve scaled parameter values on the

order of one, the scale of the i th parameter is chosen as

$$s_{x_i} = \begin{cases} 10^\alpha & \text{if } |x_{i_0}| > 1 \\ 1 & \text{if } |x_{i_0}| \leq 1 \end{cases} \quad (4.36)$$

where x_{i_0} is the initial value of the i th parameter and

$$\alpha \equiv \text{floor}(\log_{10} |x_{i_0}|) + 1 \quad (4.37)$$

The scales for the objective function and constraints are chosen in the same manner.

For cases where the simple scaling scheme does not produce satisfactory results, such as the hybrid optimal control problem, the geometric mean scaling scheme suggested by Fourer [96] is used. This method simultaneously chooses the parameter and constraint scales such that the Jacobian matrix of the constraints has entries with a minimum magnitude difference between elements. The scaling procedure is:

1. Compute the Jacobian of the constraints as

$$\mathbf{A} \equiv \begin{bmatrix} \frac{\partial \mathbf{c}}{\partial \mathbf{x}} \\ \frac{\partial \mathbf{d}}{\partial \mathbf{x}} \end{bmatrix} = \begin{bmatrix} a_{11} & a_{12} & \cdots & a_{1n} \\ a_{21} & a_{22} & & \vdots \\ a_{31} & & \ddots & \\ \vdots & & & \\ a_{(m+p)1} & \cdots & & a_{(m+p)n} \end{bmatrix}_{(m+p) \times n} \quad (4.38)$$

2. Compute the maximum element magnitude ratio in each column of the Jacobian and retain the maximum ratio ρ_0 as

$$\rho_0 = \max_j \left(\frac{\max_i |a_{ij}|}{\min_i |a_{ij}|} \right) \quad (4.39)$$

for $a_{ij} \neq 0$ where i is the Jacobian row index and j is the Jacobian column index. Set an index $k = 1$.

3. Divide each row of \mathbf{A} by that row's geometric mean, which becomes the scale of the i th constraint, given by

$$s_{c_i} = \left[\left(\min_j |a_{ij}| \right) \left(\max_j |a_{ij}| \right) \right]^{\frac{1}{2}} \quad (4.40)$$

4. Divide each column of \mathbf{A} by that column's geometric mean, which is the inverse scale of the j th parameter, given by

$$\frac{1}{s_{x_j}} = \left[\left(\min_i |a_{ij}| \right) \left(\max_i |a_{ij}| \right) \right]^{\frac{1}{2}} \quad (4.41)$$

5. Set the new maximum value of the maximum column element magnitude ratios to

$$\rho_k = \max_j \left(\frac{\max_i |a_{ij}|}{\min_i |a_{ij}|} \right) \quad (4.42)$$

for $a_{ij} \neq 0$.

6. If $\rho_k \geq 0.99\rho_{k-1}$, then scaling is complete; otherwise, set $k = k + 1$ and return to step 3. When step 3 and step 4 are repeated, subsequent scales are multiplied together.

This scaling scheme has proved effective when the optimizer does not make progress with the simple scaling scheme and when the optimizer is near the optimal solution but not converged.

4.3 Optimal Control Theory

Optimal control theory provides a method for extremizing a performance index, the sum of a terminal cost function plus an integrated cost function over

a continuous time domain. The theory establishes mathematical requirements on a piecewise continuous control $\mathbf{u}(t)$ that drives the state $\mathbf{x}(t)$ from initial to final conditions, subject to the system dynamics $\dot{\mathbf{x}}(t) = \mathbf{f}(t, \mathbf{x}, \mathbf{u})$, in such a way that the performance index is optimized. At an optimal solution, the performance index is stationary with respect to the control. This requirement that the first differential of the performance index vanish imposes necessary conditions on the optimal solution.

The general optimal control problem is to minimize the performance index given by

$$J = \phi(t_f, \mathbf{x}_f) + \int_{t_0}^{t_f} L(t, \mathbf{x}(t), \mathbf{u}(t))dt \quad (4.43)$$

subject to the system dynamics

$$\dot{\mathbf{x}} = \mathbf{f}(t, \mathbf{x}, \mathbf{u}) \quad (4.44)$$

the initial conditions

$$\boldsymbol{\theta}(t_0, \mathbf{x}_0) = \mathbf{0} \quad (4.45)$$

and the final conditions

$$\boldsymbol{\psi}(t_f, \mathbf{x}_f) = \mathbf{0} \quad (4.46)$$

where ϕ is the terminal cost and L is the Lagrangian which determines the accumulated cost [97]. Because the solution must satisfy the system dynamics and the prescribed constraints, the minimization of J must be constrained such that it satisfies these requirements. This is accomplished by adjoining the constraints to the performance index with Lagrange multipliers to form an augmented performance index, given by

$$J' = \phi(t_f, \mathbf{x}_f) + \boldsymbol{\nu}^\top \boldsymbol{\psi}(t_f, \mathbf{x}_f) + \boldsymbol{\xi}^\top \boldsymbol{\theta}(t_0, \mathbf{x}_0) + \int_{t_0}^{t_f} [L(t, \mathbf{x}, \mathbf{u}) + \boldsymbol{\lambda}^\top (\mathbf{f} - \dot{\mathbf{x}})] dt \quad (4.47)$$

where $\boldsymbol{\nu}$, $\boldsymbol{\xi}$, and $\boldsymbol{\lambda}(t)$ are Lagrange multipliers. The time varying multipliers $\boldsymbol{\lambda}(t)$ are also called the costates of the optimal control problem. The augmented performance index can be more succinctly written as

$$J' = G + \int_{t_0}^{t_f} [H - \boldsymbol{\lambda}^\top \dot{\boldsymbol{x}}] dt \quad (4.48)$$

where G is the endpoint function, defined as

$$G(t_f, \boldsymbol{x}_f, \boldsymbol{\nu}, t_0, \boldsymbol{x}_0, \boldsymbol{\xi}) \equiv \phi(t_f, \boldsymbol{x}_f) + \boldsymbol{\nu}^\top \boldsymbol{\psi}(t_f, \boldsymbol{x}_f) + \boldsymbol{\xi}^\top \boldsymbol{\theta}(t_0, \boldsymbol{x}_0) \quad (4.49)$$

and H is the Hamiltonian, defined as

$$H(t, \boldsymbol{x}, \boldsymbol{u}, \boldsymbol{\lambda}) \equiv L(t, \boldsymbol{x}, \boldsymbol{u}) + \boldsymbol{\lambda}^\top \boldsymbol{f}(t, \boldsymbol{x}, \boldsymbol{u}) \quad (4.50)$$

At a minimum point, it is necessary that the first differential of the performance index is zero. Taking the differential of J' and requiring $dJ' = 0$ gives necessary conditions for an optimal point. Collectively, the conditions that concern the state evolution, costate evolution, and control history are called the Euler-Lagrange equations, and the conditions that specify the boundary conditions of the costates and the Hamiltonian are called the natural boundary conditions or transversality conditions.

As derived in Appendix C, the Euler-Lagrange equations are

$$\dot{\boldsymbol{x}} = \boldsymbol{f} \quad (4.51)$$

$$\dot{\boldsymbol{\lambda}} = - \left(\frac{\partial H}{\partial \boldsymbol{x}} \right)^\top \quad (4.52)$$

$$\mathbf{0} = \left(\frac{\partial H}{\partial \boldsymbol{u}} \right)^\top \quad (4.53)$$

and the natural boundary conditions are

$$H_0 = \frac{\partial G}{\partial t_0} \tag{4.54}$$

$$\boldsymbol{\lambda}_0 = - \left(\frac{\partial G}{\partial \mathbf{x}_0} \right)^\top \tag{4.55}$$

$$H_f = - \frac{\partial G}{\partial t_f} \tag{4.56}$$

$$\boldsymbol{\lambda}_f = \left(\frac{\partial G}{\partial \mathbf{x}_f} \right)^\top \tag{4.57}$$

Two common numerical solution methods for optimal control problems are the indirect method and the hybrid method. In the indirect method, the performance index is optimized indirectly by solving a square system of nonlinear equations comprised of the problem constraints and the natural boundary conditions. The time evolution of the state, costates, and control is governed by the Euler-Lagrange equations. Numerical convergence of the indirect method may be difficult due to the sensitivity of the costate equations and the inability to generate an initial estimate within the convergence envelope of the algorithm. By contrast, the hybrid method utilizes a parameter optimization algorithm to directly optimize the performance index while the control is driven according to optimal control theory. Thus, the transversality conditions will be satisfied implicitly when the performance index is optimized. One advantage of the hybrid method is that state and control constraints can be easily applied in a parameter optimization framework. Both the indirect and hybrid method can be aided by an adjoint control transformation which produces estimates of the costates based on physically meaningful quantities.

In spacecraft trajectory optimization, it is customary to estimate the costates based on the angular orientation of the thrust vector.

4.3.1 Optimal Thrust Pointing

Consider the minimization of a performance index given by

$$J \equiv m_0 - m_f \quad (4.58)$$

where m_0 is the initial spacecraft mass and m_f is the final spacecraft mass; thus, the total propellant mass is minimized. The spacecraft state is

$$\mathbf{x} = \begin{bmatrix} \mathbf{r} \\ \mathbf{v} \\ m \end{bmatrix}_{7 \times 1} \quad (4.59)$$

where \mathbf{r} , \mathbf{v} , and m represent the spacecraft's position, velocity, and mass; each quantity is an implicit function of time. The state time derivative is

$$\dot{\mathbf{x}} = \begin{bmatrix} \dot{\mathbf{r}} \\ \dot{\mathbf{v}} \\ \dot{m} \end{bmatrix} = \begin{bmatrix} \mathbf{v} \\ \mathbf{g} + \frac{T}{m} \hat{\mathbf{u}} \\ -\frac{T}{c} \end{bmatrix} \quad (4.60)$$

where \mathbf{g} is the position-dependent gravitational acceleration, which may be time-varying, T is the thrust magnitude, $\hat{\mathbf{u}}$ is the thrust direction, and c is the constant exhaust velocity. The spacecraft state is controlled by specifying control histories for T and $\hat{\mathbf{u}}$, where the controls are subject to the following constraints:

$$\hat{\mathbf{u}}^\top \hat{\mathbf{u}} - 1 = 0 \quad (4.61)$$

$$(T_{MAX} - T)T - \alpha^2 = 0 \quad (4.62)$$

where α is a slack variable. Forming the variational Hamiltonian of the optimal control problem,

$$H = \boldsymbol{\lambda}_r^\top \mathbf{v} + \boldsymbol{\lambda}_v^\top \mathbf{g} + T \left(\frac{\boldsymbol{\lambda}_v^\top \hat{\mathbf{u}}}{m} - \frac{\lambda_m}{c} \right) \quad (4.63)$$

where $\boldsymbol{\lambda}$ is a vector of time-varying Lagrange multipliers. Adjoining the control constraints to the Hamiltonian with Lagrange multipliers gives the extended Hamiltonian as

$$\hat{H} = \boldsymbol{\lambda}_r^\top \mathbf{v} + \boldsymbol{\lambda}_v^\top \mathbf{g} + T \left(\frac{\boldsymbol{\lambda}_v^\top \hat{\mathbf{u}}}{m} - \frac{\lambda_m}{c} \right) + \mu_1 (\hat{\mathbf{u}}^\top \hat{\mathbf{u}} - 1) + \mu_2 [(T_{MAX} - T)T - \alpha^2] \quad (4.64)$$

The Euler-Lagrange equations are

$$\dot{\mathbf{x}} = \mathbf{f} \quad (4.65)$$

$$\dot{\boldsymbol{\lambda}} = - \left(\frac{\partial \hat{H}}{\partial \mathbf{x}} \right)^\top \quad (4.66)$$

$$\mathbf{0} = \left(\frac{\partial \hat{H}}{\partial \mathbf{u}} \right)^\top \quad (4.67)$$

where \mathbf{u} represents the controls. Expanding the costate equation,

$$\dot{\boldsymbol{\lambda}}_r = - \left(\frac{\partial \hat{H}}{\partial \mathbf{r}} \right)^\top = -\mathbf{G}\boldsymbol{\lambda}_v \quad (4.68)$$

where $\mathbf{G} \equiv \partial \mathbf{g} / \partial \mathbf{r}$ is the symmetric gravity gradient matrix. Continuing,

$$\dot{\boldsymbol{\lambda}}_v = - \left(\frac{\partial \hat{H}}{\partial \mathbf{v}} \right)^\top = -\boldsymbol{\lambda}_r \quad (4.69)$$

Last,

$$\dot{\lambda}_m = - \left(\frac{\partial \hat{H}}{\partial m} \right) = \frac{T}{m^2} \boldsymbol{\lambda}_v^\top \hat{\mathbf{u}} \quad (4.70)$$

Expanding the control equation gives

$$\mathbf{0} = \left(\frac{\partial \hat{H}}{\partial \hat{\mathbf{u}}} \right)^\top = \frac{T}{m} \boldsymbol{\lambda}_v + 2\mu_1 \hat{\mathbf{u}} \quad (4.71)$$

$$0 = \frac{\partial \hat{H}}{\partial T} = \frac{\boldsymbol{\lambda}_v^\top \hat{\mathbf{u}}}{m} - \frac{\lambda_m}{c} + \mu_2 (T_{MAX} - 2T) \quad (4.72)$$

$$0 = \frac{\partial \hat{H}}{\partial \alpha} = -2\mu_2 \alpha \quad (4.73)$$

Solving Eq. (4.71) for $\hat{\mathbf{u}}$ gives

$$\hat{\mathbf{u}} = \frac{-T}{2\mu_1 m} \boldsymbol{\lambda}_v \quad (4.74)$$

Depending on the sign of μ_1 , $\hat{\mathbf{u}}$ points either in the direction of $\boldsymbol{\lambda}_v$ or in the direction of $-\boldsymbol{\lambda}_v$. Pontryagin's minimum principle [98] states that the optimal values of the controls T and $\hat{\mathbf{u}}$ minimize the Hamiltonian at all points along the optimal path.

To minimize H , $\hat{\mathbf{u}}$ should be chosen as

$$\hat{\mathbf{u}} = -\frac{\boldsymbol{\lambda}_v}{\lambda_v} \quad (4.75)$$

The Hamiltonian becomes

$$H = \boldsymbol{\lambda}_r^\top \mathbf{v} + \boldsymbol{\lambda}_v^\top \mathbf{g} - T \left(\frac{\lambda_v}{m} + \frac{\lambda_m}{c} \right) \quad (4.76)$$

$$= \boldsymbol{\lambda}_r^\top \mathbf{v} + \boldsymbol{\lambda}_v^\top \mathbf{g} - ST \quad (4.77)$$

where the switching function is defined as

$$S \equiv \frac{\lambda_v}{m} + \frac{\lambda_m}{c} \quad (4.78)$$

Since the thrust magnitude is limited to the range $0 \leq T \leq T_{MAX}$, the value of T that minimizes H depends on the value of the switching function. If $S < 0$, T

should be minimized; if $S = 0$, T is free; and if $S > 0$, T should be maximized.

Thus, the optimal value of T is

$$T = \begin{cases} 0 & \text{if } S < 0 \\ T_{MAX} & \text{if } S > 0 \\ 0 \leq T \leq T_{MAX} & \text{if } S = 0 \end{cases} \quad (4.79)$$

Now that the optimal values of $\hat{\mathbf{u}}$ and T are known, the evolution of the mass costate becomes

$$\dot{\lambda}_m = -\frac{T\lambda_v}{m^2} \quad (4.80)$$

4.3.1.1 Switching Function Evolution

Differentiating the switching function (Eq. (4.78)) with respect to time,

$$\dot{S} = \frac{\dot{\lambda}_v}{m} - \frac{\lambda_v}{m^2}\dot{m} + \frac{\dot{\lambda}_m}{c} = \frac{\dot{\lambda}_v}{m} \quad (4.81)$$

On a null-thrust arc, $T = 0$, so $\dot{m} = 0$. Integrating \dot{S} on a null-thrust arc gives

$$S = \frac{\lambda_v}{m} + C \quad (4.82)$$

where C is a constant. Maximum thrusting occurs where $S > 0$; null-thrusting occurs where $S < 0$. Thus, the propulsion system is activated when $S = 0$ and $\dot{S} > 0$; the propulsion system is deactivated when $S = 0$ and $\dot{S} < 0$.

To understand the behavior of the switching function at the endpoints of a transfer, consider the problem of minimizing the amount of propellant used for orbit transfer where the departure time along the initial orbit is constrained. Figure 4.3 shows the orbit transfer where the departure time τ_0 , which specifies the elapsed

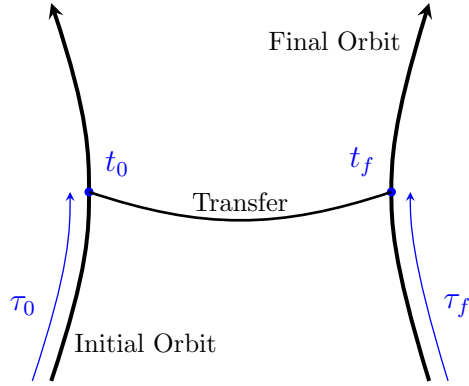


Figure 4.3: Orbit transfer problem.

time from a reference epoch on the first orbit, is required to be greater than some minimum time. The objective function is

$$J = m_0 - m_f \quad (4.83)$$

The position, velocity, and mass are required to be continuous for a valid orbit transfer. Additionally, the constraint on the departure time is $\tau_0 \geq \tau_{MIN}$, and if this constraint is assumed to be active, $\tau_0 - \tau_{MIN} = 0$. Therefore, the constraints at the initial time are

$$\boldsymbol{\theta} = \begin{bmatrix} \mathbf{r}_0 - \mathbf{r}(\tau_0) \\ \mathbf{v}_0 - \mathbf{v}(\tau_0) \\ m_0 - m(\tau_0) \\ \tau_0 - \tau_{MIN} \end{bmatrix} = \mathbf{0} \quad (4.84)$$

where t_0 is the initial time; \mathbf{r}_0 , \mathbf{v}_0 , and m_0 are the initial position, velocity, and mass on the transfer segment; and $\mathbf{r}(\tau_0)$, $\mathbf{v}(\tau_0)$, and $m(\tau_0)$ are the position, velocity, and mass at the departure point along the initial orbit. The kinematic constraints at the final time require

$$\boldsymbol{\psi} = \begin{bmatrix} \mathbf{r}_f - \mathbf{r}(\tau_f) \\ \mathbf{v}_f - \mathbf{v}(\tau_f) \end{bmatrix} = \mathbf{0} \quad (4.85)$$

where \mathbf{r}_f and \mathbf{v}_f are the position and velocity at the transfer orbit's endpoint, and $\mathbf{r}(\tau_f)$ and $\mathbf{v}(\tau_f)$ are the position and velocity at the endpoint along the final orbit; the quantity τ_f is the elapsed time on the final orbit relative to a reference epoch. The endpoint function is

$$G = m_0 - m_f + \boldsymbol{\xi}_r^\top [\mathbf{r}_0 - \mathbf{r}(\tau_0)] + \boldsymbol{\xi}_v^\top [\mathbf{v}_0 - \mathbf{v}(\tau_0)] + \xi_m [m_0 - m(\tau_0)] - \xi_t [\tau_0 - \tau_{MIN}] + \boldsymbol{\nu}_r^\top [\mathbf{r}_f - \mathbf{r}(\tau_f)] + \boldsymbol{\nu}_v^\top [\mathbf{v}_f - \mathbf{v}(\tau_f)] \quad (4.86)$$

where the constraints have been adjoined to the cost function with Lagrange multipliers. The Hamiltonian is

$$H = \boldsymbol{\lambda}_r^\top \mathbf{v} + \boldsymbol{\lambda}_v^\top \mathbf{g} - ST \quad (4.87)$$

The transversality conditions require

$$\boldsymbol{\lambda}_0 = - \left(\frac{\partial G}{\partial \mathbf{x}_0} \right)^\top = \begin{bmatrix} -\boldsymbol{\xi}_r \\ -\boldsymbol{\xi}_v \\ -\xi_m \end{bmatrix} \quad (4.88)$$

and the condition on the parameter τ_0 is

$$0 = \frac{\partial G}{\partial \tau_0} + \int_{t_0}^{t_f} \frac{\partial H}{\partial \tau_0} dt \quad (4.89)$$

$$0 = -\boldsymbol{\xi}_r^\top \mathbf{v}(\tau_0) - \boldsymbol{\xi}_v^\top \mathbf{g}(\tau_0) - \xi_t \quad (4.90)$$

as shown in Appendix C. Applying the transversality conditions to Eq. (4.90) gives

$$\boldsymbol{\lambda}_{r_0}^\top \mathbf{v}(\tau_0) + \boldsymbol{\lambda}_{v_0}^\top \mathbf{g}(\tau_0) - \xi_t = 0 \quad (4.91)$$

Once the kinematic constraints are satisfied,

$$\boldsymbol{\lambda}_{r_0}^\top \mathbf{v}_0 + \boldsymbol{\lambda}_{v_0}^\top \mathbf{g}_0 - \xi_t = 0 \quad (4.92)$$

The condition on the initial value of the Hamiltonian is

$$H_0 = \frac{\partial G}{\partial t_0} \quad (4.93)$$

$$\boldsymbol{\lambda}_{r_0}^\top \mathbf{v}_0 + \boldsymbol{\lambda}_{v_0}^\top \mathbf{g}_0 - S_0 T_0 = 0 \quad (4.94)$$

Combining Eq. (4.92) and Eq. (4.94) and solving for S_0 gives

$$0 = \xi_t - S_0 T_0 \quad (4.95)$$

$$S_0 = \frac{\xi_t}{T_0} \quad (4.96)$$

Thus, S_0 is nonzero unless $\xi_t = 0$. To initiate the orbit transfer, $T > 0$, and if the transfer is optimal, $S > 0$ while the engine is thrusting. It is expected, therefore, that S_0 will be nonzero and positive when the constraint on the departure time is active.

At the final time, the transversality conditions require

$$\boldsymbol{\lambda}_{r_f}^\top \mathbf{v}_f + \boldsymbol{\lambda}_{v_f}^\top \mathbf{g}_f = 0 \quad (4.97)$$

and the final value of the Hamiltonian is

$$H_f = -\frac{\partial G}{\partial t_f} \quad (4.98)$$

$$\boldsymbol{\lambda}_{r_f}^\top \mathbf{v}_f + \boldsymbol{\lambda}_{v_f}^\top \mathbf{g}_f - S_f T_f = 0 \quad (4.99)$$

Combining Eq. (4.97) and Eq. (4.99) gives

$$S_f T_f = 0 \quad (4.100)$$

At the end of the transfer, the thrust should switch from T_{MAX} to null thrust, so

$$S_f = 0 \quad \dot{S}_f < 0 \quad (4.101)$$

4.3.2 Adjoint Control Transformation

It was shown that the velocity costate points in the anti-thrust direction along finite thrust arcs, and the negative position costate is the time derivative of the velocity costate. The orientation of $\boldsymbol{\lambda}_r$ and the orientation of $\boldsymbol{\lambda}_v$ over null-thrust arcs, however, do not have a simple physical interpretation. In order to estimate these quantities, it is desired to derive a relationship between the costates and physically meaningful quantities. The method chosen here uses the right ascension and declination and corresponding rates of a linearly steered finite burn to estimate the position and velocity costates.³

The thrust direction $\hat{\mathbf{u}}$ must satisfy

$$\hat{\mathbf{u}}^\top \hat{\mathbf{u}} = 1 \quad (4.102)$$

by the definition of a unit vector. Differentiating,

$$\dot{\hat{\mathbf{u}}}^\top \hat{\mathbf{u}} + \hat{\mathbf{u}}^\top \dot{\hat{\mathbf{u}}} = 0 \quad (4.103)$$

$$\dot{\hat{\mathbf{u}}}^\top \hat{\mathbf{u}} = 0 \quad (4.104)$$

which simply indicates the velocity of a unit vector must be perpendicular to the unit vector. Differentiating again,

$$\ddot{\hat{\mathbf{u}}}^\top \hat{\mathbf{u}} + \dot{\hat{\mathbf{u}}}^\top \dot{\hat{\mathbf{u}}} = 0 \quad (4.105)$$

$$\ddot{\hat{\mathbf{u}}}^\top \hat{\mathbf{u}} = -\dot{\hat{\mathbf{u}}}^\top \dot{\hat{\mathbf{u}}} \quad (4.106)$$

³Ocampo, C. A., "Exact Impulsive to Time Optimal Finite Burn Trajectory Automation," Unpublished, Department of Aerospace Engineering and Engineering Mechanics, University of Texas at Austin, Jun. 2011.

Suppose a linearly steered finite thrust maneuver is specified in a non-rotating frame with basis vectors $\hat{\mathbf{x}}$, $\hat{\mathbf{y}}$, and $\hat{\mathbf{z}}$. In terms of the finite burn's initial right ascension α , measured relative to the $\hat{\mathbf{x}}$ axis, and the initial declination β , measured relative to the $\hat{\mathbf{x}}\hat{\mathbf{y}}$ plane, the thrust pointing vector is

$$\hat{\mathbf{u}} = \cos \alpha \cos \beta \hat{\mathbf{x}} + \sin \alpha \cos \beta \hat{\mathbf{y}} + \sin \beta \hat{\mathbf{z}} \quad (4.107)$$

Differentiating,

$$\dot{\hat{\mathbf{u}}} = (-\dot{\alpha} \sin \alpha \cos \beta - \dot{\beta} \cos \alpha \sin \beta) \hat{\mathbf{x}} + (\dot{\alpha} \cos \alpha \cos \beta - \dot{\beta} \sin \alpha \sin \beta) \hat{\mathbf{y}} + \dot{\beta} \cos \beta \hat{\mathbf{z}} \quad (4.108)$$

Differentiating again,

$$\begin{aligned} \ddot{\hat{\mathbf{u}}} = & \left(-\dot{\alpha}^2 \cos \alpha \cos \beta + 2\dot{\alpha}\dot{\beta} \sin \alpha \sin \beta - \dot{\beta}^2 \cos \alpha \cos \beta \right) \hat{\mathbf{x}} \\ & + \left(-\dot{\alpha}^2 \sin \alpha \cos \beta - 2\dot{\alpha}\dot{\beta} \cos \alpha \sin \beta - \dot{\beta}^2 \sin \alpha \cos \beta \right) \hat{\mathbf{y}} \\ & + \left(-\dot{\beta}^2 \sin \beta \right) \hat{\mathbf{z}} \end{aligned} \quad (4.109)$$

where $\ddot{\alpha}$ and $\ddot{\beta}$ are set to zero.

At this point, given the initial right ascension and declination and rates, the initial thrust direction, velocity, and acceleration are known. Application of the Pontryagin minimum principle showed that the velocity costate is

$$\boldsymbol{\lambda}_v = -\lambda_v \hat{\mathbf{u}} \quad (4.110)$$

where the value of λ_v may be set to scale the magnitudes of the costates. Differentiating Eq. (4.110) gives

$$\dot{\boldsymbol{\lambda}}_v = -\dot{\lambda}_v \hat{\mathbf{u}} - \lambda_v \dot{\hat{\mathbf{u}}} \quad (4.111)$$

$$\boldsymbol{\lambda}_r = \dot{\lambda}_v \hat{\mathbf{u}} + \lambda_v \dot{\hat{\mathbf{u}}} \quad (4.112)$$

where $\hat{\mathbf{u}}$ and $\dot{\hat{\mathbf{u}}}$ are known and λ_v is set, but $\dot{\lambda}_v$ is unknown. Differentiating again,

$$\dot{\boldsymbol{\lambda}}_r = \ddot{\lambda}_v \hat{\mathbf{u}} + \dot{\lambda}_v \dot{\hat{\mathbf{u}}} + \lambda_v \ddot{\hat{\mathbf{u}}} + \lambda_v \ddot{\hat{\mathbf{u}}} \quad (4.113)$$

$$-\mathbf{G}\boldsymbol{\lambda}_v = \ddot{\lambda}_v \hat{\mathbf{u}} + 2\dot{\lambda}_v \dot{\hat{\mathbf{u}}} + \lambda_v \ddot{\hat{\mathbf{u}}} \quad (4.114)$$

where $\ddot{\hat{\mathbf{u}}}$ is known. Substituting for $\boldsymbol{\lambda}_v$,

$$\lambda_v \mathbf{G}\hat{\mathbf{u}} = \ddot{\lambda}_v \hat{\mathbf{u}} + 2\dot{\lambda}_v \dot{\hat{\mathbf{u}}} + \lambda_v \ddot{\hat{\mathbf{u}}} \quad (4.115)$$

Dotting each side with $\dot{\hat{\mathbf{u}}}$ gives

$$\lambda_v (\mathbf{G}\hat{\mathbf{u}})^\top \dot{\hat{\mathbf{u}}} = \ddot{\lambda}_v \hat{\mathbf{u}}^\top \dot{\hat{\mathbf{u}}} + 2\dot{\lambda}_v \dot{\hat{\mathbf{u}}}^\top \dot{\hat{\mathbf{u}}} + \lambda_v \ddot{\hat{\mathbf{u}}}^\top \dot{\hat{\mathbf{u}}} \quad (4.116)$$

By Eq. (4.104) it is known that $\dot{\hat{\mathbf{u}}}^\top \hat{\mathbf{u}} = 0$, so

$$\lambda_v (\mathbf{G}\hat{\mathbf{u}})^\top \dot{\hat{\mathbf{u}}} = 2\dot{\lambda}_v \dot{\hat{\mathbf{u}}}^\top \dot{\hat{\mathbf{u}}} + \lambda_v \ddot{\hat{\mathbf{u}}}^\top \dot{\hat{\mathbf{u}}} \quad (4.117)$$

Solving for $\dot{\lambda}_v$,

$$2\dot{\lambda}_v \dot{\hat{\mathbf{u}}}^\top \dot{\hat{\mathbf{u}}} = \lambda_v (\mathbf{G}\hat{\mathbf{u}})^\top \dot{\hat{\mathbf{u}}} - \lambda_v \ddot{\hat{\mathbf{u}}}^\top \dot{\hat{\mathbf{u}}} \quad (4.118)$$

$$\dot{\lambda}_v = \frac{\lambda_v}{2\dot{\hat{\mathbf{u}}}^\top \dot{\hat{\mathbf{u}}}} \left[\lambda_v (\mathbf{G}\hat{\mathbf{u}})^\top \dot{\hat{\mathbf{u}}} - \lambda_v \ddot{\hat{\mathbf{u}}}^\top \dot{\hat{\mathbf{u}}} \right] \quad (4.119)$$

Now $\boldsymbol{\lambda}_r$ and $\boldsymbol{\lambda}_v$ are known.

Finally, it is known that the switching function must be zero when a burn is initiated or terminated at an internal switching point. If the activation or deactivation time is t_i then

$$S_i = \frac{\lambda_{v_i}}{m_i} + \frac{\lambda_{m_i}}{c} = 0 \quad (4.120)$$

where the subscript i indicates the quantity is evaluated at t_i . Solving for the mass costate gives

$$\lambda_{m_i} = -\frac{c}{m_i} \lambda_{v_i} \quad (4.121)$$

Now λ_m is known in addition to $\boldsymbol{\lambda}_r$ and $\boldsymbol{\lambda}_v$, so the adjoint control transformation is complete.

4.3.3 Optimal Control Variational Equations

The optimal control variational equations are used to propagate the STM, which is used for gradient computation. First, define the augmented state as

$$\mathbf{z} \equiv \begin{bmatrix} \mathbf{r} \\ \mathbf{v} \\ m \\ \boldsymbol{\lambda}_r \\ \boldsymbol{\lambda}_v \\ \lambda_m \end{bmatrix}_{14 \times 1} \quad (4.122)$$

The time derivative of the augmented state is

$$\dot{\mathbf{z}} = \begin{bmatrix} \mathbf{v} \\ \mathbf{g} - \frac{T}{m} \hat{\boldsymbol{\lambda}}_v \\ -\frac{c}{m} \\ -\mathbf{G} \boldsymbol{\lambda}_v \\ -\boldsymbol{\lambda}_r \\ -\frac{T}{m^2} \lambda_v \end{bmatrix} \quad (4.123)$$

The state propagation matrix is

$$\frac{\partial \dot{\mathbf{z}}}{\partial \mathbf{z}} = \begin{bmatrix} \mathbf{0} & \mathbf{I} & \mathbf{0} & \mathbf{0} & \mathbf{0} & \mathbf{0} \\ \mathbf{G} & \mathbf{0} & \frac{T}{m^2} \hat{\boldsymbol{\lambda}}_v & \mathbf{0} & \frac{\partial}{\partial \boldsymbol{\lambda}_v} \left(-\frac{T}{m} \hat{\boldsymbol{\lambda}}_v \right) & \mathbf{0} \\ \mathbf{0}^\top & \mathbf{0}^\top & \mathbf{0} & \mathbf{0}^\top & \mathbf{0}^\top & \mathbf{0} \\ -\frac{\partial}{\partial \mathbf{r}} (\mathbf{G} \boldsymbol{\lambda}_v) & \mathbf{0} & \mathbf{0} & \mathbf{0} & -\mathbf{G} & \mathbf{0} \\ \mathbf{0} & \mathbf{0} & \mathbf{0} & -\mathbf{I} & \mathbf{0} & \mathbf{0} \\ \mathbf{0}^\top & \mathbf{0}^\top & \frac{2T \boldsymbol{\lambda}_v}{m^3} & \mathbf{0}^\top & -\frac{T}{m^2} \hat{\boldsymbol{\lambda}}_v^\top & \mathbf{0} \end{bmatrix}_{14 \times 14} \quad (4.124)$$

The partial of the thrust acceleration with respect to the velocity costate is

$$\frac{\partial}{\partial \boldsymbol{\lambda}_v} \left(-\frac{T}{m} \hat{\boldsymbol{\lambda}}_v \right) = -\frac{T}{m} \frac{\partial}{\partial \boldsymbol{\lambda}_v} \left[\boldsymbol{\lambda}_v (\boldsymbol{\lambda}_v^\top \boldsymbol{\lambda}_v)^{-\frac{1}{2}} \right] \quad (4.125)$$

$$= -\frac{T}{m} \left[\frac{\mathbf{I}}{\lambda_v} - \frac{1}{2} \boldsymbol{\lambda}_v (\boldsymbol{\lambda}_v^\top \boldsymbol{\lambda}_v)^{-\frac{3}{2}} 2 \boldsymbol{\lambda}_v^\top \right] \quad (4.126)$$

$$= \frac{T}{m} \left[\frac{\boldsymbol{\lambda}_v \boldsymbol{\lambda}_v^\top}{\lambda_v^3} - \frac{\mathbf{I}}{\lambda_v} \right] \quad (4.127)$$

The partial of the position costate rate with respect to the spacecraft position is

$$\frac{\partial}{\partial \mathbf{r}} (-\mathbf{G} \boldsymbol{\lambda}_v) = - \left[\frac{\partial \mathbf{G}}{\partial x} \boldsymbol{\lambda}_v \quad \frac{\partial \mathbf{G}}{\partial y} \boldsymbol{\lambda}_v \quad \frac{\partial \mathbf{G}}{\partial z} \boldsymbol{\lambda}_v \right]_{3 \times 3} \quad (4.128)$$

The gravity gradient matrix in moon-centered coordinates is

$$\mathbf{G} = \frac{3\mu_M}{r^5} \mathbf{r} \mathbf{r}^\top - \frac{\mu_M}{r^3} \mathbf{I} + \frac{3\mu_E}{r_{EP}^5} \mathbf{r}_{EP} \mathbf{r}_{EP}^\top - \frac{\mu_E}{r_{EP}^3} \mathbf{I} + \frac{3\mu_S}{r_{SP}^5} \mathbf{r}_{SP} \mathbf{r}_{SP}^\top - \frac{\mu_S}{r_{SP}^3} \mathbf{I} \quad (4.129)$$

The gradient of the first term in \mathbf{G} with respect to x is

$$\frac{\partial}{\partial x} \left(\frac{3\mu_M}{r^5} \mathbf{r} \mathbf{r}^\top \right) = 3\mu_M \mathbf{r} \mathbf{r}^\top \frac{\partial}{\partial x} (r^{-5}) + \frac{3\mu_M}{r^5} \frac{\partial}{\partial x} (\mathbf{r} \mathbf{r}^\top) \quad (4.130)$$

$$= 3\mu_M \mathbf{r} \mathbf{r}^\top \frac{\partial}{\partial x} \left[(x^2 + y^2 + z^2)^{-\frac{5}{2}} \right] + \frac{3\mu_M}{r^5} \frac{\partial}{\partial x} \begin{bmatrix} x^2 & xy & xz \\ xy & y^2 & yz \\ xz & yz & z^2 \end{bmatrix} \quad (4.131)$$

$$= 3\mu_M \mathbf{r} \mathbf{r}^\top \left[-\frac{5}{2} (x^2 + y^2 + z^2)^{-\frac{7}{2}} 2x \right] + \frac{3\mu_M}{r^5} \begin{bmatrix} 2x & y & z \\ y & 0 & 0 \\ z & 0 & 0 \end{bmatrix} \quad (4.132)$$

$$= \frac{-15\mu_M x}{r^7} \mathbf{r} \mathbf{r}^\top + \frac{3\mu_M}{r^5} \begin{bmatrix} 2x & y & z \\ y & 0 & 0 \\ z & 0 & 0 \end{bmatrix} \quad (4.133)$$

The gradient of the second term in \mathbf{G} with respect to x is

$$\frac{\partial}{\partial x} \left(-\frac{\mu_M}{r^3} \mathbf{I} \right) = \frac{\partial}{\partial x} \left[-\mu_M (x^2 + y^2 + z^2)^{-\frac{3}{2}} \right] \mathbf{I} \quad (4.134)$$

$$= \frac{3}{2} (x^2 + y^2 + z^2)^{-\frac{5}{2}} 2x \mathbf{I} \quad (4.135)$$

$$= \frac{3\mu_M x}{r^5} \mathbf{I} \quad (4.136)$$

The gradient of the third term in \mathbf{G} with respect to x is

$$\frac{\partial}{\partial x} \left(\frac{3\mu_E}{r_{EP}^5} \mathbf{r}_{EP} \mathbf{r}_{EP}^\top \right) = \frac{-15\mu_E x_{EP}}{r_{EP}^7} \mathbf{r}_{EP} \mathbf{r}_{EP}^\top + \frac{3\mu_E}{r_{EP}^5} \begin{bmatrix} 2x_{EP} & y_{EP} & z_{EP} \\ y_{EP} & 0 & 0 \\ z_{EP} & 0 & 0 \end{bmatrix} \quad (4.137)$$

And the gradient of the fourth term in \mathbf{G} with respect to x is

$$\frac{\partial}{\partial x} \left(-\frac{\mu_E}{r_{EP}^3} \mathbf{I} \right) = \frac{3\mu_E x_{EP}}{r_{EP}^5} \mathbf{I} \quad (4.138)$$

The gradients of the last two terms in \mathbf{G} are similar. Thus, the derivative of \mathbf{G} with respect to x is

$$\begin{aligned} \frac{\partial \mathbf{G}}{\partial x} &= \frac{3\mu_M x}{r^5} \mathbf{I} - \frac{15\mu_M x}{r^7} \mathbf{r} \mathbf{r}^\top + \frac{3\mu_M}{r^5} \begin{bmatrix} 2x & y & z \\ y & 0 & 0 \\ z & 0 & 0 \end{bmatrix} \\ &+ \frac{3\mu_E x_{EP}}{r_{EP}^5} \mathbf{I} - \frac{15\mu_E x_{EP}}{r_{EP}^7} \mathbf{r}_{EP} \mathbf{r}_{EP}^\top + \frac{3\mu_E}{r_{EP}^5} \begin{bmatrix} 2x_{EP} & y_{EP} & z_{EP} \\ y_{EP} & 0 & 0 \\ z_{EP} & 0 & 0 \end{bmatrix} \\ &+ \frac{3\mu_S x_{SP}}{r_{SP}^5} \mathbf{I} - \frac{15\mu_S x_{SP}}{r_{SP}^7} \mathbf{r}_{SP} \mathbf{r}_{SP}^\top + \frac{3\mu_S}{r_{SP}^5} \begin{bmatrix} 2x_{SP} & y_{SP} & z_{SP} \\ y_{SP} & 0 & 0 \\ z_{SP} & 0 & 0 \end{bmatrix} \end{aligned} \quad (4.139)$$

The gradients of \mathbf{G} with respect to y and z are similarly derived. Now that the partial derivative of $-\mathbf{G}\boldsymbol{\lambda}_v$ with respect to \mathbf{r} is known, the state propagation matrix can be constructed, and the STM can be numerically integrated, which is necessary for the analytical gradient formulation.

Chapter 5

Lunar Orbit Insertion from a Free Return in the Three-Body Model

In this chapter, the transfer of a spacecraft from a free return trajectory to a closed lunar orbit is optimized in the circular restricted three-body problem (CRTBP). An impulsive engine model is used, and the sum of the lunar orbit insertion (LOI) maneuver magnitudes is minimized. First, an initial estimate of the three-burn LOI sequence is developed in the two-body model. Optimal solutions are then determined with a fixed, minimum time free return to establish baseline propulsion requirements. The free return is then allowed to vary but must remain symmetric. In the most general case, the free return may be asymmetric. Analytical gradients are derived for each case to facilitate convergence.

The engine model in this chapter is said to be impulsive since it is capable of producing an instantaneous change in the spacecraft's velocity. In reality, a finite amount of time is required to alter the spacecraft's velocity. Impulsive changes in the velocity, however, can provide an adequate estimate of finite thrust maneuvers if the available thrust level is high enough that firing times do not constitute a significant portion of the trajectory. The maximum thrust level of the Apollo service propulsion system was approximately 90 kN [69], and the maximum thrust of the Orion crew

vehicle currently under development is approximately 35 kN.¹ It will subsequently be shown for an example case of the free return and LOI optimization problem that the longest continuous activation of a 35 kN finite thrust engine is about 0.05% of the total flight time, indicating the impulsive maneuver approximation is appropriate.

5.1 Initial Estimate

The initial estimate of the LOI sequence is constructed by connecting the incoming free return to the low lunar orbit (LLO) through an impulsive three-burn sequence. The spacecraft state along the free return at its entry to the lunar sphere of influence is determined numerically by propagating the base free return from translunar injection (TLI) towards the moon and utilizing a root-finding routine to determine the time at which the trajectory enters the lunar sphere of influence. The radius of the sphere of influence used here is $R = r_{EM}(\mu_M/\mu_E)^{2/5} \approx 66170$ km, which is approximately 17% of the earth-moon distance [99]. The state is then transferred to a moon-centered frame, and, if no maneuvers were performed, a spacecraft following this trajectory would perform a hyperbolic flyby of the moon. The goal here, however, is to transfer the spacecraft to a closed lunar parking orbit. A feasible LOI sequence is constructed analytically with the Keplerian model by ignoring Earth's gravity and lunar motion over the time of LOI. Neither of these conditions reflect reality, but the two-body targeting algorithm needs only to generate an LOI sequence that is near a feasible trajectory in the three-body model.

¹Information available at http://www.nasa.gov/pdf/510449main_SLS_MPCV_90-day_Report.pdf [accessed 15 March 2012]

Once the Earth's gravity is activated, the sequence will be integrated backwards in time from the LLO, resulting in a position and velocity mismatch at the lunar sphere of influence. By iterating on the LOI maneuvers and transfer times, state continuity can be satisfied and the resultant feasible trajectory will be the initial estimate for subsequent optimization.

Between the Earth and moon, the spacecraft performs a maneuver, LOI-0, to depart the free return path and target a more favorable approach for parking orbit insertion. At the moon, three maneuvers are performed. The first, LOI-1, produces an orbit with negative Keplerian energy relative to the moon; the second, LOI-2, performs the majority of the required plane change; and the third, LOI-3, circularizes the trajectory. An overview is shown in Fig. 5.1. The incoming hyperbola will be labeled orbit 0 or \mathcal{O}^0 , the first transfer ellipse is orbit 1 or \mathcal{O}^1 , the second transfer ellipse is orbit 2 or \mathcal{O}^2 , and the LLO is orbit 3 or \mathcal{O}^3 .

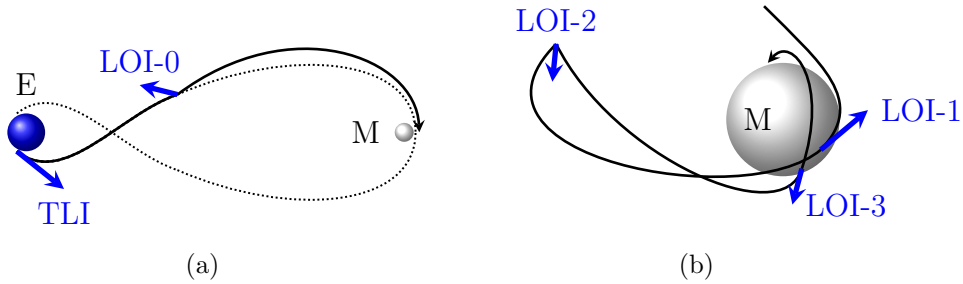


Figure 5.1: Earth to moon transfer: a) Free return and cislunar maneuver, and b) lunar orbit insertion.

Orbit 0 is a hyperbolic flyby of the moon. Its initial state is the free return state relative to the moon at the point where the spacecraft enters the lunar sphere of influence. This gives the incoming hyperbolic velocity \mathbf{v}_{∞}^- and the initial position

\mathbf{r}_∞^- relative to the moon. The angular momentum direction of the hyperbolic flyby trajectory is

$$\hat{\mathbf{h}}_\infty = \frac{\mathbf{r}_\infty^- \times \mathbf{v}_\infty^-}{|\mathbf{r}_\infty^- \times \mathbf{v}_\infty^-|} \quad (5.1)$$

Next, it is necessary to determine the post-flyby hyperbolic velocity. The incoming velocity \mathbf{v}_∞^- is rotated through the turning angle δ about $\hat{\mathbf{h}}_\infty$. Define a set of axes as

$$\hat{\mathbf{n}}_1 \equiv \hat{\mathbf{h}}_\infty \times \hat{\mathbf{v}}_\infty^- \quad \hat{\mathbf{n}}_2 \equiv \hat{\mathbf{v}}_\infty^- \quad \hat{\mathbf{n}}_3 \equiv \hat{\mathbf{n}}_1 \times \hat{\mathbf{n}}_2 \quad (5.2)$$

Define a second set of axes as

$$\hat{\mathbf{n}}'_1 \equiv \hat{\mathbf{h}}_\infty \times \hat{\mathbf{v}}_\infty^+ \quad \hat{\mathbf{n}}'_2 \equiv \hat{\mathbf{v}}_\infty^+ \quad \hat{\mathbf{n}}'_3 \equiv \hat{\mathbf{n}}'_1 \times \hat{\mathbf{n}}'_2 \quad (5.3)$$

The second set of axes is achieved by rotating the first set about $\hat{\mathbf{n}}_3$ through an angle of $-\delta$ as

$$\begin{bmatrix} \hat{\mathbf{n}}_1'^\top \\ \hat{\mathbf{n}}_2'^\top \\ \hat{\mathbf{n}}_3'^\top \end{bmatrix}_{3 \times 3} = \mathbf{R}_3(-\delta) \begin{bmatrix} \hat{\mathbf{n}}_1^\top \\ \hat{\mathbf{n}}_2^\top \\ \hat{\mathbf{n}}_3^\top \end{bmatrix}_{3 \times 3} \quad (5.4)$$

where \mathbf{R}_i is the rotation matrix about the i th axis. Expanding,

$$\begin{bmatrix} \hat{\mathbf{n}}_1'^\top \\ \hat{\mathbf{n}}_2'^\top \\ \hat{\mathbf{n}}_3'^\top \end{bmatrix} = \begin{bmatrix} \cos \delta & -\sin \delta & 0 \\ \sin \delta & \cos \delta & 0 \\ 0 & 0 & 1 \end{bmatrix} \begin{bmatrix} \hat{\mathbf{n}}_1^\top \\ \hat{\mathbf{n}}_2^\top \\ \hat{\mathbf{n}}_3^\top \end{bmatrix} \quad (5.5)$$

$$= \begin{bmatrix} \cos \delta \hat{\mathbf{n}}_1^\top - \sin \delta \hat{\mathbf{n}}_2^\top \\ \sin \delta \hat{\mathbf{n}}_1^\top + \cos \delta \hat{\mathbf{n}}_2^\top \\ \hat{\mathbf{n}}_3^\top \end{bmatrix} \quad (5.6)$$

Now, the post-flyby hyperbolic velocity direction can be computed as

$$\hat{\mathbf{n}}'_2 = \sin \delta \hat{\mathbf{n}}_1 + \cos \delta \hat{\mathbf{n}}_2 \quad (5.7)$$

$$\hat{\mathbf{v}}_\infty^+ = \sin \delta (\hat{\mathbf{h}}_\infty \times \hat{\mathbf{v}}_\infty^-) + \cos \delta (\hat{\mathbf{v}}_\infty^-) \quad (5.8)$$

where the turning angle is

$$\delta = 2 \sin^{-1} \frac{1}{e_0} \quad (5.9)$$

and e_0 is the eccentricity of the hyperbolic flyby. The eccentricity is the magnitude of the eccentricity vector, which is given by

$$\mathbf{e}_0 = \frac{\mathbf{v}_\infty^- \times \mathbf{h}_\infty}{\mu_M} - \frac{\mathbf{r}_\infty^-}{r_\infty^-} \quad (5.10)$$

With the pre- and post-flyby hyperbolic velocity vectors known, the periapsis direction of \mathcal{O}^0 is

$$\hat{\mathbf{p}}_0 = \frac{\mathbf{v}_\infty^- - \mathbf{v}_\infty^+}{|\mathbf{v}_\infty^- - \mathbf{v}_\infty^+|} \quad (5.11)$$

The LOI-1 capture maneuver is performed at the intersection of \mathcal{O}^0 and the plane of \mathcal{O}^3 , provided that $-90 \text{ deg} \leq \nu_1 \leq 90 \text{ deg}$ where ν_1 is the true anomaly along \mathcal{O}^0 where LOI-1 is performed. LOI-1 is constructed such that \mathcal{O}^0 and \mathcal{O}^1 are coplanar and the post-maneuver point is the periapsis point of a transfer ellipse with a specified apoapsis radius. The periapsis direction of \mathcal{O}^1 is

$$\hat{\mathbf{p}}_1 = \psi \frac{\hat{\mathbf{h}}_3 \times \hat{\mathbf{h}}_\infty}{|\hat{\mathbf{h}}_3 \times \hat{\mathbf{h}}_\infty|} \quad (5.12)$$

where $\hat{\mathbf{h}}_3$ is the angular momentum direction of the LLO and

$$\psi \equiv \text{sign} \left[\left(\hat{\mathbf{h}}_3 \times \hat{\mathbf{h}}_\infty \right)^\top \hat{\mathbf{p}}_0 \right] \quad (5.13)$$

The coefficient ψ keeps the magnitude of the true anomaly of the LOI-1 point along \mathcal{O}^0 less than 90 deg. When this true anomaly is zero, there is no flight path angle change across LOI-1 since this is always the periapsis of \mathcal{O}^1 . As the magnitude of ν_1 increases, so does the flight path angle change across LOI-1 and, consequently,

the ΔV requirement. This non-optimal flight path change over LOI-1 is the main shortcoming of this initial estimate strategy, but because of the method's simplicity and the ability of the optimizer to later reduce the magnitude of this maneuver, it is not judged as a major drawback.

The flight time from entry into the lunar sphere of influence to LOI-1 along Θ^0 is

$$t_1 - t_\infty = \sqrt{\frac{(-a_0)^3}{\mu_M}} \left[(e_0 \sinh F_1 - F_1) - (e_0 \sinh F_\infty - F_\infty) \right] \quad (5.14)$$

where F_∞ and F_1 are the hyperbolic eccentric anomalies at lunar sphere of influence entry and at LOI-1 [99]. These are given by

$$F_\infty = -\cosh^{-1} \left[\frac{e_0 + \cos \nu_\infty}{1 + e_0 \cos \nu_\infty} \right] \quad (5.15)$$

$$F_1 = \xi \cosh^{-1} \left[\frac{e_0 + \cos \nu_1}{1 + e_0 \cos \nu_1} \right] \quad (5.16)$$

and the true anomalies at lunar sphere of influence entry and LOI-1 along Θ^0 are given by

$$\nu_\infty = \cos^{-1} \left[\frac{\frac{p_0}{r_\infty} - 1}{e_0} \right] \quad (5.17)$$

$$\nu_1 = \xi \cos^{-1}(\hat{\boldsymbol{p}}_0^\top \hat{\boldsymbol{p}}_1) \quad (5.18)$$

where

$$\xi \equiv \text{sign}(\hat{\boldsymbol{p}}_1^\top \hat{\boldsymbol{v}}_{p_0}) \quad (5.19)$$

The periapsis velocity direction on Θ^0 is

$$\hat{\boldsymbol{v}}_{p_0} = \frac{\boldsymbol{v}_\infty^- + \boldsymbol{v}_\infty^+}{|\boldsymbol{v}_\infty^- + \boldsymbol{v}_\infty^+|} \quad (5.20)$$

The velocity immediately before LOI-1 is

$$\mathbf{v}_1^- = -\sqrt{\frac{\mu_M}{p_0}} \sin \nu_1 \hat{\mathbf{p}}_0 + \sqrt{\frac{\mu_M}{p_0}} (e_0 + \cos \nu_1) \hat{\mathbf{q}}_0 \quad (5.21)$$

where

$$\hat{\mathbf{q}}_0 \equiv \hat{\mathbf{h}}_\infty \times \hat{\mathbf{p}}_0 \quad (5.22)$$

The semi-major axis of \mathcal{O}^0 is found by applying the vis-viva equation, which gives

$$-\frac{\mu_M}{2a_0} = \frac{v_\infty^2}{2} - \frac{\mu_M}{r_\infty} \quad (5.23)$$

$$a_0 = -\frac{\mu_M}{2} \left(\frac{v_\infty^2}{2} - \frac{\mu_M}{r_\infty} \right)^{-1} \quad (5.24)$$

where $\mu_M/r_\infty \neq 0$ since the lunar sphere of influence has a known, finite radius.

The semi-latus rectum of \mathcal{O}^0 is

$$p_0 = a_0 (1 - e_0^2) \quad (5.25)$$

The velocity immediately after LOI-1 on \mathcal{O}^1 is

$$\mathbf{v}_1^+ = -\sqrt{\frac{\mu_M}{p_1}} \sin 0 \hat{\mathbf{p}}_1 + \sqrt{\frac{\mu_M}{p_1}} (e_1 + \cos 0) \hat{\mathbf{q}}_1 \quad (5.26)$$

$$\mathbf{v}_1^+ = \sqrt{\frac{\mu_M}{p_1}} (e_1 + 1) \hat{\mathbf{q}}_1 \quad (5.27)$$

The eccentricity of \mathcal{O}^1 is

$$e_1 = \frac{r_{a_1} - r_{p_1}}{r_{a_1} + r_{p_1}} \quad (5.28)$$

where the apoapsis radius r_{a_1} of \mathcal{O}^1 is set at 10000 km and

$$\hat{\mathbf{q}}_1 \equiv \hat{\mathbf{h}}_1 \times \hat{\mathbf{p}}_1 \quad (5.29)$$

Because it is known that \mathcal{O}^0 and \mathcal{O}^1 are coplanar,

$$\hat{\mathbf{h}}_1 = \hat{\mathbf{h}}_\infty \quad (5.30)$$

The periapsis radius of \mathcal{O}^1 is

$$r_{p1} = \frac{p_0}{1 + e_0 \cos \nu_1} \quad (5.31)$$

Now that \mathbf{v}_1^- and \mathbf{v}_1^+ are known, LOI-1 can be computed as

$$\Delta \mathbf{v}_1 = \mathbf{v}_1^+ - \mathbf{v}_1^- \quad (5.32)$$

$$\Delta \mathbf{v}_1 = \sqrt{\frac{\mu_M}{p_1}}(e_1 + 1) \hat{\mathbf{q}}_1 + \sqrt{\frac{\mu_M}{p_0}} \sin \nu_1 \hat{\mathbf{p}}_0 - \sqrt{\frac{\mu_M}{p_0}}(e_0 + \cos \nu_1) \hat{\mathbf{q}}_0 \quad (5.33)$$

Values of 20000 km and 30000 km were also considered for the apoapsis radius, but although these are closer to the optimal solution, the increased apolune altitude resulted in greater dispersion when changing from the two-body to the three-body model. This incurred position errors significant enough that feasible trajectories could not be found numerically in some cases when propagated with Earth's gravity. These errors result from the fact that both Earth gravity and lunar movement during the period of LOI are neglected in the conic model.

The spacecraft travels from periapsis to apoapsis on \mathcal{O}^1 ; therefore, the time of flight on \mathcal{O}^1 from LOI-1 to LOI-2 is

$$t_{12} = \pi \sqrt{\frac{a_1^3}{\mu_M}} \quad (5.34)$$

where

$$a_1 = \frac{1}{2}(r_{p1} + r_{a1}) \quad (5.35)$$

LOI-2 occurs at apoapsis of \mathcal{O}^1 . The velocity immediately before LOI-2 is

$$\mathbf{v}_2^- = -\sqrt{\frac{\mu_M}{p_1}} \sin \pi \hat{\mathbf{p}}_1 + \sqrt{\frac{\mu_M}{p_1}} (e_1 + \cos \pi) \hat{\mathbf{q}}_1 \quad (5.36)$$

$$\mathbf{v}_2^- = \sqrt{\frac{\mu_M}{p_1}} (e_1 - 1) \hat{\mathbf{q}}_1 \quad (5.37)$$

All the plane change is performed by LOI-2 since \mathcal{O}^1 is in the plane of the incoming hyperbola and \mathcal{O}^2 is in the plane of the LLO.

The Earth-moon plane is spanned by the $\hat{\mathbf{x}}\hat{\mathbf{y}}$ axes of the fixed, moon-centered frame. These axes span the \mathcal{O}^3 plane after a rotation of $+\Omega$ about the $\hat{\mathbf{z}}$ axis and a rotation of $-i$ about the $\hat{\mathbf{x}}'$ axis. The transformation is

$$\begin{bmatrix} \hat{\mathbf{x}}''^\top \\ \hat{\mathbf{y}}''^\top \\ \hat{\mathbf{z}}''^\top \end{bmatrix} = \mathbf{R}_1(-i)\mathbf{R}_3(\Omega) \begin{bmatrix} \hat{\mathbf{x}}^\top \\ \hat{\mathbf{y}}^\top \\ \hat{\mathbf{z}}^\top \end{bmatrix} \quad (5.38)$$

$$\begin{bmatrix} \hat{\mathbf{x}}''^\top \\ \hat{\mathbf{y}}''^\top \\ \hat{\mathbf{z}}''^\top \end{bmatrix} = \begin{bmatrix} 1 & 0 & 0 \\ 0 & \cos i & -\sin i \\ 0 & \sin i & \cos i \end{bmatrix} \begin{bmatrix} \cos \Omega & \sin \Omega & 0 \\ -\sin \Omega & \cos \Omega & 0 \\ 0 & 0 & 1 \end{bmatrix} \begin{bmatrix} \hat{\mathbf{x}}^\top \\ \hat{\mathbf{y}}^\top \\ \hat{\mathbf{z}}^\top \end{bmatrix} \quad (5.39)$$

$$\begin{bmatrix} \hat{\mathbf{x}}''^\top \\ \hat{\mathbf{y}}''^\top \\ \hat{\mathbf{z}}''^\top \end{bmatrix} = \begin{bmatrix} \cos \Omega & \sin \Omega & 0 \\ -\sin \Omega \cos i & \cos \Omega \cos i & -\sin i \\ -\sin \Omega \sin i & \cos \Omega \sin i & \cos i \end{bmatrix} \begin{bmatrix} \hat{\mathbf{x}}^\top \\ \hat{\mathbf{y}}^\top \\ \hat{\mathbf{z}}^\top \end{bmatrix} \quad (5.40)$$

The longitude of the ascending node Ω is measured in the Earth-moon plane relative to the Earth-moon line, and the inclination i is measured relative to the Earth-moon plane, as seen in Fig. 5.2. The angular momentum of \mathcal{O}^2 is in the direction of $\hat{\mathbf{z}}''$.

Thus,

$$\hat{\mathbf{h}}_2 = \hat{\mathbf{z}}'' = -\sin \Omega \sin i \hat{\mathbf{x}} + \cos \Omega \sin i \hat{\mathbf{y}} + \cos i \hat{\mathbf{z}} \quad (5.41)$$

Orbits 1 and 2 have the same periapsis direction, regardless of \mathcal{O}^0 and \mathcal{O}^3 geometry, so

$$\hat{\mathbf{p}}_2 = \hat{\mathbf{p}}_1 \quad (5.42)$$

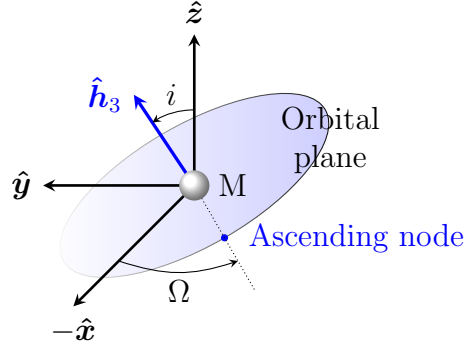


Figure 5.2: LLO orientation.

The perilune radius of \mathcal{O}^2 is the radius of the LLO, which is given by

$$r_{p_2} = R_M + h_{MIN} \quad (5.43)$$

where R_M is the mean lunar radius and $h_{MIN} = 100$ km is the minimum allowed parking orbit altitude. Determining \hat{p}_2 allows \hat{q}_2 to be calculated as

$$\hat{q}_2 = \hat{h}_2 \times \hat{p}_2 \quad (5.44)$$

The velocity immediately after LOI-2 is

$$\mathbf{v}_2^+ = -\sqrt{\frac{\mu_M}{p_2}} \sin \pi \hat{p}_2 + \sqrt{\frac{\mu_M}{p_2}} (e_2 + \cos \pi) \hat{q}_2 \quad (5.45)$$

$$\mathbf{v}_2^+ = \sqrt{\frac{\mu_M}{p_2}} (e_2 - 1) \hat{q}_2 \quad (5.46)$$

where

$$e_2 = \frac{r_{a_2} - r_{p_2}}{r_{a_2} + r_{p_2}} \quad (5.47)$$

$$r_{a_2} = r_{a_1} \quad (5.48)$$

and

$$a_2 = \frac{1}{2}(r_{p_2} + r_{a_2}) \quad (5.49)$$

$$p_2 = a_2(1 - e_2^2) \quad (5.50)$$

Now that \mathbf{v}_2^- and \mathbf{v}_2^+ are known, LOI-2 is

$$\Delta \mathbf{v}_2 = \mathbf{v}_2^+ - \mathbf{v}_2^- \quad (5.51)$$

$$\Delta \mathbf{v}_2 = \sqrt{\frac{\mu_M}{p_2}}(e_2 - 1) \hat{\mathbf{q}}_2 - \sqrt{\frac{\mu_M}{p_1}}(e_1 - 1) \hat{\mathbf{q}}_1 \quad (5.52)$$

The velocity immediately before LOI-3 is

$$\mathbf{v}_3^- = -\sqrt{\frac{\mu_M}{p_2}} \sin 0 \hat{\mathbf{p}}_2 + \sqrt{\frac{\mu_M}{p_2}}(e_2 + \cos 0) \hat{\mathbf{q}}_2 \quad (5.53)$$

$$\mathbf{v}_3^- = \sqrt{\frac{\mu_M}{p_2}}(e_2 + 1) \hat{\mathbf{q}}_2 \quad (5.54)$$

The time of flight from LOI-2 to LOI-3 along \mathcal{O}^2 is

$$t_{23} = \pi \sqrt{\frac{a_2^3}{\mu_M}} \quad (5.55)$$

The periapsis direction of \mathcal{O}^3 is undefined since the orbit is circular, but an arbitrary periapsis direction is specified to coincide with the periapsis directions of \mathcal{O}^1 and \mathcal{O}^2 . Thus,

$$\hat{\mathbf{p}}_3 \equiv \hat{\mathbf{p}}_2 \quad (5.56)$$

The remaining basis vectors of the perifocal coordinate system of \mathcal{O}^3 are

$$\hat{\mathbf{h}}_3 = \hat{\mathbf{h}}_2 \quad (5.57)$$

$$\hat{\mathbf{q}}_3 = \hat{\mathbf{h}}_3 \times \hat{\mathbf{p}}_3 \quad (5.58)$$

where the position at LOI-3 is

$$\mathbf{p}_3 = r_{p_3} \hat{\mathbf{p}}_3 \quad (5.59)$$

$$r_{p_3} = R_M + h_{MIN} \quad (5.60)$$

The velocity immediately after LOI-3 is

$$\mathbf{v}_3^+ = -\sqrt{\frac{\mu_M}{p_3}} \sin 0 \hat{\mathbf{p}}_3 + \sqrt{\frac{\mu_M}{p_3}} (e_3 + \cos 0) \hat{\mathbf{q}}_3 \quad (5.61)$$

$$\mathbf{v}_3^+ = \sqrt{\frac{\mu_M}{p_3}} \hat{\mathbf{q}}_3 \quad (5.62)$$

Thus, LOI-3 is

$$\Delta \mathbf{v}_3 = \mathbf{v}_3^+ - \mathbf{v}_3^- \quad (5.63)$$

$$\Delta \mathbf{v}_3 = \sqrt{\frac{\mu_M}{p_3}} \hat{\mathbf{q}}_3 - \sqrt{\frac{\mu_M}{p_2}} (e_2 + 1) \hat{\mathbf{q}}_2 \quad (5.64)$$

This initial estimate method is summarized in Fig. 5.3. In Fig. 5.3(a), the free return is numerically integrated in the CRTBP until it intersects the lunar sphere of influence. The position and velocity are then transferred to the two-body, moon-centered model in Fig. 5.3(b) where the incoming trajectory is terminated upon intersection with the LLO plane. Next, the LOI-1 maneuver is performed as shown in Fig. 5.3(c). Finally, Fig. 5.3(d) shows the complete two-body LOI sequence.

The method has been tested through a parametric scan over the range of interest of parking orbit orientations, and the method converges for all cases studied. The algorithm is applied to circular, retrograde LLOs of 100 km altitude across a five degree grid of longitude and inclination. The longitude of the ascending node varies from 0 deg to 360 deg and the LLO inclination varies from 90 deg to 180 deg.

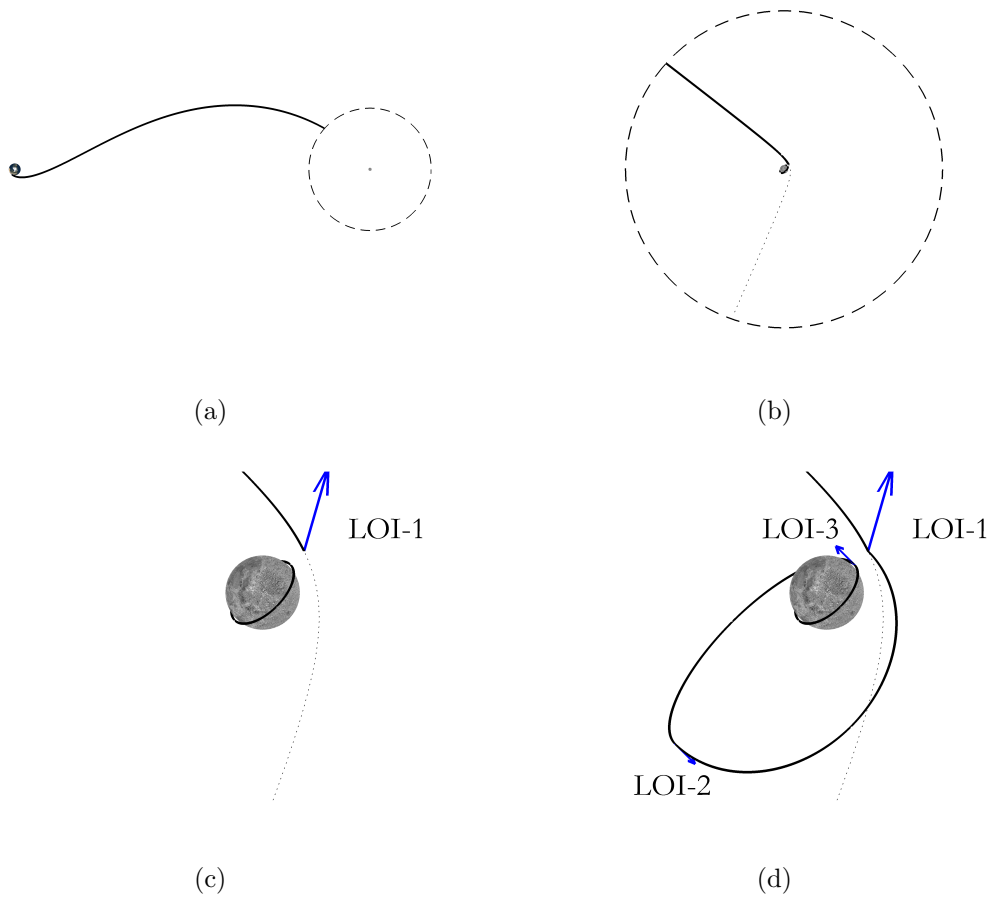


Figure 5.3: Initial estimate: a) free return and lunar sphere of influence (rotating frame), b) incoming hyperbola and LLO, c) capture maneuver, and d) complete LOI sequence.

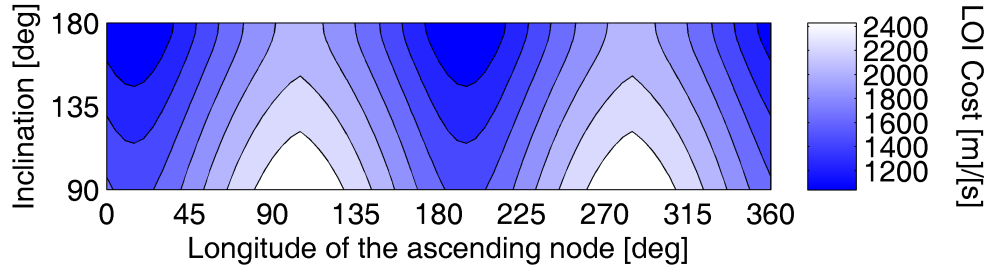


Figure 5.4: Initial estimate cost.

Figure 5.4 shows the total ΔV cost of the three-burn LOI sequence in the Keplerian model; the maximum LOI cost is 2630 m/s. For a given inclination, there are two regions of increased cost, observed near $\Omega = 100$ deg and $\Omega = 280$ deg. This is not a physical phenomenon but an artifact of the targeting method due to the change in flight path angle across the LOI-1 maneuver. The minimum ΔV requirement for a given inclination occurs when there is no change in flight path angle across LOI-1, which happens when LOI-1 occurs at perilune of the incoming lunar hyperbola, near $\Omega = 10$ deg and $\Omega = 190$ deg. It is anticipated that LOI-1 will move nearer to perilune in the optimization process. The two-body targeter also allows entry into posigrade lunar orbits where $i < 90$ deg, but because the free return is retrograde with an inclination of 180 deg, entering a posigrade orbit results in a higher ΔV cost, due to a required plane change greater than 90 deg. Because of this increased cost and no apparent benefit over retrograde orbits for human missions, posigrade orbits are not considered in this investigation. Retrograde orbits are also preferred over posigrade orbits because of a decreased transearth injection (TEI) abort cost [40].

Once an LOI sequence has been constructed in the Keplerian model, the trajectories are propagated in the CRTBP where the Earth's gravity is active at all times. The LOI sequence is propagated backwards in time from the LLO ascending node to LOI-0 to meet the outbound free return that is propagated from TLI to LOI-0. The LOI trajectories deviate from the two-body idealization, producing a state disparity at the lunar sphere of influence. State equality is enforced numerically, resulting in a feasible trajectory after the addition of the LOI-0 maneuver at the union of the free return and LOI trajectories. Figure 5.5 shows the cost of the four-maneuver LOI sequence in the three-body model. The trend mirrors that seen in Fig. 5.4, and each feasible trajectory in the three-body model was achieved numerically in fewer than 10 iterations. The irregularities in Fig. 5.5 appear because any feasible path is targeted, regardless of its LOI cost. The feasible transfer was targeted first because it was found that the optimizer made better progress from this starting point as compared to the infeasible starting transfer taken directly from the initial estimate.

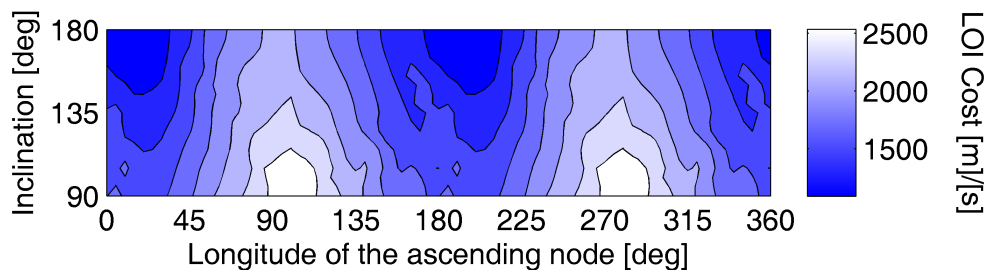


Figure 5.5: Feasible LOI sequence cost.

5.2 Lunar Orbit Insertion from a Fixed Free Return

In this section, optimal trajectories are constructed to transport the spacecraft from a fixed lunar free return trajectory to a closed lunar orbit. The free return chosen for this portion of the investigation is the minimum time type 0 free return, which remains in the Earth-moon moon plane, has a round trip flight time of 5.6 days, and has a lunar flyby altitude of 100 km. By studying the LOI cost with the minimum time free return, a baseline is established which is later used to compare with cases that allow variable free return geometry that enable a decreased ΔV cost at the expense of an increase in the free return flight time.

5.2.1 Optimization Algorithm

The goal of the optimization algorithm is to minimize the total velocity impulse magnitude required to transfer the spacecraft from the free return trajectory to a circular LLO. Nominally, this is executed with four impulsive maneuvers, each free to vary in direction, magnitude, and time of activation. The objective function is the sum of the magnitudes of the four maneuvers, given by

$$J \equiv \sum_{i=0}^3 \Delta v_i \quad (5.65)$$

where Δv_i is the magnitude of the i th maneuver. Nominally, the LOI maneuvers would be performed by a crew vehicle whereas the TLI maneuver would be performed by an Earth-departure booster. It is assumed that this booster has the capability to place the spacecraft on any desired free return; therefore, the TLI maneuver is not included in the objective function. Chapter 3 explored the variation of this maneuver as a function of free return geometry.

The free parameters are

$$\mathbf{x}_p \equiv [t_R \ t_0 \ t_1 \ t_2 \ t_3 \ \Delta\mathbf{v}_0^\top \ \Delta\mathbf{v}_1^\top \ \Delta\mathbf{v}_2^\top \ \Delta\mathbf{v}_3^\top]_{1 \times 17}^\top \quad (5.66)$$

where t_R is the time from TLI to LOI-0, t_i is the time from the LLO ascending node to the i th LOI maneuver, and $\Delta\mathbf{v}_i$ represents the i th LOI maneuver. The initial value of each parameter except $\Delta\mathbf{v}_0$ is taken from the two-body targeter; the initial value of LOI-0 is determined when a feasible solution is found in the three-body model.

A direct, multiple shooting method is used with two trajectory branches. The outbound free return is propagated from TLI to LOI-0, and the LOI sequence is propagated backwards in time from the LLO through LOI-0. Because this multiple shooting produces a state discontinuity in cislunar space, equality constraints placed on the optimization require the position and velocity along each trajectory segment to be equal immediately before LOI-0. The equality constraints are

$$\mathbf{c} = \begin{bmatrix} \mathbf{r}(t_R) - \mathbf{r}(t_0^-) \\ \mathbf{v}(t_R) - \mathbf{v}(t_0^-) \end{bmatrix}_{6 \times 1} = \mathbf{0} \quad (5.67)$$

where $\mathbf{r}(t_R)$ and $\mathbf{v}(t_R)$ are the position and velocity immediately before LOI-0, integrated forward from TLI, and $\mathbf{r}(t_0^-)$ and $\mathbf{v}(t_0^-)$ are the position and velocity immediately before LOI-0, integrated backwards in time from the LLO epoch. Since the CRTBP in rotating coordinates is an autonomous system, it is not necessary to match the times at LOI-0.

Other constraints placed on the optimization require the spacecraft to spend a minimum amount of time on the outbound free return, enforce sequential times,

limit the time between the first and third LOI maneuvers, and bound the minimum altitude at the moon. The inequality constraints are

$$\mathbf{d} = \begin{bmatrix} t_R - t_{MIN} \\ t_1 - t_0 \\ t_2 - t_1 \\ t_3 - t_2 \\ -t_3 \\ t_{MAX} - (t_3 - t_1) \\ h_{LOI} - h_{MIN} \end{bmatrix}_{7 \times 1} \geq \mathbf{0} \quad (5.68)$$

where $t_{MIN} \equiv 1$ day is the minimum amount of time that the spacecraft must remain on the free return, $t_{MAX} \equiv 1$ day is the maximum allowed flight time from LOI-1 to LOI-3, h_{LOI} is the osculating perilune altitude of the trajectory computed immediately before LOI-1, and $h_{MIN} \equiv 100$ km is the minimum allowed perilune altitude of that trajectory. The constraint on the minimum outbound flight time to LOI-0 is imposed because if $t_R = 0$ and $\Delta \mathbf{v}_0 \neq \mathbf{0}$ then the outbound path is no longer a free return trajectory. On a human lunar mission, this flight time on the free return path would be used to evaluate the status of the spacecraft's systems before deciding to retarget for LOI. The constraint on t_3 ensures the LOI sequence is integrated backwards in time. Next, the LOI flight time constraint between LOI-1 and LOI-3 is necessary because the ΔV cost of changing orbital inclination goes to zero as the radius goes to infinity in the two-body model, so the radius where LOI-2 is performed will increase when optimizing LOI for minimum ΔV ; thus, this flight time is bounded. The inequality constraint on h_{LOI} is necessary to ensure the spacecraft does not impact the lunar surface.

5.2.2 Numerical Optimization Setup

Feasible trajectories will be optimized with the sequential quadratic programming algorithm VF13.² It allows specified maximum inter-iteration stepsizes for the parameters, which will be used to ensure the iterations do not diverge from a feasible solution. The optimizer has sufficient freedom to choose trajectories that will not be acceptable solutions; for example, an unacceptable trajectory is an ‘escape’ trajectory that remains bounded to the moon. Maximum stepsizes are chosen in a systematic manner to ensure the optimizer retains sufficient freedom and avoids excessive iteration but is also prevented from moving away from the desired solution. Each maximum stepsize was determined by independently perturbing each parameter and observing the change in position at LOI-0. The maximum stepsize was set where the parameter perturbation resulted in a position deviation at LOI-0 of approximately 100 km. Because of the back propagation method used from the LLO epoch to LOI-0, parameters closer to the LLO epoch were more sensitive than parameters closer to LOI-0.

5.2.3 Analytical Gradients

The gradients of the cost and constraints are computed analytically using linear perturbation theory where necessary. As discussed in Chapter 2, the state transition matrix Φ maps the state perturbation $\delta\mathbf{x}(t_0)$ at a reference time t_0 to

²Information available at <http://www.hsl.rl.ac.uk/archive/specs/vf13.pdf> [accessed 15 March 2012]

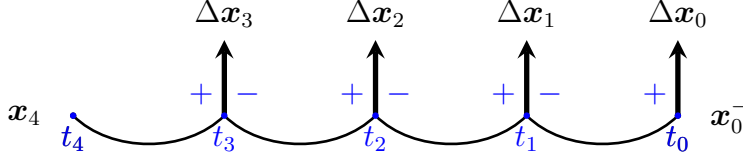


Figure 5.6: Transfer segments.

the state perturbation $\delta \mathbf{x}(t)$ at time t , to first order, as

$$\delta \mathbf{x}(t) = \mathbf{\Phi}(t, t_0) \delta \mathbf{x}(t_0) \quad (5.69)$$

where the state transition matrix satisfies

$$\mathbf{\Phi}(t, t_0) = \frac{\partial \mathbf{x}(t)}{\partial \mathbf{x}(t_0)} \quad (5.70)$$

and \mathbf{x} is the spacecraft state.

Consider the simplified transfer trajectories from the LLO to the retargeting maneuver shown in Figure 5.6. Here, four ballistic arcs are delineated by four state discontinuities, each denoted by $\Delta \mathbf{x}_i$ occurring at t_i . By Eq. (4.29), the total differential at t_0^- is

$$\begin{aligned} d\mathbf{x}_0^- &= \mathbf{\Phi}(t_0, t_1) \mathbf{\Phi}(t_1, t_2) \mathbf{\Phi}(t_2, t_3) (\Delta \dot{\mathbf{x}}_3 dt_3 - d(\Delta \mathbf{x}_3)) \\ &\quad + \mathbf{\Phi}(t_0, t_1) \mathbf{\Phi}(t_1, t_2) (\Delta \dot{\mathbf{x}}_2 dt_2 - d(\Delta \mathbf{x}_2)) \\ &\quad + \mathbf{\Phi}(t_0, t_1) (\Delta \dot{\mathbf{x}}_1 dt_1 - d(\Delta \mathbf{x}_1)) + \dot{\mathbf{x}}_0^+ dt_0 - d(\Delta \mathbf{x}_0) \end{aligned} \quad (5.71)$$

where the sequential order of the indices are reversed relative to Eq. (4.29) since the LOI segments are integrated backwards in time from the LLO epoch through the retargeting maneuver. Terms associated with t_4 are zero since the spacecraft state

at that time is fixed. Equation (5.71) enables the computation of gradients through the LOI portion of the Earth to moon transfer.

The gradient of J with respect to the free parameters \mathbf{x}_p is

$$\frac{dJ}{d\mathbf{x}_p} = [\mathbf{0}_{5 \times 1}^\top \quad \Delta \hat{\mathbf{v}}_0^\top \quad \Delta \hat{\mathbf{v}}_1^\top \quad \Delta \hat{\mathbf{v}}_2^\top \quad \Delta \hat{\mathbf{v}}_3^\top]_{1 \times 17} \quad (5.72)$$

where

$$\Delta \hat{\mathbf{v}}_i \equiv \frac{\Delta \mathbf{v}_i}{|\Delta \mathbf{v}_i|} \quad (5.73)$$

The gradient of the objective function with respect to each maneuver time is zero because the maneuvers themselves are independent parameters, so their magnitude does not depend on the time of activation.

The only equality constraints enforced in this problem require the position and velocity of the forward propagated segment from the Earth to match the backwards propagated position and velocity from the moon immediately before LOI-0. The gradient of these constraints with respect to the free parameters is

$$\frac{d\mathbf{c}}{d\mathbf{x}_p} = \left[\frac{\partial \mathbf{x}(t_R)}{\partial t_R} \quad -\frac{\partial \mathbf{x}_0^-}{\partial t_0} \quad -\frac{\partial \mathbf{x}_0^-}{\partial t_1} \quad -\frac{\partial \mathbf{x}_0^-}{\partial t_2} \quad -\frac{\partial \mathbf{x}_0^-}{\partial t_3} \quad -\frac{\partial \mathbf{x}_0^-}{\partial \Delta \mathbf{v}_0} \quad -\frac{\partial \mathbf{x}_0^-}{\partial \Delta \mathbf{v}_1} \quad -\frac{\partial \mathbf{x}_0^-}{\partial \Delta \mathbf{v}_2} \quad -\frac{\partial \mathbf{x}_0^-}{\partial \Delta \mathbf{v}_3} \right] \quad (5.74)$$

Substituting the derivatives from Equation (5.71) gives

$$\frac{\partial \mathbf{x}(t_R)}{\partial t_R} = \dot{\mathbf{x}}(t_R) \quad (5.75)$$

$$-\frac{\partial \mathbf{x}_0^-}{\partial t_0} = -\dot{\mathbf{x}}_0^+ \quad (5.76)$$

$$-\frac{\partial \mathbf{x}_0^-}{\partial t_1} = -\Phi(t_0, t_1) \Delta \dot{\mathbf{x}}_1 \quad (5.77)$$

$$-\frac{\partial \mathbf{x}_0^-}{\partial t_2} = -\Phi(t_0, t_1) \Phi(t_1, t_2) \Delta \dot{\mathbf{x}}_2 \quad (5.78)$$

$$-\frac{\partial \mathbf{x}_0^-}{\partial t_3} = -\Phi(t_0, t_1) \Phi(t_1, t_2) \Phi(t_2, t_3) \Delta \dot{\mathbf{x}}_3 \quad (5.79)$$

$$-\frac{\partial \mathbf{x}_0^-}{\partial \Delta \mathbf{v}_0} = \mathbf{I} \mathbf{C}_{3:6} \quad (5.80)$$

$$-\frac{\partial \mathbf{x}_0^-}{\partial \Delta \mathbf{v}_1} = \Phi(t_0, t_1) \mathbf{C}_{3:6} \quad (5.81)$$

$$-\frac{\partial \mathbf{x}_0^-}{\partial \Delta \mathbf{v}_2} = \Phi(t_0, t_1) \Phi(t_1, t_2) \mathbf{C}_{3:6} \quad (5.82)$$

$$-\frac{\partial \mathbf{x}_0^-}{\partial \Delta \mathbf{v}_3} = \Phi(t_0, t_1) \Phi(t_1, t_2) \Phi(t_2, t_3) \mathbf{C}_{3:6} \quad (5.83)$$

where

$$\mathbf{C}_{3:6} \equiv \begin{bmatrix} \mathbf{0}_{3 \times 3} \\ \mathbf{I}_{3 \times 3} \end{bmatrix}_{6 \times 3} \quad (5.84)$$

Post-multiplying an $r \times 6$ matrix by $\mathbf{C}_{3:6}$ results in an $r \times 3$ matrix that consists of the last three columns of the original matrix, as discussed in Appendix D.

The gradients of the inequality constraints with respect to the free parameters are

$$\frac{\partial(t_R - t_{MIN})}{\partial \mathbf{x}_p} = [1 \quad \mathbf{0}_{16 \times 1}^\top] \quad (5.85)$$

$$\frac{\partial(t_1 - t_0)}{\partial \mathbf{x}_p} = [0 \quad -1 \quad 1 \quad \mathbf{0}_{14 \times 1}^\top] \quad (5.86)$$

$$\frac{\partial(t_2 - t_1)}{\partial \mathbf{x}_p} = [0 \quad 0 \quad -1 \quad 1 \quad \mathbf{0}_{13 \times 1}^\top] \quad (5.87)$$

$$\frac{\partial(t_3 - t_2)}{\partial \mathbf{x}_p} = [\mathbf{0}_{3 \times 1}^\top \quad -1 \quad 1 \quad \mathbf{0}_{12 \times 1}^\top] \quad (5.88)$$

$$\frac{\partial(-t_3)}{\partial \mathbf{x}_p} = [\mathbf{0}_{4 \times 1}^\top \quad -1 \quad \mathbf{0}_{12 \times 1}^\top] \quad (5.89)$$

$$\frac{\partial(t_{MIN} - (t_3 - t_1))}{\partial \mathbf{x}_p} = [0 \ 0 \ 1 \ 0 \ -1 \ \mathbf{0}_{12 \times 1}^\top] \quad (5.90)$$

$$\frac{\partial(h_{LOI} - h_{MIN})}{\partial \mathbf{x}_p} = \left[0 \ 0 \ \frac{\partial r_p}{\partial t_1} \ \frac{\partial r_p}{\partial t_2} \ \frac{\partial r_p}{\partial t_3} \ \mathbf{0}_{3 \times 1}^\top \ \frac{\partial r_p}{\partial \Delta \mathbf{v}_1} \ \frac{\partial r_p}{\partial \Delta \mathbf{v}_2} \ \frac{\partial r_p}{\partial \Delta \mathbf{v}_3} \right] \quad (5.91)$$

where r_p is the osculating periapsis radius. Its gradient with respect to the spacecraft position \mathbf{r} relative to the central body is

$$\frac{\partial r_p}{\partial \mathbf{r}} = \frac{\partial r_p}{\partial a} \frac{\partial a}{\partial \mathbf{r}} + \frac{\partial r_p}{\partial e} \frac{\partial e}{\partial \mathbf{r}} \quad (5.92)$$

$$= (1 - e) \frac{\mu^2}{2\mathcal{E}^2 r^3} \mathbf{r}^\top - a \left[\frac{h^2}{e\mu r^3} \mathbf{r}^\top + \frac{2\mathcal{E}h}{e\mu^2} \hat{\mathbf{h}}^\top (\mathbf{I} \times \mathbf{v}) \right] \quad (5.93)$$

$$= \frac{-r_p^2}{er^3} \mathbf{r}^\top + \frac{1}{\mu e} \mathbf{h}^\top (\mathbf{I} \times \mathbf{v}) \quad (5.94)$$

where e is the orbital eccentricity, μ is the central body gravitational parameter, \mathcal{E} is the spacecraft's Keplerian energy, \mathbf{v} is the spacecraft's velocity relative to the central body, \mathbf{h} is the spacecraft's angular momentum, and the 3×3 matrix $\mathbf{I} \times \mathbf{v}$ is constructed by crossing each column of \mathbf{I} into \mathbf{v} . Similarly, the gradient of the periapsis radius with respect to the spacecraft velocity \mathbf{v} relative to the central body is

$$\frac{\partial r_p}{\partial \mathbf{v}} = \frac{\partial r_p}{\partial a} \frac{\partial a}{\partial \mathbf{v}} + \frac{\partial r_p}{\partial e} \frac{\partial e}{\partial \mathbf{v}} \quad (5.95)$$

$$= (1 - e) \frac{\mu}{2\mathcal{E}^2} \mathbf{v}^\top - a \left[\frac{h^2}{e\mu^2} \mathbf{v}^\top + \frac{2\mathcal{E}h}{e\mu^2} \hat{\mathbf{h}}^\top (\mathbf{r} \times \mathbf{I}) \right] \quad (5.96)$$

$$= \frac{-r_p^2}{\mu e} \mathbf{v}^\top + \frac{1}{\mu e} \mathbf{h}^\top (\mathbf{r} \times \mathbf{I}) \quad (5.97)$$

where the 3×3 matrix $\mathbf{r} \times \mathbf{I}$ is constructed by crossing \mathbf{r} into each column of \mathbf{I} . For notational simplicity, define

$$\Upsilon^\top \equiv \frac{\partial r_p}{\partial \mathbf{x}_1} = \left[\frac{\partial r_p}{\partial \mathbf{r}_1} \ \frac{\partial r_p}{\partial \mathbf{v}_1} \right]_{1 \times 6} \quad (5.98)$$

The nonzero gradients of r_p are

$$\frac{\partial r_p}{\partial t_1} = \frac{\partial r_p}{\partial \mathbf{x}_1^-} \frac{\partial \mathbf{x}_1^-}{\partial t_1} = \mathbf{\Upsilon}^\top \dot{\mathbf{x}}_1^+ \quad (5.99)$$

$$\frac{\partial r_p}{\partial t_2} = \frac{\partial r_p}{\partial \mathbf{x}_1^-} \frac{\partial \mathbf{x}_1^-}{\partial t_2} = \mathbf{\Upsilon}^\top \Phi(t_1, t_2) \Delta \dot{\mathbf{x}}_2 \quad (5.100)$$

$$\frac{\partial r_p}{\partial t_3} = \frac{\partial r_p}{\partial \mathbf{x}_1^-} \frac{\partial \mathbf{x}_1^-}{\partial t_3} = \mathbf{\Upsilon}^\top \Phi(t_1, t_2) \Phi(t_2, t_3) \Delta \dot{\mathbf{x}}_3 \quad (5.101)$$

$$\frac{\partial r_p}{\partial \Delta \mathbf{v}_1} = \frac{\partial r_p}{\partial \mathbf{x}_1^-} \frac{\partial \mathbf{x}_1^-}{\partial \Delta \mathbf{v}_1} = -\mathbf{\Upsilon}^\top \mathbf{C}_{3:6} \quad (5.102)$$

$$\frac{\partial r_p}{\partial \Delta \mathbf{v}_2} = \frac{\partial r_p}{\partial \mathbf{x}_1^-} \frac{\partial \mathbf{x}_1^-}{\partial \Delta \mathbf{v}_2} = -\mathbf{\Upsilon}^\top \Phi(t_1, t_2) \mathbf{C}_{3:6} \quad (5.103)$$

$$\frac{\partial r_p}{\partial \Delta \mathbf{v}_3} = \frac{\partial r_p}{\partial \mathbf{x}_1^-} \frac{\partial \mathbf{x}_1^-}{\partial \Delta \mathbf{v}_3} = -\mathbf{\Upsilon}^\top \Phi(t_1, t_2) \Phi(t_2, t_3) \mathbf{C}_{3:6} \quad (5.104)$$

5.2.4 Numerical Results

With all necessary gradients derived, the targeting and optimization process is illustrated with an example for an LLO of orientation $\Omega = 225$ deg and $i = 120$ deg where Ω is measured in the Earth-moon plane relative to the rotating Earth-moon line, and i is measured relative to the Earth-moon plane. The initial estimate requires $\Delta V = 1735$ m/s, and when propagated in the CRTBP, a position discontinuity of 8600 km results at the lunar sphere of influence (Fig. 5.7(a)). Table 5.1 shows the analytically generated initial parameters, and Table 5.2 shows the initial values of the constraints. In the initial parameters, the retargeting maneuver used to depart the free return is taken as $\Delta \mathbf{v}_0 = \mathbf{0}$. The cost of the feasible transfer is $\Delta V = 1727$ m/s (Fig. 5.7(b)), and after optimization the minimized cost is $\Delta V = 1206$ m/s (Fig. 5.8). For the optimal solution, t_R decreased to one day, which

is the limit imposed by the first inequality constraint. This means the retargeting maneuver moved closer to TLI but was stopped at this point. Additionally, the optimal solution uses a full day from LOI-1 to LOI-3, which is the most time allowed. The flight time from TLI to the LLO epoch is 94.7 hr or approximately four days.

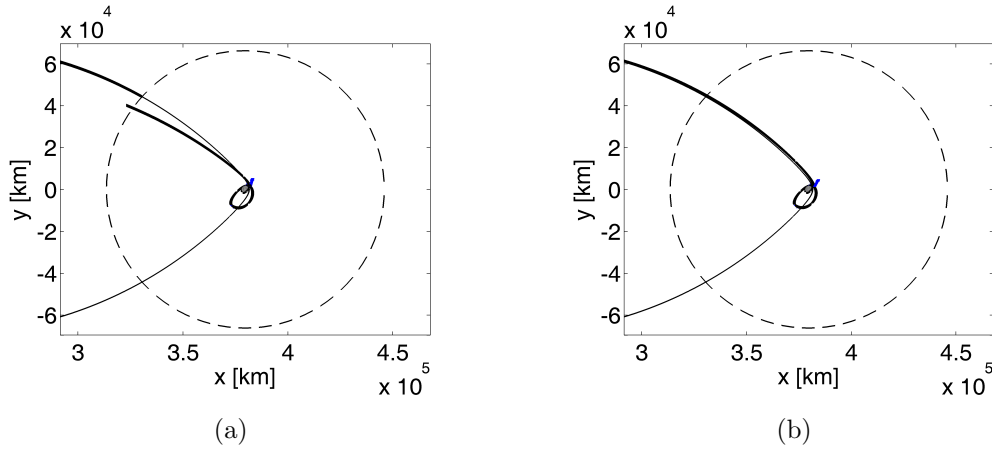


Figure 5.7: Transfer trajectories (rotating frame): a) initial LOI sequence, and b) feasible LOI sequence.

To observe the change in LOI ΔV requirements for different LLO orientations, LLOs are parametrically scanned from $\Omega = 0$ deg to $\Omega = 360$ deg with inclination varying from $i = 90$ deg to $i = 180$ deg, both in 10 deg increments, and Figure 5.9 shows the results. The maximum value of $\Delta V = 1351$ m/s occurs at $(\Omega, i) = (30$ deg, 90 deg) and (210 deg, 90 deg) whereas the minimum value of $\Delta V = 925$ m/s occurs at any Ω with $i = 180$ deg. For each longitude, $i = 90$ deg is the most costly case, and the total ΔV decreases with increasing inclination magnitude. The hotspots of increased ΔV , centered at $\Omega = 30$ deg and $\Omega = 210$ deg occur where the incoming velocity vector at the moon, \mathbf{v}_∞ , is nearly perpendicular

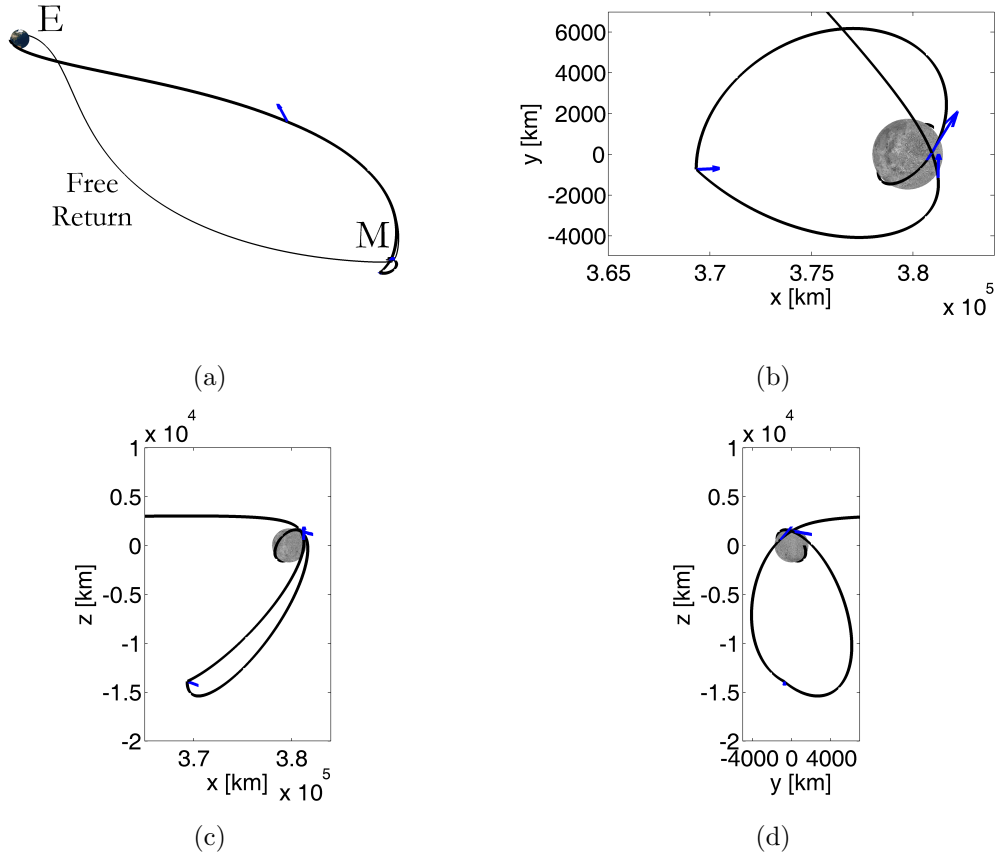


Figure 5.8: Optimal hybrid Earth to moon transfer (rotating frame): a) free return and cislunar maneuver, b) view normal to $\hat{x}\hat{y}$ plane, c) view normal to $\hat{x}\hat{z}$ plane, and d) view normal to $\hat{y}\hat{z}$ plane.

Table 5.1: Free parameters for fixed free return example case

Parameter	Units	Initial	Feasible	Optimal
t_R	s	194976	199784	86400
t_0	s	-101715	-96845	-254660
t_1	s	-50314	-50148	-91981
t_2	s	-27510	-27372	-62563
t_3	s	-7072	-7038	-5581
$\Delta v_{0,x}$	km/s	0.000	0.034	-0.016
$\Delta v_{0,y}$	km/s	0.000	0.006	-0.004
$\Delta v_{0,z}$	km/s	0.000	0.002	0.023
$\Delta v_{1,x}$	km/s	0.226	0.323	0.005
$\Delta v_{1,y}$	km/s	0.785	0.701	0.235
$\Delta v_{1,z}$	km/s	0.000	0.004	0.273
$\Delta v_{2,x}$	km/s	0.186	0.189	0.232
$\Delta v_{2,y}$	km/s	-0.186	-0.188	0.011
$\Delta v_{2,z}$	km/s	-0.338	-0.338	-0.086
$\Delta v_{3,x}$	km/s	-0.173	-0.173	0.300
$\Delta v_{3,y}$	km/s	0.173	0.173	0.478
$\Delta v_{3,z}$	km/s	-0.424	-0.424	-0.086

Table 5.2: Constraints for fixed free return example case

Constraint	Units	Initial	Feasible	Optimal
$x - x_0 = 0$	km	7603.826	8.2×10^{-4}	-1.3×10^{-4}
$y - y_0 = 0$	km	4050.006	3.6×10^{-3}	-3.0×10^{-5}
$z - z_0 = 0$	km	97.596	1.0×10^{-4}	-1.1×10^{-4}
$v_x - v_{x_0} = 0$	km/s	-0.151	6.8×10^{-9}	1.0×10^{-9}
$v_y - v_{y_0} = 0$	km/s	-0.095	-8.3×10^{-8}	7.0×10^{-10}
$v_z - v_{z_0} = 0$	km/s	-0.002	-1.8×10^{-9}	5.0×10^{-10}
$t_R - t_{MIN} \geq 0$	s	108576	113384	0
$t_1 - t_0 \geq 0$	s	51400	46696	162679
$t_2 - t_1 \geq 0$	s	22804	22777	29418
$t_3 - t_2 \geq 0$	s	20437	20334	56982
$-t_3 \geq 0$	s	7073	7038	5581
$t_{MAX} - (t_3 - t_1) \geq 0$	s	43159	43290	0
$h_P - h_{P_{MIN}} \geq 0$	km	886.684	1156.968	0.000

to the LLO plane. The regions of lower ΔV result from LLO orientations where \mathbf{v}_∞ is nearly parallel to the LLO plane. Since the incoming free return trajectory has an inclination of $i = 180$ deg, less plane change is required as the LLO inclination approaches 180 deg, and thus the ΔV cost is lower. The trajectories converge to the same LOI sequence at $i = 180$ deg because the LLO is unchanged regardless of what Ω is specified. In these cases, a three-burn LOI sequence is not needed since a plane change is not required. Cases near $\Omega = 130$ deg and $\Omega = 310$ deg of any inclination were also observed to require little plane change because the retargeting maneuver enabled a \mathbf{v}_∞ approach in or near the LLO plane. In these cases, LOI-2 tends to zero in the optimization process and LOI-1 and LOI-3 occur at nearly the same point. This indicates that a single burn LOI sequence may be optimal here. In each case requiring a plane change maneuver at the moon, the retargeting maneuver moves back to the one day limit imposed by the inequality constraint on t_R . Additionally, the time from LOI-1 to LOI-3 reaches the limit of one day in the optimal solution. Another trend observed is the tendency of the lunar periapsis altitude to settle at the minimum value of 100 km.

Though not utilized in this investigation, adding loiter time in lunar orbit can be used to lower the total LOI ΔV cost. Because the Earth and moon revolve about their common barycenter approximately once every 27 days, a fixed orbit's ascending node location will rotate by approximately 13 deg per day in the rotating frame. Thus, a spacecraft may enter another parking orbit and allow the node line to advance to the desired location at the desired time. Loiter time of up to seven days was used in a recent LOI study to achieve LOI ΔV cost savings [39].

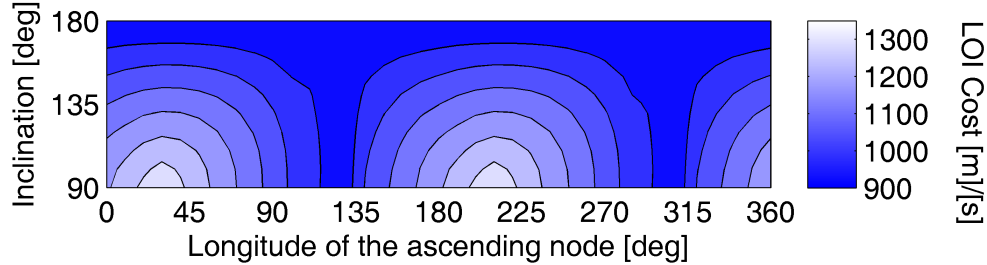


Figure 5.9: Minimum LOI cost contours with fixed free return formulation.

5.2.5 Retargeting Time Variation

Recall that the retargeting time is the time at which the spacecraft activates its propulsion system to depart the free return path and target a desired LLO. The period spent on the free return affords time to assess spacecraft systems and maintain an Earth return option. Selection of the retargeting time requires consideration of crew scheduling and the amount of confidence in the lunar architecture. A minimum retargeting time of one day after TLI was chosen as a baseline reference, but the optimal location that minimizes the LOI cost may be located closer to TLI. To study the variation of the retargeting maneuver's magnitude, cases are examined with three different LLO orientations and retargeting times ranging from one hour to 60 hours. Figure 5.10 shows the variation in Δv_0 and the overall LOI cost, including the retargeting maneuver. Cases with $\Omega = 225$ deg are shown with three different LLO inclinations. The first example that was shown is seen at (225 deg, 120 deg) with $\Delta V = 1206$ m/s at a retargeting time of $t_R = 24$ hr. At $i = 120$ deg, the overall ΔV decreases with decreasing t_R until $t_R \approx 9.4$ hr where $\Delta V = 1202$ m/s, a

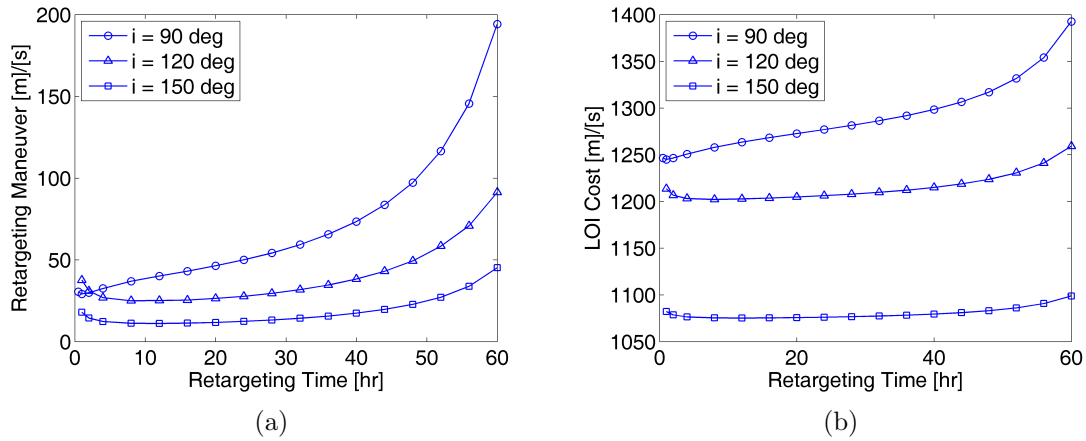


Figure 5.10: Effect of variable retargeting time: a) retargeting maneuver magnitude, and b) overall LOI cost.

savings of 0.3% relative to the baseline case. Past this point, the ΔV cost increases as $\Delta \mathbf{v}_0$ approaches TLI. When the retargeting time is increased past one day, the total ΔV increases. Similar trends are seen for $i = 90$ deg and $i = 150$ deg where the optimal retargeting time is not at TLI but approximately one and 12 hours after TLI, respectively. For $i = 90$ deg, the cost at $t_R = 60$ hr increases over 8% relative to the cost at $t_R = 24$ hr. It is seen in these cases that the ΔV penalty of increasing t_R is greater than the ΔV savings from decreasing t_R .

It may be expected that the retargeting maneuver would move as close to TLI as possible since small perturbations near TLI can achieve large deviations at the moon, resulting in a lower LOI cost. The algorithm, however, is choosing $\Delta \mathbf{v}_0$, not the TLI velocity itself, and the algorithm cannot change the TLI position. In the cases studied here, it is optimal for the spacecraft to remain on the free return for several hours before applying the retargeting maneuver.

5.3 Lunar Orbit Insertion from a Variable Symmetric Free Return

In this section, the optimization of a multiple impulse LOI sequence from a symmetric free return trajectory is presented where both the inclination and altitude at lunar flyby along the free return are variable during the optimization process. The algorithm optimizes the orbit insertion sequence while simultaneously generating a free return trajectory. Examples are presented for both classes of symmetric, prograde circumlunar free returns, and a range of lunar orbit orientations is examined to assess the impact on velocity impulse requirements.

5.3.1 Optimization Algorithm

The minimum impulse trajectory from the variable free return to the LLO is computed within a parameter optimization framework. The multiple shooting method is comprised of a forward-time segment from TLI to LOI-0, a backwards-time segment from the LLO to LOI-0, and a forward-time segment from lunar flyby to Earth entry interface (EEI). The free return is now variable, but it must remain symmetric, which ensures the TLI to lunar flyby segment is an image of the lunar flyby to EEI segment. Therefore, the TLI segment does not need to be numerically integrated. The initial estimate is identical to that used in the fixed free return case, and the cost function to be minimized is the sum of the magnitudes of the four impulsive maneuvers.

The free parameters include the time, direction, and magnitude of each LOI maneuver, and, because the free return is not fixed, four quantities associated with

its orientation are added as optimization variables. The free parameters are

$$\mathbf{x}_p \equiv [t_R \ t_0 \ t_1 \ t_2 \ t_3 \ \Delta\mathbf{v}_0^\top \ \Delta\mathbf{v}_1^\top \ \Delta\mathbf{v}_2^\top \ \Delta\mathbf{v}_3^\top \ h \ \phi \ v \ t_{EEI}]_{1 \times 21}^\top \quad (5.105)$$

where h is the free return altitude at lunar flyby, ϕ is the lunar flyby angle, v is the velocity magnitude at the flyby point, and t_{EEI} is the time from the flyby to EEI. At the onset of the optimization algorithm, the free return lies in the Earth-moon plane with a lunar flyby altitude of $h = 100$ km and a lunar flyby angle of $\phi = 0$ deg. If type 1 free returns are used, ϕ represents the velocity azimuth at lunar flyby, measured positive north from west; if type 2 free returns are used, ϕ represents the latitude at lunar flyby, measured relative to the Earth-moon plane. The initial estimates of the final two free parameters are taken from the previously converged minimum time free return. The number of iterations is increased by the limits placed on the inter-iteration stepsize of the optimization variables. For example, the maximum free return flight time stepsize is 100 s. Because this flight time is maximized in the optimal solution, extra iterations are incurred by the stepsize bound.

Three equality constraints are imposed during the optimization process:

$$\mathbf{c} \equiv \begin{bmatrix} \mathbf{x}(t_R) - \mathbf{x}(t_0^-) \\ h_{EEI} - h_T \\ \gamma_{EEI} - \gamma_T \end{bmatrix}_{8 \times 1} = \mathbf{0} \quad (5.106)$$

The first equality constraint ensures continuity between the forward integrated TLI segment from the Earth and the backwards integrated LOI segments from the moon. The final two equality constraints target the specified altitude and flight path angle at Earth on the free return. The targeted conditions at Earth are $h_T = 121$ km and $\gamma_T = 0$ deg.

The inequality constraints are given by

$$\mathbf{d} \equiv \begin{bmatrix} t_R - t_{MIN} \\ t_1 - t_0 \\ t_2 - t_1 \\ t_3 - t_2 \\ -t_3 \\ t_{MAX} - (t_3 - t_1) \\ h_{LOI} - h_{MIN} \\ h - h_{MIN} \\ \phi_{MAX} - |\phi| \\ T_{MAX}/2 - t_{EEI} \end{bmatrix}_{10 \times 1} \geq \mathbf{0} \quad (5.107)$$

The eighth inequality constraint requires the flyby altitude along the free return to be greater than or equal to 100 km. The ninth constraint bounds the out-of-plane free return angle, and the final inequality constraint imposes a 10 day maximum round trip flight time on the free return. It will be seen in some cases that increasing the free return flight time decreases the LOI cost; however, if a mission abort scenario requires a return to Earth, the return time should be as short as possible. Additionally, the spacecraft must possess sufficient life support capability for the return voyage. Because of these reasons, the free return flight time is bounded.

The maximum out-of-plane flyby angle of the free return is a function of the altitude at that point. The behavior of ϕ_{MAX} is determined empirically by incrementing the flyby angle by 0.01 deg, converging to a feasible free return using the algorithm developed in Chapter 3, and repeating until a feasible solution is not possible. The trends are fit with an exponential function of the form

$$\phi_{MAX}(h) = ae^{bh} + ce^{dh} - 180 \quad (5.108)$$

where ϕ_{MAX} is in degrees. For type 1 free returns, the coefficients are given by $a = 1.951$, $b = -2.13 \times 10^{-5}$, $c = 188.553$, and $d = -1.19 \times 10^{-7}$ (Fig. 5.11(a)). For type 2 free returns with $h \leq 19450$ km, $a = 193.3$, $b = 1.276 \times 10^{-5}$, $c = 4.463 \times 10^{-5}$, and $d = 6.743 \times 10^{-4}$ (Fig. 5.11(b)). For type 2 free returns with $h > 19450$ km, $\phi_{MAX} = 90$ deg. The data are shown in Tables 5.3–5.4. Apparent in Fig. 5.11, type 2 free returns offer a larger out-of-plane angle at lunar flyby. Applying this knowledge of type 1 and type 2 free returns to constrain $|\phi|$ keeps the optimizer in the domain of feasible free returns.

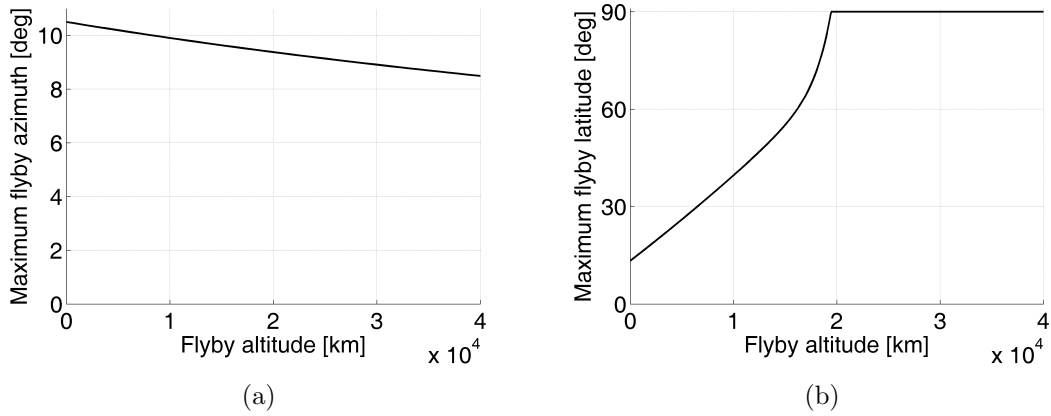


Figure 5.11: Maximum out-of-plane free return angle: a) type 1 free returns, and b) type 2 free returns.

5.3.2 Analytical Gradients

The gradient of the objective function is

$$\frac{dJ}{d\mathbf{x}_p} = [\mathbf{0}_{5 \times 1}^T \quad \Delta \hat{\mathbf{v}}_0^T \quad \Delta \hat{\mathbf{v}}_1^T \quad \Delta \hat{\mathbf{v}}_2^T \quad \Delta \hat{\mathbf{v}}_3^T \quad \mathbf{0}_{4 \times 1}^T]_{1 \times 21} \quad (5.109)$$

Table 5.3: Maximum flyby azimuth for type 1 free returns

Altitude [km]	Max Azimuth [deg]	Curve Fit [deg]
0	10.51	10.50
100	10.50	10.50
1000	10.44	10.44
10000	9.88	9.91
20000	9.37	9.38
30000	8.91	8.91
40000	8.49	8.49
50000	8.10	8.11
90000	6.79	6.83

Table 5.4: Maximum flyby latitude for type 2 free returns

Altitude [km]	Max Latitude [deg]	Curve Fit [deg]
100	13.41	13.55
1000	15.98	15.78
2500	19.90	19.57
5000	26.15	26.04
7500	32.54	32.72
10000	39.35	39.65
12500	46.92	46.93
15000	55.77	55.18
17500	67.48	67.61
19450	90.00	89.91

The final four parameters control the geometry of the free return path, so an independent perturbation of these quantities does not affect the LOI trajectories.

The gradients of the first equality constraint with respect to the maneuvers and their activation times are identical to those in the fixed free return case. The gradient of the first equality constraint with respect to the lunar flyby altitude of the free return, for a type i free return, is

$$\frac{\partial (\mathbf{x}(t_R) - \mathbf{x}(t_0^-))}{\partial h} = \frac{\partial \mathbf{x}(t_R)}{\partial \mathbf{x}_{TLI}} \frac{\partial \mathbf{x}_{TLI}}{\partial \mathbf{x}_{EEI}} \frac{\partial \mathbf{x}_{EEI}}{\partial \mathbf{x}_{FR}} \frac{\partial \mathbf{x}_{FR_i}}{\partial h} \quad (5.110)$$

$$= \Phi_{TLI} \mathbf{K}_i \Phi_{FR} \frac{\partial \mathbf{x}_{FR_i}}{\partial h} \quad (5.111)$$

where the matrices that transform the EEI spacecraft state to the TLI state are $\mathbf{K}_1 \equiv \text{diag}(1, -1, -1, -1, 1, 1)$ and $\mathbf{K}_2 \equiv \text{diag}(1, -1, 1, -1, 1, -1)$ and the lunar flyby states and state derivatives are

$$\mathbf{x}_{FR_1} = \begin{bmatrix} x_M + R_M + h \\ 0 \\ 0 \\ 0 \\ -v \cos \phi \\ v \sin \phi \end{bmatrix} \quad \mathbf{x}_{FR_2} = \begin{bmatrix} x_M + (R_M + h) \cos \phi \\ 0 \\ (R_M + h) \sin \phi \\ 0 \\ -v \\ 0 \end{bmatrix} \quad (5.112)$$

$$\frac{\partial \mathbf{x}_{FR_1}}{\partial h} = \begin{bmatrix} 1 \\ 0 \\ 0 \\ 0 \\ \mathbf{0} \end{bmatrix}_{6 \times 1} \quad \frac{\partial \mathbf{x}_{FR_2}}{\partial h} = \begin{bmatrix} \cos \phi \\ 0 \\ \sin \phi \\ \mathbf{0} \end{bmatrix}_{6 \times 1} \quad (5.113)$$

Similarly, the gradient with respect to the lunar flyby angle of the free return is given by

$$\frac{\partial (\mathbf{x}(t_R) - \mathbf{x}(t_0^-))}{\partial \phi} = \frac{\partial \mathbf{x}(t_R)}{\partial \mathbf{x}_{TLI}} \frac{\partial \mathbf{x}_{TLI}}{\partial \mathbf{x}_{EEI}} \frac{\partial \mathbf{x}_{EEI}}{\partial \mathbf{x}_{FR}} \frac{\partial \mathbf{x}_{FR_i}}{\partial \phi} \quad (5.114)$$

$$= \Phi_{TLI} \mathbf{K}_i \Phi_{FR} \frac{\partial \mathbf{x}_{FR_i}}{\partial \phi} \quad (5.115)$$

where the lunar flyby state derivatives are

$$\frac{\partial \mathbf{x}_{FR_1}}{\partial \phi} = \begin{bmatrix} \mathbf{0} \\ 0 \\ v \sin \phi \\ v \cos \phi \end{bmatrix}_{6 \times 1} \quad \frac{\partial \mathbf{x}_{FR_2}}{\partial \phi} = \begin{bmatrix} -(R_M + h) \sin \phi \\ 0 \\ (R_M + h) \cos \phi \\ \mathbf{0} \end{bmatrix}_{6 \times 1} \quad (5.116)$$

Similarly,

$$\frac{\partial (\mathbf{x}(t_R) - \mathbf{x}(t_0^-))}{\partial v} = \Phi_{TLI} \mathbf{K}_i \Phi_{FR} \begin{bmatrix} \mathbf{0} \\ \mathbf{I} \end{bmatrix} \hat{v} \quad (5.117)$$

$$\frac{\partial (\mathbf{x}(t_R) - \mathbf{x}(t_0^-))}{\partial t_{EEI}} = \Phi_{TLI} \mathbf{K}_i \dot{\mathbf{x}}_{EEI} \quad (5.118)$$

The altitude at Earth arrival is

$$h_{EEI} = |\mathbf{r}_{EP}| - R_E \quad (5.119)$$

where \mathbf{r}_{EP} is the Earth-spacecraft vector at EEI, and the flight path angle at Earth arrival is

$$\gamma_{EEI} = \sin^{-1} \left(\frac{\mathbf{v}_{EEI} \cdot \mathbf{r}_{EP}}{v_{EEI} r_{EP}} \right) \quad (5.120)$$

where \mathbf{v}_{EEI} is the velocity at EEI. The gradient of the EEI altitude with respect to the free return flyby altitude is

$$\frac{\partial h_{EEI}}{\partial h} = \frac{\partial h_{EEI}}{\partial \mathbf{x}_{EEI}} \frac{\partial \mathbf{x}_{EEI}}{\partial \mathbf{x}_{FR}} \frac{\partial \mathbf{x}_{FR_i}}{\partial h} \quad (5.121)$$

$$= \boldsymbol{\alpha}^\top \Phi_{FR} \frac{\partial \mathbf{x}_{FR_i}}{\partial h} \quad (5.122)$$

where

$$\boldsymbol{\alpha}^\top \equiv [\hat{\mathbf{r}}_{EP}^\top \quad \mathbf{0}^\top]_{1 \times 6} \quad (5.123)$$

Similarly, the gradient of h_{EEI} with respect to the free return flyby angle is

$$\frac{\partial h_{EEI}}{\partial \phi} = \boldsymbol{\alpha}^\top \Phi_{FR} \frac{\partial \mathbf{x}_{FR_i}}{\partial \phi} \quad (5.124)$$

The gradients of the EEI flight path angle with respect to h and ϕ are

$$\frac{\partial \gamma_{EEI}}{\partial h} = \boldsymbol{\beta}^\top \boldsymbol{\Phi}_{FR} \frac{\partial \mathbf{x}_{FR_i}}{\partial h} \quad (5.125)$$

$$\frac{\partial \gamma_{EEI}}{\partial \phi} = \boldsymbol{\beta}^\top \boldsymbol{\Phi}_{FR} \frac{\partial \mathbf{x}_{FR_i}}{\partial \phi} \quad (5.126)$$

where

$$\boldsymbol{\beta}^\top \equiv \begin{bmatrix} \frac{\partial \gamma_{EEI}}{\partial \mathbf{r}_{EEI}} & \frac{\partial \gamma_{EEI}}{\partial \mathbf{v}_{EEI}} \end{bmatrix}_{1 \times 6} \quad (5.127)$$

and

$$\frac{\partial \gamma_{EEI}}{\partial \mathbf{r}_{EEI}} = \frac{\hat{\mathbf{v}}_{EEI}^\top}{r_{EP} \sqrt{1 - \sin^2 \gamma_{EEI}}} [\mathbf{I} - \hat{\mathbf{r}}_{EP} \hat{\mathbf{r}}_{EP}^\top] \quad (5.128)$$

$$\frac{\partial \gamma_{EEI}}{\partial \mathbf{v}_{EEI}} = \frac{\hat{\mathbf{r}}_{EP}^\top}{v_{EEI} \sqrt{1 - \sin^2 \gamma_{EEI}}} [\mathbf{I} - \hat{\mathbf{v}}_{EEI} \hat{\mathbf{v}}_{EEI}^\top] \quad (5.129)$$

The gradient of the EEI altitude with respect to the free return flyby velocity

is

$$\frac{\partial h_{EEI}}{\partial \mathbf{v}} = \frac{\partial h_{EEI}}{\partial \mathbf{x}_{EEI}} \frac{\partial \mathbf{x}_{EEI}}{\partial \mathbf{x}_{FR}} \frac{\partial \mathbf{x}_{FR}}{\partial \mathbf{v}} \frac{\partial \mathbf{v}}{\partial \mathbf{v}} \quad (5.130)$$

$$= \boldsymbol{\alpha}^\top \boldsymbol{\Phi}_{FR} \begin{bmatrix} \mathbf{0} \\ \mathbf{I} \end{bmatrix} \hat{\mathbf{v}} \quad (5.131)$$

Next,

$$\frac{\partial h_{EEI}}{\partial t_{EEI}} = \frac{\partial h_{EEI}}{\partial \mathbf{x}_{EEI}} \frac{\partial \mathbf{x}_{EEI}}{\partial t_{EEI}} = \boldsymbol{\alpha}^\top \dot{\mathbf{x}}_{EEI} \quad (5.132)$$

The gradient of the flight path angle with respect to the flyby velocity is

$$\frac{\partial \gamma_{EEI}}{\partial \mathbf{v}} = \frac{\partial \gamma_{EEI}}{\partial \mathbf{x}_{EEI}} \frac{\partial \mathbf{x}_{EEI}}{\partial \mathbf{x}_{FR}} \frac{\partial \mathbf{x}_{FR}}{\partial \mathbf{v}} \frac{\partial \mathbf{v}}{\partial \mathbf{v}} \quad (5.133)$$

$$= \boldsymbol{\beta}^\top \boldsymbol{\Phi}_{FR} \begin{bmatrix} \mathbf{0} \\ \mathbf{I} \end{bmatrix} \hat{\mathbf{v}} \quad (5.134)$$

Finally,

$$\frac{\partial \gamma_{EEI}}{\partial t_{EEI}} = \frac{\partial \gamma_{EEI}}{\partial \mathbf{x}_{EEI}} \frac{\partial \mathbf{x}_{EEI}}{\partial t_{EEI}} = \boldsymbol{\beta}^\top \dot{\mathbf{x}}_{EEI} \quad (5.135)$$

The gradients of the nonlinear inequality constraints with respect to the free parameters are

$$\frac{\partial (h_{LOI} - h_{MIN})}{\partial \mathbf{x}_p} = \left[0 \quad 0 \quad \frac{\partial r_p}{\partial t_1} \quad \frac{\partial r_p}{\partial t_2} \quad \frac{\partial r_p}{\partial t_3} \quad \mathbf{0}_{3 \times 1}^\top \quad \frac{\partial r_p}{\partial \Delta v_1} \quad \frac{\partial r_p}{\partial \Delta v_2} \quad \frac{\partial r_p}{\partial \Delta v_3} \quad \mathbf{0}_{4 \times 1}^\top \right] \quad (5.136)$$

$$\frac{\partial (\phi_{MAX} - |\phi|)}{\partial \mathbf{x}_p} = \left[\mathbf{0}_{17 \times 1}^\top \quad \frac{\partial \phi_{MAX_i}}{\partial h} \quad -\text{sign}(\phi) \quad 0 \quad 0 \right] \quad (5.137)$$

where

$$\frac{\partial \phi_{MAX_i}}{\partial h} = \begin{cases} abe^{bh} + cde^{dh} & \text{if } \phi_{MAX_i} \neq 90 \text{ deg} \\ 0 & \text{if } \phi_{MAX_i} = 90 \text{ deg} \end{cases} \quad (5.138)$$

The gradients of the osculating perilune radius of the LOI sequence are identical to those shown in the fixed free return case.

5.3.3 Numerical Results

The optimization process is illustrated by targeting an LLO of orientation $(\Omega, i) = (225 \text{ deg}, 120 \text{ deg})$. Using the two-body targeting algorithm, an LOI sequence requiring $\Delta V = 1735 \text{ m/s}$ is generated as the initial estimate. On the first iteration of the optimization algorithm, the free return is in the Earth-moon plane with a lunar flyby altitude of 100 km. Satisfying state continuity at the lunar sphere of influence, the feasible initial solution in the CRTBP requires $\Delta V = 1727 \text{ m/s}$. Optimization begins from this trajectory for both type 1 and type 2 free returns.

For LOI from a type 1 free return, the algorithm converges to a total cost of $\Delta V = 1014 \text{ m/s}$, which represents a savings of nearly 200 m/s relative to the

1206 m/s required for the fixed, type 0 minimum time free return case. The total transfer time from TLI to LLO is 6.1 days whereas the transfer time was 3.9 days with the minimum time free return. The optimal trajectory is shown in Fig. 5.12 with the optimal parameters shown in Table 5.5 and the final constraint values shown in Table 5.6. Views in Earth-centered and moon-centered non-rotating frames are presented in Figs. 5.12(c)–5.12(d). In these subfigures, the moon and Earth are plotted at TLI (denoted M_0 and E_0), free return flyby, and EEI (denoted M_f and E_f). As in the minimum time free return example, the time of the retargeting maneuver backs up to the one day limit imposed by the inequality constraint. The osculating perilune altitude of the LOI sequence decreases to the minimum of 100 km. Additionally, the altitude at free return flyby increases to 32233 km, which is the maximum value allowed by the imposed limit of 10 days on the free return’s round trip flight time. The time between LOI-1 and LOI-3 is maximized at one day. The velocity azimuth at free return flyby is 4.9 deg, which is nearly 4 deg below the maximum possible azimuth at this altitude.

The optimization results using a type 2 free return are shown in Fig. 5.13 and Tables 5.5–5.6. The optimal solution requires $\Delta V = 1019$ m/s, which is 5 m/s higher than the type 1 case. The time of the retargeting maneuver and the LOI flight time both reach the limits imposed by the inequality constraints. The altitude at free return flyby increases to 32694 km, the limit required by the round trip flight time constraint. The latitude at free return flyby is 11 deg even though the maximum allowed latitude at this altitude is 90 deg. The transfer time from TLI to LLO is 6.1 days. The savings of nearly 200 m/s in ΔV over the type 0 minimum time free

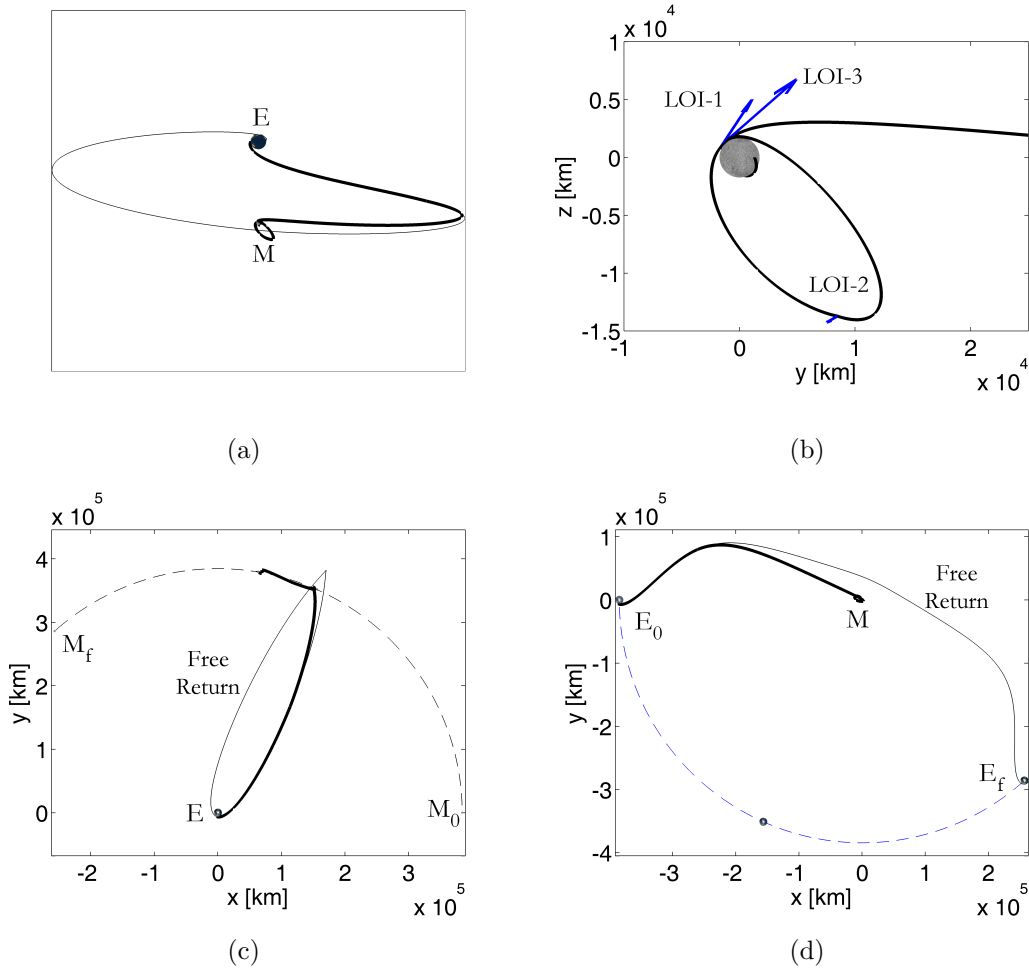


Figure 5.12: Type 1 free return and LOI into an LLO orientation of $(\Omega, i) = (225 \text{ deg}, 120 \text{ deg})$: a) oblique view in barycentered rotating frame where the spacecraft's path is indicated with the thick line, and the free return is indicated with the thin line, b) moon zoom in barycentered rotating frame, c) Earth-centered non-rotating frame where the moon's motion is indicated with the dashed line, and d) moon-centered non-rotating frame where the Earth's motion is indicated with the dashed line.

return case is accompanied by an increase in the round trip free return flight time of more than four days. For human missions, it is essential to ensure crew survival through the time of Earth return; thus, the decreased LOI cost may not be worth the required increase in life support supplies.

The effect of the maximum free return flight time constraint is shown in Fig. 5.14. Targeting the same LLO as in the example cases with an orientation of $(\Omega, i) = (225 \text{ deg}, 120 \text{ deg})$, T_{MAX} is reduced incrementally from 10 to six days to observe trends in LOI cost. In each case here—though not true in general—the optimal LOI sequence requires the free return to assume its maximum possible flight time. The cost increases with decreasing free return flight time for both type 1 and type 2 free returns, as shown in Fig. 5.14(a). The cost trends are similar for type 1 and type 2 free returns with type 2 free returns requiring a lower ΔV except for cases where the round trip free return flight time is greater than nine days. The incoming energy relative to the moon and the relative declination between the incoming velocity and the LLO plane are shown in Fig. 5.14(b) and Fig. 5.14(c); both quantities are computed immediately before LOI-1. Because the LLO has a fixed negative Keplerian energy relative to the moon, an increased incoming energy relative to the moon necessitates a larger ΔV to decelerate into the LLO; thus, increasing the incoming energy will increase the magnitude of LOI-1. Likewise, the larger the relative declination between the incoming velocity and the LLO plane, the larger the required plane change; therefore, increasing the relative declination will increase the magnitude of LOI-2, the maneuver responsible for a majority of the plane change. Allowing the spacecraft to begin on a non-planar free return with an

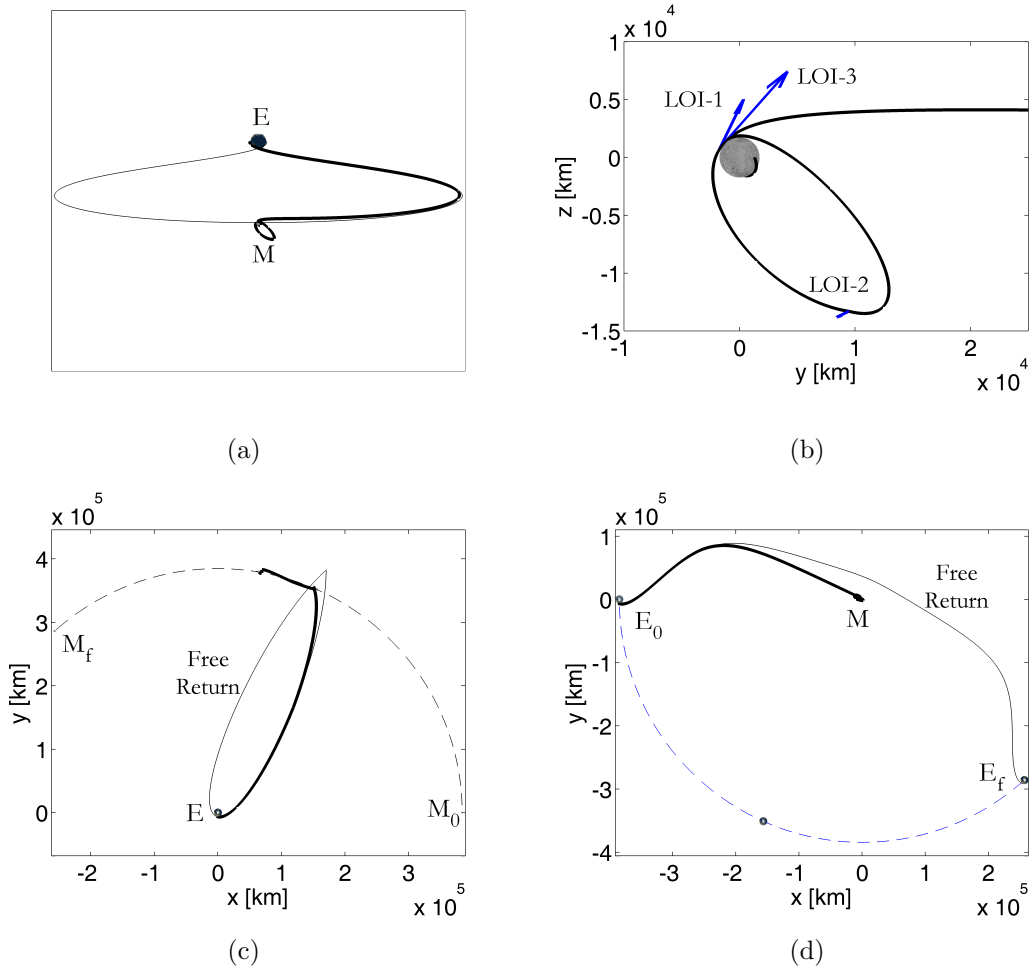


Figure 5.13: Type 2 free return and LOI into an LLO orientation of $(\Omega, i) = (225 \text{ deg}, 120 \text{ deg})$: a) oblique view in barycentered rotating frame where the spacecraft's path is indicated with the thick line, and the free return is indicated with the thin line, b) moon zoom in barycentered rotating frame, c) Earth-centered non-rotating frame where the moon's motion is indicated with the dashed line, and d) moon-centered non-rotating frame where the Earth's motion is indicated with the dashed line.

Table 5.5: Optimal parameters for variable symmetric example

Parameter	Units	Type 1	Type 2
t_R	day	1.00	1.00
t_0	day	-5.10	-5.10
t_1	day	-1.06	-1.05
t_2	day	-0.73	-0.73
t_3	day	-0.06	-0.05
Δv_{0_x}	m/s	-64	-64
Δv_{0_y}	m/s	-38	-38
Δv_{0_z}	m/s	11	-10
Δv_{1_x}	m/s	66	52
Δv_{1_y}	m/s	138	107
Δv_{1_z}	m/s	208	220
Δv_{2_x}	m/s	98	110
Δv_{2_y}	m/s	-45	-25
Δv_{2_z}	m/s	-26	-86
Δv_{3_x}	m/s	401	399
Δv_{3_y}	m/s	305	270
Δv_{3_z}	m/s	266	304
h	km	32233	32694
ϕ	deg	4.9	11.1
v	m/s	1107	1085
t_{EEI}	day	5.00	5.00

Table 5.6: Constraints for variable symmetric example

Constraint	Units	Type 1	Type 2
$x - x_0 = 0$	km	-1.2×10^{-5}	-2.9×10^{-5}
$y - y_0 = 0$	km	2.3×10^{-5}	-3.8×10^{-5}
$z - z_0 = 0$	km	1.2×10^{-5}	-3.9×10^{-5}
$v_x - v_{x_0} = 0$	m/s	1.0×10^{-8}	1.0×10^{-7}
$v_y - v_{y_0} = 0$	m/s	1.0×10^{-8}	3.0×10^{-7}
$v_z - v_{z_0} = 0$	m/s	1.0×10^{-8}	1.0×10^{-8}
$h_{EEI} - h_T = 0$	km	9.7×10^{-7}	7.4×10^{-6}
$\gamma_{EEI} - \gamma_T = 0$	deg	-6.5×10^{-8}	2.1×10^{-7}
$t_R - t_{MIN} \geq 0$	day	0.00	0.00
$t_1 - t_0 \geq 0$	day	4.05	4.05
$t_2 - t_1 \geq 0$	day	0.32	0.32
$t_3 - t_2 \geq 0$	day	0.68	0.68
$-t_3 \geq 0$	day	0.06	0.05
$t_{MAX} - (t_3 - t_1) \geq 0$	day	0.00	0.00
$h_{LOI} - h_{MIN} \geq 0$	km	-7.2×10^{-6}	4.5×10^{-8}
$h - h_{MIN} \geq 0$	km	32133	32594
$\phi_{MAX} - \phi \geq 0$	deg	3.9	78.9
$T_{MAX}/2 - t_{EEI} \geq 0$	day	0.00	0.00

increased flight time enables a lower Keplerian energy at the moon and a reduced relative declination, as compared to the type 0 case. This provides ΔV savings when initiating LOI along a type 1 or type 2 free return.

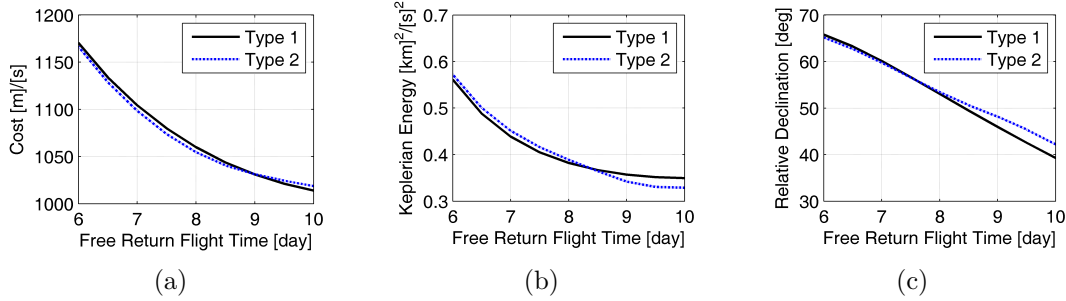


Figure 5.14: Effect of maximum free return flight time on LOI optimization for an LLO orientation of $(\Omega, i) = (225 \text{ deg}, 120 \text{ deg})$: a) LOI ΔV cost, b) incoming Keplerian energy relative to the moon, and c) relative declination.

To observe trends in the optimal LOI ΔV , transfers are optimized for all retrograde LLOs from $(\Omega, i) = (0 \text{ deg}, 90 \text{ deg})$ to $(360 \text{ deg}, 180 \text{ deg})$, both advanced in 10 deg increments for a total of 370 cases for each free return type. The ΔV contours for type 1 and type 2 free returns are shown in Figs. 5.15–5.16 where white represents an optimal transfer requiring $\Delta V \geq 1200 \text{ m/s}$, and the darkest shade represents an optimal transfer requiring $\Delta V \leq 900 \text{ m/s}$. In all cases, the osculating perilune altitude of the LOI sequence reaches the minimum of 100 km. For each LLO orientation requiring a retargeting maneuver, the time of LOI-0 backs up to the one day limit. For cases that require a plane change, the time from LOI-1 to LOI-3 is maximized at one day. In the optimal solution, the flyby altitude may be maximized, but the magnitude of the flyby angle is generally not maximized. The maximum value of $\Delta V \approx 1215 \text{ m/s}$ is required for LLOs of orientation $(0 \text{ deg},$

90 deg) and (180 deg, 90 deg), and the minimum requirement is $\Delta V \approx 860$ m/s. Hotspots of increased ΔV are centered at $\Omega \approx 0$ deg and $\Omega \approx 180$ deg, indicating that it is most difficult to enter a lunar orbit with its line of nodes coincident with the Earth-moon line. Regions of lower ΔV , regardless of inclination, observed near $\Omega = 90$ deg and $\Omega = 270$ deg, occur because the retargeting maneuver produces an incoming velocity at the moon that can enter the LLO plane with little or no plane change; achieving these LLOs may require only one LOI maneuver. These regions are also observed with type 0 free returns, but with type 1 and type 2 free returns, the regions of decreased ΔV are more expansive and are associated with transfers that are approximately 50 m/s less costly than in the minimum time free return case. Trends in the ΔV requirement are similar for type 1 and type 2 free returns with both classes offering a lower cost than the minimum time free return used previously by providing more control over the magnitude and orientation of the incoming velocity at the moon. The ΔV requirements for type 1 and type 2 free returns are always within 15 m/s with the type 1 free return offering the lower ΔV on average. All LLOs studied here can be achieved within a ΔV budget of 1220 m/s while providing one day of flight time on the outbound free return path.

5.4 Lunar Orbit Insertion from a General Free Return

The lunar orbit insertion problem using a general free return removes the symmetry requirement and, thus, allows the lunar flyby velocity orientation to be free. Therefore, a perpendicular crossing of the Earth-moon line or the vertical plane is no longer required. As observed in Chapter 3, general free returns offer a

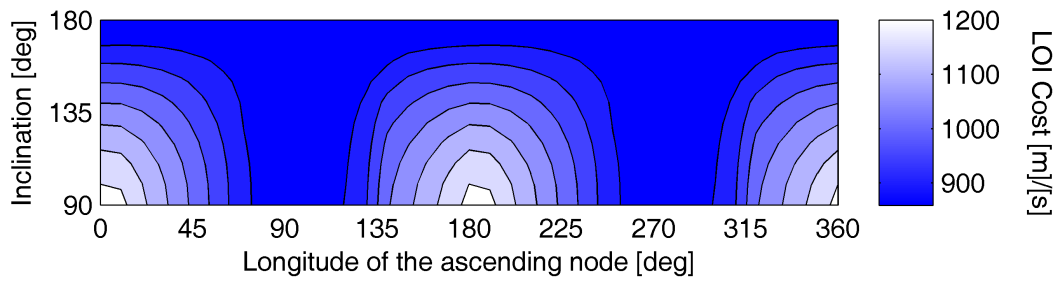


Figure 5.15: Type 1 free return LOI ΔV contours.

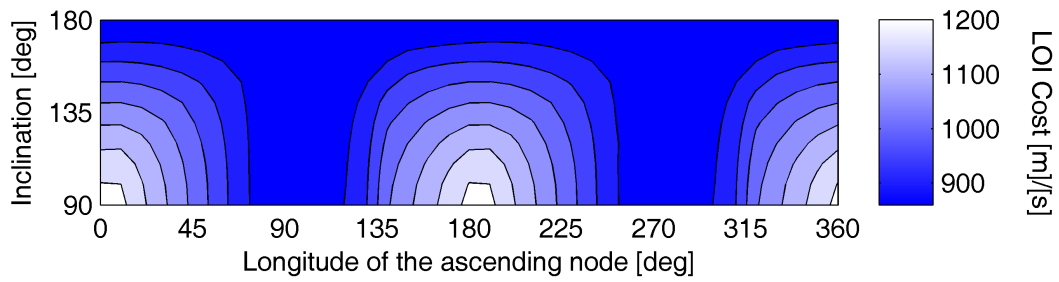


Figure 5.16: Type 2 free return LOI ΔV contours.

wide range of Earth departure, lunar passage, and Earth return conditions. The additional control over the incoming velocity at the moon provides further LOI cost savings.

5.4.1 Optimization Algorithm

Since the free return no longer must be symmetric, two free return segments are propagated from the lunar flyby point. One segment is propagated forward in time to EEI while the other segment is propagated backwards in time to TLI. The optimization variables associated with the LOI sequence are identical to the previous cases, but the parameters associated with the free return are modified. The free parameters are

$$\mathbf{x}_p \equiv [t_R \ t_0 \ t_1 \ t_2 \ t_3 \ \Delta \mathbf{v}_0^\top \ \Delta \mathbf{v}_1^\top \ \Delta \mathbf{v}_2^\top \ \Delta \mathbf{v}_3^\top \ h \ \phi \ \mathbf{v}^\top \ t_{TLI} \ t_{EEI}]_{1 \times 24}^\top \quad (5.139)$$

where t_R is the time from lunar flyby to the retargeting maneuver, and the free return flyby state is parameterized by its altitude h , latitude ϕ relative to the Earth-moon plane, and velocity \mathbf{v} ; the time from lunar flyby on the free return to EEI is t_{EEI} , and the time from lunar flyby on the free return to TLI is t_{TLI} .

The equality constraint is

$$\mathbf{c} \equiv [\mathbf{x}(t_R) - \mathbf{x}(t_0^-)]_{6 \times 1} = \mathbf{0} \quad (5.140)$$

The inequality constraints are

$$\mathbf{d} \equiv \begin{bmatrix} f(h_{TLI}) \\ f(\gamma_{TLI}) \\ f(h_{EEI}) \\ f(\gamma_{EEI}) \\ (t_R - t_{TLI}) - t_{MIN} \\ t_1 - t_0 \\ t_2 - t_1 \\ t_3 - t_2 \\ -t_3 \\ t_{MAX} - (t_3 - t_1) \\ h_{LOI} - h_{MIN} \\ h - h_{MIN} \\ T_{MAX} - (t_{EEI} - t_{TLI}) \\ -t_{TLI} \\ t_{EEI} \end{bmatrix}_{15 \times 1} \geq \mathbf{0} \quad (5.141)$$

where h_{TLI} is the altitude at TLI, γ_{TLI} is the flight path angle at TLI, h_{FR} is the osculating lunar periapsis altitude calculated at the free return flyby point, and the smooth function $f(x)$ is given by

$$f(x) \equiv (x - x_{MIN})(x_{MAX} - x) \quad (5.142)$$

where x_{MIN} and x_{MAX} give the lower and upper bounds on variable x . Now that the free return departure and approach characteristics may vary widely at the Earth due to asymmetry, a range of acceptable altitudes and flight path angles are targeted via the first four inequality constraints. The ranges are

$$300 \text{ km} \leq h_{TLI} \leq 400 \text{ km} \quad (5.143)$$

$$7 \text{ deg} \leq \gamma_{TLI} \leq 9 \text{ deg} \quad (5.144)$$

$$120 \text{ km} \leq h_{EEI} \leq 125 \text{ km} \quad (5.145)$$

$$-7 \text{ deg} \leq \gamma_{EEI} \leq -6 \text{ deg} \quad (5.146)$$

The numbers are based on Apollo mission data [52] as these are the only human lunar missions to date. To streamline constraint implementation, the eight inequalities bounding the TLI and EEI conditions, given in Eqs. (5.143)–(5.146), are reduced to four inequalities by combining each pair as $f(x) \geq 0$. Requiring a non-negative value of $f(x)$ ensures that x is within the specified bounds. This technique reduces the number of constraints and the amount of coding and computation time. The locations of TLI and EEI are free to float, but actual mission requirements on launch azimuth, return latitude and longitude, or maximum re-entry velocity, for example, will further constrain the free return geometry, perhaps increasing the LOI cost and possibly providing no feasible free return at certain epochs. However, specific constraints were not placed on these quantities because it was not desired to tie the analysis to any particular mission or launch site. The absence of the constraints allows for a larger solution space that can be reduced later if it desired to simulate a specific mission. Thus, the results obtained here should be viewed as an overview of the free return abort space that may be diminished depending on mission requirements.

5.4.2 Analytical Gradients

The derivation of the analytical gradients for the general free return problem is similar to that of the fixed and variable symmetric problems. The only significant difference is the addition of new inequality constraints that bound the altitude and flight path angle at TLI and EEI. The gradient of the first inequality constraint is

$$\frac{\partial f(h_{TLI})}{\partial \mathbf{x}_p} = \left[\mathbf{0}_{17 \times 1}^\top \quad \frac{\partial f(h_{TLI})}{\partial h} \quad \frac{\partial f(h_{TLI})}{\partial \phi} \quad \frac{\partial f(h_{TLI})}{\partial \mathbf{v}} \quad \frac{\partial f(h_{TLI})}{\partial t_{TLI}} \quad 0 \right]_{1 \times 24} \quad (5.147)$$

The gradient of $f(h_{TLI})$ with respect to h is

$$\frac{\partial f(h_{TLI})}{\partial h} = \frac{\partial f}{\partial h_{TLI}} \frac{\partial h_{TLI}}{\partial h} \quad (5.148)$$

$$= \frac{\partial f}{\partial h_{TLI}} \frac{\partial h_{TLI}}{\partial \mathbf{x}_{TLI}} \frac{\partial \mathbf{x}_{TLI}}{\partial \mathbf{x}_{FR}} \frac{\partial \mathbf{x}_{FR}}{\partial h} \quad (5.149)$$

$$= (h_{MIN_1} + h_{MAX_1} - 2h_{TLI}) \boldsymbol{\alpha}_{TLI}^\top \boldsymbol{\Phi}_{TLI} \begin{bmatrix} \cos \phi \\ 0 \\ \sin \phi \\ \mathbf{0} \end{bmatrix}_{6 \times 1} \quad (5.150)$$

where h_{MIN_1} is the minimum allowed TLI altitude, h_{MAX_1} is the maximum allowed TLI altitude, \mathbf{x}_{TLI} is the TLI spacecraft state, $\boldsymbol{\alpha}_{TLI}^\top$ is the gradient of the TLI altitude with respect to the TLI state, and $\boldsymbol{\Phi}_{TLI}$ is the state transition matrix from the lunar flyby point to TLI. The remaining nonzero gradients of the first inequality constraint are

$$\frac{\partial f(h_{TLI})}{\partial \phi} = (h_{MIN_1} + h_{MAX_1} - 2h_{TLI}) \boldsymbol{\alpha}_{TLI}^\top \boldsymbol{\Phi}_{TLI} \begin{bmatrix} -(R_M + h) \sin \phi \\ 0 \\ (R_M + h) \cos \phi \\ \mathbf{0} \end{bmatrix}_{6 \times 1} \quad (5.151)$$

$$\frac{\partial f(h_{TLI})}{\partial \mathbf{v}} = (h_{MIN_1} + h_{MAX_1} - 2h_{TLI}) \boldsymbol{\alpha}_{TLI}^\top \boldsymbol{\Phi}_{TLI} \begin{bmatrix} \mathbf{0} \\ \mathbf{I} \end{bmatrix}_{6 \times 3} \quad (5.152)$$

$$\frac{\partial f(h_{TLI})}{\partial t_{TLI}} = (h_{MIN_1} + h_{MAX_1} - 2h_{TLI}) \boldsymbol{\alpha}_{TLI}^\top \dot{\mathbf{x}}_{TLI} \quad (5.153)$$

The gradients of $f(\gamma_{TLI})$, $f(h_{EEI})$, and $f(\gamma_{EEI})$ are similar.

5.4.3 Numerical Results

The targeting and optimization procedure with a general free return is illustrated with an example that targets an LLO of orientation (225 deg, 120 deg) where the initial estimate used for this case is the same as in the fixed and variable symmetric cases. Figure 5.17 shows the optimal free return and LOI sequence,

Table 5.7 shows the initial and final values of the free parameters, and Table 5.8 shows the converged values of the constraints. The additional variability of the free return lowers the LOI cost to 951 m/s, which is a savings of about 65 m/s over the variable symmetric case and about 265 m/s over the fixed, minimum time free return case. From Fig. 5.17(a), it is clear that the free return in this case is not symmetric since the TLI to lunar flyby segment is longer than the lunar flyby to EEI segment; the duration of the TLI segment is approximately 6.4 days, and the duration of the EEI segment is approximately 3.6 days. Therefore, the round trip free return flight time is maximized at 10 days. This flight time disparity between the TLI and EEI legs is consistent with general free returns with a negative flight path angle at lunar flyby, as seen in Fig. 5.17(b) and as discussed in Chapter 3. The plane change maneuver, LOI-2, decreased to 40 m/s from approximately 250 m/s in the fixed free return case because the asymmetry allows an approach trajectory at the moon nearer to the LLO plane. The LOI-1 to LOI-3 flight time is maximized at one day, and the time from TLI to the retargeting maneuver is minimized at one day. Note in Table 5.8 that the free return flight time is maximized, but the flyby altitude has decreased to under 20000 km. The asymmetry of the free return allows increased flight time at a lower flyby altitude relative to symmetric free returns.

To assess the impact of the free return requirement, a non-free return outbound trajectory from Earth is used to optimize LOI for minimum ΔV using the same LLO geometry. The optimal transfer costs 943 m/s which indicates the free return requires approximately 10 m/s additional ΔV than the non-free return case. The penalty may grow for other LLO orientations, and the additional ΔV costs

should be weighed against the confidence of having a guaranteed trajectory back to Earth with the free return.

Figure 5.18 shows the LOI cost contours as a function of LLO orientation. The trend is similar to the variable symmetric case, but the LOI cost using a general free return is, on average, 16 m/s cheaper than a type 1 free return and 19 m/s cheaper than a type 2 free return. The maximum ΔV requirement using a general free return is 1190 m/s to achieve an LLO of orientation (0 deg, 90 deg); the minimum requirement is 860 m/s, which is necessary for any LLO with $i = 180$ deg.

These results show that removing the symmetry requirement decreases the ΔV cost of the mission. Allowing the free return to vary during optimization, however, for both symmetric and asymmetric cases, incurred an increased round trip free return flight time. Also, when the free return became non-planar, certain cases required a polar or near-polar Earth departure azimuth, which may not be feasible depending on the launch site location. Thus, an appropriate free return for a given mission must satisfy both launch and return requirements and not exceed the maximum flight time capability of the spacecraft.

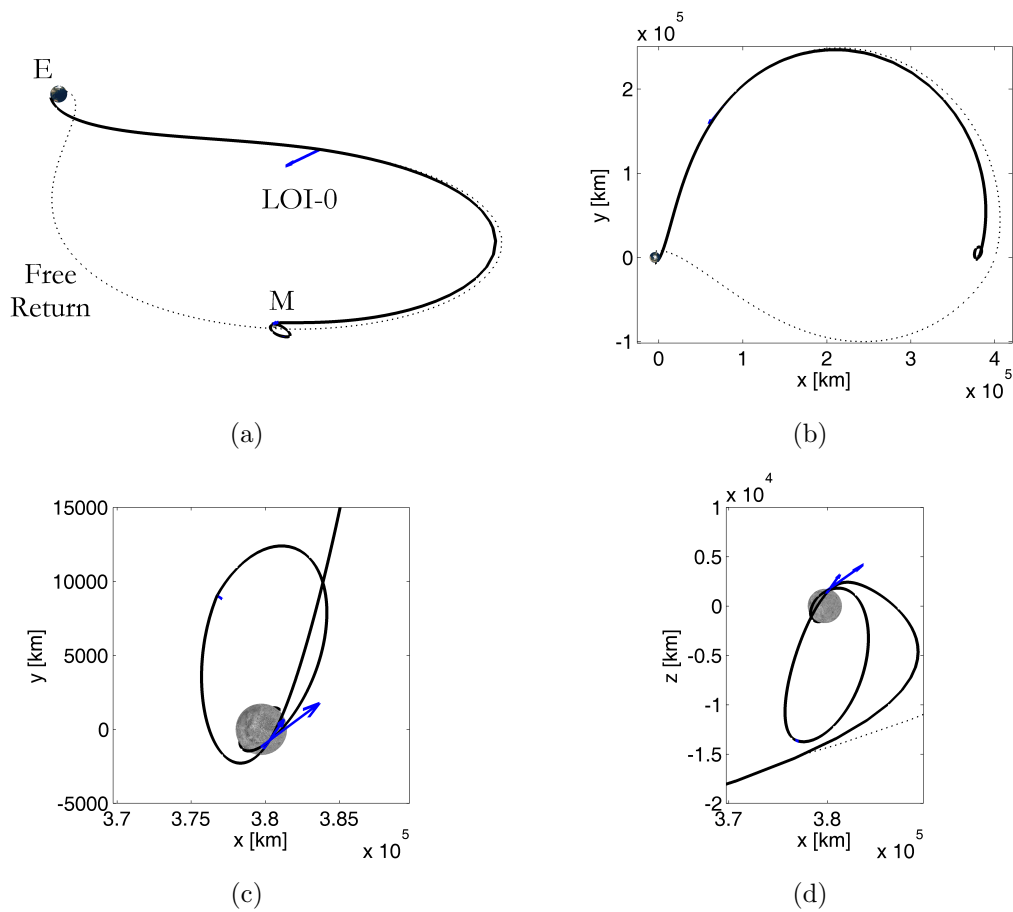


Figure 5.17: General free return and LOI into an LLO orientation of $(\Omega, i) = (225 \text{ deg}, 120 \text{ deg})$ in barycentered rotating frame: a) oblique view, b) $\hat{x}\hat{y}$ plane view, c) $\hat{x}\hat{y}$ plane view at moon, and d) $\hat{x}\hat{z}$ plane view at moon.

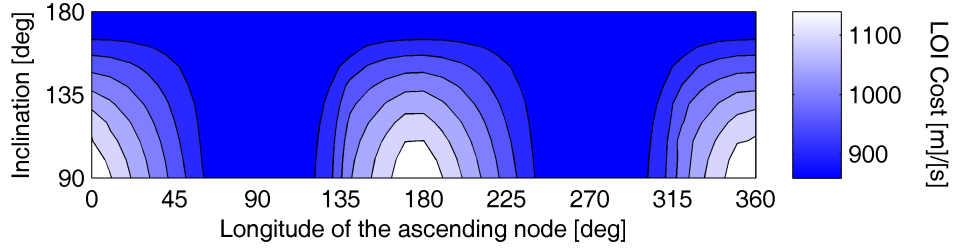


Figure 5.18: LOI cost contours with general free return formulation.

Table 5.7: Free parameters for general free return example case

Parameter	Units	Initial	Optimal
t_R	s	-52068	-469321
t_0	s	-101715	-559984
t_1	s	-50314	-91128
t_2	s	-27510	-61492
t_3	s	-7073	-4728
Δv_{0_x}	km/s	0.000	-0.017
Δv_{0_y}	km/s	0.000	-0.021
Δv_{0_z}	km/s	0.000	-0.018
Δv_{1_x}	km/s	0.226	0.136
Δv_{1_y}	km/s	0.785	0.200
Δv_{1_z}	km/s	0.000	0.192
Δv_{2_x}	km/s	0.186	0.032
Δv_{2_y}	km/s	-0.186	-0.020
Δv_{2_z}	km/s	-0.338	-0.014
Δv_{3_x}	km/s	-0.173	0.397
Δv_{3_y}	km/s	0.173	0.296
Δv_{3_z}	km/s	-0.424	0.280
h	km	100	19885
ϕ	deg	0.0	19.8
v_x	km/s	0.000	-0.374
v_y	km/s	-2.563	-1.160
v_z	km/s	0.000	0.122
t_{TLI}	s	-247044	-555721
t_{EEI}	s	247044	308279

Table 5.8: Constraints for general free return example case targeting an LLO orientation of $(\Omega, i) = (225 \text{ deg}, 120 \text{ deg})$

Constraint	Units	Value
$x - x_0 = 0$	km	-6.9×10^{-5}
$y - y_0 = 0$	km	-1.8×10^{-4}
$z - z_0 = 0$	km	-1.3×10^{-4}
$v_x - v_{x_0} = 0$	m/s	-1.0×10^{-10}
$v_y - v_{y_0} = 0$	m/s	1.1×10^{-9}
$v_z - v_{z_0} = 0$	m/s	-4.0×10^{-10}
$f(h_{TLI}) \geq 0$	km ²	-1.8×10^{-4}
$f(\gamma_{TLI}) \geq 0$	deg ²	2.1×10^{-9}
$f(h_{EEI}) \geq 0$	km ²	-1.5×10^{-5}
$f(\gamma_{EEI}) \geq 0$	deg ²	1.3×10^{-9}
$(t_R - t_{TLI}) - t_{MIN} \geq 0$	day	0.00
$t_1 - t_0 \geq 0$	day	5.43
$t_2 - t_1 \geq 0$	day	0.34
$t_3 - t_2 \geq 0$	day	0.66
$-t_3 \geq 0$	day	0.05
$t_{MAX} - (t_3 - t_1) \geq 0$	day	0.00
$h_{LOI} - h_{MIN} \geq 0$	km	1.5×10^{-6}
$h - h_{MIN} \geq 0$	km	18865
$T_{MAX} - (t_{EEI} - t_{TLI}) \geq 0$	day	0.00
$-t_{TLI} \geq 0$	day	6.43
$t_{EEI} \geq 0$	day	3.57

Chapter 6

Lunar Orbit Insertion from a Free Return in the Four-Body Model

The previous optimal lunar orbit insertion (LOI) results were presented in the circular restricted three-body problem (CRTBP) and, thus, are not valid in the actual Earth-moon system. The simplified model ignored the eccentricity of the moon's orbit, solar gravity, and the nonspherical Earth. Additionally, the simplified model assumed the spacecraft had the ability to instantaneously change its velocity even though this change requires a finite amount of time. In this chapter, the physical system is modeled more realistically by adding solar gravity to the equations of motion and computing celestial geometry with an accurate ephemeris. The effects of solar radiation pressure and the nonspherical Earth are also considered. Finally, the spacecraft's propulsion system is modeled with both linearly steered and optimal control finite thrust engines.

6.1 Lunar Orbit Insertion with an Impulsive Engine Model

The spacecraft engine is initially assumed to be capable of producing infinite thrust; thus, the spacecraft's velocity may change instantly. The force field used for both the impulsive and finite burn algorithms is the four-body model that includes

the gravity of the spherical Earth, moon, and sun. The spacecraft acceleration in the moon-centered frame is given by Eq. (2.18). This non-rotating J2000 frame is used to integrate all LOI segments, and the free return segments are integrated in the non-rotating J2000 Earth-centered frame. Recall that the fundamental plane is the Earth’s equator at the J2000 epoch with $\hat{\mathbf{z}}$ axis normal to the equator and positive in the direction of the north pole. The principal direction along the positive $\hat{\mathbf{x}}$ axis points to the vernal equinox at the J2000 epoch. The $\hat{\mathbf{y}}$ axis completes the right-handed system. Celestial data are accessed with the planetary and lunar ephemeris DE 421 [48].

6.1.1 Numerical Algorithm

The spacecraft departs Earth on a free return trajectory and subsequently achieves an orbit about the moon of specified orientation. As in the CRTBP, the performance metric chosen to be minimized is the sum of the magnitudes of the four impulsive maneuvers. The cost function is

$$J \equiv \sum_{i=0}^3 \Delta v_i \quad (6.1)$$

where Δv_i is the magnitude of the i th maneuver. The time, magnitude, and direction of each maneuver are free to vary during optimization. The ballistic free return state at lunar passage is also free, along with the times of translunar injection (TLI) and Earth entry interface (EEI). The free parameters are given by

$$\mathbf{x}_p \equiv [t_R \ t_0 \ \cdots \ t_4 \ \Delta \mathbf{v}_0^\top \ \cdots \ \Delta \mathbf{v}_3^\top \ h \ \phi \ \mathbf{v}^\top \ t_{TLI} \ t_{EEI}]_{1 \times 25}^\top \quad (6.2)$$

where t_4 is the epoch along the low lunar orbit (LLO). This time was arbitrary in the CRTBP; however, in the ephemeris model, t_4 is a free parameter that affects the planetary geometry.

Twenty two constraints placed on the optimization process ensure a feasible transfer trajectory and target conditions consistent with a real-world lunar mission. The equality constraints require state and time continuity at the patch point, which joins the free return segment with the LOI segment. The equality constraints are

$$\mathbf{c} \equiv \begin{bmatrix} \mathbf{x}_R - \mathbf{x}_0^- \\ t_R - t_0 \end{bmatrix}_{7 \times 1} = \mathbf{0} \quad (6.3)$$

The inequality constraints are

$$\mathbf{d} \equiv \begin{bmatrix} f(h_{TLI}) \\ f(\gamma_{TLI}) \\ f(h_{EEI}) \\ f(\gamma_{EEI}) \\ (t_R - t_{TLI}) - t_{MIN} \\ t_1 - t_0 \\ t_2 - t_1 \\ t_3 - t_2 \\ t_4 - t_3 \\ t_{MAX} - (t_3 - t_1) \\ h_{LOI} - h_{MIN} \\ h_{FR} - h_{MIN} \\ T_{MAX} - (t_{EEI} - t_{TLI}) \\ t_{FR} - t_{TLI} \\ t_{EEI} - t_{FR} \end{bmatrix}_{15 \times 1} \geq \mathbf{0} \quad (6.4)$$

The first four inequality constraints allow the TLI and EEI locations to float but dictate acceptable ranges for the TLI and EEI altitudes and flight path angles. The ranges, given in Eq. (5.143)–Eq. (5.146), are the same as in the general free return case in the CRTBP. Again, actual mission requirements on launch azimuth or return

latitude and longitude, for example, will further constrain the free return geometry, perhaps increasing the LOI cost and possibly providing no feasible free return at certain epochs. The remaining constraints require: that the spacecraft remain on the outbound free return path at least one day after TLI; that the maximum time between the first and third LOI maneuvers is one day; that the minimum altitude at the moon is 100 km; and that the maximum free return flight time is 10 days.

6.1.2 Initial Estimate

The initial estimate of the parameter vector is constructed from the previously converged optimal general free return solution in the CRTBP. In that model, the spacecraft is assumed to be of negligible mass, the moon's orbit is assumed to be circular, and all perturbations other than gravity from a spherical Earth and moon are ignored. To transition from the CRTBP, the unit vectors of a reference frame rotating with the Earth-moon line are defined by

$$\hat{\mathbf{r}}(t) \equiv \frac{\mathbf{r}_M(t)}{r_M(t)} \quad \hat{\mathbf{t}}(t) \equiv \hat{\mathbf{n}}(t) \times \hat{\mathbf{r}}(t) \quad \hat{\mathbf{n}}(t) \equiv \frac{\mathbf{r}_M(t) \times \mathbf{v}_M(t)}{|\mathbf{r}_M(t) \times \mathbf{v}_M(t)|} \quad (6.5)$$

where $\mathbf{r}_M(t)$ and $\mathbf{v}_M(t)$ are the lunar position and velocity relative to Earth at time t . The moon's instantaneous orbital plane about the Earth, called the Earth-moon plane, is the plane spanned by $\hat{\mathbf{r}}$ and $\hat{\mathbf{t}}$, and the vertical plane is defined as the plane spanned by $\hat{\mathbf{r}}$ and $\hat{\mathbf{n}}$. The vector $\hat{\mathbf{t}}$ is not parallel to \mathbf{v}_M unless the moon is at apogee or perigee. Since the moon's position and velocity vectors are not always perpendicular, there will be a discrepancy between the $\hat{\mathbf{r}}\hat{\mathbf{t}}\hat{\mathbf{n}}$ axes and the idealized CRTBP axes.

After propagation in the ephemeris model, the initial estimate produces trajectories that are discontinuous at the patch point due to the solar perturbation and the non-circular lunar orbit. Figure 6.1 shows contours of the position error at the patch point as a function of LLO orientation where the longitude of the ascending node is measured relative to the Earth-moon line and the inclination is measured relative to the Earth-moon plane. The average discontinuity is 14900 km; elevated values seen between longitudes of 0 deg and 90 deg and between 180 deg and 270 deg occur when the LOI plane change is large and the round trip free return flight time is at or near its maximum. These conditions lead to larger dispersions because of an increased propagation time in the perturbed gravitational field. The maximum position error is 62000 km, but this maximum is within the convergence envelope of the optimization algorithm.

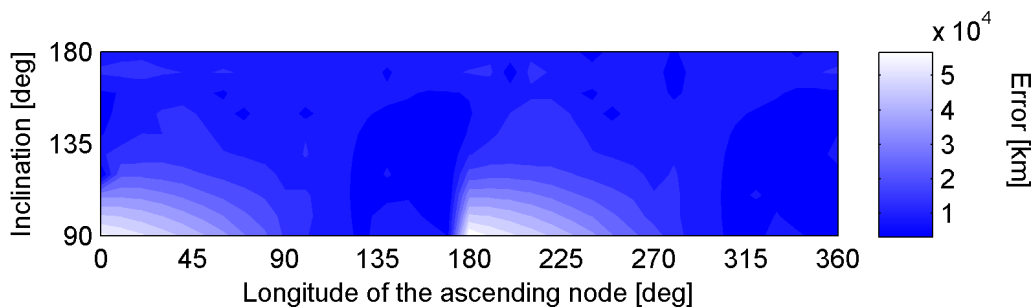


Figure 6.1: Initial estimate position error at patch point as a function of LLO orientation.

6.1.3 Free Return Targeting Strategy

The spacecraft's trajectory along the free return is hyperbolic with respect to the moon, and the hyperbolic path must intersect the vertical plane. This vertical plane passage occurs on the far side of the moon relative to the Earth for a circumlunar free return. The point of vertical plane passage is fixed at a time called the free return epoch (FRE) which is nominally chosen to be 6:00 AM, Dec. 31, 2024, a time when the moon is near its maximum inclination relative to the Earth's equator and when the Earth-moon distance is near its average value of 384400 km. The state at the FRE is free in the optimization process and is parameterized by its altitude, latitude relative to the Earth-moon plane, and velocity. Though the state here is free, it must have an osculating lunar periapsis altitude greater than or equal to 100 km.

The free return is constructed with a multiple shooting strategy from the moon to the Earth. The TLI segment is propagated backwards in time, targeting an altitude and flight path angle at Earth within the specified bounds. The EEI segment is propagated forward in time to target the EEI conditions at Earth. The free return epoch state calculated from the CRTBP model provides an adequate initial estimate for a feasible circumlunar free return in the ephemeris model.

6.1.4 Analytical Gradients

All gradients are derived analytically to reduce computation time and to avoid the problems associated with finite differencing due to the sensitivity of the problem. The decreased runtime comes at the cost of increased derivation and im-

plementation time. Where necessary, linear perturbation theory is used to compute the partial derivatives of the spacecraft state at one time with respect to the state at another time with the state transition matrix (STM) as shown in Chapter 4. The speedup factor observed with STM-based derivatives relative to central differences for the present problem is about 11, which is greater than the speedup observed in the CRTBP algorithm. The majority of the gradient derivations are similar to those presented in Chapter 5, so they are omitted; however, the gradients with respect to t_4 , the LLO ascending node time, are shown here.

The position and velocity at t_4 in the moon-centered J2000 frame are

$$\mathbf{r}_4 = \mathbf{R}\mathbf{r}_4^{rtn} \quad (6.6)$$

$$\mathbf{v}_4 = \mathbf{R}\mathbf{v}_4^{rtn} \quad (6.7)$$

where the superscript rtn indicates a quantity in the $\hat{\mathbf{r}}\hat{\mathbf{t}}\hat{\mathbf{n}}$ frame, and the transformation matrix \mathbf{R} from the rotating $\hat{\mathbf{r}}\hat{\mathbf{t}}\hat{\mathbf{n}}$ frame to the non-rotating frame is

$$\mathbf{R}(t) = \begin{bmatrix} \hat{\mathbf{r}}(t) & \hat{\mathbf{t}}(t) & \hat{\mathbf{n}}(t) \end{bmatrix}_{3 \times 3} \quad (6.8)$$

Thus, the spacecraft state at t_4 is

$$\mathbf{x}_4 = \mathbf{K}\mathbf{x}_4^{rtn} \quad (6.9)$$

where

$$\mathbf{K} \equiv \begin{bmatrix} \mathbf{R} & \mathbf{0} \\ \mathbf{0} & \mathbf{R} \end{bmatrix}_{6 \times 6} \quad (6.10)$$

The total differential at t_4 is

$$d\mathbf{x}_4 = \frac{\partial \mathbf{x}_4}{\partial t_4} dt_4 \quad (6.11)$$

$$= \frac{\partial}{\partial t_4} (\mathbf{K} \mathbf{x}_4^{rtn}) dt_4 \quad (6.12)$$

$$= \dot{\mathbf{K}} \mathbf{x}_4^{rtn} dt_4 \quad (6.13)$$

where $\dot{\mathbf{x}}_4^{rtn} = \mathbf{0}$ since \mathbf{x}_4^{rtn} is constant in the rotating frame, and

$$\dot{\mathbf{K}} = \begin{bmatrix} \dot{\mathbf{R}} & \mathbf{0} \\ \mathbf{0} & \dot{\mathbf{R}} \end{bmatrix} \quad (6.14)$$

The time derivative of the transformation matrix is

$$\dot{\mathbf{R}} = \begin{bmatrix} \dot{\hat{\mathbf{r}}} & \dot{\hat{\mathbf{t}}} & \dot{\hat{\mathbf{n}}} \end{bmatrix} \quad (6.15)$$

where

$$\dot{\hat{\mathbf{r}}} = \frac{\mathbf{v}_M}{r_M} - \frac{\mathbf{r}_M^\top \mathbf{v}_M}{r_M^3} \mathbf{r}_M \quad (6.16)$$

$$\dot{\hat{\mathbf{t}}} = \dot{\hat{\mathbf{n}}} \times \hat{\mathbf{r}} + \hat{\mathbf{n}} \times \dot{\hat{\mathbf{r}}} \quad (6.17)$$

$$\dot{\hat{\mathbf{n}}} = \dot{\hat{\mathbf{r}}} \times \hat{\mathbf{v}}_M + \hat{\mathbf{r}} \times \left[\frac{\mathbf{g}_M}{v_M} - \frac{\mathbf{v}_M^\top \mathbf{g}_M}{v_M^3} \mathbf{v}_M \right] \quad (6.18)$$

The lunar acceleration \mathbf{g}_M is calculated by finite differencing the ephemeris-tabulated lunar velocity. The time-fixed differential at t_4 is

$$\delta \mathbf{x}_4 = d\mathbf{x}_4 - \dot{\mathbf{x}}_4 dt_4 \quad (6.19)$$

$$= \left(\dot{\mathbf{K}} \mathbf{x}_4^{rtn} - \dot{\mathbf{x}}_4^{ijk} \right) dt_4 \quad (6.20)$$

Thus,

$$\frac{\partial (\mathbf{x}_R - \mathbf{x}_0^-)}{\partial t_4} = -\Phi(t_0, t_1) \Phi(t_1, t_2) \Phi(t_2, t_3) \Phi(t_3, t_4) \left(\dot{\mathbf{K}} \mathbf{x}_4^{rtn} - \dot{\mathbf{x}}_4^{ijk} \right) \quad (6.21)$$

The main point here is that since the CRTBP is an autonomous system, the mission times are arbitrary; only the elapsed time between mission events is relevant. In the ephemeris model, changing the time at which the spacecraft arrives in the LLO changes the relative geometry of the Earth, moon, and sun. Thus, the gradient given by Eq. (6.21) is nonzero since the LLO epoch time affects the geometry of the integrated trajectory.

6.1.5 Numerical Results

To study the free return abort cost of missions targeting different orbits at the moon, the orientation of the LLO is parametrically varied in its longitude of the ascending node Ω and its inclination i . The longitude is measured in the Earth-moon plane relative to the moon-Earth line ($-\hat{r}$), and the inclination is measured relative to the Earth-moon plane. Each LLO is retrograde relative to the \hat{n} axis and circular with an altitude of 100 km. After the LLO orientation is set, the optimizer iterates

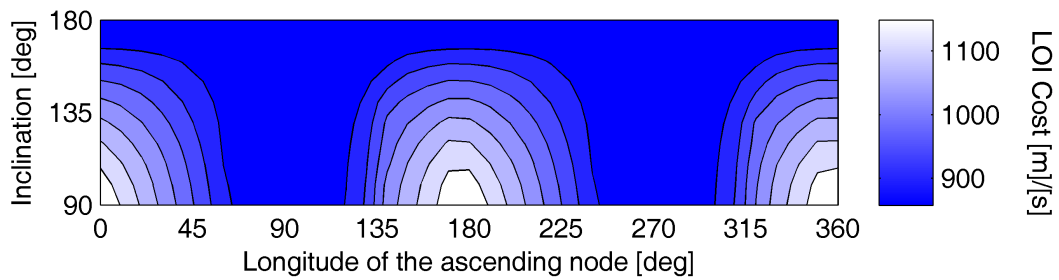


Figure 6.2: Minimum hybrid mission LOI cost contours as a function of LLO orientation with an impulsive engine model.

on the free parameters to minimize the cost and satisfy the constraints. The ΔV cost of the optimal LOI sequences for the full range of LLOs is shown in Figure 6.2. The average absolute difference between corresponding optimal LOI sequences in the ephemeris model and in the CRTBP is 1.56 m/s. The maximum LOI cost of 1190 m/s occurs at an LLO orientation of $(\Omega, i) = (0 \text{ deg}, 90 \text{ deg})$. This orientation indicates the LLO is normal to the Earth-moon plane and the LLO ascending node is on the Earth-moon line between the Earth and moon. The minimum LOI cost of 858 m/s occurs when the LLO has an inclination of 180 deg, indicating the LLO is in the Earth-moon plane.

The optimal free return trajectory and LOI sequence for the maximum cost LOI case are shown in Fig. 6.3; additional views of the mission are shown in Fig. 6.5. The round trip free return time is maximized at 10 days, and the time between LOI-1 and LOI-3 is maximized at one day to maximize the radius of the plane change maneuver. A plane change is necessary in this case because the angle between the velocity immediately before LOI-1 and the LLO plane is nearly 70 deg. The retargeting maneuver (LOI-0) has a magnitude of 30 m/s. The free return and LOI sequence associated with the minimum ΔV case are shown in Figure 6.4; additional views are shown in Fig. 6.6. The free return has a flight time of approximately 8 days and remains near the moon's orbital plane about the Earth, indicated by zero latitude at the FRE. An apparent one-burn sequence is used for LOI since the trajectory approaches the moon in the LLO plane. The retargeting maneuver magnitude is 32 m/s.

One predictor of the cost of entering a particular orbit about the moon is the relative declination between the incoming velocity and the LLO plane. The relative declination is computed by determining the angle between the angular momentum immediately before LOI-1 and the angular momentum at the LLO ascending node. Consider the range of LLOs with inclination $i = 90$ deg; the ΔV cost of the optimal LOI sequence and the relative declination are shown in Figure 6.7. Where the relative declination is minimized near $\Omega = 90$ deg and $\Omega = 270$ deg, the LOI cost is also minimized. This geometry allows the spacecraft to enter the desired lunar orbit with fewer than three maneuvers. Though the algorithm does not allow maneuvers and segments to be removed, the optimizer is free to decrease any maneuver's magnitude to zero; this occurs for all cases with a relative declination below 4 deg. The free return and LOI geometry are adjusted to reduce the relative declination and consequently decrease the magnitude of the plane change maneuver. Where the relative declination is above 7 deg, a three-burn sequence minimizes the ΔV necessary to enter lunar orbit. It is difficult to predict how many maneuvers will minimize the LOI cost at a declination of 5 ± 2 deg because cases in this range are observed to utilize one-, two-, and three-burn sequences. To determine the minimum, it may be necessary to calculate each and directly compare the LOI cost. Operational considerations may also be a factor in determining the number of maneuvers. Though a three-burn sequence may save ΔV , it may be desired to ignite the engine fewer times. On the other hand, it may be desired to perform more than one maneuver if errors in a single maneuver are likely to produce a trajectory that has an unacceptably low or subsurface perilune altitude. This was the rationale behind using two

maneuvers in the Apollo program. Even though less than 10 deg of plane change was necessary and could be accomplished in one burn, potential errors in a single maneuver were deemed to be undesirable. Some cases in this dissertation also utilize a two-burn sequence where loiter time is used to produce a small plane change.

Next, consider the TLI to LLO flight time for $i = 90$ deg as shown in Figure 6.8. Observing the cost variation only, it is not obvious that the free return geometry of the minimum impulse solution fundamentally changes between $\Omega = 170$ deg and $\Omega = 180$ deg, transitioning from a “short” free return (round trip flight time less than 10 days) to a “long” free return (round trip flight time of 10 days). The short free return is shown in Figure 6.9(a) and the long free return is shown in Figure 6.9(b). The change in free return geometry from the short to the long solution is indicated by a jump of approximately 3.5 days in TLI to LLO flight time between $\Omega = 170$ deg and $\Omega = 180$ deg as seen in Figure 6.8. At both longitudes, there are actually two local minima: a short free return and a long free return. This is seen in Figure 6.10 where the free return time is varied from 5.7 days to 10 days. The long solution represents the on-boundary minimum, and it requires more ΔV than the short solution at a longitude of 170 deg. The on-boundary minimum, however, becomes the global minimum in the solution space at 180 deg. This causes the 3.5 day flight time increase between $\Omega = 170$ deg and $\Omega = 180$ deg, and the same jump is observed between $\Omega = 350$ deg and $\Omega = 360$ deg. The decreasing flight time between $\Omega = 70$ deg and $\Omega = 130$ deg is due to the decreasing free return flight time and the decreasing LOI flight time as the LOI sequence transitions from a three-burn through a two-burn to a one-burn sequence. Though the spacecraft departs

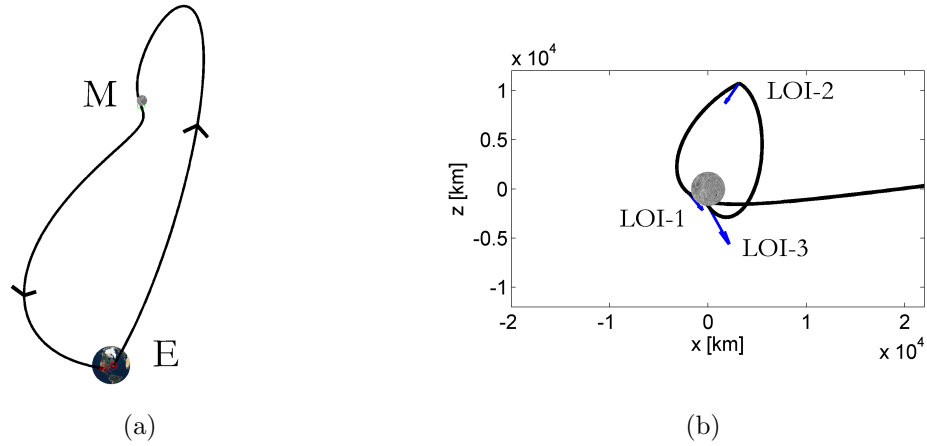


Figure 6.3: Hybrid trajectory for the maximum ΔV requirement necessary to achieve an LLO of orientation (0 deg, 90 deg): a) Free return without LOI segments, in Earth-centered non-rotating frame, and b) LOI sequence in moon-centered non-rotating frame.

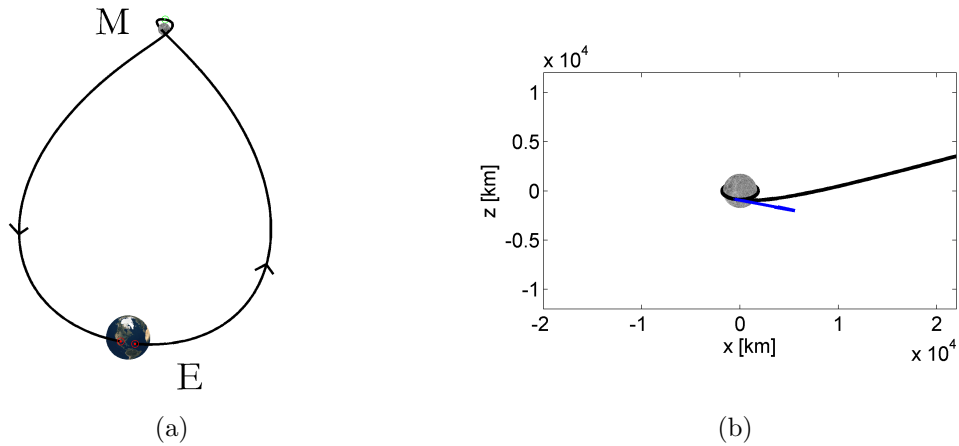


Figure 6.4: Hybrid trajectory for the minimum ΔV requirement necessary to achieve an LLO of orientation (90 deg, 180 deg): a) Free return without LOI segments, in Earth-centered non-rotating frame, and b) LOI sequence in moon-centered non-rotating frame.

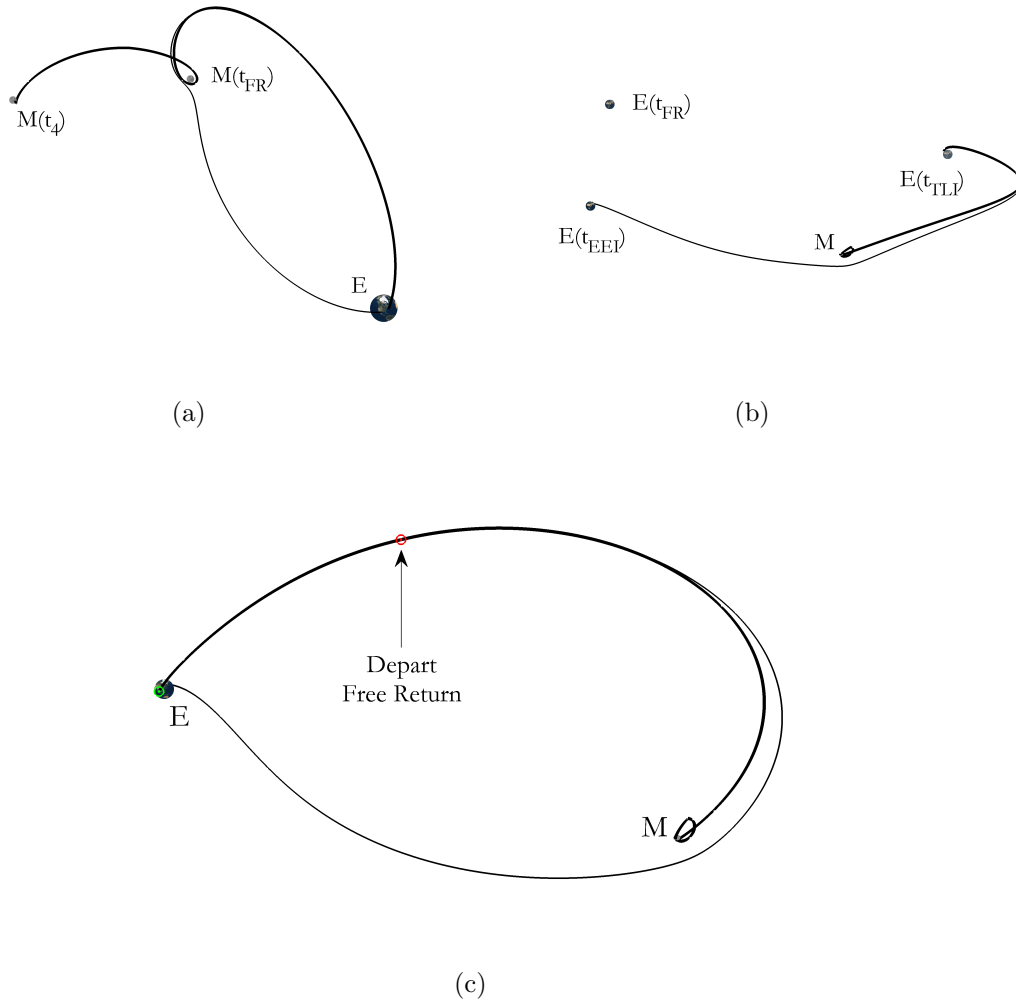


Figure 6.5: Additional views for the maximum cost hybrid trajectory: a) Earth-centered non-rotating frame, b) moon-centered non-rotating frame, and c) Earth-centered rotating-pulsating frame.

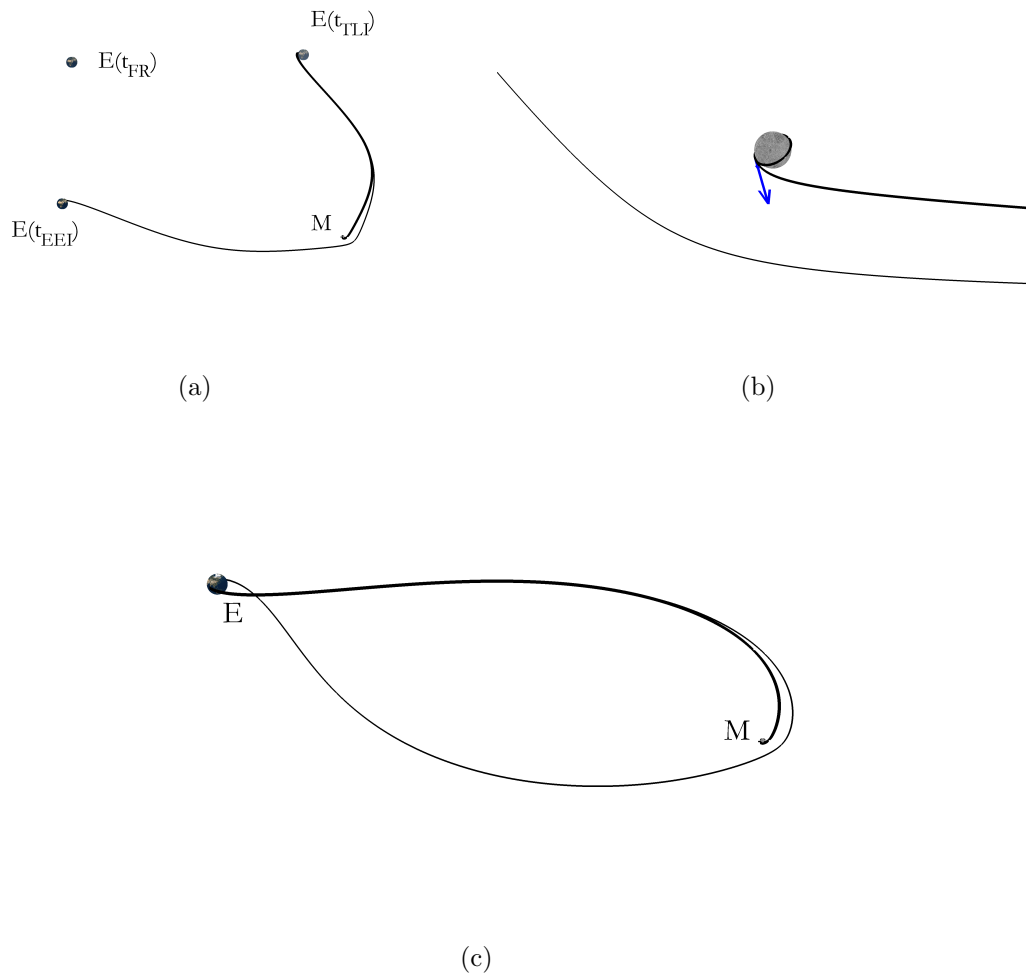


Figure 6.6: Additional views for the minimum cost hybrid trajectory: a) moon-centered non-rotating frame, b) LOI zoom in moon-centered non-rotating frame, and c) Earth-centered rotating-pulsating frame.

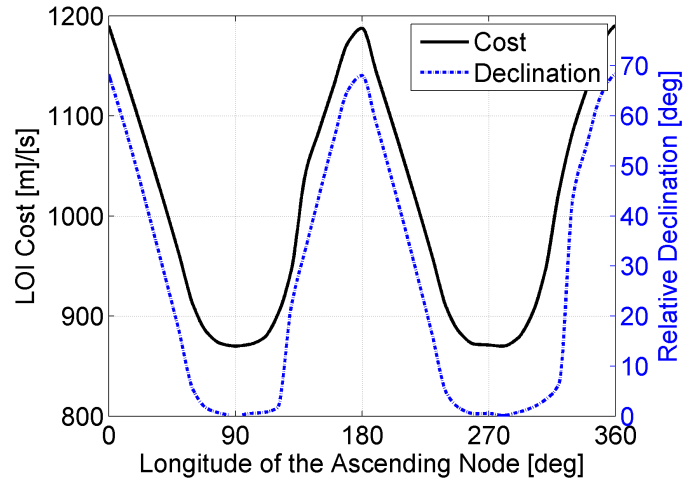


Figure 6.7: LOI cost and relative declination for LLOs at an inclination of 90 deg.

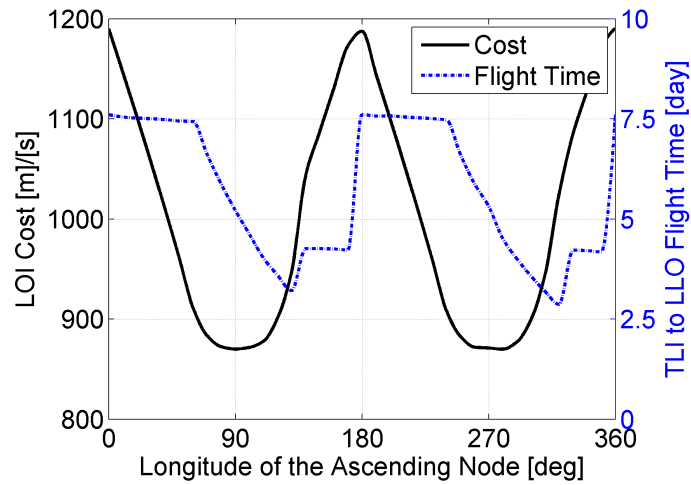


Figure 6.8: LOI cost and flight time for LLOs at an inclination of 90 deg.

both short and long free returns after one day, the retargeting maneuver magnitude is small enough that the pre-maneuver state is a significant factor in determining the flight time required to reach the moon.

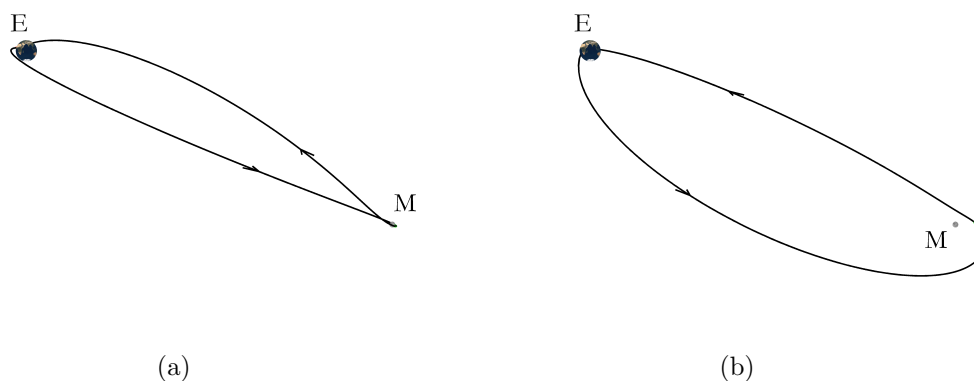


Figure 6.9: Free return types: a) “short” free return solution for an LLO orientation of (170 deg, 90 deg), and b) “long” free return solution for an LLO orientation of (180 deg, 90 deg).

An increase in flight time of approximately one day is observed in Figure 6.8 between $\Omega = 130$ deg and $\Omega = 140$ deg. This occurs because the minimum impulse solution is a one-burn LOI sequence at $\Omega = 130$ deg while the minimum impulse solution is a three-burn LOI sequence at $\Omega = 140$ deg. The relative declination is greater than 30 deg at $\Omega = 140$ deg, indicating three maneuvers are optimal for orbit insertion. To decrease the plane change cost, the radius of $\Delta\mathbf{v}_2$ increases until the time between LOI-1 and LOI-3 is maximized at one day as imposed by the inequality constraint. This also accounts for the increased flight time between $\Omega = 320$ deg and $\Omega = 330$ deg.

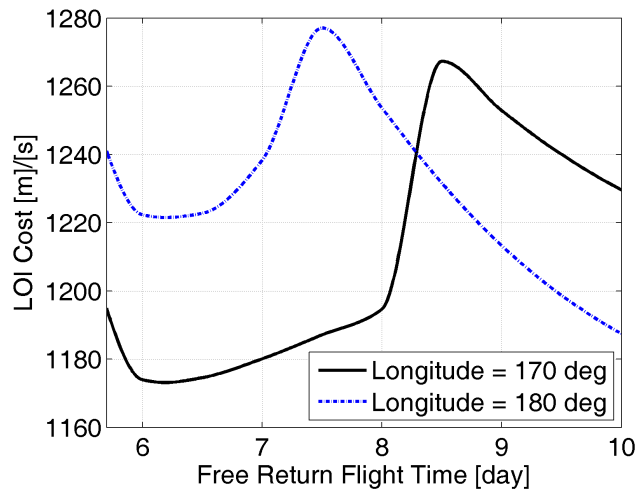


Figure 6.10: LOI cost as a function of free return flight time for LLO longitudes of 170 deg and 180 deg at an inclination of 90 deg.

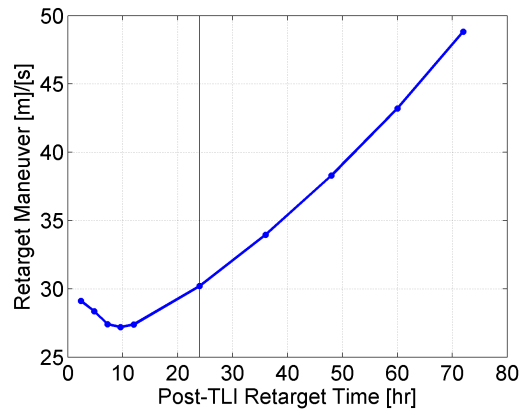


Figure 6.11: Retargeting maneuver magnitude as a function of the time after TLI for an LLO of orientation (180 deg, 90 deg).

For every case presented, the retargeting maneuver is performed one day after TLI. This limit was imposed in the optimization process to ensure the spacecraft remained on the free return to provide an abort option for this minimum amount of time. As was observed in the CRTBP, the time of the retargeting maneuver decreased to this boundary during LOI cost minimization, suggesting that the maneuver's magnitude decreases as it moves closer to TLI. To investigate this trend, the retargeting time is varied from 0.1 days to 3 days after TLI and the hybrid trajectory is reoptimized. Figure 6.11 shows the cost of the retargeting maneuver as a function of its activation time past TLI for an LLO orientation of (180 deg, 90 deg). The default post-TLI retargeting time of one day is indicated at 24 hrs giving a retargeting cost of approximately 30 m/s. Past one day, the retargeting cost rises at a rate of approximately 10 m/s/day. As expected, the magnitude of LOI-0 decreases as it approaches TLI; however, the magnitude is minimized near 10 hrs and increases as it approaches TLI past that point. At 10 hrs after TLI on this free return, the spacecraft is 115000 km from Earth.

6.1.6 Algorithm Extensions

In this subsection, the impulsive, four-body algorithm is extended to examine the effects of variable mission epoch, an upgraded force model including J_2 effects and solar radiation pressure, and an alternate objective function which seeks to maximize the time spent on the free return while simultaneously minimizing the LOI cost.

6.1.6.1 Epoch Variation

The FRE was initially chosen to be 6:00 AM, Dec. 31, 2024, but the algorithm accommodates any mission epoch. In the CRTBP, the Earth-moon distance was taken as 384400 km, but this distance actually fluctuates between approximately 357000 km and 407000 km. As shown in Chapter 2, when the mass ratio of the primaries is constant but the inter-primary distance is changed, an equivalent trajectory in one system can be attained through a dilation of a corresponding trajectory in the other system. After the epoch is selected for a given mission, the converged parameters from the CRTBP are scaled through the method outlined in Chapter 2, where the ratios of distance units, time units, and velocity units are

$$\frac{DU_2}{DU_1} = \frac{r_{EM}(t_2)}{r_{EM}(t_1)} \quad \frac{TU_2}{TU_1} = \left(\frac{r_{EM}(t_2)}{r_{EM}(t_1)} \right)^{\frac{3}{2}} \quad \frac{VU_2}{VU_1} = \sqrt{\frac{r_{EM}(t_1)}{r_{EM}(t_2)}} \quad (6.22)$$

One problem with this approach is that the radius of the moon does not scale with the Earth-moon distance, so neither does the LLO with a fixed altitude of 100 km. An effective strategy to avoid this problem was implemented where the free parameters associated with LOI-1, LOI-2, and LOI-3 are not scaled with the Earth-moon distance, but all other parameters are. Because of the proximity of the LOI sequence to the moon, these trajectories behave more as Keplerian orbits and are not as sensitive to Earth's gravitational perturbation. It was found that this technique ensured the free return and LOI sequence were within the convergence envelope of the optimization algorithm for all cases studied.

To examine the change in the LOI cost when the epoch is varied, 25 free return epochs are chosen randomly between Jan. 1, 2020 and Jan. 1, 2030, and

the hybrid sequence is optimized for insertion into an LLO of orientation (225 deg, 120 deg). Figure 6.12 shows the variation in the minimum LOI cost as a function of the free return flyby time and the Earth-moon distance. The minimum cost is 950 m/s, which occurs on Mar. 4, 2028; the maximum cost is 965 m/s, which occurs on Feb. 24, 2028; and the average LOI cost is 957 m/s. LOI cost, however, is not the only consideration in selecting the mission date. Also necessary to consider are launch site conditions, the timing of solar storms, and return site conditions.

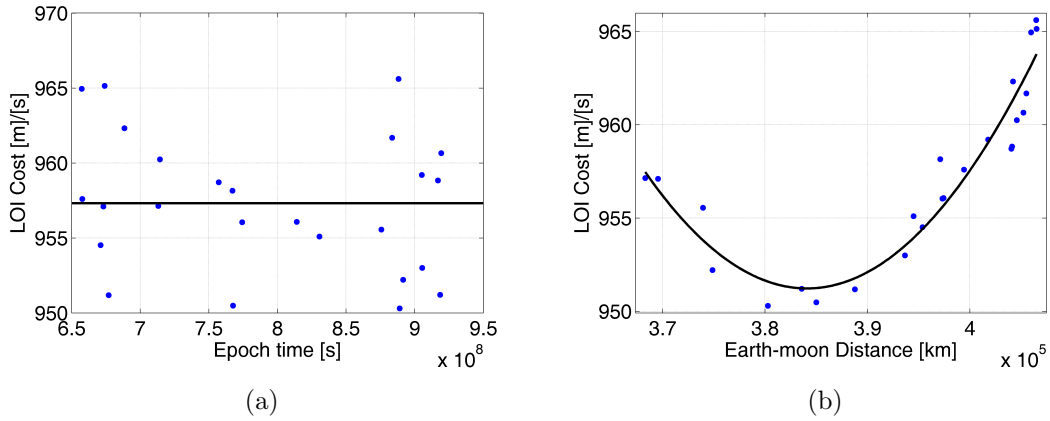


Figure 6.12: Epoch variation and LOI cost for an LLO of orientation (225 deg, 120 deg): a) LOI cost as a function of ephemeris time, and b) LOI cost as a function of Earth-moon distance.

6.1.6.2 Force Model Extension

In this subsection, the effects of Earth’s oblateness and solar radiation pressure are added to the dynamic model. The initial minimum LOI cost when targeting an LLO of orientation of (225 deg, 120 deg) is 953.386 m/s, and the minimum cost when J_2 effects and solar radiation pressure are considered is 953.377 m/s, a differ-

ence of $9 \times 10^{-4} \%$. Thus, the effects on the LOI cost are small in this case, but the effects on the trajectory displacement are more significant. Figure 6.13 shows the difference in spacecraft position between the two dynamic models; the position deviation at TLI is approximately 17 km, and the deviation at EEI is approximately 9 km. As seen in Fig. 6.13(b), the effects near the moon are less significant since the maximum position deviation along the LOI segments is approximately 900 m. Table 6.1 shows the accelerations on the spacecraft at EEI. The oblateness acceleration of the Earth is the second most significant acceleration at this phase of the mission near the Earth. The calculation of solar radiation pressure assumed a spacecraft area of 80 m^2 , and a coefficient of reflectivity of 0.9.

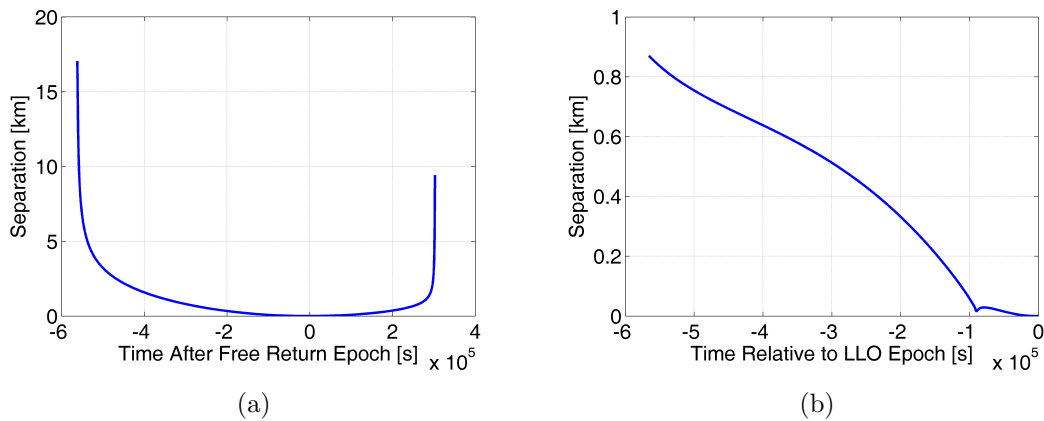


Figure 6.13: Effect of Earth oblateness and solar radiation pressure: a) position deviation on free return, and b) position deviation on LOI segments.

6.1.6.3 Multi-Objective Optimization

The spacecraft is nominally constrained to remain on the free return path for at least one day. This inequality constraint was active in each case to minimize the

Table 6.1: Spacecraft accelerations at EEI

Source	Acceleration	Units
Earth (spherical)	9.35×10^{-3}	km/s ²
Earth (oblateness only)	1.30×10^{-5}	km/s ²
Moon	7.11×10^{-10}	km/s ²
Sun	5.14×10^{-10}	km/s ²
Solar radiation pressure	1.62×10^{-11}	km/s ²

LOI cost. It may be desired, however, to remain on the free return longer if the ΔV capability of the spacecraft is sufficient to do so. To investigate hybrid trajectories that offer a longer duration on the free return, and to understand the LOI cost of these missions, the objective function of the algorithm is modified. The new optimization problem seeks to minimize the LOI cost and maximize the time spent on the free return. Representative quantities are summed into a scalar objective function, given by

$$J \equiv \sum_{i=0}^3 \Delta v_i + \frac{t_{MIN}}{t_R - t_{TLI}} \quad (6.23)$$

Because $t_{MIN} = 86400$ s, the second term of J represents the inverse of the number of days spent on the free return. This additional term and its effective weighting were chosen so that the most expensive case has an LOI cost near 1250 m/s, an assumed maximum ΔV capability. If a specific architecture is known, it may be desired to change the relative weighting of the terms in J , or the maximum ΔV capability could be bounded by an inequality constraint.

An example is presented that targets an LLO of orientation (0 deg, 90 deg). The optimal solution, shown in Fig. 6.14, has an LOI cost of 1264 m/s and provides

a flight time of 5.14 days on the free return. This represents an increase of about 75 m/s over the nominal case where the spacecraft remained on the free return for only one day (Fig. 6.5). As confirmed by this example and by Fig. 6.11, the penalties for increasing the flight time on the free return, when reoptimizing the free return and LOI sequence, are not as severe as the penalties from remaining on the free return longer without reoptimizing the free return (Fig. 5.10(a)). Thus, the maximum LOI capability should be specified before a mission, and the spacecraft's flight time on the free return should be maximized within this capability.

6.2 Lunar Orbit Insertion with a Finite Thrust Engine Model

The impulsive model is converted to a constant thrust, linearly-steered finite burn engine model. The cost function to be minimized is the propellant mass, given by

$$J \equiv m_0 - m_f \quad (6.24)$$

where the initial mass m_0 is the post-TLI spacecraft mass, and the spacecraft mass delivered to lunar orbit is fixed at $m_f = 20000$ kg. The propellant mass is

$$m_0 - m_f = - \sum_{i=0}^3 \Delta m_i \quad (6.25)$$

The change in mass across the i th burn is

$$\Delta m_i = - \frac{T}{c} \Delta t_i \quad (6.26)$$

where $T = 35$ kN is the fixed engine thrust, c is the exhaust velocity, and Δt_i is the burn time. The exhaust velocity is $c = I_{sp}g_0$, where the specific impulse

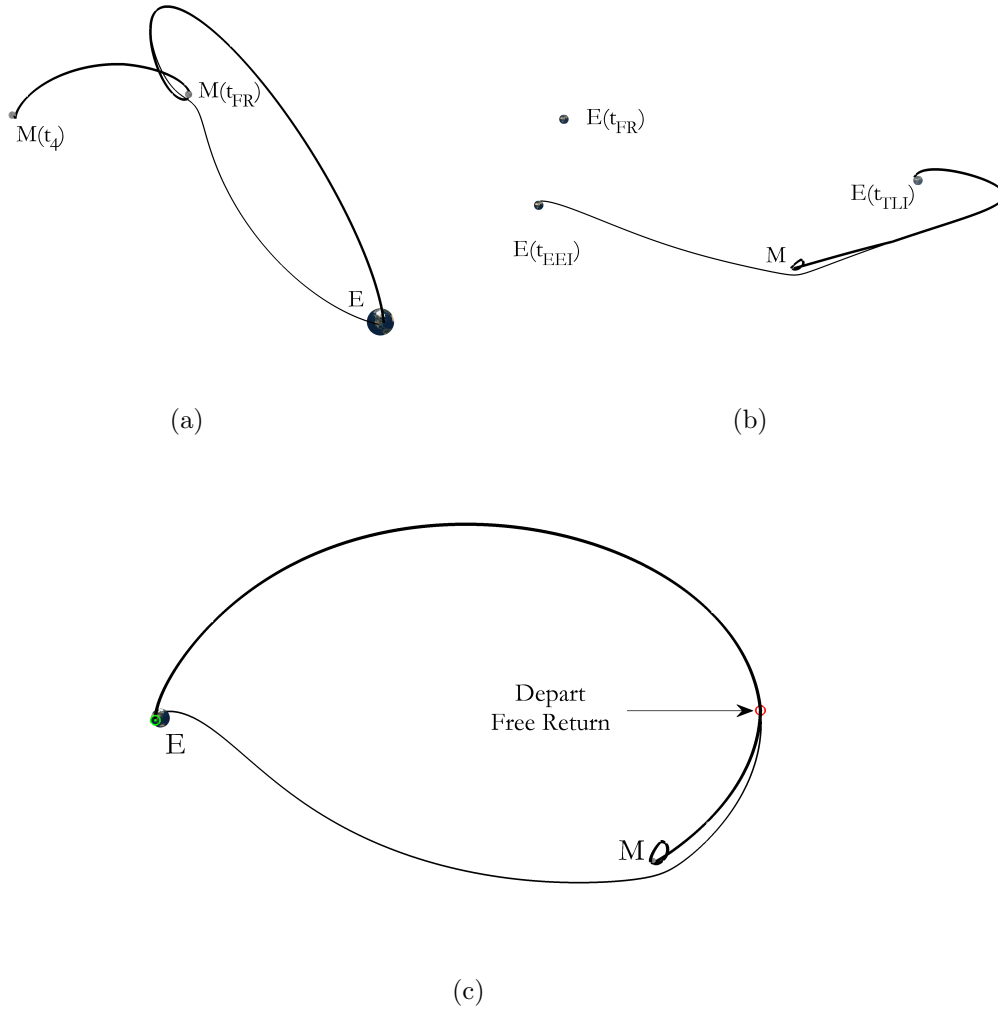


Figure 6.14: Multi-objective optimization example for an LLO of orientation of (0 deg, 90 deg): a) Earth-centered non-rotating frame, b) moon-centered non-rotating frame, and c) Earth-centered rotating-pulsating frame.

is $I_{sp} = 320$ s, and the standard gravitational acceleration at Earth's surface is $g_0 = 9.80665 \times 10^{-3}$ km/s² [100]. The cost function becomes

$$J = \frac{T}{c} \sum_{i=0}^3 \Delta t_i \quad (6.27)$$

During each thrust phase, the thrust direction is parameterized by α , the initial right ascension of the thrust direction, β , the initial thrust declination, $\dot{\alpha}$, the right ascension rate, and $\dot{\beta}$, the declination rate. The vector of optimization parameters is

$$\mathbf{x}_p \equiv [t_0^- \ t_0^+ \ \cdots \ t_4 \ \alpha_0 \ \beta_0 \ \dot{\alpha}_0 \ \dot{\beta}_0 \ \cdots \ h \ \phi \ \mathbf{v}^\top \ t_{TLI} \ t_R \ t_{EEI}]_{1 \times 33}^\top \quad (6.28)$$

where t_i^- and t_i^+ indicate the start and end times of the i th burn, and t_4 is the time of the LLO ascending node. The state at the FRE is again parameterized by its altitude h , latitude ϕ relative to the Earth-moon plane, and velocity \mathbf{v} . The equality constraints are

$$\mathbf{c} \equiv \begin{bmatrix} \mathbf{x}_R - \mathbf{x}_0^{--} \\ t_R - t_0^- \end{bmatrix}_{7 \times 1} = \mathbf{0} \quad (6.29)$$

where \mathbf{x}_R is the state before the retargeting maneuver, integrated along the free return, and \mathbf{x}_0^{--} is the state before the retargeting maneuver, integrated from the moon through the LOI sequence. The 19 inequality constraints require sequential trajectory segments and enforce the same flight time and altitude conditions as in the impulsive algorithm.

6.2.1 Impulse Conversion

Each impulsive maneuver is converted to a linearly-steered finite burn with a method that exactly reproduces the impulsive trajectory, except along thrust arcs, as developed in Ref. [90]. Beginning at a point after the impulse time t_i on the impulsive trajectory, a finite thrust arc is initiated. This thrusting trajectory begins at a time $t_B \geq t_i$ and terminates at a time $t_A \leq t_i$. The finite thrust arc conversion is initiated after the impulse time because the LOI trajectories are integrated backwards in time from the LLO where the spacecraft has a fixed mass. Using the ideal rocket equation (Appendix E), the burn time $\Delta t \equiv t_B - t_A$ is initially estimated as

$$\Delta t = \frac{c}{T} m_B (e^{\Delta v/c} - 1) \quad (6.30)$$

where m_B is the post-burn mass and Δv is the known impulse magnitude. It is desired to match the position and velocity at the endpoints of the thrust arc to any points along the ballistic trajectory before and after the impulse. Thus, it is necessary to determine a finite burn trajectory that satisfies

$$\mathbf{c} \equiv \mathbf{x}_f - \mathbf{x}_A = \mathbf{0} \quad (6.31)$$

where \mathbf{x}_A is the state on the reference ballistic trajectory at t_A , and \mathbf{x}_f is the state on the integrated finite burn trajectory at t_A . To target the six element constraint vector, a vector of free parameters is defined as

$$\mathbf{x}_p \equiv \begin{bmatrix} \alpha \\ \beta \\ \dot{\alpha} \\ \dot{\beta} \\ \sqrt{\Delta t_A} \\ \sqrt{\Delta t_B} \end{bmatrix} \quad (6.32)$$

where

$$\Delta t_A = t_i - t_A \quad (6.33)$$

$$\Delta t_B = t_B - t_i \quad (6.34)$$

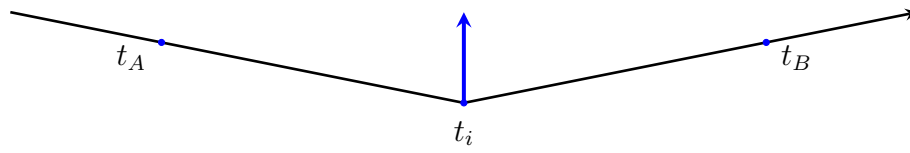
Initially, α and β are computed from the impulse direction, and both $\dot{\alpha}$ and $\dot{\beta}$ are set to zero. Since $\mathbf{x}_p \in \mathbb{R}^6$, Δt_A and Δt_B are required to be non-negative; this guarantees $t_A \leq t_i$ and $t_i \leq t_B$ without imposing constraints to maintain sequential times. The method, illustrated in Fig. 6.15, is used to convert the four impulsive maneuvers from the previously optimized case to finite burns, and the resulting feasible trajectory is used as the starting point for subsequent optimization.

6.2.2 System Dynamics

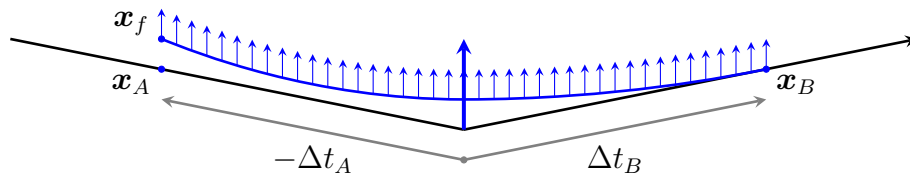
A state vector is defined to include the position, velocity, mass, and thrust direction parameters. Though the right ascension rate and declination rate are constant throughout each burn and irrelevant throughout each coast, these quantities are added to the state vector so that each time the engine is switched on or off, the event can be represented by a state impulse. The augmented state vector and its time derivative are

$$\mathbf{z} \equiv \begin{bmatrix} \mathbf{r} \\ \mathbf{v} \\ m \\ \mathbf{q} \end{bmatrix}_{11 \times 1} \quad \dot{\mathbf{z}} = \begin{bmatrix} \mathbf{v} \\ \mathbf{g} + \frac{T}{m} \hat{\mathbf{u}} \\ -\frac{T}{c} \\ \dot{\mathbf{q}} \end{bmatrix}_{11 \times 1} \quad (6.35)$$

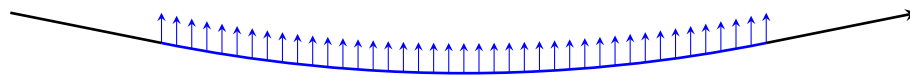
where \mathbf{r} is the spacecraft position, \mathbf{v} is the velocity, m is the mass, \mathbf{q} is a vector of control parameters, \mathbf{g} is the gravitational acceleration, and $\hat{\mathbf{u}}$ is the thrust direction.



(a)



(b)



(c)

Figure 6.15: Impulse to finite burn conversion: a) impulsive trajectory, b) finite burn targeting, and c) continuous finite burn trajectory.

The \mathbf{q} vector and its time derivative are

$$\mathbf{q} \equiv \begin{bmatrix} \alpha \\ \beta \\ \dot{\alpha} \\ \dot{\beta} \end{bmatrix} \quad \dot{\mathbf{q}} = \begin{bmatrix} \dot{\alpha} \\ \dot{\beta} \\ 0 \\ 0 \end{bmatrix} \quad (6.36)$$

and the thrust direction is computed as

$$\hat{\mathbf{u}} = \cos \alpha \cos \beta \hat{\mathbf{x}} + \sin \alpha \cos \beta \hat{\mathbf{y}} + \sin \beta \hat{\mathbf{z}} \quad (6.37)$$

6.2.3 Analytical Gradients

The partials of the cost and constraints with respect to the free parameters are necessary for optimization with the chosen gradient-based method. With 33 free parameters, a cost function, and 26 constraints, 891 individual derivatives are needed. Analytical gradients were derived previously for the impulsive LOI optimization model in the CRTBP and the ephemeris model via a generalized procedure. Because the free parameters that fully specify the thrust direction are now included in the state vector, gradient derivation largely remains the same. This choice of state vector allows a state impulse to represent an engine start or stop event, so derivations are mathematically analogous to the previous derivations that considered only impulsive changes in spacecraft velocity. Impulsive changes in the thrust direction parameters are now used to represent engine events. Relative to central differencing, the algorithm with STM-based derivatives is approximately 13 times faster.

The state transition matrix Φ of the system is propagated as

$$\dot{\Phi} = \mathbf{F}\Phi \quad (6.38)$$

where the state propagation matrix is

$$\mathbf{F} \equiv \frac{\partial \dot{\mathbf{z}}}{\partial \mathbf{z}} = \begin{bmatrix} \mathbf{0} & \mathbf{I} & \mathbf{0} & \mathbf{0} \\ \mathbf{G} & \mathbf{0} & -\frac{T}{m^2} \hat{\mathbf{u}} & \frac{T}{m} \frac{\partial \hat{\mathbf{u}}}{\partial \mathbf{q}} \\ \mathbf{0}^\top & \mathbf{0}^\top & 0 & \mathbf{0}^\top \\ \mathbf{0} & \mathbf{0} & \mathbf{0} & \frac{\partial \dot{\mathbf{q}}}{\partial \mathbf{q}} \end{bmatrix}_{11 \times 11} \quad (6.39)$$

With moon-centered coordinates, the gravity gradient matrix is

$$\begin{aligned} \mathbf{G} &= \frac{3\mu_M}{r^5} \mathbf{r} \mathbf{r}^\top - \frac{\mu_M}{r^3} \mathbf{I} \\ &+ \frac{3\mu_E}{|\mathbf{r} - \mathbf{r}_{ME}|^5} (\mathbf{r} - \mathbf{r}_{ME})(\mathbf{r} - \mathbf{r}_{ME})^\top - \frac{\mu_E}{|\mathbf{r} - \mathbf{r}_{ME}|^3} \mathbf{I} \\ &+ \frac{3\mu_S}{|\mathbf{r} - \mathbf{r}_{MS}|^5} (\mathbf{r} - \mathbf{r}_{MS})(\mathbf{r} - \mathbf{r}_{MS})^\top - \frac{\mu_S}{|\mathbf{r} - \mathbf{r}_{MS}|^3} \mathbf{I} \end{aligned} \quad (6.40)$$

The derivative of the thrust direction with respect to the control vector is

$$\frac{\partial \hat{\mathbf{u}}}{\partial \mathbf{q}} = \begin{bmatrix} -\sin \alpha \cos \beta & -\cos \alpha \sin \beta & 0 & 0 \\ \cos \alpha \cos \beta & -\sin \alpha \sin \beta & 0 & 0 \\ 0 & \cos \beta & 0 & 0 \end{bmatrix} \quad (6.41)$$

and the derivative of the control vector rate with respect to the control vector is

$$\frac{\partial \dot{\mathbf{q}}}{\partial \mathbf{q}} = \begin{bmatrix} \mathbf{0} & \mathbf{I} \\ \mathbf{0} & \mathbf{0} \end{bmatrix}_{4 \times 4} \quad (6.42)$$

The total differential of the pre-LOI-0 state is

$$\begin{aligned} d\mathbf{z}_0^- &= \Phi(t_0^-, t_0^+) \Phi(t_0^+, t_1^-) \cdots \Phi(t_3^+, t_4) \delta \mathbf{z}_4 \\ &+ \Phi(t_0^-, t_0^+) \Phi(t_0^+, t_1^-) \cdots \Phi(t_3^-, t_3^+) [-d(\Delta \mathbf{z}_3^+) + \Delta \dot{\mathbf{z}}_3^+ dt_3^+] \\ &+ \Phi(t_0^-, t_0^+) \Phi(t_0^+, t_1^-) \cdots \Phi(t_2^+, t_3^-) [-d(\Delta \mathbf{z}_3^-) + \Delta \dot{\mathbf{z}}_3^- dt_3^-] \\ &+ \cdots + \Phi(t_0^-, t_0^+) [-d(\Delta \mathbf{z}_0^+) + \Delta \dot{\mathbf{z}}_0^+ dt_0^+] \\ &+ \dot{\mathbf{z}}_0^- dt_0^- - d(\Delta \mathbf{z}_0^-) \end{aligned} \quad (6.43)$$

An engine start is represented as a state impulse of the form

$$\Delta \mathbf{z}_i^- \equiv \mathbf{z}_i^- - \mathbf{z}_i^{--} = \begin{bmatrix} \mathbf{0} \\ \mathbf{0} \\ 0 \\ \alpha_i \\ \beta_i \\ \dot{\alpha}_i \\ \dot{\beta}_i \end{bmatrix}_{11 \times 1} \quad (6.44)$$

and an engine stop is represented as a state impulse of the form

$$\Delta \mathbf{z}_i^+ \equiv \mathbf{z}_i^{++} - \mathbf{z}_i^+ = \begin{bmatrix} \mathbf{0} \\ \mathbf{0} \\ 0 \\ -(\alpha_i + \dot{\alpha}_i \Delta t_i) \\ -(\beta_i + \dot{\beta}_i \Delta t_i) \\ -\dot{\alpha}_i \\ -\dot{\beta}_i \end{bmatrix}_{11 \times 1} \quad (6.45)$$

where t_i^{--} and t_i^- represent the time immediately before and after the i th burn begins, and t_i^+ and t_i^{++} represent the time immediately before and after the i th burn ends. Figure 6.16 illustrates this nomenclature to distinguish the four times associated with each finite burn.

The analytical gradient architecture is similar to the impulsive case, but gradients with respect to the finite thrust control vectors are now needed for the

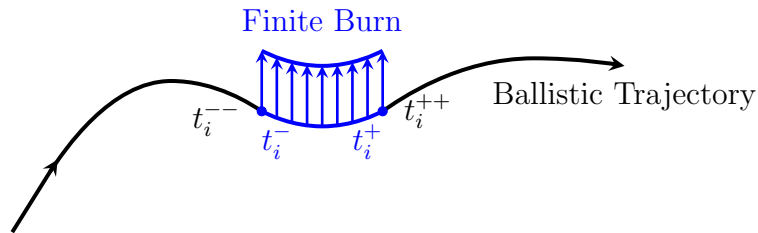


Figure 6.16: Finite burn node nomenclature.

optimization process. Combining each group of thrust orientation parameters as \mathbf{q}_i streamlines the notation for gradient derivation. The gradient of the first equality constraint with respect to the \mathbf{q}_0 control vector associated with the retargeting maneuver is

$$\frac{\partial(\mathbf{x}_R - \mathbf{x}_0^{--})}{\partial \mathbf{q}_0} = \frac{\partial(-\mathbf{x}_0^{--})}{\partial \mathbf{z}_0^{--}} \frac{\partial \mathbf{z}_0^{--}}{\partial \Delta \mathbf{z}_0^-} \frac{\partial \Delta \mathbf{z}_0^-}{\partial \mathbf{q}_0} + \frac{\partial(-\mathbf{x}_0^{--})}{\partial \mathbf{z}_0^{--}} \frac{\partial \mathbf{z}_0^{--}}{\partial \Delta \mathbf{z}_0^+} \frac{\partial \Delta \mathbf{z}_0^+}{\partial \mathbf{q}_0} \quad (6.46)$$

$$= \mathbf{R}_{1:6} \mathbf{I} \mathbf{Q}_0^- + \mathbf{R}_{1:6} \Phi(t_0^-, t_0^+) \mathbf{Q}_0^+ \quad (6.47)$$

where

$$\mathbf{R}_{1:6} = [\mathbf{I}_{6 \times 6} \quad \mathbf{0}_{6 \times 5}]_{6 \times 11} \quad (6.48)$$

and

$$\mathbf{Q}_i^- \equiv \frac{\partial \Delta \mathbf{z}_i^-}{\partial \mathbf{q}_i} = \begin{bmatrix} \mathbf{0} & \mathbf{0} & \mathbf{0} & \mathbf{0} \\ 1 & 0 & 0 & 0 \\ 0 & 1 & 0 & 0 \\ 0 & 0 & 1 & 0 \\ 0 & 0 & 0 & 1 \end{bmatrix}_{11 \times 4} \quad (6.49)$$

$$\mathbf{Q}_i^+ \equiv \frac{\partial \Delta \mathbf{z}_i^+}{\partial \mathbf{q}_i} = \begin{bmatrix} \mathbf{0} & \mathbf{0} & \mathbf{0} & \mathbf{0} \\ -1 & 0 & -\Delta t_i & 0 \\ 0 & -1 & 0 & -\Delta t_i \\ 0 & 0 & -1 & 0 \\ 0 & 0 & 0 & -1 \end{bmatrix}_{11 \times 4} \quad (6.50)$$

Pre-multiplying an $11 \times c$ matrix by $\mathbf{R}_{1:6}$ results in a $6 \times c$ matrix that consists of the first six rows of the original matrix, as shown in Appendix D. The gradients of the first equality constraint with respect to the remaining control vectors are

$$\frac{\partial(\mathbf{x}_R - \mathbf{x}_0^{--})}{\partial \mathbf{q}_1} = \mathbf{R}_{1:6} \Phi(t_0^-, t_0^+) \Phi(t_0^+, t_1^-) \left[\mathbf{Q}_1^- + \Phi(t_1^-, t_1^+) \mathbf{Q}_1^+ \right] \quad (6.51)$$

$$\frac{\partial(\mathbf{x}_R - \mathbf{x}_0^{--})}{\partial \mathbf{q}_2} = \mathbf{R}_{1:6} \Phi(t_0^-, t_0^+) \Phi(t_0^+, t_1^-) \Phi(t_1^-, t_1^+) \Phi(t_1^+, t_2^-) \left[\mathbf{Q}_2^- + \Phi(t_2^-, t_2^+) \mathbf{Q}_2^+ \right] \quad (6.52)$$

$$\frac{\partial(\mathbf{x}_R - \mathbf{x}_0^{--})}{\partial \mathbf{q}_3} = \mathbf{R}_{1:6} \Phi(t_0^-, t_0^+) \Phi(t_0^+, t_1^-) \cdots \Phi(t_2^-, t_2^+) \Phi(t_2^+, t_3^-) \left[\mathbf{Q}_3^- + \Phi(t_3^-, t_3^+) \mathbf{Q}_3^+ \right] \quad (6.53)$$

The osculating lunar periapsis altitude h_{LOI} at t_1^{--} is required to be greater than or equal to 100 km. The gradients of this constraint with respect to the first two control vectors are

$$\frac{\partial h_{LOI}}{\partial \mathbf{q}_0} = \mathbf{0}_{4 \times 1}^T \quad (6.54)$$

$$\frac{\partial h_{LOI}}{\partial \mathbf{q}_1} = -\boldsymbol{\Upsilon}^T \left[\mathbf{Q}_1^- + \Phi(t_1^-, t_1^+) \mathbf{Q}_1^+ \right] \quad (6.55)$$

where

$$\boldsymbol{\Upsilon}^T \equiv \frac{\partial h_{LOI}}{\partial \mathbf{z}_1^{--}} \quad (6.56)$$

Similarly,

$$\frac{\partial h_{LOI}}{\partial \mathbf{q}_2} = -\boldsymbol{\Upsilon}^T \Phi(t_1^-, t_1^+) \Phi(t_1^+, t_2^-) \left[\mathbf{Q}_2^- + \Phi(t_2^-, t_2^+) \mathbf{Q}_2^+ \right] \quad (6.57)$$

$$\frac{\partial h_{LOI}}{\partial \mathbf{q}_3} = -\boldsymbol{\Upsilon}^T \Phi(t_1^-, t_1^+) \Phi(t_1^+, t_2^-) \Phi(t_2^-, t_2^+) \Phi(t_2^+, t_3^-) \left[\mathbf{Q}_3^- + \Phi(t_3^-, t_3^+) \mathbf{Q}_3^+ \right] \quad (6.58)$$

The remaining gradient derivations are similar to those previously shown.

6.2.4 Numerical Results

The LLO orientation is parametrically varied, and the hybrid TLI to LLO sequence is optimized for minimum LOI propellant mass; Figure 6.18 shows the results. The trends in the optimal values mirror the trends seen in the impulsive case, and the necessary propellant mass is greatest where the relative declination is the greatest. The maximum requirement, occurring at (0 deg, 90 deg), is 9255 kg, and the minimum requirement is 6300 kg which occurs at $i = 180$ deg. The maximum

propellant hybrid trajectory is shown in Fig. 6.17 in moon-centered and Earth-centered rotating-pulsating frames. The engine thrust of 35 kN is high enough for the finite burn solution to remain geometrically similar to the impulsive solution. For the maximum propellant case, the maximum burn time is 360 s, which is 0.05% of the TLI to LLO flight time. The maximum right ascension rate or declination rate is 2×10^{-4} deg/s. With burns of this duration and orientation, it is difficult to differentiate the finite thrust segments from impulses when viewing the trajectories on the scale of the Earth-moon distance.

Because of the similar character of the impulsive and finite burn solutions, it is desired to compare the consumed propellant mass predicted by the ideal rocket equation to the actual propellant mass as determined with the finite burn optimization algorithm. Figure 6.19 shows the variation in required propellant mass for LLOs with 90 deg inclination. The residuals plotted in Figure 6.19 show the rocket equation under-predicts the actual mass in every case; the average difference is -33 kg. The persistent negative bias indicates that gravity losses—unaccounted for in the rocket equation—lead to an increased propellant cost. Even with this error, the maximum percent difference is -1.04 %. If this level of error is acceptable, it would be advantageous to conduct optimization scans with the impulsive model to reduce runtime and then convert to the finite burn algorithm for specific missions of interest for a more realistic simulation.

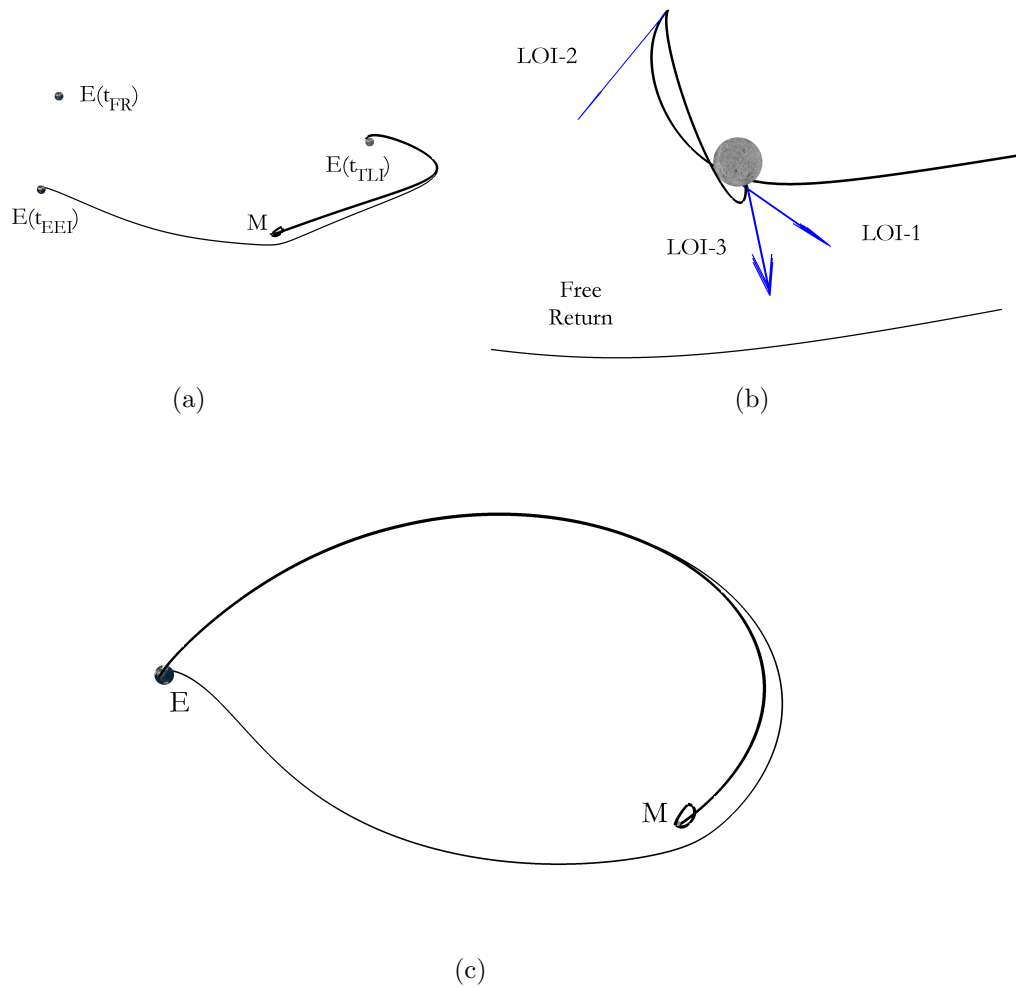


Figure 6.17: Maximum propellant finite burn hybrid trajectory: a) moon-centered non-rotating frame, b) LOI zoom in moon-centered non-rotating frame, and c) Earth-centered rotating-pulsating frame.

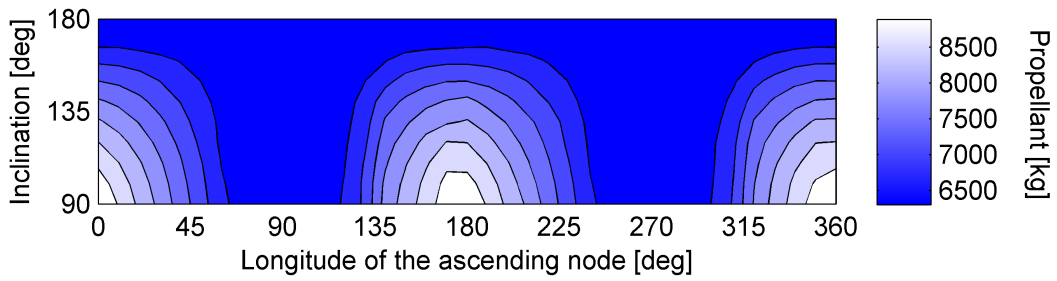


Figure 6.18: Minimum hybrid mission propellant mass contours.

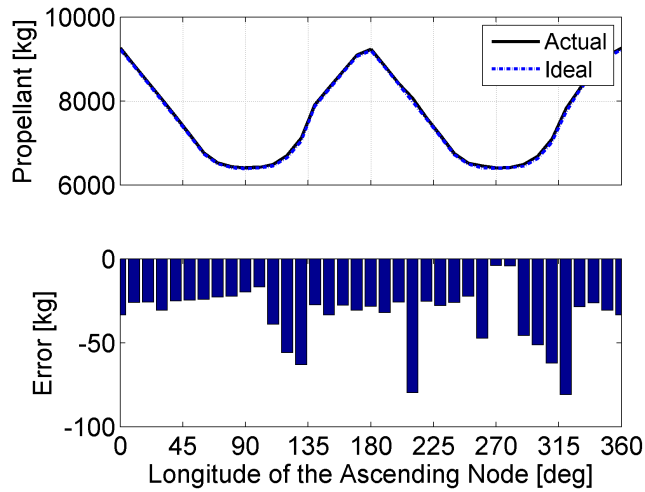


Figure 6.19: Minimum propellant mass comparison with ideal rocket equation prediction for LLOs of 90 deg inclination.

6.2.5 One-Burn Lunar Orbit Insertion

Nominally, three finite thrust segments at the moon are included in the algorithm. The optimizer may not add or remove segments or burns, but it is free to decrease the duration of any coast segment to zero and decrease the duration of any burn to zero. Therefore, the optimizer may effectively change the number of propulsive maneuvers at the moon if it finds that it is optimal to do so. In cases where less than four degrees of plane change is required at the moon, the optimizer reverts to an approximate one-burn insertion, meaning that after the retargeting maneuver, only one maneuver is used at the moon for orbit insertion. An example is shown in Fig. 6.20(a) where LOI-3 has disappeared and LOI-1 and LOI-2 are executed nearly at the same point; the LLO orientation is (130 deg, 90 deg), and the required propellant mass is 7111 kg. Closer examination, however, shows that this is actually a two-maneuver sequence since the two burns used have different thrust orientations, as seen in Fig. 6.20(b). To compare the cost of this two-burn sequence with a true one-burn sequence, the problem is reformulated with LOI-1 and LOI-2 removed. In this case, shown in Fig. 6.21, the total LOI cost including the retargeting maneuver decreases to 7047 kg, which is a decrease of 64 kg relative to the two-burn case. Therefore, with the three-burn formulation, the optimizer located a local minimum with the two-burn solution without reaching the optimal one-burn solution.

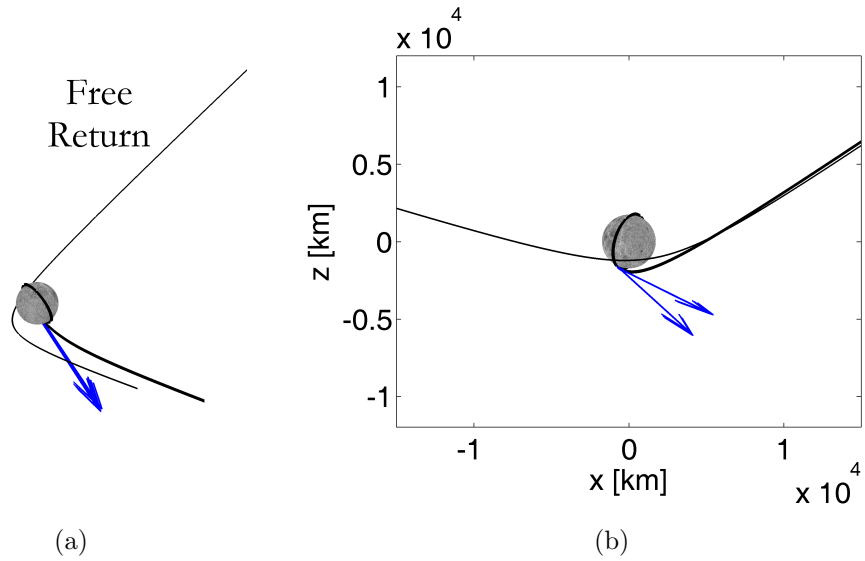


Figure 6.20: Three-burn formulation in moon-centered non-rotating frame: a) oblique view showing an apparent one-burn insertion, and b) view normal to $\hat{x}\hat{z}$ plane showing the true two-burn insertion.

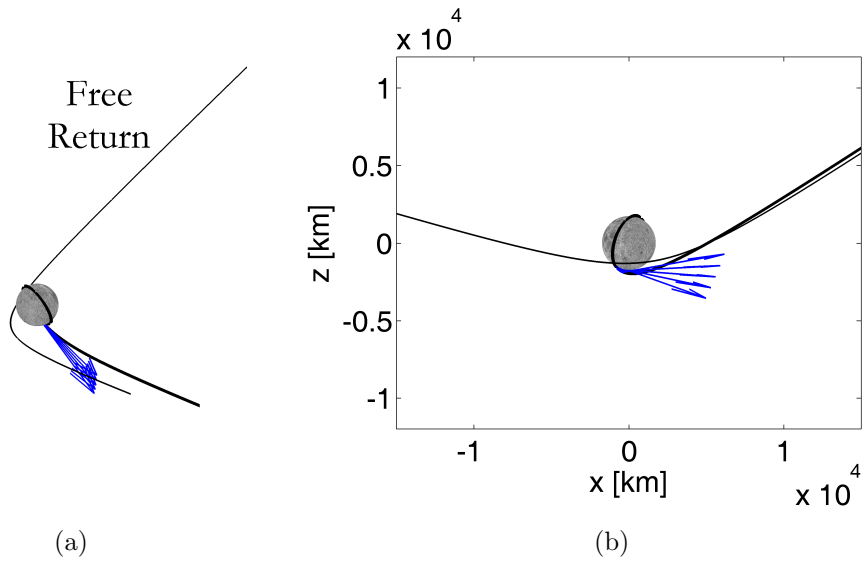


Figure 6.21: One-burn formulation in moon-centered non-rotating frame: a) oblique view, and b) view normal to the $\hat{x}\hat{z}$ plane.

6.3 Lunar Orbit Insertion with an Optimal Control Finite Thrust Engine Model

The transfer from the free return to the closed lunar orbit is now optimized with finite thrust segments which are guided with steering laws derived from optimal control theory. As shown in Chapter 4, it is known that the thrust vector which minimizes the cost function will point in the direction opposite the velocity costate. A hybrid method is implemented to solve the optimal control problem where the cost function will be directly minimized through sequential quadratic programming [101, 102]. The finite thrust segments are parameterized by the position and velocity costates, so the transversality conditions are implicitly satisfied when the cost is minimized. Due to the sensitivity of the costate equations of the optimal control problem, convergence of the optimal control finite burn model is more difficult than convergence of the linearly steered engine model.

6.3.1 System Dynamics

Both a one-burn and a three-burn formulation are implemented. The cost function in both cases is the total consumed propellant mass, given by

$$J = m_0 - m_f \tag{6.59}$$

$$= \frac{T}{c} \sum_i \Delta t_i \tag{6.60}$$

where $m_0 \equiv m(t_0^-)$ and $m_f \equiv m(t_4) \equiv 20000$ kg. The ballistic state is augmented with the costates of optimal control problem. The augmented state and its time

derivative are

$$\mathbf{z} \equiv \begin{bmatrix} \mathbf{r} \\ \mathbf{v} \\ m \\ \boldsymbol{\lambda}_r \\ \boldsymbol{\lambda}_v \\ \lambda_m \end{bmatrix}_{14 \times 1} \quad \dot{\mathbf{z}} = \begin{bmatrix} \mathbf{v} \\ \mathbf{g} - \frac{T}{m} \hat{\boldsymbol{\lambda}}_v \\ -\frac{T}{m} \\ -\mathbf{G} \boldsymbol{\lambda}_v \\ -\boldsymbol{\lambda}_r \\ -\frac{T}{m^2} \lambda_v \end{bmatrix}_{14 \times 1} \quad (6.61)$$

It is observed that $T \geq 0$, $m > 0$, and $\lambda_v > 0$, so $\dot{\lambda}_m \leq 0 \forall t$.

The kinematic constraints at the initial time require

$$\boldsymbol{\theta} = \begin{bmatrix} \mathbf{r}_0^{--} - \mathbf{r}(t_R) \\ \mathbf{v}_0^{--} - \mathbf{v}(t_R) \end{bmatrix}_{7 \times 1} = \mathbf{0} \quad (6.62)$$

where \mathbf{r}_0^{--} and \mathbf{v}_0^{--} are the position and velocity along the LOI segment immediately before LOI-0 begins; and $\mathbf{r}(t_R)$ and $\mathbf{v}(t_R)$ are the position and velocity along the free return immediately before LOI-0 begins. The kinematic constraints at the final time require

$$\boldsymbol{\psi} = \begin{bmatrix} \mathbf{r}_3^+ - \mathbf{r}(t_3^{++}) \\ \mathbf{v}_3^+ - \mathbf{v}(t_3^{++}) \\ m_3^+ - m(t_3^{++}) \end{bmatrix} = \mathbf{0} \quad (6.63)$$

where \mathbf{r}_3^+ , \mathbf{v}_3^+ , and m_3^+ are the position, velocity, and mass along the transfer segment immediately before LOI-3 terminates; and $\mathbf{r}(t_3^{++})$, $\mathbf{v}(t_3^{++})$, and $m(t_3^{++})$ are the position, velocity, and mass along the LLO immediately after LOI-3 terminates.

The endpoint function is

$$\mathbf{G} = m_0 - m_f + [\boldsymbol{\xi}_r^\top \quad \boldsymbol{\xi}_v^\top] \begin{bmatrix} \mathbf{r}_0^{--} - \mathbf{r}(t_R) \\ \mathbf{v}_0^{--} - \mathbf{v}(t_R) \end{bmatrix} + [\boldsymbol{\nu}_r^\top \quad \boldsymbol{\nu}_v^\top \quad \nu_m] \begin{bmatrix} \mathbf{r}_3^+ - \mathbf{r}(t_3^{++}) \\ \mathbf{v}_3^+ - \mathbf{v}(t_3^{++}) \\ m_3^+ - m(t_3^{++}) \end{bmatrix} \quad (6.64)$$

Expanding,

$$\begin{aligned} \mathbf{G} &= m_0 - m_f + \boldsymbol{\xi}_r^\top [\mathbf{r}_0^{--} - \mathbf{r}(t_R)] + \boldsymbol{\xi}_v^\top [\mathbf{v}_0^{--} - \mathbf{v}(t_R)] \\ &\quad + \boldsymbol{\nu}_r^\top [\mathbf{r}_3^+ - \mathbf{r}(t_3^{++})] + \boldsymbol{\nu}_v^\top [\mathbf{v}_3^+ - \mathbf{v}(t_3^{++})] + \nu_m [m_3^+ - m(t_3^{++})] \end{aligned} \quad (6.65)$$

By the transversality conditions, the initial costate is given by

$$\boldsymbol{\lambda}_0^{--} = - \left(\frac{\partial G}{\partial \mathbf{x}_0^{--}} \right)^\top \quad (6.66)$$

$$= \begin{bmatrix} -\boldsymbol{\xi}_r \\ -\boldsymbol{\xi}_v \\ -1 \end{bmatrix} \quad (6.67)$$

and the final costate is

$$\boldsymbol{\lambda}_3^+ = - \left(\frac{\partial G}{\partial \mathbf{x}_3^+} \right)^\top \quad (6.68)$$

$$= \begin{bmatrix} \nu_r \\ \nu_v \\ \nu_m \end{bmatrix} \quad (6.69)$$

The initial value of the mass costate is negative one, and since it is known that $\dot{\lambda}_m < 0$, the mass costate at t_4 should be initialized to a value less than negative one. Or, if the cost function is redefined as

$$J \equiv k(m_0 - m_f) \quad (6.70)$$

where $k > 0$, then $\lambda_{m_0}^{--} = -k$, and the mass costate at t_4 should be initialized to some value less than $-k$.

6.3.2 One-Burn Formulation

The hybrid optimization method will be first implemented for a case requiring only one LOI maneuver at the moon; the spacecraft still performs the retargeting maneuver to depart the outbound free return trajectory at a point to be determined by the optimizer.

The vector of independent optimization variables is

$$\mathbf{x}_p \equiv \left[t_0^- \quad t_0^+ \quad t_3^- \quad t_3^+ \quad t_4 \quad \Delta \boldsymbol{\lambda}_0^{+\top} \quad \Delta \boldsymbol{\lambda}_3^{+\top} \quad \boldsymbol{\lambda}_4^\top \quad h \quad \phi \quad \mathbf{v}^\top \quad t_{TLI} \quad t_R \quad t_{EEI} \right]_{1 \times 31}^\top \quad (6.71)$$

where $\Delta \boldsymbol{\lambda}_i^+$ is the discontinuity in the position and velocity costates at t_i^+ , and $\boldsymbol{\lambda}_4$ represents the position and velocity costates at t_4 expressed in the $\hat{\mathbf{r}}\hat{\mathbf{t}}\hat{\mathbf{n}}$ frame. The equality constraints require

$$\mathbf{c} \equiv \begin{bmatrix} \mathbf{x}_R - \mathbf{x}_0^{--} \\ t_R - t_0^- \\ \Delta \boldsymbol{\lambda}_0^+ \\ \Delta \boldsymbol{\lambda}_3^+ \\ S_0^+ \end{bmatrix}_{20 \times 1} = \mathbf{0} \quad (6.72)$$

where S_0^+ is the switching function at t_0^+ . If no errors were present in the problem implementation, the value of the switching function should be exactly zero at the time LOI-0 is deactivated. Due to numerical errors, however, this is not always the case, so the final constraint is added to drive S to zero at that point. A constraint requiring $S = 0$ at t_3^- is not implemented because this point is near enough to the starting point of numerical integration that it is zero upon convergence.

The initial estimates of all times and free return parameters are taken directly from the previous finite burn formulation. To compute initial estimates of the costates, the linearly steered finite burns of the previous formulation are converted to the optimal control formulation via the adjoint control transformation developed in Chapter 4. In summary, each finite thrust maneuver was specified by its initial right ascension α and declination β and their respective rates, $\dot{\alpha}$ and $\dot{\beta}$. The velocity costate is

$$\boldsymbol{\lambda}_v = -\lambda_v \hat{\mathbf{u}} \quad (6.73)$$

where λ_v is set, and the thrust direction is given by

$$\hat{\mathbf{u}} = \cos \alpha \cos \beta \hat{\mathbf{x}} + \sin \alpha \cos \beta \hat{\mathbf{y}} + \sin \beta \hat{\mathbf{z}} \quad (6.74)$$

The position costate is

$$\boldsymbol{\lambda}_r = \dot{\lambda}_v \hat{\mathbf{u}} + \lambda_v \dot{\hat{\mathbf{u}}} \quad (6.75)$$

where

$$\dot{\lambda}_v = \frac{\lambda_v}{2\dot{\hat{\mathbf{u}}}^\top \dot{\hat{\mathbf{u}}}} \left[\lambda_v (\mathbf{G}\hat{\mathbf{u}})^\top \dot{\hat{\mathbf{u}}} - \lambda_v \ddot{\hat{\mathbf{u}}}^\top \dot{\hat{\mathbf{u}}} \right] \quad (6.76)$$

This adjoint control transformation gives the values of the position and velocity costates at t_0^+ and t_3^+ . Also, the mass costate at t_3^+ is

$$\lambda_{m_3}^+ = -\frac{c}{m_3^+} \lambda_{v_3}^+ \quad (6.77)$$

by requiring $S_3^+ = 0$. The value of $\boldsymbol{\lambda}_4$ can be found by numerically integrating the augmented state from t_3^+ , which is known, to t_4 .

6.3.2.1 Analytical Gradients

The gradients of the first constraint with respect to the new parameters are

$$\frac{\partial(\mathbf{x}_R - \mathbf{x}_0^{--})}{\partial \Delta \boldsymbol{\lambda}_0^+} = -\frac{\partial \mathbf{x}_0^{--}}{\partial \mathbf{z}_0^{--}} \frac{\partial \mathbf{z}_0^{--}}{\partial \Delta \mathbf{z}_0^+} \frac{\partial \Delta \mathbf{z}_0^+}{\partial \Delta \boldsymbol{\lambda}_0^+} \quad (6.78)$$

$$= \mathbf{R}_{1:6} \boldsymbol{\Phi}(t_0^-, t_0^+) \mathbf{C}_{8:13} \quad (6.79)$$

$$\frac{\partial(\mathbf{x}_R - \mathbf{x}_0^{--})}{\partial \Delta \boldsymbol{\lambda}_3^+} = \mathbf{R}_{1:6} \boldsymbol{\Phi}(t_0^-, t_0^+) \boldsymbol{\Phi}(t_0^+, t_3^-) \boldsymbol{\Phi}(t_3^-, t_3^+) \mathbf{C}_{8:13} \quad (6.80)$$

$$\frac{\partial(\mathbf{x}_R - \mathbf{x}_0^{--})}{\partial \boldsymbol{\lambda}_4} = -\mathbf{R}_{1:6} \boldsymbol{\Phi}(t_0^-, t_0^+) \boldsymbol{\Phi}(t_0^+, t_3^-) \boldsymbol{\Phi}(t_3^-, t_3^+) \boldsymbol{\Phi}(t_3^+, t_4) \mathbf{K} \mathbf{C}_{8:13} \quad (6.81)$$

and

$$\Delta \dot{\mathbf{x}}_i^- = \begin{bmatrix} \mathbf{0} \\ -\frac{T}{m} \hat{\boldsymbol{\lambda}}_v^- \\ -\frac{T}{c} \\ \mathbf{0} \\ \mathbf{0} \\ \frac{T}{m^2} \boldsymbol{\lambda}_v^- \end{bmatrix}_{14 \times 1} \quad (6.90)$$

$$\Delta \dot{\mathbf{x}}_i^+ = \begin{bmatrix} \mathbf{0} \\ \frac{T}{m} \hat{\boldsymbol{\lambda}}_v^+ \\ \frac{T}{c} \\ \mathbf{G}^+(\boldsymbol{\lambda}_v^+ - \boldsymbol{\lambda}_v^{++}) \\ \boldsymbol{\lambda}_r^+ - \boldsymbol{\lambda}_r^{++} \\ -\frac{T}{m^2} \boldsymbol{\lambda}_v^+ \end{bmatrix}_{14 \times 1} \quad (6.91)$$

Finally,

$$\frac{\partial S_0^+}{\partial \Delta \boldsymbol{\lambda}_0^+} = -\frac{1}{m_0^+ \boldsymbol{\lambda}_{v_0}^+} \boldsymbol{\lambda}_{v_0}^{+\top} (\mathbf{R}_{11:13} \mathbf{C}_{8:13}) - \frac{1}{c} \mathbf{R}_{14:14} \mathbf{C}_{8:13} \quad (6.92)$$

$$\frac{\partial S_0^+}{\partial \Delta \boldsymbol{\lambda}_3^+} = -\frac{1}{m_0^+ \boldsymbol{\lambda}_{v_0}^+} \boldsymbol{\lambda}_{v_0}^{+\top} (\mathbf{R}_{11:13} \boldsymbol{\Phi}_{30} \boldsymbol{\Phi}_{33} \mathbf{C}_{8:13}) - \frac{1}{c} \mathbf{R}_{14:14} \boldsymbol{\Phi}_{30} \boldsymbol{\Phi}_{33} \mathbf{C}_{8:13} \quad (6.93)$$

$$\frac{\partial S_0^+}{\partial \boldsymbol{\lambda}_4} = \frac{1}{m_0^+ \boldsymbol{\lambda}_{v_0}^+} \boldsymbol{\lambda}_{v_0}^{+\top} (\mathbf{R}_{11:13} \boldsymbol{\Phi}_{30} \boldsymbol{\Phi}_{33} \boldsymbol{\Phi}_{43} \mathbf{K} \mathbf{C}_{8:13}) + \frac{1}{c} \mathbf{R}_{14:14} \boldsymbol{\Phi}_{30} \boldsymbol{\Phi}_{33} \boldsymbol{\Phi}_{43} \mathbf{K} \mathbf{C}_{8:13} \quad (6.94)$$

6.3.2.2 Numerical Results

To illustrate the optimal control one-burn algorithm, an example is presented for an LLO of orientation (130 deg, 90 deg). This case utilizes two maneuvers: one to depart the free return and one to arrive in lunar orbit; it is referred to as a “one-burn” insertion since only one maneuver is used at the moon. Figure 6.22 shows the optimal LOI sequence with a total propellant cost of 7044 kg, a savings of 3 kg over the linearly steered model. With an engine thrust of 35 kN, the linearly steered optimal solution is within 0.05% of the optimal control solution. It is anticipated

that the disparity will grow as the thrust magnitude is decreased since the burn duration will increase. Figure 6.23 shows the evolution of the switching function where the transfer time is normalized so that LOI-0 is initiated at a normalized time of zero and LOI-3 is terminated at a normalized time of one. As expected, $S \geq 0$ for the duration of LOI-0 and LOI-3 and $S < 0$ otherwise. The switching function is zero at both internal switching nodes and at the terminal boundary since the insertion location on the LLO is free. The switching function is nonzero at the initial time since it abuts with the inequality constraint requiring LOI-0 to occur at least one day after TLI.

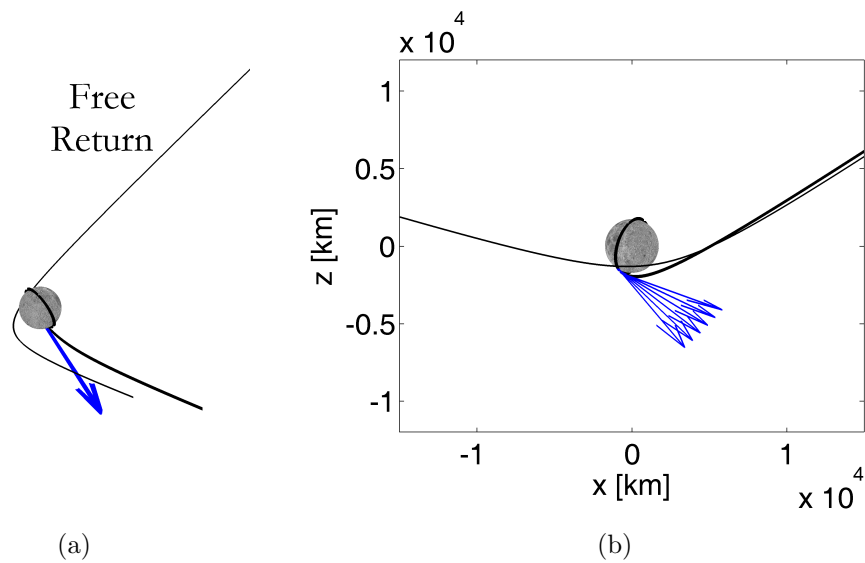
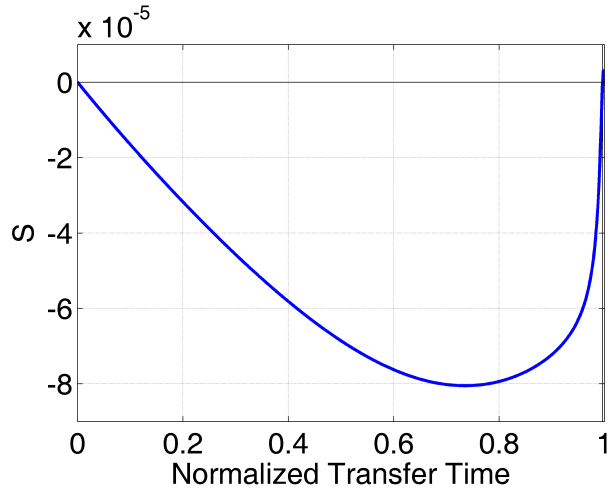
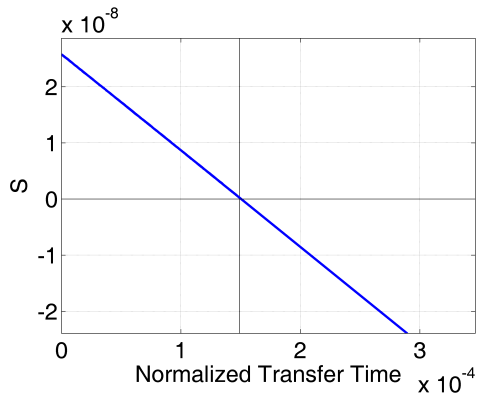


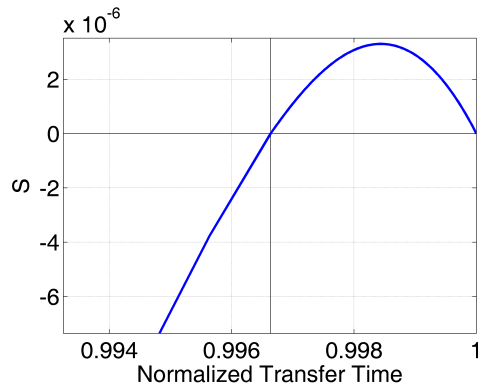
Figure 6.22: One-burn optimal control formulation in moon-centered non-rotating frame: a) oblique view, and b) view normal to $\hat{x}\hat{z}$ plane.



(a)



(b)



(c)

Figure 6.23: Switching function evolution for one-burn formulation: a) overall evolution and b) zoom at LOI-0 where the vertical line indicates the termination of the maneuver, and c) zoom at LOI-3 where the vertical line indicates the initiation of the maneuver.

6.3.3 Three-Burn Formulation

In the most general case, three propulsive maneuvers are allowed at the moon, and the propellant mass is again minimized. The costates of the optimal control problem are computed with the adjoint control transformation based on the angles and rates from the linearly steered model, and each finite burn points in the direction opposite of the velocity costate orientation. Due to the sensitivity of the costate equations, a new shooting scheme is used for optimization where one trajectory branch is integrated backwards from the LLO to t_1^- , and another trajectory branch is integrated forward from t_0^- to t_1^- . Full augmented state equality is enforced at the t_1^- patch point, and t_1^- is required to equal t_1^- in the converged solution. With three maneuvers at the moon and the modified shooting method, the vector of free parameters expands to

$$\mathbf{x}_p \equiv \left[t_0^- \quad t_0^+ \quad t_1^- \quad t_1^- \quad \cdots \quad t_3^+ \quad t_4 \quad m_0^- \quad \boldsymbol{\lambda}_0^{-\top} \quad \Delta \boldsymbol{\lambda}_1^{+\top} \quad \cdots \quad \boldsymbol{\lambda}_4^\top \quad h \quad \cdots \quad t_{EEI} \right]_{1 \times 49}^\top \quad (6.95)$$

where $\boldsymbol{\lambda}_0^-$ is the full costate at t_0^- , and the free return parameters are the same as those given in Eq. (6.28), except that t_R is removed. The equality constraints are

$$\mathbf{c} \equiv \begin{bmatrix} \mathbf{z}_1^{--} - \mathbf{z}_1^- \\ t_1^{--} - t_1^- \\ \Delta \boldsymbol{\lambda}_1^+ \\ \Delta \boldsymbol{\lambda}_2^+ \\ \Delta \boldsymbol{\lambda}_3^+ \\ S_0^+ \\ S_1^+ \\ S_2^+ \\ S_3^+ \end{bmatrix}_{37 \times 1} = \mathbf{0} \quad (6.96)$$

and the inequality constraints remain the same.

With 49 optimization variables, 37 equality constraints, 17 inequality constraints, and a cost function, 2695 partials are required for optimization; all gradients are derived analytically. The algorithm with STM-based derivatives is approximately 16 times faster than the algorithm with central differencing. The derivative of the first equality constraint is

$$\frac{\partial(z_1^{--} - z_1^-)}{\partial t_0^-} = -\Phi_{01}\Phi_{00}\Delta z_0^- \quad (6.97)$$

where $\Phi_{00} \equiv \Phi(t_0^+, t_0^-)$. Continuing,

$$\frac{\partial(z_1^{--} - z_1^-)}{\partial t_0^+} = -\Phi_{01}\Delta z_0^+ \quad (6.98)$$

$$\frac{\partial(z_1^{--} - z_1^-)}{\partial t_1^-} = z_1^{--} \quad (6.99)$$

$$\frac{\partial(z_1^{--} - z_1^-)}{\partial t_1^-} = -z_1^- \quad (6.100)$$

$$\frac{\partial(z_1^{--} - z_1^-)}{\partial t_1^+} = -\Phi_{11}\Delta z_1^+ \quad (6.101)$$

where $\Phi_{11} \equiv \Phi(t_1^-, t_1^+)$. Continuing,

$$\frac{\partial(z_1^{--} - z_1^-)}{\partial t_2^-} = -\Phi_{11}\Phi_{21}\Delta z_2^- \quad (6.102)$$

$$\frac{\partial(z_1^{--} - z_1^-)}{\partial t_2^+} = -\Phi_{11}\Phi_{21}\Phi_{22}\Delta z_2^+ \quad (6.103)$$

where $\Phi_{22} \equiv \Phi(t_2^-, t_2^+)$. Continuing,

$$\frac{\partial(z_1^{--} - z_1^-)}{\partial t_3^-} = -\Phi_{11}\Phi_{21}\Phi_{22}\Phi_{32}\Delta z_3^- \quad (6.104)$$

$$\frac{\partial(z_1^{--} - z_1^-)}{\partial t_3^+} = -\Phi_{11}\Phi_{21}\Phi_{22}\Phi_{32}\Phi_{33}\Delta z_3^+ \quad (6.105)$$

where $\Phi_{33} \equiv \Phi(t_3^-, t_3^+)$. Continuing,

$$\frac{\partial(z_1^{--} - z_1^-)}{\partial t_4} = -\Phi_{11}\Phi_{21}\Phi_{22}\Phi_{32}\Phi_{33}\Phi_{43}\frac{\delta z_4}{dt_4} \quad (6.106)$$

$$\frac{\partial(z_1^{--} - z_1^-)}{\partial m_0^-} = -\Phi_{01}\Phi_{00}C_{7:7} \quad (6.107)$$

$$\frac{\partial(z_1^{--} - z_1^-)}{\partial \lambda_0^-} = \Phi_{01}\Phi_{00}C_{8:14} \quad (6.108)$$

$$\frac{\partial(z_1^{--} - z_1^-)}{\partial \Delta \lambda_1^+} = \Phi_{11}C_{8:13} \quad (6.109)$$

$$\frac{\partial(z_1^{--} - z_1^-)}{\partial \Delta \lambda_2^+} = \Phi_{11}\Phi_{21}\Phi_{22}C_{8:13} \quad (6.110)$$

$$\frac{\partial(z_1^{--} - z_1^-)}{\partial \Delta \lambda_3^+} = \Phi_{11}\Phi_{21}\Phi_{22}\Phi_{32}\Phi_{33}C_{8:13} \quad (6.111)$$

$$\frac{\partial(z_1^{--} - z_1^-)}{\partial \lambda_4} = -\Phi_{11}\Phi_{21}\Phi_{22}\Phi_{32}\Phi_{33}\Phi_{43}KC_{8:13} \quad (6.112)$$

The gradients of the first constraint with respect to the free return parameters are

$$\frac{\partial(z_1^{--} - z_1^-)}{\partial h} = \Phi_{01}\Phi_{00}\Phi_R K \begin{bmatrix} \cos \phi \\ 0 \\ \sin \phi \\ \mathbf{0} \end{bmatrix}_{14 \times 1} \quad (6.113)$$

$$\frac{\partial(z_1^{--} - z_1^-)}{\partial \phi} = \Phi_{01}\Phi_{00}\Phi_R K \begin{bmatrix} -(R_M + h) \sin \phi \\ 0 \\ (R_M + h) \cos \phi \\ \mathbf{0} \end{bmatrix}_{14 \times 1} \quad (6.114)$$

$$\frac{\partial(z_1^{--} - z_1^-)}{\partial \mathbf{v}} = \Phi_{01}\Phi_{00}\Phi_R K \begin{bmatrix} \mathbf{0}_{3 \times 3} \\ \mathbf{I}_{3 \times 3} \\ \mathbf{0}_{8 \times 3} \end{bmatrix} \quad (6.115)$$

$$\frac{\partial(z_1^{--} - z_1^-)}{\partial t_{TLI}} = 0 \quad (6.116)$$

$$\frac{\partial(z_1^{--} - z_1^-)}{\partial t_{EEI}} = 0 \quad (6.117)$$

where $\Phi_R \equiv \Phi(t_0^{--}, t_{FR})$. The gradients of the switching function constraints are similar to those of the one-burn formulation.

6.3.3.1 Numerical Results

An example is presented to illustrate the three-burn optimal control formulation. The minimum propellant transfer from the variable free return to the LLO of orientation (225 deg, 120 deg) is computed. Figures 6.24(a)–6.24(b) show the optimal LOI sequence with a total propellant cost of 7117 kg, a savings of 10 kg over the linearly steered model. Figure 6.24(c) shows the evolution of the switching function where the transfer time is normalized so that LOI-0 is initiated at a normalized time of zero and LOI-3 is terminated at a normalized time of one. As expected, $S \geq 0$ for the duration of each finite thrust segment and $S < 0$ otherwise. The switching function is zero at all internal switching points and at the terminal boundary since the insertion location on the LLO is free. The switching function is nonzero at the initial time since it abuts with the inequality constraint requiring LOI-0 to occur at least one day after TLI.

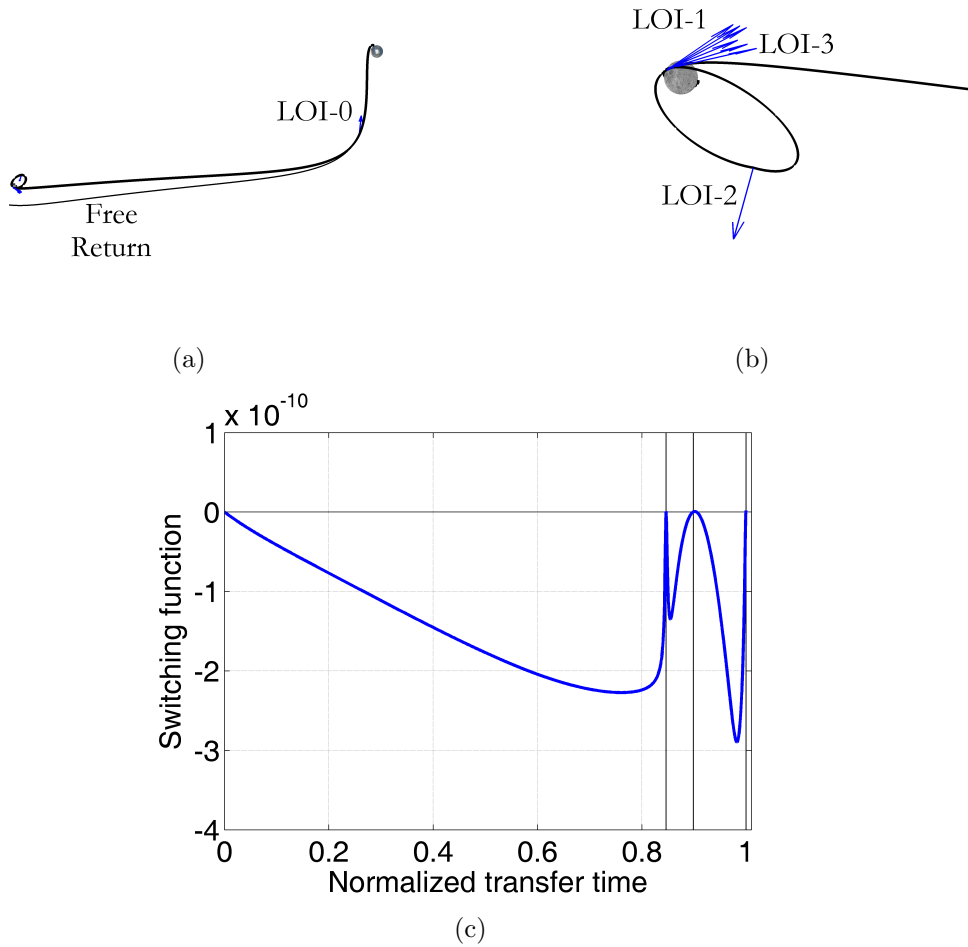


Figure 6.24: Three-burn optimal control formulation in moon-centered non-rotating frame: a) oblique view, b) LOI zoom at moon, and c) switching function evolution.

Chapter 7

Conclusions

7.1 Summary

The problem of optimal lunar orbit insertion in this dissertation was motivated primarily by applications to human missions. During such missions, it is necessary to plan for adverse circumstances that may jeopardize crew safety. In what is called a hybrid trajectory, the free return orbit was combined with the lunar orbit insertion sequence to guarantee a ballistic Earth return trajectory. The addition of this free return requirement complicates lunar orbit insertion and the associated algorithms used to compute it.

After the problem background and an overview of the previous research were presented in Chapter 1, the equations of motion in the circular restricted three-body problem and the four-body ephemeris model were presented in Chapter 2. Also discussed was the ability to scale trajectories in the circular model when the inter-primary distance changes but the mass ratio of the primaries does not. The dynamics of a spacecraft in the more realistic model were assumed to be affected only by the Earth, moon, and sun since the spacecraft remains in the Earth-moon system. The variational equations were presented for both dynamic models, and the effects of Earth's oblateness and solar radiation pressure were incorporated.

Chapter 3 dealt with the construction and analysis of Earth-moon-Earth free return trajectories. An original derivation of the theorem of image trajectories was presented because the theorem is useful in the generation of symmetric free returns. A strategy for constructing an initial estimate of different types of free returns was developed with two-body and circular restricted three-body models. Free returns were analyzed with posigrade and retrograde Earth departures, circumlunar and cislunar flybys, in and out of the Earth-moon plane. A continuation method was used to advance from the initial estimate to subsequent free returns. The algorithm was extended to general free returns that are not symmetric. Free returns may now be generated without a user-supplied initial guess.

An overview of optimization was provided in Chapter 4. The most important content was the development of analytical gradients that utilized the state transition matrix. A closed form expression for the state differential following n ballistic arcs and $n + 1$ state discontinuities was derived. Practical numerical issues of gradient validation and problem scaling were discussed. Chapter 4 also presented the basics of optimal control theory along with an adjoint control transformation to estimate the costates. Finally, the optimal control variational equations were derived.

Chapter 5 combined free returns and lunar orbit insertion sequences in the circular restricted three-body model. A fully-automated initial estimate for lunar orbit insertion was formulated and discussed. The orientation of a low lunar parking orbit was parametrically varied, and the minimum impulse orbit insertion sequence was found via a sequential quadratic programming algorithm with analytical gradients. First, the minimum time symmetric free return was used. Next, the free

return was allowed to vary during optimization but was required to remain symmetric. Finally, the free return was allowed to be completely free, subject to a maximum round trip flight time of 10 days and specified conditions at Earth departure and return. In this chapter, the spacecraft employed an impulsive propulsion system that allowed instantaneous changes in velocity.

Last, Chapter 6 extended the hybrid trajectory optimization algorithm from the circular restricted three-body model to the ephemeris model with a force field including the Earth, moon, and sun. The sum of the maneuver magnitudes required for lunar orbit insertion was minimized. The impulsive algorithm was then transitioned to include a finite thrust engine model where the propellant mass was minimized. For both engine models, the orientation of the target parking orbit was parametrically varied over the domain of circular, retrograde low lunar orbits, and the optimal hybrid transfer was computed for each case. Convergence of the sequential quadratic programming algorithm was facilitated by utilizing a multiple shooting method, and analytical gradients were implemented with both methods to achieve a fast and robust optimization algorithm. The initial estimate provided by the circular restricted three-body model was within the convergence envelope of the optimization algorithm in the four-body ephemeris model. The optimal impulsive solution subsequently served as an adequate initial estimate for the finite burn model. The linearly steered finite thrust model was then used as an initial estimate in the optimal control model via the adjoint control transformation developed in Chapter 4. The optimal control model realized savings over the linearly-steered algorithm.

7.2 Final Conclusions

As a result of this work, hybrid trajectories that combine free returns and lunar orbit insertion sequences may now be generated automatically. This work demonstrated that hybrid trajectories are feasible for a range of lunar parking orbit orientations. The orbit insertion costs necessary to achieve retrograde parking orbits with this method have been documented for impulsive, linearly steered finite thrust, and optimal control finite burn engine models in both the three-body and four-body models. The most favorable and least favorable parking orbit geometries in terms of the overall orbit insertion cost were identified.

To achieve the results presented in this dissertation required intermediate accomplishments. These included an automated method to generate free return trajectories, which is applicable to all types of single-flyby free returns, including circumlunar, cislunar, posigrade, retrograde, non-planar, and asymmetric free returns. Additionally, an algorithm was created to automate the generation of an initial estimate for lunar orbit insertion. Also helpful to the trajectory optimization process was the development and implementation of analytic gradients. The explicit n -segment state differential developed here will be useful in future applications of gradient-based optimization. An automated method was implemented to convert from the impulsive propulsion model to the finite burn model, and an adjoint control transformation was applied to the linearly steered burns to transition to an optimal control formulation. Also developed was a strategy to dilate trajectories in the circular restricted three-body model for transition to the four-body model.

Because humans first traveled to the moon more than 40 years ago, some assume that the task is not difficult or that everything possible to know about how to do it is already known. But space travel will always be intrinsically dangerous for humans, and the first trips to the moon accessed limited areas and favorable landing sites. To conduct successful missions to new landing sites, including polar sites, it is necessary to design abort trajectories that guarantee crew safety without compromising global access. Building on the legacy of Apollo, the current work extends hybrid trajectories to all retrograde low lunar orbits. Hybrid trajectories provide an attractive architecture for human lunar missions because they offer a period of maneuver-free Earth return capability. Where possible, a direct abort should be performed. But in cases when this is impossible, such as the loss of propulsive power, the free return is the most promising option. The methods developed here allow a mission designer, without advance knowledge of the trajectory geometry, to construct optimal, hybrid free return and lunar orbit insertion sequences for any mission epoch in a realistic solar system model. The results presented in this dissertation will be useful for future lunar mission planning.

Appendices

Appendix A

Gravitational Potential

A.1 Spherical Harmonics

Consider a central body of arbitrary shape with mass M and a spacecraft with mass \tilde{m} as shown in Fig. A.1. The gravitational potential of the body, with $\tilde{m} \equiv 1$, is

$$U = G \int_M \frac{dm'}{\rho} \quad (\text{A.1})$$

where G is the universal constant of gravitation, dm' is a differential piece of mass in the body, and ρ is the distance between the differential mass and the spacecraft. By the law of cosines,

$$\rho^2 = r^2 + r'^2 - 2rr' \cos \psi \quad (\text{A.2})$$

$$\rho^2 = r^2 \left(1 + \left(\frac{r'}{r} \right)^2 - 2 \left(\frac{r'}{r} \right) \cos \psi \right) \quad (\text{A.3})$$

$$\rho = r \sqrt{1 + \left(\frac{r'}{r} \right)^2 - 2 \left(\frac{r'}{r} \right) \cos \psi} \quad (\text{A.4})$$

where r is the distance from the body's mass center to the spacecraft, r' is the distance from the body's mass center to the differential mass, and ψ is the angle between the spacecraft vector and the differential mass vector. Thus, Eq. (A.1)

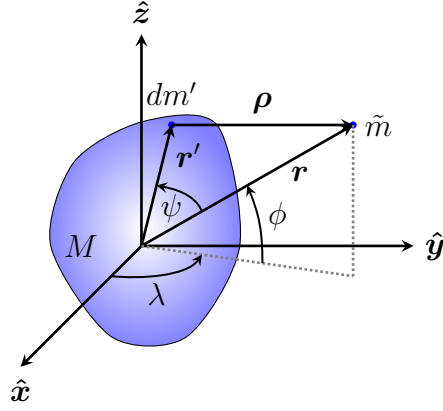


Figure A.1: General gravitating body.

becomes

$$U = \frac{G}{r} \int_M \frac{dm'}{\sqrt{1 + \left(\frac{r'}{r}\right)^2 - 2\left(\frac{r'}{r}\right) \cos \psi}} \quad (\text{A.5})$$

where r was taken out of the integral since it is independent of the central body's mass distribution.

The denominator inside the integral can be rewritten with the binomial expansion. Consider the Taylor series expansion of an arbitrary function $f(x)$ about a point x_0 , given by

$$f(x) = \sum_{k=0}^{\infty} \frac{f^{(k)}(x_0)}{k!} (x - x_0)^k \quad (\text{A.6})$$

$$= f(x_0) + f'(x_0)(x - x_0) + \frac{1}{2}f''(x_0)(x - x_0)^2 + \dots \quad (\text{A.7})$$

Consider now the expansion of $(1 + x)^a$ about $x_0 = 0$, given by

$$(1 + x)^a = (1 + x_0)^a + a(1 + x_0)^{a-1}(x - x_0) + \frac{1}{2}a(a-1)(1 + x_0)^{a-2}(x - x_0)^2 + \dots \quad (\text{A.8})$$

$$= 1 + ax + \frac{1}{2}a(a-1)x^2 + \dots \quad (\text{A.9})$$

Assuming $(r'/r)^2 - 2(r'/r) \cos \psi$ is small, the denominator of Eq. (A.5) can be expanded with Eq. (A.9) as

$$\begin{aligned} \left[1 + \left(\frac{r'}{r}\right)^2 - 2\left(\frac{r'}{r}\right) \cos \psi\right]^{-\frac{1}{2}} &= 1 + -\frac{1}{2} \left[-2\left(\frac{r'}{r}\right) \cos \psi + \left(\frac{r'}{r}\right)^2\right] \\ &+ \frac{1}{2}(-\frac{1}{2})(-\frac{3}{2}) \left[-2\left(\frac{r'}{r}\right) \cos \psi + \left(\frac{r'}{r}\right)^2\right]^2 + \dots \end{aligned} \quad (\text{A.10})$$

$$\begin{aligned} \left[1 + \left(\frac{r'}{r}\right)^2 - 2\left(\frac{r'}{r}\right) \cos \psi\right]^{-\frac{1}{2}} &= 1 + \left(\frac{r'}{r}\right) \cos \psi - \frac{1}{2} \left(\frac{r'}{r}\right)^2 \\ &+ \frac{3}{8} \left[4\left(\frac{r'}{r}\right)^2 \cos^2 \psi - 4\left(\frac{r'}{r}\right)^3 \cos \psi + \left(\frac{r'}{r}\right)^4\right] + \dots \end{aligned} \quad (\text{A.11})$$

Considering only the first four terms on the right hand side of Eq. (A.11),

$$\begin{aligned} \left[1 + \left(\frac{r'}{r}\right)^2 - 2\left(\frac{r'}{r}\right) \cos \psi\right]^{-\frac{1}{2}} &= 1 + \left(\frac{r'}{r}\right) \cos \psi - \frac{1}{2} \left(\frac{r'}{r}\right)^2 + \frac{3}{2} \left[\left(\frac{r'}{r}\right)^2 \cos^2 \psi\right] + \dots \end{aligned} \quad (\text{A.12})$$

$$= 1 + \left(\frac{r'}{r}\right) \cos \psi + \left[\frac{3}{2} \cos^2 \psi - \frac{1}{2}\right] \left(\frac{r'}{r}\right)^2 + \dots \quad (\text{A.13})$$

The terms of the expansion can be grouped into terms called Legendre polynomials.

The first three Legendre polynomials are

$$P_0(x) = 1 \quad (\text{A.14})$$

$$P_1(x) = x \quad (\text{A.15})$$

$$P_2(x) = \frac{3}{2}x^2 - \frac{1}{2} \quad (\text{A.16})$$

Additional Legendre polynomials can be generated explicitly and recursively [103].

Rewriting Eq. (A.13) with Legendre polynomials gives

$$\begin{aligned} \left[1 + \left(\frac{r'}{r}\right)^2 - 2\left(\frac{r'}{r}\right) \cos \psi\right]^{-\frac{1}{2}} &= P_0(\cos \psi) + \left(\frac{r'}{r}\right) P_1(\cos \psi) + \left(\frac{r'}{r}\right)^2 P_2(\cos \psi) + \dots \\ &= \sum_{\ell=0}^{\infty} \left(\frac{r'}{r}\right)^{\ell} P_{\ell}(\cos \psi) \end{aligned} \quad (\text{A.17})$$

The gravitational potential of Eq. (A.5) can now be rewritten as

$$U = \frac{G}{r} \int_M \sum_{\ell=0}^{\infty} \left(\frac{r'}{r}\right)^{\ell} P_{\ell}(\cos \psi) dm' \quad (\text{A.18})$$

The angle ψ represents the angular separation between the position vector of the spacecraft and the position vector of the differential mass. It is beneficial, however, to use the spacecraft's latitude and longitude instead. To rewrite $\cos \psi$ in terms of latitude and longitude, consider the coordinates of the spacecraft and the differential mass, given by

$$\mathbf{r} = r \cos \phi \cos \lambda \hat{\mathbf{x}} + r \cos \phi \sin \lambda \hat{\mathbf{y}} + r \sin \phi \hat{\mathbf{z}} \quad (\text{A.19})$$

$$\mathbf{r}' = r' \cos \phi' \cos \lambda' \hat{\mathbf{x}} + r' \cos \phi' \sin \lambda' \hat{\mathbf{y}} + r' \sin \phi' \hat{\mathbf{z}} \quad (\text{A.20})$$

where ϕ and λ are the latitude and longitude of the spacecraft, and ϕ' and λ' are the latitude and longitude of the differential mass. Now consider the dot product of these two position vectors as

$$\mathbf{r}^{\top} \mathbf{r}' = rr' \cos \psi \quad (\text{A.21})$$

$$\cos \psi = \frac{\mathbf{r}^{\top} \mathbf{r}'}{rr'} \quad (\text{A.22})$$

Expanding the right hand side gives

$$\cos \psi = \frac{rr' \cos \phi \cos \phi' \cos \lambda \cos \lambda' + rr' \cos \phi \cos \phi' \sin \lambda \sin \lambda' + rr' \sin \phi \sin \phi'}{rr'} \quad (\text{A.23})$$

$$= \cos \phi \cos \phi' \cos \lambda \cos \lambda' + \cos \phi \cos \phi' \sin \lambda \sin \lambda' + \sin \phi \sin \phi' \quad (\text{A.24})$$

$$= \cos \phi \cos \phi' \cos(\lambda - \lambda') + \sin \phi \sin \phi' \quad (\text{A.25})$$

By the Decomposition Formula [104], the ℓ th Legendre polynomial evaluated at the expanded value of $\cos \psi$ becomes

$$P_\ell(\cos \psi) = P_\ell(\cos \phi \cos \phi' \cos(\lambda - \lambda') + \sin \phi \sin \phi') \quad (\text{A.26})$$

$$= P_\ell(\sin \phi)P_\ell(\sin \phi') + 2 \sum_{m=1}^{\ell} \frac{(\ell - m)!}{(\ell + m)!} P_{\ell,m}(\sin \phi)P_{\ell,m}(\sin \phi') \cos(m(\lambda - \lambda')) \quad (\text{A.27})$$

where $P_{\ell,m}$ is known as the associated Legendre function of degree ℓ and order m .

Substituting Eq. (A.27) into Eq. (A.18) gives

$$U = \frac{G}{r} \int_M \sum_{\ell=0}^{\infty} \left(\frac{r'}{r}\right)^\ell \left[P_\ell(\sin \phi)P_\ell(\sin \phi') + 2 \sum_{m=1}^{\ell} \frac{(\ell - m)!}{(\ell + m)!} P_{\ell,m}(\sin \phi)P_{\ell,m}(\sin \phi') \cos(m(\lambda - \lambda')) \right] dm' \quad (\text{A.28})$$

Separating terms gives

$$U = \frac{G}{r} \int_M \sum_{\ell=0}^{\infty} \left(\frac{r'}{r}\right)^\ell P_\ell(\sin \phi)P_\ell(\sin \phi') dm' + \frac{G}{r} \int_M \sum_{\ell=1}^{\infty} \left(\frac{r'}{r}\right)^\ell \sum_{m=1}^{\ell} \frac{(\ell - m)!}{(\ell + m)!} P_{\ell,m}(\sin \phi)P_{\ell,m}(\sin \phi') \left[\cos m\lambda \cos m\lambda' + \sin m\lambda \sin m\lambda' \right] dm' \quad (\text{A.29})$$

Continuing,

$$U = \frac{G}{r} \sum_{\ell=0}^{\infty} \left(\frac{1}{r}\right)^\ell P_\ell(\sin \phi) \int_M (r')^\ell P_\ell(\sin \phi') dm' + \frac{G}{r} \sum_{\ell=1}^{\infty} \left(\frac{1}{r}\right)^\ell \sum_{m=1}^{\ell} 2 \frac{(\ell - m)!}{(\ell + m)!} P_{\ell,m}(\sin \phi) \int_M (r')^\ell P_{\ell,m}(\sin \phi') \left[\cos m\lambda \cos m\lambda' + \sin m\lambda \sin m\lambda' \right] dm' \quad (\text{A.30})$$

Define

$$a_{\ell,0} \equiv \int_M (r')^\ell P_\ell(\sin \phi') dm' \quad (\text{A.31})$$

$$a_{\ell,m} \equiv 2 \frac{(\ell - m)!}{(\ell + m)!} \int_M (r')^\ell P_{\ell,m}(\sin \phi') \cos m\lambda' dm' \quad (\text{A.32})$$

$$b_{\ell,m} \equiv 2 \frac{(\ell - m)!}{(\ell + m)!} \int_M (r')^\ell P_{\ell,m}(\sin \phi') \sin m\lambda' dm' \quad (\text{A.33})$$

These coefficients describe the mass properties of the central body. Closed form integrals may be possible for known shapes and mass distributions. For the Earth, the coefficients are determined empirically from artificial satellite motion. After substituting these coefficients into Eq. (A.30), the potential becomes

$$U = \frac{G}{r} \sum_{\ell=0}^{\infty} \left(\frac{1}{r}\right)^\ell P_\ell(\sin \phi) a_{\ell,0} + \frac{G}{r} \sum_{\ell=1}^{\infty} \left(\frac{1}{r}\right)^\ell \sum_{m=1}^{\ell} P_{\ell,m}(\sin \phi) [a_{\ell,m} \cos m\lambda + b_{\ell,m} \sin m\lambda] \quad (\text{A.34})$$

Separating the $\ell = 0$ term gives

$$U = \frac{GM}{r} + \frac{G}{r} \sum_{\ell=1}^{\infty} \left(\frac{1}{r}\right)^\ell P_\ell(\sin \phi) a_{\ell,0} + \frac{G}{r} \sum_{\ell=1}^{\infty} \left(\frac{1}{r}\right)^\ell \sum_{m=1}^{\ell} P_{\ell,m}(\sin \phi) [a_{\ell,m} \cos m\lambda + b_{\ell,m} \sin m\lambda] \quad (\text{A.35})$$

Define nondimensional coefficients as

$$C_{\ell,0} \equiv \frac{a_{\ell,0}}{M_* a_e^\ell} \quad (\text{A.36})$$

$$C_{\ell,m} \equiv \frac{a_{\ell,m}}{M_* a_e^\ell} \quad (\text{A.37})$$

$$S_{\ell,m} \equiv \frac{b_{\ell,m}}{M_* a_e^\ell} \quad (\text{A.38})$$

where a_e is the characteristic distance, and M_* is the characteristic mass, usually taken as the best estimate of the central body's mass. With the Earth as the central

body, a_e will be the mean equatorial radius and M_* will be M , the mass of the Earth.

Substituting the nondimensional coefficients into Eq. (A.35) gives

$$\begin{aligned}
U &= \frac{GM}{r} + \frac{GM}{r} \sum_{\ell=1}^{\infty} \left(\frac{a_e}{r}\right)^{\ell} P_{\ell}(\sin \phi) C_{\ell,0} \\
&+ \frac{GM}{r} \sum_{\ell=1}^{\infty} \sum_{m=1}^{\ell} \left(\frac{a_e}{r}\right)^{\ell} P_{\ell,m}(\sin \phi) [C_{\ell,m} \cos m\lambda + S_{\ell,m} \sin m\lambda] \quad (\text{A.39})
\end{aligned}$$

Furthermore, defining $J_{\ell} \equiv -C_{\ell,0}$ gives

$$\begin{aligned}
U &= \frac{GM}{r} - \frac{GM}{r} \sum_{\ell=1}^{\infty} \left(\frac{a_e}{r}\right)^{\ell} P_{\ell}(\sin \phi) J_{\ell} \\
&+ \frac{GM}{r} \sum_{\ell=1}^{\infty} \sum_{m=1}^{\ell} \left(\frac{a_e}{r}\right)^{\ell} P_{\ell,m}(\sin \phi) [C_{\ell,m} \cos m\lambda + S_{\ell,m} \sin m\lambda] \quad (\text{A.40})
\end{aligned}$$

The effects of this nonspherical central body gravitational potential on satellite motion are presented by Kaula [105].

A.2 Oblateness Acceleration

The general expression of the gravitational potential in terms of spherical coordinates (Eq. (A.40)) contains an infinite number of terms. The first term to the right of the equals sign is the spherical gravitational term, which is the dominant term for quasi-spherical bodies, such as the planets of the solar system. Higher order terms define the gravitational potential due to the asphericity of the central body. If the origin of the reference frame is chosen at the center of mass of the central body, the degree one coefficients ($\ell = 1$) in the gravitational potential are zero. The degree two coefficients ($\ell = 2$) are related to the central body's moments and products of inertia. For the Earth, which is an oblate spheroid, the most significant

higher order term is called the second zonal harmonic, which corresponds to the term in U containing the coefficient J_2 .

The gravitational potential due only to the J_2 term is

$$U_2 = -\frac{GM}{r} \left(\frac{a_e}{r}\right)^2 P_2(\sin \phi) J_2 \quad (\text{A.41})$$

$$= -\frac{\mu a_e^2 J_2}{r^3} P_2\left(\frac{\mathbf{r}^\top \hat{\mathbf{z}}}{r}\right) \quad (\text{A.42})$$

$$= -\frac{\mu a_e^2 J_2}{r^3} \left[\frac{3}{2} \left(\frac{\mathbf{r}^\top \hat{\mathbf{z}}}{r}\right)^2 - \frac{1}{2} \right] \quad (\text{A.43})$$

$$= -\frac{3\mu J_2}{2r} \left(\frac{a_e}{r}\right)^2 \left[\left(\frac{\mathbf{r}^\top \hat{\mathbf{z}}}{r}\right)^2 - \frac{1}{3} \right] \quad (\text{A.44})$$

The force on the spacecraft due only to this potential is

$$\mathbf{f}_{J_2} = \tilde{m} \left(\frac{\partial U_2}{\partial \mathbf{r}} \right)^\top \quad (\text{A.45})$$

The partial of the potential with respect to the spacecraft position is

$$\frac{\partial U_2}{\partial \mathbf{r}} = \frac{\partial}{\partial \mathbf{r}} \left\{ -\frac{3\mu J_2}{2r} \left(\frac{a_e}{r}\right)^2 \left[\left(\frac{\mathbf{r}^\top \hat{\mathbf{z}}}{r}\right)^2 - \frac{1}{3} \right] \right\} \quad (\text{A.46})$$

$$= \frac{\partial}{\partial \mathbf{r}} \left\{ -\frac{3\mu J_2 a_e^2}{2} (\mathbf{r}^\top \mathbf{r})^{-\frac{3}{2}} \left[\left(\mathbf{r}^\top \hat{\mathbf{z}} (\mathbf{r}^\top \mathbf{r})^{-\frac{1}{2}}\right)^2 - \frac{1}{3} \right] \right\} \quad (\text{A.47})$$

$$= \frac{9J_2 \mu a_e^2}{2r^5} \mathbf{r}^\top \left[\left(\frac{\mathbf{r}^\top \hat{\mathbf{z}}}{r}\right)^2 - \frac{1}{3} \right] - \frac{3J_2 \mu a_e^2}{r^3} \left[\left(\frac{\mathbf{r}^\top \hat{\mathbf{z}}}{r}\right) \left(\frac{\hat{\mathbf{z}}^\top}{r} - \frac{\mathbf{r}^\top \hat{\mathbf{z}}}{r^3} \mathbf{r}^\top \right) \right] \quad (\text{A.48})$$

Continuing,

$$\left(\frac{\partial U_2}{\partial \mathbf{r}} \right)^\top = -\frac{3J_2 \mu a_e^2}{2r^5} \left[-5 \left(\frac{\mathbf{r}^\top \hat{\mathbf{z}}}{r}\right)^2 \mathbf{r} + \mathbf{I} \mathbf{r} + 2 (\mathbf{r}^\top \hat{\mathbf{z}}) \mathbf{I} \hat{\mathbf{z}} \right] \quad (\text{A.49})$$

With $\tilde{m} \equiv 1$, the acceleration on the spacecraft due to J_2 effects becomes

$$\ddot{\mathbf{r}}_{J_2} = -\frac{3J_2 \mu a_e^2}{2r^5} \left(\begin{bmatrix} 1 & 0 & 0 \\ 0 & 1 & 0 \\ 0 & 0 & 3 \end{bmatrix} - 5 \left(\frac{\mathbf{r}^\top \hat{\mathbf{z}}}{r}\right)^2 \mathbf{I} \right) \mathbf{r} \quad (\text{A.50})$$

Appendix B

Lunar Flyby Velocity

The reference frame associated with the rotating basis vectors of the CRTBP is referred to as the $\hat{\mathbf{x}}\hat{\mathbf{y}}\hat{\mathbf{z}}$ frame, where $\hat{\mathbf{x}}$ is along the Earth-moon line, and $\hat{\mathbf{y}}$ is in the direction of the moon's velocity. Since the free return lunar flyby velocity orientation is completely specified by the latitude ϕ relative to the Earth-moon plane, the velocity azimuth θ , and the flight path angle γ , it is convenient to develop an expression for the velocity in terms of the $\hat{\mathbf{x}}\hat{\mathbf{y}}\hat{\mathbf{z}}$ basis as a function of these three angles.

First, rotate the $\hat{\mathbf{x}}$ axis so it is coincident with \mathbf{r}_{MP} , the lunar flyby position relative to the moon; this is equivalent to a rotation of $-\phi$ about the $\hat{\mathbf{y}}$ axis (Fig. B.1(a)). Next, rotate $\hat{\mathbf{z}}'$ through an azimuth of θ ; this is equivalent to a rotation of $-\theta$ about the $\hat{\mathbf{x}}'$ axis since the azimuth is measured east from north (Fig. B.1(b)). Finally, perform a rotation of γ about the $\hat{\mathbf{y}}''$ axis to rotate the $\hat{\mathbf{z}}''$ axis so it is coincident with the flyby velocity vector (Fig. B.1(c)). Thus, the transformation from the $\hat{\mathbf{x}}\hat{\mathbf{y}}\hat{\mathbf{z}}$ frame to the $\hat{\mathbf{t}}\hat{\mathbf{u}}\hat{\mathbf{v}}$ frame is

$$\begin{bmatrix} \hat{\mathbf{t}}^\top \\ \hat{\mathbf{u}}^\top \\ \hat{\mathbf{v}}^\top \end{bmatrix} = \mathbf{R}_2(\gamma)\mathbf{R}_1(-\theta)\mathbf{R}_2(-\phi) \begin{bmatrix} \hat{\mathbf{x}}^\top \\ \hat{\mathbf{y}}^\top \\ \hat{\mathbf{z}}^\top \end{bmatrix} \quad (\text{B.1})$$

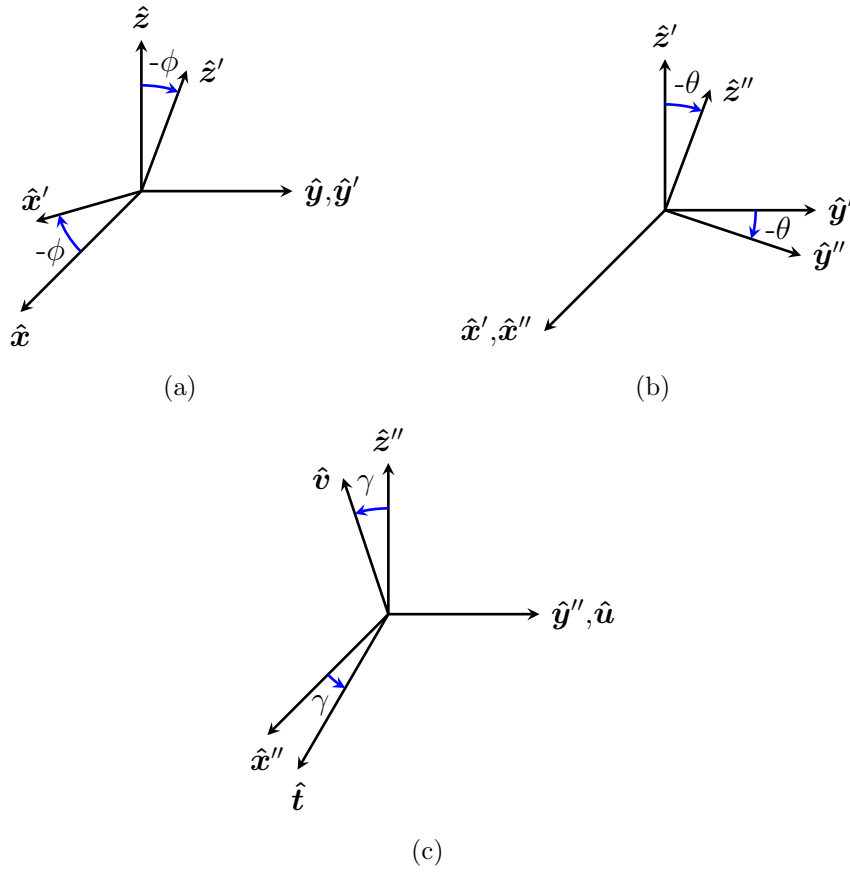


Figure B.1: Basis transformation: a) latitude rotation, b) azimuth rotation, and c) flight path angle rotation.

The inverse transformation is

$$\begin{bmatrix} \hat{\mathbf{x}}^\top \\ \hat{\mathbf{y}}^\top \\ \hat{\mathbf{z}}^\top \end{bmatrix} = \mathbf{R}_2^\top(-\phi)\mathbf{R}_1^\top(-\theta)\mathbf{R}_2^\top(\gamma) \begin{bmatrix} \hat{\mathbf{t}}^\top \\ \hat{\mathbf{u}}^\top \\ \hat{\mathbf{v}}^\top \end{bmatrix} \quad (\text{B.2})$$

Expanding,

$$\begin{bmatrix} \hat{\mathbf{x}}^\top \\ \hat{\mathbf{y}}^\top \\ \hat{\mathbf{z}}^\top \end{bmatrix} = \begin{bmatrix} \cos -\phi & 0 & \sin -\phi \\ 0 & 1 & 0 \\ -\sin -\phi & 0 & \cos -\phi \end{bmatrix} \begin{bmatrix} 1 & 0 & 0 \\ 0 & \cos -\theta & -\sin -\theta \\ 0 & \sin -\theta & \cos -\theta \end{bmatrix} \begin{bmatrix} \cos \gamma & 0 & \sin \gamma \\ 0 & 1 & 0 \\ -\sin \gamma & 0 & \cos \gamma \end{bmatrix} \begin{bmatrix} \hat{\mathbf{t}}^\top \\ \hat{\mathbf{u}}^\top \\ \hat{\mathbf{v}}^\top \end{bmatrix} \quad (\text{B.3})$$

$$\begin{bmatrix} \hat{\mathbf{x}}^\top \\ \hat{\mathbf{y}}^\top \\ \hat{\mathbf{z}}^\top \end{bmatrix} = \begin{bmatrix} \cos \phi & \sin \phi \sin \theta & -\sin \phi \cos \theta \\ 0 & \cos \theta & \sin \theta \\ \sin \phi & -\cos \phi \sin \theta & \cos \phi \cos \theta \end{bmatrix} \begin{bmatrix} \cos \gamma & 0 & \sin \gamma \\ 0 & 1 & 0 \\ -\sin \gamma & 0 & \cos \gamma \end{bmatrix} \begin{bmatrix} \hat{\mathbf{t}}^\top \\ \hat{\mathbf{u}}^\top \\ \hat{\mathbf{v}}^\top \end{bmatrix} \quad (\text{B.4})$$

$$\begin{bmatrix} \hat{\mathbf{x}}^\top \\ \hat{\mathbf{y}}^\top \\ \hat{\mathbf{z}}^\top \end{bmatrix} = \begin{bmatrix} \cos \phi \cos \gamma + \sin \phi \cos \theta \sin \gamma & \sin \phi \sin \theta & \cos \phi \sin \gamma - \sin \phi \cos \theta \cos \gamma \\ -\sin \theta \sin \gamma & \cos \theta & \sin \theta \cos \gamma \\ \sin \phi \cos \gamma - \cos \phi \cos \theta \sin \gamma & -\cos \phi \sin \theta & \sin \phi \sin \gamma + \cos \phi \cos \theta \cos \gamma \end{bmatrix} \begin{bmatrix} \hat{\mathbf{t}}^\top \\ \hat{\mathbf{u}}^\top \\ \hat{\mathbf{v}}^\top \end{bmatrix} \quad (\text{B.5})$$

Thus, any vector written in the $\hat{\mathbf{t}}\hat{\mathbf{u}}\hat{\mathbf{v}}$ basis can be expressed in the $\hat{\mathbf{x}}\hat{\mathbf{y}}\hat{\mathbf{z}}$ basis by multiplying the vector by the transformation matrix in Eq. (B.5). Since the flyby velocity is $\mathbf{v} = v\hat{\mathbf{v}}$, the velocity expressed in the $\hat{\mathbf{x}}\hat{\mathbf{y}}\hat{\mathbf{z}}$ basis is

$$\begin{aligned} \mathbf{v} &= v (\cos \phi \sin \gamma - \sin \phi \cos \theta \cos \gamma) \hat{\mathbf{x}} \\ &+ v (\sin \theta \cos \gamma) \hat{\mathbf{y}} \\ &+ v (\sin \phi \sin \gamma + \cos \phi \cos \theta \cos \gamma) \hat{\mathbf{z}} \end{aligned} \quad (\text{B.6})$$

Appendix C

Optimal Control Necessary Conditions

Consider the problem of choosing a control history $\mathbf{u}(t)$ that minimizes a scalar performance index given by

$$J = \phi(t_0, \mathbf{x}_0, t_f, \mathbf{x}_f, \mathbf{a}) + \int_{t_0}^{t_f} L(t, \mathbf{x}, \mathbf{u}, \mathbf{a}) dt \quad (\text{C.1})$$

where ϕ is the scalar cost, L is the Lagrangian which determines the accumulated cost, \mathbf{x} is the state, and \mathbf{a} is a vector of parameters. The minimization of the performance index is subject to the system dynamics given by

$$\dot{\mathbf{x}} = \mathbf{f}(t, \mathbf{x}, \mathbf{u}, \mathbf{a}) \quad (\text{C.2})$$

In general, constraints placed on the initial conditions are given by

$$\boldsymbol{\theta}(t_0, \mathbf{x}_0, \mathbf{a}) = \mathbf{0} \quad (\text{C.3})$$

and constraints on the final conditions are given by

$$\boldsymbol{\psi}(t_f, \mathbf{x}_f, \mathbf{a}) = \mathbf{0} \quad (\text{C.4})$$

Augmenting the performance index with the constraints gives

$$\begin{aligned} J' = & \phi(t_0, \mathbf{x}_0, t_f, \mathbf{x}_f, \mathbf{a}) + \boldsymbol{\nu}^\top \boldsymbol{\psi}(t_f, \mathbf{x}_f, \mathbf{a}) + \boldsymbol{\xi}^\top \boldsymbol{\theta}(t_0, \mathbf{x}_0, \mathbf{a}) \\ & + \int_{t_0}^{t_f} [L(t, \mathbf{x}, \mathbf{u}, \mathbf{a}) + \boldsymbol{\lambda}^\top (\mathbf{f} - \dot{\mathbf{x}})] dt \end{aligned} \quad (\text{C.5})$$

where $\boldsymbol{\nu}$, $\boldsymbol{\xi}$, and $\boldsymbol{\lambda}(t)$ are Lagrange multipliers. Define the endpoint function as

$$G(t_f, \mathbf{x}_f, \boldsymbol{\nu}, t_0, \mathbf{x}_0, \boldsymbol{\xi}, \mathbf{a}) \equiv \phi(t_0, \mathbf{x}_0, t_f, \mathbf{x}_f, \mathbf{a}) + \boldsymbol{\nu}^\top \boldsymbol{\psi}(t_f, \mathbf{x}_f, \mathbf{a}) + \boldsymbol{\xi}^\top \boldsymbol{\theta}(t_0, \mathbf{x}_0, \mathbf{a}) \quad (\text{C.6})$$

and the Hamiltonian as

$$H(t, x, \mathbf{u}, \boldsymbol{\lambda}, \mathbf{a}) \equiv L(t, \mathbf{x}, \mathbf{u}, \mathbf{a}) + \boldsymbol{\lambda}^\top \mathbf{f}(t, \mathbf{x}, \mathbf{u}, \mathbf{a}) \quad (\text{C.7})$$

Substituting these definitions into Eq. (C.5) gives

$$J' = G(t_f, \mathbf{x}_f, \boldsymbol{\nu}, t_0, \mathbf{x}_0, \boldsymbol{\xi}, \mathbf{a}) + \int_{t_0}^{t_f} [H(t, x, \mathbf{u}, \boldsymbol{\lambda}, \mathbf{a}) - \boldsymbol{\lambda}^\top \dot{\mathbf{x}}] dt \quad (\text{C.8})$$

At a minimum point, it is necessary that the first differential of the performance index is zero. Taking the differential of J' gives

$$\begin{aligned} dJ' = & G_{t_f} dt_f + G_{\mathbf{x}_f} d\mathbf{x}_f + G_{\boldsymbol{\nu}} d\boldsymbol{\nu} + G_{t_0} dt_0 + G_{\mathbf{x}_0} d\mathbf{x}_0 + G_{\boldsymbol{\xi}} d\boldsymbol{\xi} + G_{\mathbf{a}} d\mathbf{a} + [H - \boldsymbol{\lambda}^\top \dot{\mathbf{x}}] dt \Big|_{t_0}^{t_f} \\ & + \int_{t_0}^{t_f} [H_{\mathbf{x}} \delta \mathbf{x} + H_{\mathbf{u}} \delta \mathbf{u} + H_{\boldsymbol{\lambda}} \delta \boldsymbol{\lambda} + H_{\mathbf{a}} d\mathbf{a} - \delta \boldsymbol{\lambda}^\top \dot{\mathbf{x}} - \boldsymbol{\lambda}^\top \delta \dot{\mathbf{x}}] dt \end{aligned} \quad (\text{C.9})$$

where subscripts indicate partial derivatives for notational simplicity; for example, $G_{t_f} \equiv \partial G / \partial t_f$. It is seen that $G_{\boldsymbol{\nu}} = \boldsymbol{\psi}^\top = \mathbf{0}^\top$ and $G_{\boldsymbol{\xi}} = \boldsymbol{\theta}^\top = \mathbf{0}^\top$. Also, $H_{\boldsymbol{\lambda}} = \mathbf{f}^\top$, so $H_{\boldsymbol{\lambda}} \delta \boldsymbol{\lambda} - \delta \boldsymbol{\lambda}^\top \dot{\mathbf{x}} = 0$. Integrating the last term in the integral of Eq. (C.9) by parts gives

$$- \int_{t_0}^{t_f} \boldsymbol{\lambda}^\top \delta \dot{\mathbf{x}} dt = - \left[\boldsymbol{\lambda}^\top \delta \mathbf{x} \Big|_{t_0}^{t_f} - \int_{t_0}^{t_f} \dot{\boldsymbol{\lambda}}^\top \delta \mathbf{x} dt \right] \quad (\text{C.10})$$

Inserting these results into Eq. (C.9) gives

$$\begin{aligned} dJ' = & G_{t_f} dt_f + G_{\mathbf{x}_f} d\mathbf{x}_f + G_{t_0} dt_0 + G_{\mathbf{x}_0} d\mathbf{x}_0 + G_{\mathbf{a}} d\mathbf{a} + [H - \boldsymbol{\lambda}^\top \dot{\mathbf{x}}] dt \Big|_{t_0}^{t_f} \\ & - \boldsymbol{\lambda}^\top \delta \mathbf{x} \Big|_{t_0}^{t_f} + \int_{t_0}^{t_f} [H_{\mathbf{x}} \delta \mathbf{x} + H_{\mathbf{u}} \delta \mathbf{u} + H_{\mathbf{a}} d\mathbf{a} + \dot{\boldsymbol{\lambda}}^\top \delta \mathbf{x}] dt \end{aligned} \quad (\text{C.11})$$

Expanding,

$$\begin{aligned}
dJ' &= G_{t_f} dt_f + G_{\mathbf{x}_f} d\mathbf{x}_f + G_{t_0} dt_0 + G_{\mathbf{x}_0} d\mathbf{x}_0 + G_{\mathbf{a}} d\mathbf{a} + \int_{t_0}^{t_f} H_{\mathbf{a}} dt d\mathbf{a} \\
&+ H_f dt_f - \boldsymbol{\lambda}_f^\top \dot{\mathbf{x}}_f dt_f - H_0 dt_0 + \boldsymbol{\lambda}_0^\top \dot{\mathbf{x}}_0 dt_0 \\
&- \boldsymbol{\lambda}_f^\top \delta \mathbf{x}_f + \boldsymbol{\lambda}_0^\top \delta \mathbf{x}_0 + \int_{t_0}^{t_f} \left[(H_{\mathbf{x}} + \dot{\boldsymbol{\lambda}}^\top) \delta \mathbf{x} + H_{\mathbf{u}} \delta \mathbf{u} \right] dt
\end{aligned} \tag{C.12}$$

$$\begin{aligned}
dJ' &= G_{t_f} dt_f + G_{\mathbf{x}_f} d\mathbf{x}_f + G_{t_0} dt_0 + G_{\mathbf{x}_0} d\mathbf{x}_0 + G_{\mathbf{a}} d\mathbf{a} + \int_{t_0}^{t_f} H_{\mathbf{a}} dt d\mathbf{a} \\
&+ H_f dt_f - \boldsymbol{\lambda}_f^\top \dot{\mathbf{x}}_f dt_f - H_0 dt_0 + \boldsymbol{\lambda}_0^\top \dot{\mathbf{x}}_0 dt_0 \\
&- \boldsymbol{\lambda}_f^\top (d\mathbf{x}_f - \dot{\mathbf{x}}_f dt_f) + \boldsymbol{\lambda}_0^\top (d\mathbf{x}_0 - \dot{\mathbf{x}}_0 dt_0) + \int_{t_0}^{t_f} \left[(H_{\mathbf{x}} + \dot{\boldsymbol{\lambda}}^\top) \delta \mathbf{x} + H_{\mathbf{u}} \delta \mathbf{u} \right] dt
\end{aligned} \tag{C.13}$$

Grouping terms,

$$\begin{aligned}
dJ' &= (G_{t_f} + H_f) dt_f + (G_{\mathbf{x}_f} - \boldsymbol{\lambda}_f^\top) d\mathbf{x}_f + (G_{t_0} - H_0) dt_0 + (G_{\mathbf{x}_0} + \boldsymbol{\lambda}_0^\top) d\mathbf{x}_0 \\
&+ \left(G_{\mathbf{a}} + \int_{t_0}^{t_f} H_{\mathbf{a}} dt \right) d\mathbf{a} + \int_{t_0}^{t_f} \left[(H_{\mathbf{x}} + \dot{\boldsymbol{\lambda}}^\top) \delta \mathbf{x} + H_{\mathbf{u}} \delta \mathbf{u} \right] dt
\end{aligned} \tag{C.14}$$

Since $dJ' = 0$ on an optimal path, choose the Lagrange multipliers such that

$$H_f = -G_{t_f} \tag{C.15}$$

$$\boldsymbol{\lambda}_f^\top = G_{\mathbf{x}_f} \tag{C.16}$$

$$H_0 = G_{t_0} \tag{C.17}$$

$$\boldsymbol{\lambda}_0^\top = -G_{\mathbf{x}_0} \tag{C.18}$$

$$\dot{\boldsymbol{\lambda}}^\top = -H_{\mathbf{x}} \tag{C.19}$$

Also require

$$G_{\mathbf{a}} + \int_{t_0}^{t_f} H_{\mathbf{a}} dt = \mathbf{0}^\top \tag{C.20}$$

Thus, the differential of the augmented performance index becomes

$$dJ' = \int_{t_0}^{t_f} H_{\mathbf{u}} \delta \mathbf{u} dt \quad (\text{C.21})$$

For the first differential to be zero,

$$H_{\mathbf{u}} = \mathbf{0}^\top \quad (\text{C.22})$$

Equations (C.15)–(C.20) and Eq. (C.22) are necessary, but not sufficient, conditions for a minimum. In summary, the conditions given by

$$\dot{\mathbf{x}} = \mathbf{f} \quad (\text{C.23})$$

$$\dot{\boldsymbol{\lambda}} = - \left(\frac{\partial H}{\partial \mathbf{x}} \right)^\top \quad (\text{C.24})$$

$$\mathbf{0} = \left(\frac{\partial H}{\partial \mathbf{u}} \right)^\top \quad (\text{C.25})$$

are called the Euler-Lagrange equations, and the conditions given by

$$H_0 = \frac{\partial G}{\partial t_0} \quad (\text{C.26})$$

$$\boldsymbol{\lambda}_0 = - \left(\frac{\partial G}{\partial \mathbf{x}_0} \right)^\top \quad (\text{C.27})$$

$$H_f = - \frac{\partial G}{\partial t_f} \quad (\text{C.28})$$

$$\boldsymbol{\lambda}_f = \left(\frac{\partial G}{\partial \mathbf{x}_f} \right)^\top \quad (\text{C.29})$$

are called the natural boundary conditions or the transversality conditions. The parameter conditions require

$$G_{\mathbf{a}} + \int_{t_0}^{t_f} H_{\mathbf{a}} dt = \mathbf{0}^\top \quad (\text{C.30})$$

The derivation of the Euler-Lagrange equations and the natural boundary conditions is discussed in more detail by Hull [97].

Appendix D

R and C Matrix Notation

The \mathbf{R} and \mathbf{C} matrix nomenclature is developed for notational simplicity. In this dissertation, the notation is used extensively in analytical gradient derivations. The purpose of these matrices is to extract specified rows and columns of a target matrix. An \mathbf{R} matrix, denoted $\mathbf{R}_{r_1:r_2}$, is an $(r_2 - r_1 + 1) \times r$ matrix where r is the number of rows of the target matrix. Pre-multiplying a matrix with $\mathbf{R}_{r_1:r_2}$ keeps rows r_1 through r_2 of the target matrix. The matrix $\mathbf{R}_{r_1:r_2}$ is given by

$$\mathbf{R}_{r_1:r_2} \equiv \begin{bmatrix} \mathbf{0}_{n_r \times (r_1-1)} & \mathbf{I}_{n_r \times n_r} & \mathbf{0}_{n_r \times (r-r_2)} \end{bmatrix}_{n_r \times r} \quad (\text{D.1})$$

where

$$n_r \equiv r_2 - r_1 + 1 \quad (\text{D.2})$$

is the number of remaining rows after multiplying $\mathbf{R}_{r_1:r_2}$ with the target matrix.

Similarly, a \mathbf{C} matrix, denoted $\mathbf{C}_{c_1:c_2}$, is a $c \times (c_2 - c_1 + 1)$ matrix where c is the number of columns of the target matrix. Post-multiplying a matrix by $\mathbf{C}_{c_1:c_2}$ keeps columns c_1 through c_2 of the target matrix. The matrix $\mathbf{C}_{c_1:c_2}$ is given by

$$\mathbf{C}_{c_1:c_2} \equiv \begin{bmatrix} \mathbf{0}_{(c_1-1) \times n_c} \\ \mathbf{I}_{n_c \times n_c} \\ \mathbf{0}_{(c-c_2) \times n_c} \end{bmatrix}_{c \times n_c} \quad (\text{D.3})$$

where

$$n_c \equiv c_2 - c_1 + 1 \quad (\text{D.4})$$

is the number of remaining columns after post-multiplying the target matrix by $\mathbf{C}_{r_1:r_2}$. It is unnecessary to explicitly specify the dimensions of \mathbf{R} and \mathbf{C} matrices since one dimension is defined by the number of target rows or columns, and the other dimension is dictated by the dimension of the target matrix. If $r_1 = r_2$, then $\mathbf{R}_{r_1:r_2}$ is a row vector, and if $c_1 = c_2$, then $\mathbf{C}_{c_1:c_2}$ is a column vector.

Appendix E

Ideal Rocket Equation

E.1 Changing Mass Systems

The impulse-momentum principle states that the change in the linear momentum of a system equals the applied linear impulse [106]. Symbolically,

$$\mathbf{p}(t_1) + \int_{t_1}^{t_2} \mathbf{f} dt = \mathbf{p}(t_2) \quad (\text{E.1})$$

where $\mathbf{p}(t_i)$ is the linear momentum at time t_i , and \mathbf{f} is the vector sum of the external forces. Consider the changing mass system shown in Fig. E.1. At time t , the linear momentum of the system is

$$\mathbf{p}(t) = \Delta m_i \dot{\mathbf{r}}_i + (M + \Delta m_o) \dot{\mathbf{r}}(t) \quad (\text{E.2})$$

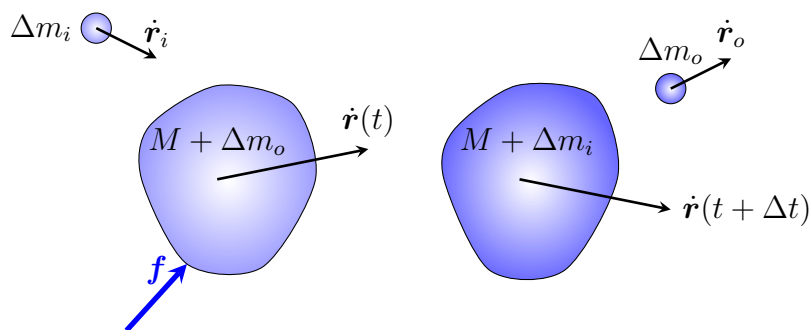


Figure E.1: Changing mass system.

where Δm_i is incoming mass, $\dot{\mathbf{r}}_i$ is the velocity of the incoming mass, $M + \Delta m_o$ is the total mass of the control volume at time t , and $\dot{\mathbf{r}}(t)$ is the velocity of all particles in the main control volume. An impulse is applied over a time period of Δt , and the linear momentum of the system becomes

$$\mathbf{p}(t + \Delta t) = (M + \Delta m_i)\dot{\mathbf{r}}(t + \Delta t) + \Delta m_o\dot{\mathbf{r}}_o \quad (\text{E.3})$$

where $M + \Delta m_i$ is the mass of the control volume at time $t + \Delta t$, $\dot{\mathbf{r}}(t + \Delta t)$ is the velocity of all the particles in the control volume, Δm_o is the outgoing mass, and $\dot{\mathbf{r}}_o$ is the velocity of the outgoing mass. By Eq. (E.1),

$$\Delta m_i\dot{\mathbf{r}}_i + (M + \Delta m_o)\dot{\mathbf{r}}(t) + \mathbf{f}\Delta t = (M + \Delta m_i)\dot{\mathbf{r}}(t + \Delta t) + \Delta m_o\dot{\mathbf{r}}_o \quad (\text{E.4})$$

Solving for \mathbf{f} ,

$$\mathbf{f}\Delta t = (M + \Delta m_i)\dot{\mathbf{r}}(t + \Delta t) + \Delta m_o\dot{\mathbf{r}}_o - [\Delta m_i\dot{\mathbf{r}}_i + (M + \Delta m_o)\dot{\mathbf{r}}(t)] \quad (\text{E.5})$$

$$\mathbf{f}\Delta t = M [\dot{\mathbf{r}}(t + \Delta t) - \dot{\mathbf{r}}(t)] + \Delta m_i(\dot{\mathbf{r}}(t + \Delta t) - \dot{\mathbf{r}}_i) + \Delta m_o(\dot{\mathbf{r}}_o - \dot{\mathbf{r}}(t)) \quad (\text{E.6})$$

$$\mathbf{f} = M \frac{\dot{\mathbf{r}}(t + \Delta t) - \dot{\mathbf{r}}(t)}{\Delta t} + \frac{\Delta m_i}{\Delta t}(\dot{\mathbf{r}}(t + \Delta t) - \dot{\mathbf{r}}_i) + \frac{\Delta m_o}{\Delta t}(\dot{\mathbf{r}}_o - \dot{\mathbf{r}}(t)) \quad (\text{E.7})$$

Taking the limit as $\Delta t \rightarrow 0$ gives

$$\mathbf{f} = M\ddot{\mathbf{r}} + \dot{m}_i(\dot{\mathbf{r}} - \dot{\mathbf{r}}_i) - \dot{m}_o(\dot{\mathbf{r}} - \dot{\mathbf{r}}_o) \quad (\text{E.8})$$

where $\ddot{\mathbf{r}}$ is the acceleration of the control volume, \dot{m}_i is the incoming mass flow rate, and \dot{m}_o is the outgoing mass flow rate. This is Newton's second law for a changing mass system. The derivation closely follows that given by Bennighof.¹

¹Bennighof, J. K., Lecture Notes for EM 381 Advanced Dynamics, Department of Aerospace Engineering and Engineering Mechanics, University of Texas at Austin, Jan. 2008.

E.2 Rocket Equation

Consider a rocket in flight with no external forces as shown in Fig. E.2. The rocket is traveling in the $\hat{\mathbf{j}}$ direction with a velocity \mathbf{v} while exhausting mass at a velocity of \mathbf{v}_E . Applying Newton's second law for a changing mass system gives

$$\mathbf{0} = M\ddot{\mathbf{r}} + \dot{m}_o(\dot{\mathbf{r}}_o - \dot{\mathbf{r}}) \quad (\text{E.9})$$

$$-M\ddot{\mathbf{r}} = \dot{m}_o(\mathbf{v}_E - \mathbf{v}) \quad (\text{E.10})$$

where the terms \mathbf{f} and \dot{m}_i of Eq. (E.8) are zero since there are no external forces and since there is no mass being added to the system. The total mass of the system is

$$M = m_* - m_o \quad (\text{E.11})$$

where m_* is the initial rocket mass, and m_o is the mass that has been expelled from the rocket. Differentiating with respect to time,

$$\frac{dM}{dt} = -\dot{m}_o \quad (\text{E.12})$$

Substituting Eq. (E.12) into Eq. (E.10) gives

$$-M \frac{d\mathbf{v}}{dt} = -\frac{dM}{dt}(\mathbf{v}_E - \mathbf{v}) \quad (\text{E.13})$$

$$M d\mathbf{v} = dM(\mathbf{v}_E - \mathbf{v}) \quad (\text{E.14})$$

The velocity of the exhaust relative to the velocity of the rocket is defined to be a constant given by $-c\hat{\mathbf{j}}$. This gives

$$M d\mathbf{v} = dM(-c\hat{\mathbf{j}}) \quad (\text{E.15})$$

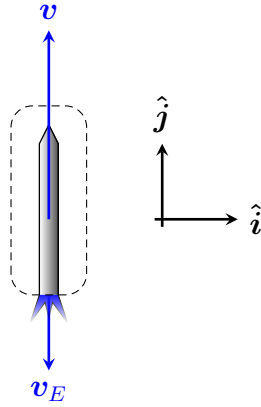


Figure E.2: Rocket and control volume.

Since all motion is along the \hat{j} axis, it is necessary to consider only scalar variables.

Continuing,

$$M dv = dM(-c) \quad (\text{E.16})$$

$$dv = -c \frac{dM}{M} \quad (\text{E.17})$$

Integrating with respect to time, from t_1 to t_2 where $t_2 > t_1$, gives

$$\int_{t_1}^{t_2} dv = -c \int_{t_1}^{t_2} \frac{dM}{M} \quad (\text{E.18})$$

$$v \Big|_{t_1}^{t_2} = -c \ln |m| \Big|_{t_1}^{t_2} \quad (\text{E.19})$$

Since the rocket's mass must always be positive, $|m| = m$. Continuing,

$$v(t_2) - v(t_1) = -c [\ln m(t_2) - \ln m(t_1)] \quad (\text{E.20})$$

$$\Delta v = -c \ln \frac{m_2}{m_1} \quad (\text{E.21})$$

$$\Delta v = c \ln \frac{m_1}{m_2} \quad (\text{E.22})$$

Equation (E.22) is known as the ideal rocket equation and gives an estimate of the change in the rocket's velocity based on its change in mass. It is seen that a mass loss ($m_2 < m_1$) due to exhausted material produces an increase in the rocket's velocity, as expected.

If the change in velocity is known, and it is desired to approximate the mass loss by the ideal rocket equation, Eq.(E.22) can be solved for the post-velocity impulse mass as

$$e^{\frac{\Delta v}{c}} = \frac{m_1}{m_2} \tag{E.23}$$

$$m_2 = m_1 e^{-\frac{\Delta v}{c}} \tag{E.24}$$

This result is known as the fuel equation. A more detailed presentation of ideal rockets is given by Sutton [107].

Bibliography

- [1] Colaprete, A., Schultz, P., Heldmann, J., et al., “Detection of Water in the LCROSS Ejecta Plume,” *Science*, Vol. 330, No. 6003, 2010, pp. 463–468.
- [2] Mitrofanov, I. G., Sanin, A. B., Boynton, W. V., et al., “Hydrogen Mapping of the Lunar South Pole Using the LRO Neutron Detector Experiment LEND,” *Science*, Vol. 330, No. 6003, 2010, pp. 483–486.
- [3] Sridharan, R., Ahmed, S. M., Das, T. P., et al., “Direct evidence for water in the sunlit lunar ambience from CHACE on MIP of Chandrayaan I,” *Planetary and Space Science*, Vol. 58, No. 6, 2010, pp. 947–950.
- [4] Cooley, D. S., Galal, K. F., Berry, K., et al., “Mission Design for the Lunar CRater Observation and Sensing Satellite (LCROSS),” *AIAA/AAS Astrodynamics Specialist Conference*, AIAA Paper 2010-8386, Aug. 2010.
- [5] Schultz, P. H., Hermalyn, B., Colaprete, A., et al., “The LCROSS Cratering Experiment,” *Science*, Vol. 330, No. 6003, 2010, pp. 468–472.
- [6] Stanley, D., Cook, S., Connolly, J., et al., *NASA’s Exploration Systems Architecture Study*, NASA-TM-2005-214062, Nov. 2005, pp. 193–197.
- [7] Senent, J. S., “Partial TLI, Post-TLI and Partial-LOI Abort Performance For Polar Lunar Missions,” NASA TN FltDyn-CEV-09-91, June 2009.
- [8] Braud, N. J., “Abort From a Coplanar Circumlunar Orbit,” NASA MTP-AERO-62-55, June 1962.
- [9] Kelly, T. J. and Adornato, R. J., “Determination of Abort Way-Stations on a Nominal Circumlunar Trajectory,” *ARS Journal*, Vol. 32, No. 6, 1962, pp. 887–893.
- [10] Merrick, R. B. and Callas, G. P., “Prediction of Velocity Requirements for Minimum Time Aborts From the Midcourse Region of a Lunar Mission,” NASA TN D-1655, April 1963.

- [11] Foggatt, C. E., "Two-Impulse Abort Maneuvers From a Lunar Mission," NASA MSC 66-FM-82, Aug. 1966.
- [12] Laszlo, W. O., "Minimum ΔV , Two- and Three-Impulse Non-Coplanar Abort Maneuvers Onto an Escape Asymptotic Velocity Vector Following Premature SPS Shutdown During LOI Phase," NASA MSC 68-FM-309, Dec. 1968.
- [13] Babb, G. R., "Translunar LM DPS Abort Techniques for Advanced Lunar Missions," NASA MSC 68-FM-189, Aug. 1968.
- [14] Babb, G. R., "Translunar Abort Techniques for Non-Free-Return Missions," NASA TM X-1806, 1969.
- [15] Weber, B. D., "Preliminary Contingency Procedures for the Translunar Injection Maneuver," NASA MSC 68-FM-122, May 1968.
- [16] Weber, B. D. and Fuller, J. D., "Preliminary Contingency Procedures for the Translunar Coast," NASA MSC 68-FM-222, Sept. 1968.
- [17] Hyle, C. T., Foggatt, C. E., and Weber, B. D., "Apollo Experience Report – Abort Planning," NASA TN D-6847, June 1972.
- [18] Caldwell, S. F. and Mummert, V. S., "Apollo Free Return Reentry Point Analysis," NASA CR-78347, Bellcomm, Inc., June 1966.
- [19] Wagner, R. L., "The Impact of Free Return Missions on the Apollo System," NASA CR-156515, Bellcomm, Inc., March 1966.
- [20] Cappellari, J. O., Kinney, W. D., Satterlee, A. A., and Tigner, R. D., "Free Return Lunar Accessibility Over Extended Time Periods," NASA CR-78563, Bellcomm, Inc., May 1965.
- [21] Stern, R. J., "Preliminary Evaluation of SM/RCS Capability to Abort to Earth Entry from the Relaxed Free Return Profile," NASA CR-113924, Bellcomm, Inc., Sept. 1970.
- [22] Caldwell, S. F., "Time Specific Apollo Lunar Surface Accessibility for Relaxed Free Return Missions - Computer Program Description," NASA CR-113509, Bellcomm, Inc., Sept. 1970.

- [23] Senent, J. S., “Fast Calculation of Abort Return Trajectories for Manned Missions to the Moon,” *AIAA/AAS Astrodynamics Specialists Conference*, AIAA Paper 2010-8132, Aug. 2010.
- [24] Wilson, S. W., “A Pseudostate Theory for the Approximation of Three-Body Trajectories,” TRW 69-FMT-765, 1969.
- [25] Egorov, V. A., *Three-Dimensional Lunar Trajectories*, Israel Program for Scientific Translations, Jerusalem, 1969, pp. 129–141.
- [26] Penzo, P., “An Analysis of Free-Flight Circumlunar Trajectories,” *AIAA Astrodynamics Conference*, AIAA Paper 63-404, New Haven, CT, Aug. 1963.
- [27] Schwaniger, A., “Trajectories in the Earth-Moon Space with Symmetrical Free Return Properties,” NASA TN D-1833, June 1963.
- [28] Gibson, T., “Application of the Matched Conic Model in the Study of Circumlunar Trajectories,” NASA Project Apollo Working Paper 1066, Feb. 1963.
- [29] Miele, A., Wang, T., and Mancuso, S., “Optimal Free-Return Trajectories for Moon Missions and Mars Missions,” *The Journal of the Astronautical Sciences*, Vol. 48, No. 2–3, 2000, pp. 183–206.
- [30] Corey, D. A., “A Discussion of the Proposed Two Burn Lunar Orbit Insertion Maneuver,” NASA CR-73521, Bellcomm, Inc., Aug. 1968.
- [31] Jenkins, M. V. and Munford, R. E., “Preliminary Study of Retrograde Velocities Required for Insertion Into Low-Altitude Lunar Orbits,” NASA TN D-1081, Sept. 1961.
- [32] Beckman, M., “Mission Design for the Lunar Reconnaissance Orbiter,” *AAS Guidance and Control Conference*, AAS Paper 07-057, Feb. 2006.
- [33] Hatch, S. J., Roncoli, R. B., and Sweetser, T. H., “GRAIL Trajectory Design: Lunar Orbit Insertion through Science,” *AIAA/AAS Astrodynamics Specialist Conference*, AIAA Paper 2010-8385, Aug. 2010.
- [34] Belbruno, E. A. and Miller, J. K., “Sun-Perturbed Earth-to-Moon Transfers with Ballistic Capture,” *Journal of Guidance, Control, and Dynamics*, Vol. 16, No. 4, 1993, pp. 770–775.

- [35] Griesemer, P. R., Ocampo, C., and Cooley, D. S., “Targeting Ballistic Lunar Capture Trajectories Using Periodic Orbits,” *Journal of Guidance, Control, and Dynamics*, Vol. 34, No. 3, 2011, pp. 893–902.
- [36] Parker, J. S., Anderson, R. L., and Peterson, A., “A Survey of Ballistic Transfers to Low Lunar Orbit,” *AAS/AIAA Space Flight Mechanics Meeting*, AAS Paper 11-277, Feb. 2011.
- [37] Nast, T., Frank, D., and Burns, K., “Cryogenic Propellant Boil-Off Reduction Approaches,” *AIAA Aerospace Sciences Meeting*, AIAA Paper 2011-806, Jan. 2011.
- [38] Doherty, M. P., Gaby, J. D., Salerno, L. J., and Sutherlin, S. G., “Cryogenic Fluid Management Technology for Moon and Mars Missions,” *AIAA Space Conference and Exposition*, AIAA Paper 2009-6532, Sept. 2009.
- [39] Garn, M., Qu, M., Chrono, J., Su, P., and Karlsgaard, C., “NASA’s Planned Return to the Moon: Global Access and Anytime Return Requirement Implications on the Lunar Orbit Insertion Burns,” *AIAA/AAS Astrodynamics Specialists Conference*, AIAA Paper 2008-7508, Aug. 2008.
- [40] Condon, G., “Lunar Orbit Insertion Targeting and Associated Outbound Mission Design for Lunar Sortie Missions,” *AIAA Guidance, Navigation, and Control Conference and Exhibit*, AIAA Paper 2007-6680, Aug. 2007.
- [41] Jesick, M. and Ocampo, C., “Automated Generation of Symmetric Lunar Free Return Trajectories,” *Journal of Guidance, Control, and Dynamics*, Vol. 34, No. 1, 2011, pp. 98–106.
- [42] Jesick, M. and Ocampo, C., “Computation and Optimization of Lunar Orbit Insertion from a Fixed Free Return,” *Journal of the Astronautical Sciences*, Vol. 58, No. 1, 2011, pp. 35–53.
- [43] Jesick, M. and Ocampo, C., “Lunar Orbit Insertion from a Variable Symmetric Free Return Trajectory,” *Journal of Guidance, Control, and Dynamics*, Vol. 34, No. 6, 2011.

- [44] Jesick, M. and Ocampo, C., “Ephemeris Model Optimization of Lunar Orbit Insertion from a Free Return Trajectory,” *AAS/AIAA Astrodynamics Specialists Conference*, AAS Paper 11-452, Aug. 2011.
- [45] Szebehely, V., *Theory of Orbits: The Restricted Problem of Three Bodies*, Academic Press, New York, 1967, pp. 7–40.
- [46] Battin, R. H., *An Introduction to the Mathematics and Methods of Astrodynamics, Revised Edition*, AIAA, Reston, VA, 1999, pp. 450–463.
- [47] Hindmarsh, A. C., *ODEPACK, A Systematized Collection of ODE Solvers*, North-Holland, Amsterdam, 1983, pp. 55–64.
- [48] Folkner, W. M., Williams, J. G., and Boggs, D. H., “The Planetary and Lunar Ephemeris DE 421,” IPN Progress Report 42-178, Aug. 2009.
- [49] Tapley, B. D., Schutz, B. E., and Born, G. H., *Statistical Orbit Determination*, Elsevier, Burlington, MA, 2004, pp. 50–61.
- [50] Vallado, D. A., *Fundamentals of Astrodynamics and Applications, Second Edition*, Microcosm Press, El Segundo, CA, 2001, pp. 359, 546.
- [51] Wie, B., *Space Vehicle Dynamics and Control*, AIAA, Reston, VA, 1998, pp. 307–310.
- [52] Orloff, R. W., *Apollo by the Numbers: A Statistical Reference*, U. S. Government Printing Office, Washington, 2000, pp. 291,305.
- [53] “Apollo 10 Press Kit,” NASA Release 69-68, May 1969.
- [54] “Apollo 11 Mission Report,” NASA MSC-00171, Nov. 1969.
- [55] “Apollo 12 Mission Report,” NASA MSC-01855, March 1970.
- [56] Lunney, G., “Discussion of Several Problem Areas During the Apollo 13 Operation,” *AIAA 7th Annual Meeting and Technical Display*, AIAA Paper 70-1260, Oct. 1970.
- [57] “Apollo 14 Mission Report,” NASA MSC-04112, April 1971.

- [58] “Apollo Program Summary Report,” NASA JSC-09423, April 1975.
- [59] “Apollo 16 Press Kit,” NASA Release 72-64, April 1972.
- [60] “Apollo 17 Press Kit,” NASA Release 72-220, Nov. 1972.
- [61] Mathur, R. and Ocampo, C. A., “An Algorithm for Computing Optimal Earth Centered Orbit Transfers via Lunar Gravity Assist,” *AIAA/AAS Astrodynamics Specialists Conference*, AIAA Paper 2010-7521, Aug. 2010.
- [62] Ocampo, C. A., “Transfers to Earth centered orbits via lunar gravity assist,” *Acta Astronautica*, Vol. 52, No. 2, 2003, pp. 173–179.
- [63] Ivashkin, V. V. and Tupitsyn, N. N., “Use of the Moon’s Gravitational Field to Inject a Space Vehicle into a Stationary Earth-Satellite Orbit,” *Cosmic Research*, Vol. 9, No. 2, 1971, pp. 151–159.
- [64] Graziani, F., Gastronuovo, M. M., and Teofilatto, P., “Geostationary orbits from mid-latitude launch sites via lunar gravity assist,” *Advances in the Astronautical Sciences*, Vol. 84, Aug. 1993, pp. 561–572.
- [65] Ocampo, C., “Trajectory Analysis for the Lunar Flyby Rescue of AsiaSat-3 / HGS-1,” *Annals of the New York Academy of Sciences*, Vol. 1065, 2005.
- [66] Miele, A., “Theorem of Image Trajectories in the Earth-Moon Space,” *Astronautica Acta*, Vol. 6, No. 5, 1960, pp. 225–232.
- [67] Powell, M. J. D., “A Fortran Subroutine for Solving Systems of Nonlinear Algebraic Equations,” *Numerical Methods for Nonlinear Algebraic Equations*, edited by P. Rabinowitz, Gordon and Breach, London, England, 1970, pp. 115–161.
- [68] Graves, C. A. and Harpold, J. C., “Apollo Experience Report – Mission Planning for Apollo Entry,” NASA TN D-6725, March 1972.
- [69] “Apollo 8 Press Kit,” NASA Release 68-208, Dec. 1968.
- [70] Bhatti, M. A., *Practical Optimization Methods*, Springer, New York, 2000, pp. 147–154.

- [71] Nelder, J. A. and Mead, R., “A simplex method for function minimization,” *Computer Journal*, Vol. 7, 1965, pp. 308–313.
- [72] Srinivas, M. and Patnaik, L. M., “Genetic Algorithms: A Survey,” *Computer*, Vol. 27, No. 6, 1994, pp. 17–26.
- [73] KrishnaKumar, K., “Genetic Algorithms – A Robust Optimization Tool,” *AIAA Aerospace Sciences Meeting and Exhibit*, AIAA Paper 93-0315, Jan. 1993.
- [74] Sentinella, M. R. and Casalino, L., “Hybrid Evolutionary Algorithm for the Optimization of Interplanetary Trajectories,” *Journal of Spacecraft and Rockets*, Vol. 46, No. 2, 2009, pp. 365–372.
- [75] Yokoyama, N. and Suzuki, S., “Modified Genetic Algorithm for Constrained Trajectory Optimization,” *Journal of Guidance, Control, and Dynamics*, Vol. 28, No. 1, 2005, pp. 139–144.
- [76] Huang, H. Y., “Unified Approach to Quadratically Convergent Algorithms for Function Minimization,” *Journal of Optimization Theory and Applications*, Vol. 5, No. 6, 1970, pp. 405–423.
- [77] Broyden, C. G., “A Class of Methods for Solving Nonlinear Simultaneous Equations,” *Mathematics of Computation*, Vol. 19, No. 92, 1965, pp. 577–593.
- [78] Fletcher, R., “A New Approach to Variable Metric Algorithms,” *Computer Journal*, Vol. 13, No. 3, 1970, pp. 317–322.
- [79] Goldfarb, D., “A Family of Variable-Metric Methods Derived by Variational Means,” *Mathematics of Computation*, Vol. 24, No. 109, 1970, pp. 23–26.
- [80] Shanno, D. F., “Conditioning of Quasi-Newton Methods for Function Minimization,” *Mathematics of Computation*, Vol. 24, No. 111, 1970, pp. 647–656.
- [81] Davidon, W. C., “Variable Metric Method for Minimization,” *SIAM Journal on Optimization*, Vol. 1, No. 1, 1991, pp. 1–17.
- [82] Fletcher, R. and Powell, M. J. D., “A rapidly convergent descent method for minimization,” *Computer Journal*, Vol. 6, No. 2, 1963, pp. 163–168.

- [83] Gill, P. E., Murray, W., and Saunders, M. A., “SNOPT: An SQP Algorithm for Large-Scale Constrained Optimization,” *SIAM Review*, Vol. 47, No. 1, 2005, pp. 99–131.
- [84] Juedes, D. W., “A Taxonomy of Automatic Differentiation Tools,” *SIAM Workshop on Automatic Differentiation*, TR 91-20, Jan. 1992.
- [85] Bischof, C. and Griewank, A., “ADIFOR: A Fortran System for Portable Automatic Differentiation,” *AIAA/USAF/NASA/OAI Symposium on Multi-disciplinary Analysis and Optimization*, AIAA 92-4744-CP, Sept. 1992.
- [86] Lyness, J. N. and Moler, C. B., “Numerical Differentiation of Analytic Functions,” *SIAM Journal on Numerical Analysis*, Vol. 4, No. 2, 1967, pp. 202–210.
- [87] Martins, J. R. R. A., Sturdza, P., and Alonso, J. J., “The Complex-Step Derivative Approximation,” *ACM Transactions on Mathematical Software*, Vol. 29, No. 3, 2003, pp. 245–262.
- [88] Hull, D. G. and Williamson, W. E., “Numerical Derivatives for Parameter Optimization,” *Journal of Guidance and Control*, Vol. 2, No. 2, 1979, pp. 158–160.
- [89] Ocampo, C. and Munoz, J.-P., “Variational Equations for a Generalized Spacecraft Trajectory Model,” *Journal of Guidance, Control, and Dynamics*, Vol. 33, No. 5, 2010, pp. 1615–1622.
- [90] Whitley, R. J., Ocampo, C. A., and Williams, J., “Performance of an Autonomous Multi-Maneuver Algorithm for Lunar Trans-Earth Injection,” *Journal of Spacecraft and Rockets*, Vol. 49, No. 1, 2012, pp. 165–174.
- [91] Ocampo, C. A. and Mathur, R., “Variational Model for Optimization of Finite-Burn Escape Trajectories Using a Direct Method,” *Journal of Guidance, Control, and Dynamics*, Vol. 35, No. 2, 2012, pp. 598–608.
- [92] Zimmer, S. and Ocampo, C., “Use of Analytical Gradients to Calculate Optimal Gravity-Assist Trajectories,” *Journal of Guidance, Control, and Dynamics*, Vol. 28, No. 2, 2005, pp. 324–332.

- [93] Zimmer, S. and Ocampo, C., “Analytical Gradients for Gravity Assist Trajectories Using Constant Specific Impulse Engines,” *Journal of Guidance, Control, and Dynamics*, Vol. 28, No. 4, 2005, pp. 753–760.
- [94] Gill, P. E., Murray, W., and Wright, M. H., *Practical Optimization*, Academic Press, Inc., London, 1981, pp. 273–275, 325–327, 346–355.
- [95] Betts, J. T., *Practical Methods for Optimal Control Using Nonlinear Programming*, Society for Industrial and Applied Mathematics, Philadelphia, 2001, pp. 35–36, 121–123.
- [96] Fourer, R., “Solving Staircase Linear Programs by the Simplex Method, 1: Inversion,” *Mathematical Programming*, Vol. 23, 1982, pp. 274–313.
- [97] Hull, D., *Optimal Control Theory for Applications*, Springer, New York, 2003, pp. 140–172.
- [98] Pontryagin, L. S., Boltyanskii, V. G., Gamkrelidze, R. V., and Mishchenko, E. F., *The Mathematical Theory of Optimal Processes*, Macmillan, New York, 1964, pp. 17–21.
- [99] Bate, R. R., Mueller, D. D., and White, J. E., *Fundamentals of Astrodynamics*, Dover, New York, 1971, pp. 188, 327, 333–334.
- [100] Taylor, B. N. and Thompson, A., “The International System of Units,” NIST SP–330, March 2008.
- [101] Zondervan, K. P., Wood, L. J., and Caughey, T. K., “Optimal Low-Thrust, Three-Burn Orbit Transfers with Large Plane Changes,” *Journal of the Astronautical Sciences*, Vol. 32, No. 3, 1984, pp. 407–427.
- [102] Kleuver, C. A. and Pierson, B. L., “Optimal Low-Thrust Three-Dimensional Earth-Moon Trajectories,” *Journal of Guidance, Control, and Dynamics*, Vol. 18, No. 4, 1995, pp. 830–837.
- [103] Lundberg, J. B. and Schutz, B. E., “Recursion Formulas of Legendre Functions for Use with Nonsingular Geopotential Models,” *Journal of Guidance, Control, and Dynamics*, Vol. 11, No. 1, 1988, pp. 31–38.

- [104] Hobson, E. W., *The Theory of Spherical and Ellipsoidal Harmonics*, Chelsea Publishing, New York, 1965, p. 141.
- [105] Kaula, W. M., *Theory of Satellite Geodesy: Applications of Satellites to Geodesy*, Dover, Mineola, NY, 2000, pp. 20–60.
- [106] Török, J. S., *Analytical Mechanics with an Introduction to Dynamical Systems*, Wiley, New York, 1999, pp. 14–16.
- [107] Sutton, G. P., *Rocket Propulsion Elements: An Introduction to the Engineering of Rockets, Sixth Edition*, Wiley, New York, 1992, pp. 23–31,41–47.

Vita

Mark Jesick graduated from the University of Notre Dame with the degree of Bachelor of Science in Aerospace Engineering in 2006. Mark performed research at the Hessert Laboratory for Aerospace Research and completed an internship with Honeywell Aerospace. At the University of Texas at Austin, he earned the degree of Master of Science in Aerospace Engineering in 2008 and was awarded a Graduate Student Researchers Program Fellowship by NASA. As part of his doctoral work, Mark completed research tours at NASA's Goddard Space Flight Center and NASA's Johnson Space Center. He earned the degree of Doctor of Philosophy in Aerospace Engineering in 2012.

This dissertation was typeset by the author.